An observational study of the western boundary currents in the Indian and South Atlantic Oceans

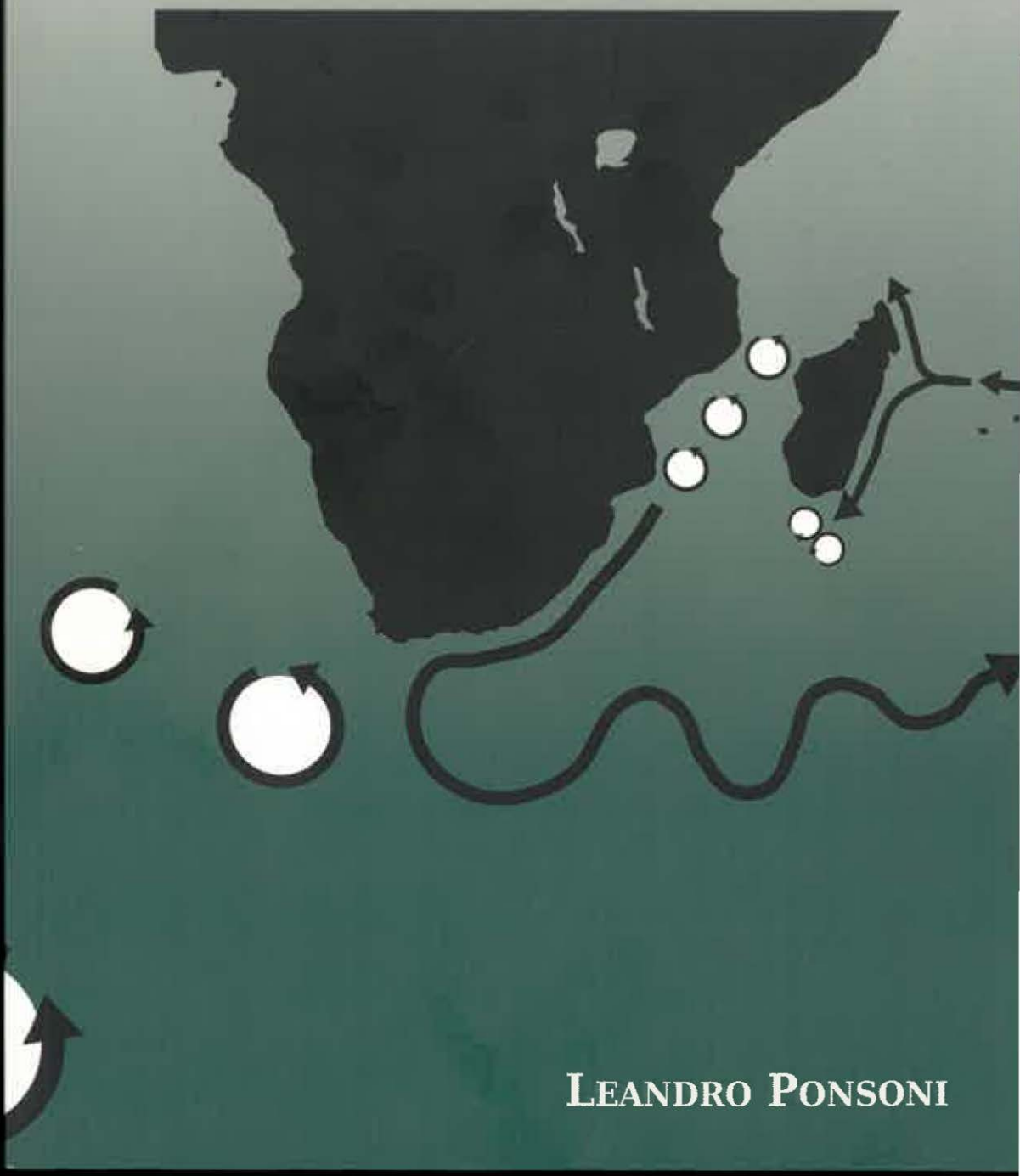

LEANDRO PONSONI

AN OBSERVATIONAL STUDY OF THE WESTERN BOUNDARY CURRENTS IN THE INDIAN AND SOUTH ATLANTIC OCEANS

LEANDRO PONSONI

Leandro Ponsoni
NIOZ - Royal Netherlands Institute for Sea Research, Utrecht University

Present address:
NIOZ - Royal Netherlands Institute for Sea Research
PO box 59, 1790AB Den Burg, Netherlands
Leandro.Ponsoni@nioz.nl
leandroponsoni@gmail.com

ISBN: 978-94-6299-374-7
Printing: Ridderprint BV

AN OBSERVATIONAL STUDY OF THE WESTERN BOUNDARY CURRENTS IN THE INDIAN AND SOUTH ATLANTIC OCEANS

Een observationele studie van de Westelijke Grenslaagstromen in de Indische en Zuid-Atlantische Oceanen
(met een samenvatting in het Nederlands)

Um estudo observacional do sistema de correntes de contorno oeste nos Oceanos Indíco e Atlântico Sul
(com resumo em Português)

Proefschrift

ter verkrijging van de graad van doctor aan de Universiteit Utrecht op gezag van de rector magnificus, prof.dr. G.J. van der Zwaan, ingevolge het besluit van het college voor promoties in het openbaar te verdedigen op maandag 4 juli 2016 des middags te 2.30 uur

door

LEANDRO PONSONI

geboren op 1 maart 1980
te São Paulo, Brazilië

PROMOTOR: **Prof. dr. L.R.M. Maas**

COPROMOTOR: **Dr. B. Aguiar-González**

The author was financially supported by “Coordenação de Aperfeiçoamento de Pessoal de Nível Superior" (CAPES), Brazil, and by the Royal Netherlands Institute for Sea Research (NIOZ), Netherlands.

I dedicate this work to my parents:
Dorival and Doralice

CONTENTS

Summary xi

Samenvatting xiii

Resumo xvii

1 General Introduction 1

1.1 Global patterns of ocean circulation 1
1.2 The Atlantic Ocean and its classical pattern of ocean gyres 5
1.3 The Indian Ocean and its peculiar ocean gyres 7
1.4 Interocean connections and a Southern Hemisphere Supergyre . . 9
1.5 Outline and open questions 11
1.6 Datasets and observational perspective of this study 13
1.7 Short guidance to the reader 15

2 The East Madagascar Current 17

2.1 Introduction 18
2.2 Data and data processing 21
2.2.1 INATEX moorings: instrumentation and data return 21
2.2.2 Mooring data processing 22
2.2.3 Supplementary data sources 26
2.3 In situ observations of the East Madagascar Current 26
2.3.1 Observed velocities, mean flow and mesoscale activity . . 26
2.3.2 Volume transport 31
2.3.3 Transport variability 33
2.4 Altimeter observations of the East Madagascar Current 35
2.4.1 Forcing of the nearly bi-monthly variability 36
2.4.2 21 years of altimeter-based surface volume transport estimates 39
2.4.3 On the interaction of the eddies with the EMC 42
2.4.4 Interannual variability 44
2.5 Discussion and conclusions 45

3 The East Madagascar Undercurrent 49
3.1 Introduction 50
3.2 Data and data processing 51
3.3 The East Madagascar Undercurrent 56
3.3.1 Observed velocities and mean flow 56
3.3.2 Equatorward volume transport 60
3.3.3 Net volume transport 62
3.3.4 Variability 64
3.4 On the EMUC baroclinic/barotropic partitioning 68
3.5 Spatial extent and thermohaline properties from Argo floats . . . 71
3.5.1 Spatial extent 71
3.5.2 Thermohaline properties at intermediate levels 72
3.6 Discussion and conclusions 74

4 First observational evidence of a North Madagascar Undercurrent 77
4.1 Introduction 78
4.2 The ACSEX3 data set 78
4.3 Velocities and volume transport 80
4.4 Thermohaline structure 82
4.5 Coastal downwelling 84
4.6 Discussion and conclusion 88

5 Brazil Current variability: an Indo-Atlantic teleconnection 91
5.1 Introduction 92
5.2 Data and methods 92
5.3 Results 93
5.3.1 Velocities and variability of the Brazil Current 93
5.3.2 The annual period: regional eddies 96
5.3.3 The trimonthly period: a link with the Agulhas Current retroflection 98
5.4 Discussion and conclusions 99

6 South Indian tropical gyre: an Indo-Pacific teleconnection 105
6.1 Introduction 106
6.2 Data and methods 109
6.2.1 Wind data 109

6.2.2 Satellite altimeter data 111
6.2.3 Global atlas of temperature and salinity 113
6.3 Seasonality of the South Indian tropical gyre 115
6.3.1 The Sverdrupian tropical gyre 115
6.3.2 Absolute dynamic topography and geostrophic circulation of the tropical gyre 117
6.3.3 The Seychelles–Chagos Thermocline Ridge 122
6.4 Local-scale wind stress forcing: Ekman upwelling 123
6.4.1 The Seychelles–Chagos Thermocline Ridge 125
6.4.2 Seychelles and Chagos Domes 125
6.5 Remote forcing: Rossby waves 129
6.6 Remote forcing: the Indonesian Throughflow 131
6.6.1 Annual cycle and westward propagation 132
6.6.2 The Indonesian Throughflow Front 135
6.7 Discussion and conclusions 139

7 General Conclusions **143**
7.1 Answering the open questions 143
7.2 Recommendations 146
7.3 Final remark: an energetic Southern Hemisphere Supergyre . . . 149

Bibliography **151**

Acknowledgments **169**

Curriculum Vitae **171**

SUMMARY

The subtropical oceans are dominated by anticyclonic gyres: anticlockwise in the southern hemisphere and clockwise in the northern hemisphere. At the western boundary of each subtropical gyre, there is a strong poleward flow which compensates for the water transported equatorward at the eastern boundary and especially in the interior of the ocean basin. This strong poleward flow is a so-called Western Boundary Current (WBC). Since the WBCs carry warm water from low latitudes to relatively colder regions at high latitudes, these currents are tightly related to the redistribution of heat on Earth, playing a major role in the climate system. In this thesis we have investigated different aspects of the WBCs in the Indian and South Atlantic Oceans, based on observational data sampled both *in situ* and from satellites.

The origin of the WBCs in both Indian and South Atlantic Oceans is related to the bifurcation of the westward directed South Equatorial Current (SEC) towards the western boundary. While the South Atlantic has a typical WBC, the Brazil Current (BC), things are quite more complex in the Indian Ocean. Due to the presence of Madagascar Island, the poleward flow is partitioned into two poleward branches: the East Madagascar Current (EMC), represented by a continuous current analogous to the BC, as well as the flow in the Mozambique Channel, which is characterized by southward-propagating anticyclonic eddies. Farther south, the EMC and the Mozambique eddies feed the Agulhas Current, the strongest WBC in the southern hemisphere.

In October 2010 an array of five moorings were deployed off eastern Madagascar, nominally at 23°S, as part of the "INdian-ATlantic EXchange in present and past climate" (INATEX) observational program, which was financially supported by the Dutch Organization for Scientific Research (Nederlandse Organisatie voor Wetenschappelijk Onderzoek – NWO). The instruments remained in the water for about 2.5 years, until March 2013. Based on the INATEX data, we study the EMC in terms of its observed velocities, estimated volume transport and variability. The EMC is dominated by a nearly bi-monthly (45–85 days) period band. Satellite data show that such variability is explained by westward-propagating eddies impinging on the EMC. Anticyclonic eddies strengthen the flow while cyclonic eddies attenuate the EMC transport.

Besides the surface patterns of the western boundary currents, the presence of an undercurrent flowing in opposite direction and beneath the surface cur-

rent is a recurring feature observed in different WBC systems. This thesis is also dedicated to the study of this counter flow, observed below the EMC: the equatorward East Madagascar Undercurrent (EMUC). Also supported by data from the INATEX moorings, we show that the EMUC is hugging the continental slope, with a core at a depth of 1200 m. Its mean equatorward volume transport amounts to nearly 10% of the mean transport estimated for the surface poleward EMC.

On approaching Madagascar, the bifurcation of the SEC also generates the equatorward directed North Madagascar Current (NMC). We here provide the first evidence of the existence of a poleward counter current below the NMC, which we named North Madagascar Undercurrent (NMUC). This evidence comes from the ACSEX oceanographic cruise carried out on 30 March 2001, as part of the “Dutch-South African Agulhas Current Sources Experiment" (ACSEX).

Two interocean teleconnections, which take place downstream and upstream of the EMC system, are also investigated in this study. First, we explore the connection between the WBCs in the Indian and South Atlantic Oceans. We mentioned that the flow in the Mozambique Channel and the EMC are sources for the Agulhas Current (AC). In turn, the AC flows downstream until the southern tip of Africa, where part of the water transported by this current turns back into a loop to the Indian Ocean, generating an important feature known as Agulhas Retroflection. Anticyclonic eddies are created and are released into the Atlantic Ocean by this retroflection process, establishing the so-called Agulhas Leakage. We reveal that this mechanism of retroflection also represents a pulse of energy that crosses the Atlantic, imposing a nearly trimonthly period of variability on the Brazil Current, at the Santos Basin.

Second, we focus on the teleconnection between Pacific and Indian Oceans by means of both Indonesian Throughflow and South Indian tropical gyre. The first represents the waters passing through the Indonesian islands, while the latter is a clockwise gyre near the equatorial region. The SEC, which is the northern branch of the subtropical gyre, can also be interpreted as the southern branch of the tropical gyre, and it has an important role in redistributing waters from the Indonesian Throughflow into the Indian Ocean. We show that the tropical gyre has a marked seasonal cycle. An analysis of major forcing mechanisms suggests the interaction of basin-scale wind stress curl, local-scale wind stress forcing, remote forcing driven by the Indonesian Throughflow, as well as westward-propagating Rossby waves.

SAMENVATTING

De subtropische oceanen worden gedomineerd door anticyclonale circulatiepatronen: anti-kloksgewijs op het Zuidelijk, kloksgewijs op het Noordelijk halfrond. Ieder van deze circulatiepatronen kent aan de westzijde een sterke, poolwaarts gerichte stroming. Deze compenseert het equatorwaarts transport dat aan de oostzijde en, vooral, in het interieur van de oceaan plaatsvindt. Deze sterke poolwaartse stroming wordt een westelijke grenslaagstroming genoemd (in het Engels: Western Boundary Current, WBC). Omdat de WBCs warm water van lage breedtegraad naar relatief koudere gebieden op hogere breedtegraad transporteren, en daarmee bijdragen aan de mondiale herverdeling van warmte, spelen deze stromingen een grote rol in het klimaatsysteem. In dit proefschrift hebben we verschillende aspecten van de WBCs in de Indische en Zuid-Atlantische Oceanen bestudeerd.

De westelijke grenslaagstromen in zowel de Indische als Zuid-Atlantische Oceanen vinden hun oorsprong in de vertakking van de westwaarts gerichte Zuid-equatoriale stroming als deze de westelijke rand van de oceaan nadert. Hoewel de Zuid-Atlantische Oceaan een typische Westelijke Grenslaagstroming kent, de Brazilië stroom, liggen de zaken in de Indische Oceaan een stuk ingewikkelder. Door de aanwezigheid van het eiland Madagaskar is de poolwaartse stroom gesplitst in twee takken: de Oost-Madagaskar stroom, een continue stroming analoog aan de Brazilië stroom, alswel de stroming door het Mozambique Kanaal, gekarakteriseerd door zuidwaarts bewegende anticyclonale wervels. Verder zuidwaarts voeden de Oost-Madagaskar stroom en de Mozambique wervels de Agulhas stroom, de sterkste westelijke grenslaagstroming van het Zuidelijk Halfrond.

In oktober 2010 is, als onderdeel van het INATEX project (INdian-ATlantic Exchange in present and past climate), een raai met vijf verankeringen weggezet, ten oosten van Madagaskar, op nominaal 23° Zuid. Dit project werd financieel ondersteund door de Nederlandse Organisatie voor Wetenschappelijk Onderzoek, NWO. De instrumenten bleven circa 2.5 jaar in het water, tot maart 2013. Gebaseerd op INATEX metingen zijn snelheid, volume transport en variabiliteit van de Oost-Madagaskar stroom bestudeerd. Satellietwaarnemingen laten zien dat diens variabiliteit verklaard wordt door westwaarts bewegende wervels als deze de Oost-Madagaskar stroom bereiken. Anticyclonale wervels

versterken de poolwaartse stroming, terwijl cyclonale wervels het transport van de Oost-Madagaskar stroom verzwakken.

Naast de aanwezigheid van een karakteristieke stroming aan het oppervlak, vormt de aanwezigheid van een tegenstroom op diepte, een terugkerend verschijnsel in de westelijke grenslaag. Dit proefschrift is ook gewijd aan de studie van deze tegenstroom, gelegen onder de Oost-Madagaskar stroming: de Oost-Madagaskar tegenstroom. Op basis van de metingen verkregen uit de INATEX-verankeringen laten we zien dat de Oost-Madagaskar tegenstroom de continentale helling volgt, met een kern op 1200 m diepte. Diens gemiddelde equatorwaarts gerichte volume transport is circa 10% van dat wat de Oost-Madagakar stroom aan het oppervlak poolwaarts transporteert.

Bij nadering van Madagaskar, genereert de vertakkende Zuid-Equatoriale stroom tevens de equatorwaarts gerichte Noord-Madagaskar stroom. Hier laten we voor het eerst zien dat zich onder deze stroming ook een poolwaarts gerichte tegenstroom bevindt, die we de Noord-Madagaskar tegenstroom noemen. Het bewijs hiervoor komt van de data verkregen tijdens de oceanografische expeditie die op 30 maart 2001 werd uitgevoerd in het kader van het Nederlands – Zuid-Afrikaanse ACSEX project (Agulhas Current Sources Experiment).

In dit proefschrift worden verder twee inter-oceaan teleconnecties bestudeerd, die stroomafwaarts en stroomopwaarts van het Oost-Madagaskar stroomsysteem gelokaliseerd zijn. Ten eerste onderzoeken we het verband tussen de westelijke grenslaagstromen in de Indische en Zuid-Atlantische Oceaan. Net zoals de stromingen in het Mozambique Kanaal en in de Oost-Madagaskar stroom de Agulhas-stroom voeden, zal op haar beurt de Agulhas-stroom zuidwaarts bewegen, tot aan de zuidpunt van Zuid-Afrika, waar een deel van deze stroom terugkeert, de Indische Oceaan in. Deze belangrijke stromingstak staat bekend als de Agulhas-retroflectie. Bij retroflectie worden echter ook anticyclonale wervels gevormd, die verder de Atlantische Oceaan in lopen, het zogenaamde Agulhas-lek. Wij tonen aan dat dit mechanisme van retroflectie een puls van energie aflevert die de Atlantische Oceaan oversteekt, en die, in de Brazilië stroom, in het Santos bekken, variabiliteit met een periode van 3 maanden veroorzaakt.

Ten tweede, concentreren we ons op het verband tussen de Stille en Indische Oceaan. Dit verband loopt via de Indonesische lekstroom en via de Zuid-Indische tropische circulatie. De eerste vertegenwoordigt het water dat de Indonesische archipel passeert, terwijl de laatste een kloksgewijze circulatie nabij de evenaar voorstelt. De Zuid-equatoriale stroom, die de Noordelijke tak vormt van de subtropische circulatie-cel, kan ook als de zuidelijke tak van de tropische circulatie-cel worden gezien, en deze speelt een grote rol in het herverdelen van water dat via de Indonesische lekstroom in de Indische Oceaan beland.

We tonen aan dat de tropische circulatie-cel een opmerkelijke seizoensvariatie kent. Analyse van de belangrijkste drijvende mechanismes suggereert een wisselwerking tussen de rotatie van de windschuifspanning op bekkenschaal, de lokale windschuifspanning, de sturing door de Indonesische lekstroom, alswel westwaarts propagerende Rossby golven.

RESUMO

Os oceanos subtropicais são dominados por giros anticiclônicos: anti-horário no hemisfério sul e horário no hemisfério norte. No contorno oeste de cada giro subtropical existe uma forte corrente direcionada ao polo, a qual é responsável por compensar a água transportada em direção ao equador no contorno leste e especialmente no interior da bacia oceânica. Esta forte corrente em direção ao polo é conhecida como Corrente de Contorno Oeste (CCO). As CCOs possuem um papel de destaque na redistribuição de calor na Terra, participando como uma das principais componentes do sistema climático global, tendo em vista que as mesmas transportam águas relativamente quentes provenientes de regiões de baixa latitude para regiões frias em latitudes elevadas. Baseado em dados coletados *in situ* e amostrados por satélites, esta tese aborda diferentes aspectos das CCOs nos Oceanos Índico e Atlântico Sul.

Tanto no Índico como no Atlântico Sul a origem da CCO está relacionada com a bifurcação da Corrente Sul Equatorial (CSE), proveniente do leste, contra a margem continental oeste. Entrentanto, enquanto o Atlântico Sul é caracterizado por uma CCO típica, a Corrente do Brazil (CB), este padrão é um pouco mais complexo no Oceano Índico. Devido a presença da Ilha de Madagascar, o fluxo em direção ao polo é particionado em duas componentes: a Corrente Leste de Madagascar (CLM), representada por uma corrente contínua análoga à CB, assim como o fluxo no Canal de Moçambique, que por sua vez é representado por vórtices anticiclônicos. Mais ao sul, tanto a CLM como os vórtices vindo do Canal de Moçambique contribuem para a formação da Corrente das Agulhas, a mais intensa das CCOs encontradas no hemisfério sul.

Em outubro de 2010 uma linha de cinco fundeios foi instalada ao largo de Madagascar, próximo a latitude de 23°S, como parte do programa observacional “INdian-ATlantic EXchange in present and past climate" (INATEX), financiado pela Organização para Pesquisa Científica Holandesa (Nederlandse Organisatie voor Wetenschappelijk Onderzoek – NWO). Os instrumentos permaneceram na água por aproximadamente 2.5 anos, até março 2013. Com base nestes dados, nós estudamos a CLM em termos de velocidade, transporte de volume e variabilidade. Os resultados mostram que a CLM é dominada por uma banda de variabilidade de período quase bimestral (45–85 days). Dados de satélite revelam que esta variabilidade é explicada por vórtices, prove-

nientes do leste, que colidem com a CLM. Vórtices anticiclônicos intensificam a corrente enquanto os vórtices ciclônicos atenuam o transporte da CLM.

Além dos padrões de circulação superficial, a presença de uma subcorrente fluindo abaixo e na direção oposta da corrente de superfície é uma feição oceanográfica recorrente, observada em diferentes sistemas de contorno oeste. Esta tese também é dedicada ao estudo desta subcorrente, observada abaixo da CLM: a Subcorrente Leste de Madagascar (SCLM). Ainda com base nos dados coletados no escopo do projeto INATEX, nós mostramos a SCLM pegada ao talude continental com núcleo em torno de 1200 m de profundidade. Seu transporte de volume médio em direção ao equador se aproxima à 10% do transporte estimado para a CLM em direção ao polo.

Ao se aproximar de Madagascar, além da CLM, a bifurcação da CSE também cria um fluxo direcionado ao equador: a Corrente Norte de Madagascar (CNM). Este trabalho apresenta a primeira evidência de uma subcorrente fluindo na direção oposta e abaixo da CNM, a qual nós batizamos de Subcorrente Norte de Madagascar (SCNM). Esta evidência vem dos dados coletados durante um cruzeiro oceanográfico realizado em 30 de março de 2001, no escopo do projeto "Dutch-South African Agulhas Current Sources Experiment" (ACSEX).

Duas teleconexões interoceânicas, que ocorrem ao norte e ao sul do Sistema CLM, também são investigadas neste estudo. Primeiro, nós exploramos a conexão entre os sistemas de CCO dos Oceanos Índico e Atlântio Sul. Conforme mencionamos acima, tanto os vórtices provenientes do Canal de Moçambique quanto a CLM atuam como fontes para a Corrente das Agulhas (CA). Por sua vez, a CA flui até a ponta sul do continente africano, onde parte do volume transportado por esta corrente sofre uma retroflexão e retorna ao Índico, gerando um importante fenômeno conhecido como Retroflexão das Agulhas. Durante este processo, vórtices anticiclônicos são criados e liberados em direção ao Atlântico, estabelecendo o vazamento das Agulhas. Nós revelamos que este mecanismo de retroflexão pode ser interpretado como um pulso de energia que cruza o Atlântico, impondo um período de variabilidade quase trimestral na Corrente do Brazil, na região da Bacia de Santos.

Segundo, nós focamos na teleconexão entre Pacífico e Índico que ocorre através das águas que passam em direção à este último por entre as ilhas da Indonésia, para então serem redistribuídas pelo o giro tropical do Índico Sul, o qual por sua vez é representado por um giro horário localizado imediatamente ao norte do giro subtropical. A CSE, que compõem o ramo norte do giro subtropical, também pode ser interpretada como o ramo sul do giro subtropical. Nossos resultados mostram que o giro tropical apresenta um marcado ciclo sazonal induzido por diferente forçantes: rotacional do vento sobre a bacia

oceânica, efeito local do cisalhamento do vento, águas que vazam pelas ilhas Indonésias, assim como ondas de Rossby.

1

GENERAL INTRODUCTION

1.1 GLOBAL PATTERNS OF OCEAN CIRCULATION

The ocean is a crucial component of the global climate system as a result of its role in storing and redistributing heat all over the planet. Due to the high heat capacity of the (sea)water, much higher than the heat capacity of atmosphere and land, most of the solar radiation which arrives at the surface of the Earth is absorbed and stored by the oceans at equatorial and tropical latitudes, where the incident insolation is larger compared to other regions. Afterwards, this heat is partially transferred to the atmosphere through air-sea interactions, while another part is redistributed to high latitude regions by organized flows, the ocean currents.

In the ocean, an organized movement of water is forced by multiple mechanisms, as well as characterized by a variety of scales in both time and space (Cushman-Roisin and Beckers, 2011). Traditionally, on the large-scale, the ocean circulation is divided into two components: **meridional overturning circulation** (Fig. 1.1) and **wind-driven circulation** (Fig. 1.2).

The first, also known in the literature as thermohaline circulation, is related to large spatial gradients of density, deep convection and formation of water masses at high latitudes. It dominates the deep circulation with very slow movements (van Aken, 2007).

The second is forced by the wind stress and it occurs in the upper few hundred meters of the water column. The wind-driven circulation manifests itself as ocean gyres: the subpolar gyres, the tropical gyres (or equatorial and tropical circulations) and, especially, the subtropical gyres, which cover the largest area and carry most of the heat (Fig. 1.2).

A typical subtropical gyre is composed of an anticyclonic pattern of circulation with four components: (i) an eastward current at its boundary of highest latitude, (ii) an equatorward cold current on the eastern side of the ocean

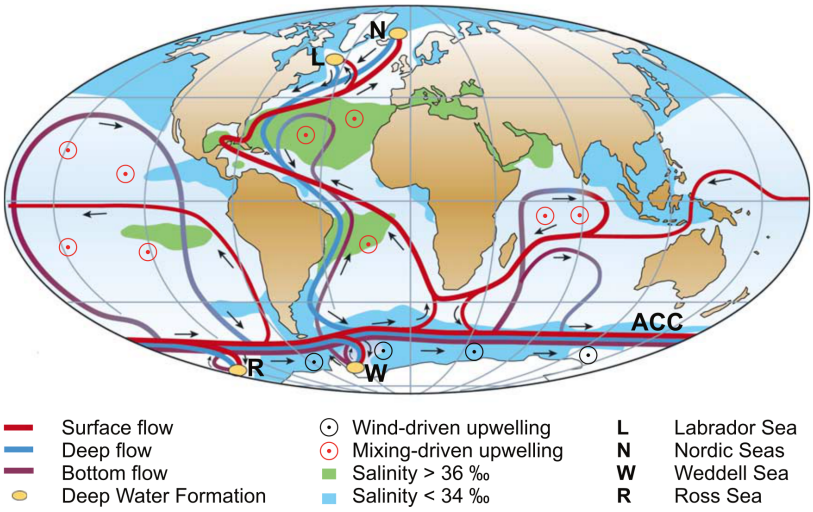

Figure 1.1: Simplified sketch of the Meridional Overturning Circulation (MOC). From Kuhlbrodt et al. (2007).

basin, (iii) a westward current near the equator and (iv) a strong poleward Western Boundary Current (WBC) closing the gyre in the western part of the basin, which transports warm waters to high latitude regions.

Much of the characteristics of the subtropical gyres, as for instance the strength of the WBCs, is known empirically since the advent of the European overseas exploration. The Portuguese Admiral Vasco da Gama, during his trip to India in 1497 already reported the difficulties of overcoming a strong south-westward flow off the eastern coast of Africa (an interesting historical description is found in Lutjeharms, 2006).

Nevertheless, the first theoretical model which explains the patterns of the subtropical gyres was proposed by Sverdrup (1947), who revealed a relationship between circulation in the upper few hundred meters of the water column with the curl of the wind stress exerted on the sea surface. In this model, wind stress acting on the ocean basins, possessing negative wind-stress curl, generates an equatorward transport all over the basin, which should be compensated by a narrow and strong flow in one of the lateral boundaries of the gyre. However, Sverdrup's gyre remained unresolved in this high energetic boundary layer (Fig. 1.3a). Not long after, Stommel (1948) further improved this theory by adding bottom friction to the same equations. With this assumption, Stommel closed the theoretical gyre and at the same time proved that the

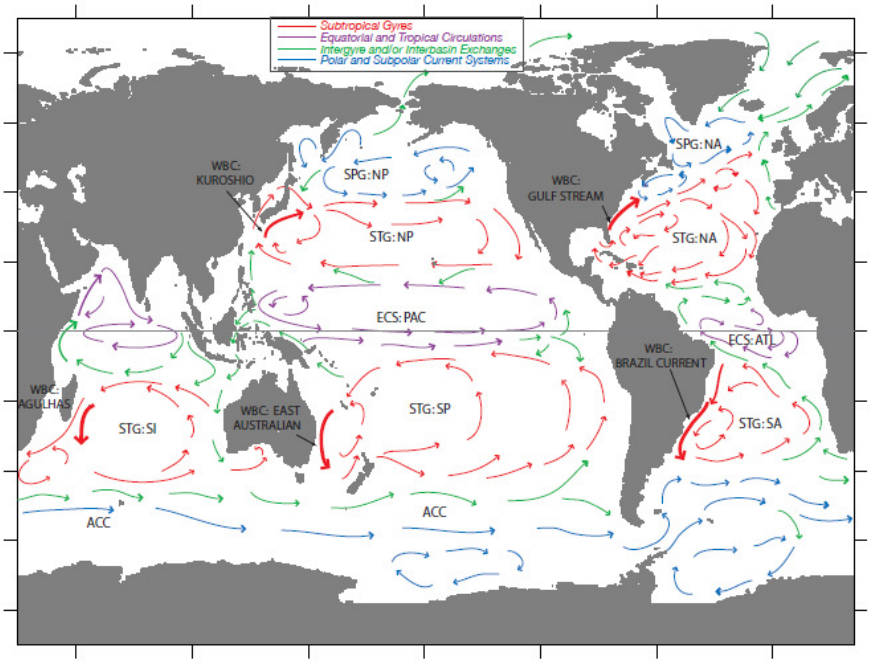

Figure 1.2: Sketch of the Ocean Gyres and main surface currents of the global ocean. Acronyms: Subtropical Gyre (STG); Subpolar Gyre (SPG); Western Boundary Current (WBC); Equatorial Current System (ECS); North Atlantic (NA); South Atlantic (SA); North Pacific (NP); South Pacific (SP); South Indian (SI); Antartic Circumpolar Current (ACC); Atlantic (ATL); Pacific (PAC). The red, blue, purple and green arrows represent, respectively, the STG, SPG, equatorial-tropical circulation and intergyre and/or interbasin exchanges. The red thick arrows highlight the strength of the WBCs. From Vallis (2006).

intensification in the western boundary layer is due to the fact that rotation varies with latitude (Fig. 1.3b). A few years later, Munk (1950) added lateral eddy viscosity to Sverdrup's model, and not only achieved the intensification in the western boundary, as in Stommel's model, but also its typical overshoot. It reproduced the observed cyclonic subpolar gyres (Fig. 1.3c), by taking into account a more realistic zonal wind stress pattern of alternating sign. It is worth to emphasize that in all three models, the wind stress forces the currents.

For the five existing subtropical gyres, the main WBCs are: Kuroshio Current in the North Pacific; East Australian Current in the South Pacific; Gulf Stream in the North Atlantic; Brazil Current in the South Atlantic; and the Agulhas Cur-

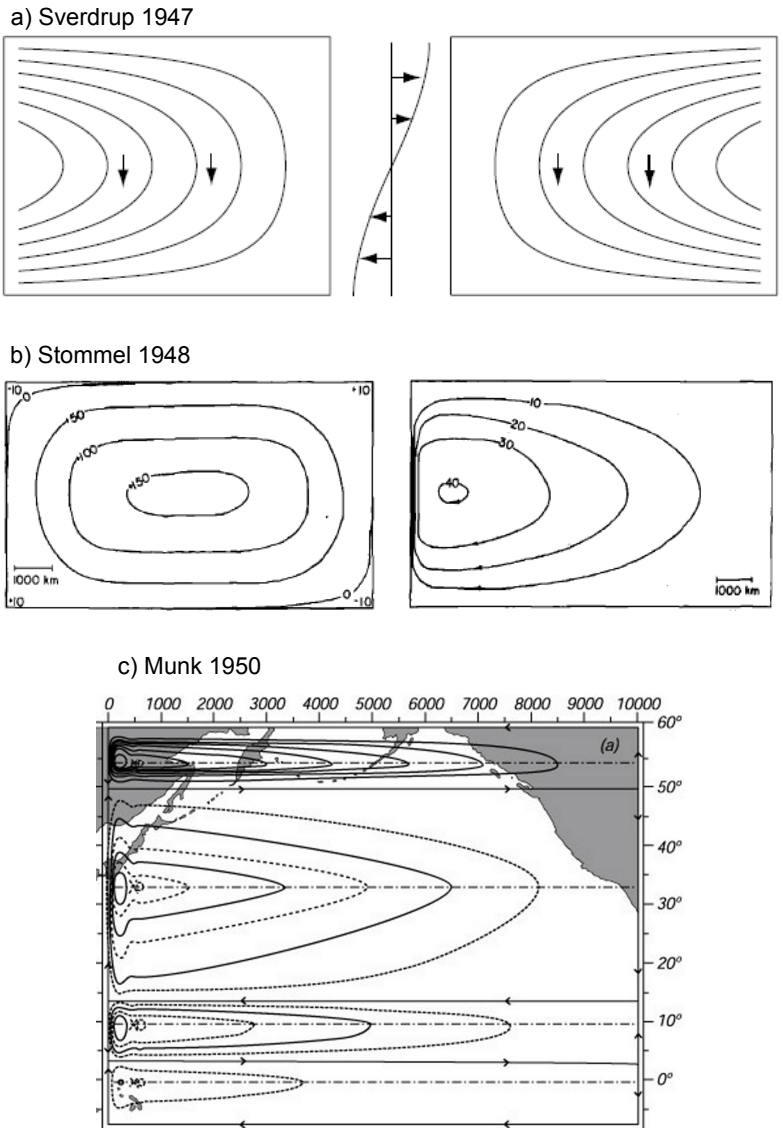

Figure 1.3: (a) Sverdrup's model: Two possible solutions for the Sverdrup flows (left and right) estimated from the wind stress shown in the center [panels/caption from Vallis (2006)]. (b) Stommel's model: Surface height contours for the uniformly rotating ocean (non-rotating or constant rotation) referred to an arbitrary level (left). Streamlines for the case where the Coriolis force is a linear function of latitude (right) [panels/captions from the original Stommel (1948)]. (c) Munk's model: Streamlines in the North Pacific calculated from a mean annual wind stress. The theoretical WBC, between 15°–50°N, represents the Kuroshio Current [panel from the original Munk (1950)].

rent (the one reported by Vasco da Gama) in the South Indian Ocean (Fig. 1.2). Notwithstanding their similarities, things are more complicated and intriguing in the Indian Ocean, as we will discuss in this work.

Besides the surface patterns of the boundary currents, the presence of an undercurrent, flowing in opposite direction and beneath the surface current, appears to be a recurring feature. The first undercurrent has been analytically predicted by Stommel (1958), as a mechanism to explain equatorward spreading of high density waters formed at high latitudes in the North Atlantic Ocean. Three years later, the undercurrent predicted by Stommel (1958) was confirmed with *in situ* observations (Swallow and Worthington, 1961). However, as we will further discuss in this thesis, a counterflow below WBCs can be forced by different mechanisms. Near western boundaries we encounter the Luzon Undercurrent in the North Pacific (Hu et al., 2013), the East Australian Undercurrent in the South Pacific (Godfrey et al., 1980; Schiller et al., 2008), the Intermediate Western Boundary Current in the South Atlantic (Evans and Signorini, 1985; da Silveira et al., 2004), and the Agulhas Undercurrent (Beal and Bryden, 1997; Beal, 2009) in the Indian Ocean.

As already indicated in its title, the core of this thesis is to study some aspects of the western boundary currents in the Indian and South Atlantic Oceans. More precisely, three of the chapters (Chapters 2–4) have the surface current and undercurrents off eastern Madagascar as their main object of study, while the remaining two chapters (Chapters 5–6) explore interocean teleconnections which take place downstream (Chapter 5) and upstream (Chapter 6) of the East Madagascar Current system. In this sense, in Chapter 5, we “sail" from the Indian to the South Atlantic, to study the Brazil Current and discuss its connection with the western boundary current of the Indian Ocean. And, in Chapter 6, we come back to the Indian Ocean, but now focusing on the South tropical gyre, which is forced by Pacific waters from the Indonesian Throughflow. To accommodate the reader not familiar with these regions, we present a brief introduction of the circulation patterns observed in both oceans.

1.2 THE ATLANTIC OCEAN AND ITS CLASSICAL PATTERN OF OCEAN GYRES

At surface level, the Atlantic Ocean presents a typical case of wind-driven circulation, with well-defined patterns that closely resemble the theoretical results from Stommel (1948) and Munk (1950). From north to south, Fig. 1.4 indicates a cyclonic subpolar gyre, an anticyclonic North subtropical gyre, a tropical–equatorial circulation, and an anticyclonic South subtropical gyre in

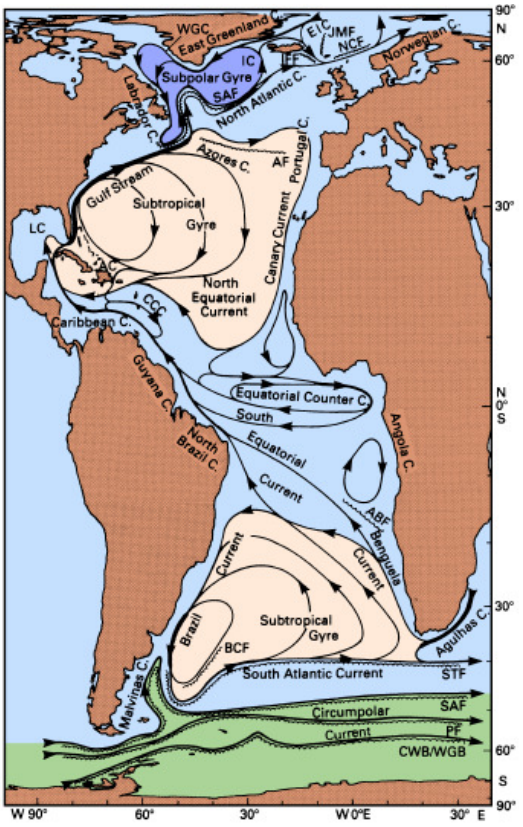

Figure 1.4: Sketch of the ocean gyres in the Atlantic Ocean. From Tomczak and Godfrey (2003).

which the southern branch, the eastward South Atlantic Current, is aligned with the, also eastward directed, Antartic Circumpolar Current.

The Brazil Current (BC) and the Gulf Stream (GS) are the warm poleward flows which counterbalance the equatorward Sverdrup transport. The latter is perhaps the most well-known example of how ocean currents and weather are tightly connected. Due to the transport of relatively warm waters by the GS, along the same latitudinal band the average temperatures are higher in Western Europe compared to the eastern part of North America.

In the southern hemisphere, the BC's origin is situated at about 15°S due to the bifurcation of the South Equatorial Current (SEC) towards the Brazilian coast (Soutelino et al., 2013). The BC is unique with respect to its vertical structure. At its origin, it is marked by a shallow flow with a vertical extension

of ∼200 m. At the center of the Santos Basin (∼26°S) the vertical level of no motion between the BC and the counterflow imposed by the Intermediate Western Boundary Current sits at around 400 m. At 27.9°S the reversal level is on average near 850 m (Rocha et al., 2014). This downstream thickening of the BC occurs due to the depth-dependent bifurcation of the SEC (Boebel et al., 1999; Legeais et al., 2013). An illustrative sketch of the SEC bifurcation and downstream thickening of the BC is found in Soutelino et al. (2013) (their Fig. 1). As a consequence of this phenomenon, the BC is much weaker than the GS and Agulhas Current.

In terms of *in situ* observations the BC is likely the least studied WBC. Most of the works devoted to this current are built on quasi-synoptic surveys (e.g. da Silveira et al., 2004), while monitoring programs with continuous measurements are scarce (Rocha et al., 2014).

1.3 THE INDIAN OCEAN AND ITS PECULIAR OCEAN GYRES

If the Atlantic Ocean, on the one hand, presents a didactic case in which ocean gyre observation approaches that predicted by the theoretical models, on the other hand, things are more complex in the Indian Ocean (Fig. 1.5), where boundary conditions differ. Broadly speaking, there are five reasons: (i) Reduced extension of the North Indian Ocean; (ii) Presence of strong Monsoon winds; (iii) A semi-open eastern boundary; (iv) The presence of Madagascar Island; (v) The southernmost tip of Africa which is placed at mid-latitudes (∼35°S).

The combination of factors (i) and (ii) determines a complex and variable pattern of circulation north of the Equator, where a typical subtropical gyre does not develop and the currents change according to the monsoonal season. For instance, the Somali Current flows northward during Southwest Monsoon but reverses southward under conditions of Northwest Monsoon (Fig. 1.5).

The semi-open eastern boundary (iii) provides the only low-latitude connection between the world oceans, where Pacific waters are transported to the Indian Ocean via the Indonesian Throughflow. Afterwards, these waters are redistributed to the Indian western boundary by the South Equatorial Current (SEC).

The last two aspects (iv) and (v) are crucial for shaping the WBC system. Upon arrival at the western boundary of the Indian Ocean, the SEC bifurcates near Madagascar, splitting in both the poleward, East Madagascar Current (EMC), and the equatorward, North Madagascar Current (NMC) (Schott et al., 1988). Due to the barrier imposed by Madagascar, another branch of

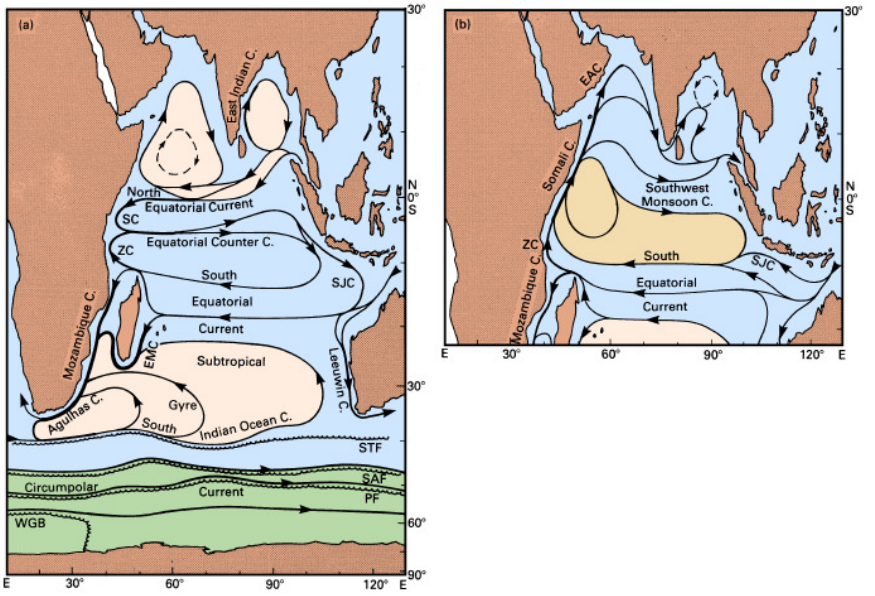

Figure 1.5: Sketch of the ocean gyres in the Indian Ocean during (a) Northeast Monsoon (January, February, March) and (b) Southwest Monsoon (July, August, September). From Tomczak and Godfrey (2003).

the poleward flow is found in the Mozambique Channel, where the circulation pattern is dominated by southward-propagating anticyclonic eddies (de Ruijter et al., 2002). Notice that this pattern in the Mozambique Channel (MC) does not match that of a continuous flow indicated in Fig. 1.5a. For a more accurate sketch the reader is referred to Fig. 4.1.

Downstream, the flow in the MC and the EMC are sources to the Agulhas Current (AC). However, they are not only providing water, but they also modulate the position where the AC retroflects to the Indian Ocean (de Ruijter et al., 2004; Ridderinkhof et al., 2013). This loop of the AC turning back to the Indian Ocean is known as AC retroflection (Fig. 1.5a). As a consequence, the AC is likely the strongest WBC in the southern hemisphere (Lutjeharms, 2006) and responsible for promoting an Indian-Atlantic link. Different from the Atlantic western boundary, where the southernmost tip of America is located farther south, the termination of Africa at mid-latitudes permits the AC to migrate towards the Atlantic Ocean. Even though the AC retroflects back into the Indian Ocean, generating the Agulhas Return Current, part of its volume leaks into the Atlantic in the retroflection area, where large anticyclonic eddies are also

released. A single such detached vortical structure is known in the literature as an Agulhas Ring (AR). This Agulhas leakage has been described as one of the main contributors to the Meridional Overturning Circulation (MOC) by transferring warm and salty waters from the Indian to the Atlantic Ocean at surface level (Olson and Evans, 1986; Gordon et al., 1992).

Finally, below the surface, at depth, three undercurrents are reported to flow beneath and in opposite direction to the surface western boundary currents in the South Indian Ocean: the Agulhas Undercurrent (AU, Beal and Bryden (1997); Beal (2009)), Mozambique Undercurrent (MU, de Ruijter et al. (2002); van Aken et al. (2004)) and East Madagascar Undercurrent (EMUC, Nauw et al. (2008); Ponsoni et al. (2015a)). This thesis provides the first piece of evidence on the existence of one additional counter current, the poleward directed North Madagascar Undercurrent (Ponsoni et al., 2015b), flowing opposite to the equatorward NMC.

1.4 INTEROCEAN CONNECTIONS AND A SOUTHERN HEMISPHERE SUPERGYRE

In the previous section we mentioned that two interocean connections occur, via the Indonesian Throughflow and via the formation of ARs, suggesting that the subtropical gyres in the southern hemisphere are somehow connected in a supergyre. In this direction, the first concept of a Southern Hemisphere Supergyre (SHS) was posed by de Ruijter (1982), who used an asymptotic analysis, supported by theoretical transport models of large-scale wind-driven ocean circulation, to show that the subtropical gyres of the South Atlantic and Indian Ocean could also be perceived as a merged structure (Fig. 1.6a). The spreading of the Indonesian Throughflow in the Indian Ocean (Song et al., 2004) and the throughflow pathway resulting in “Tasman leakage" (Tilburg et al., 2001) would also be part of the SHS, now connecting the Pacific, Indian and Atlantic basins (Fig. 1.6b). This third connection via the Tasman leakage is not further addressed in this thesis.

Ridgway and Dunn (2007) provided observational evidence for the existence of the SHS, while Speich et al. (2007) showed how the supergyre is embedded in the MOC. In a recent study, Beal et al. (2011) argued that an ongoing increase in Agulhas leakage under an anthropogenic warming could strengthen the MOC, while its input in the North Atlantic is predicted to weaken due to warming and accelerated melting of the ice cover.

However, these “intriguingly beautiful” interocean connections are really complex and still far from being fully understood. For instance, there is an ongoing discussion in the literature questioning whether the ARs are Lagrangian

coherent structures or not, having water trapping ability, or not. According to Beron-Vera et al. (2013), most of the ARs previously identified in the literature indeed do not transport water masses, which has led to an overestimation of the Agulhas leakage in previous estimates.

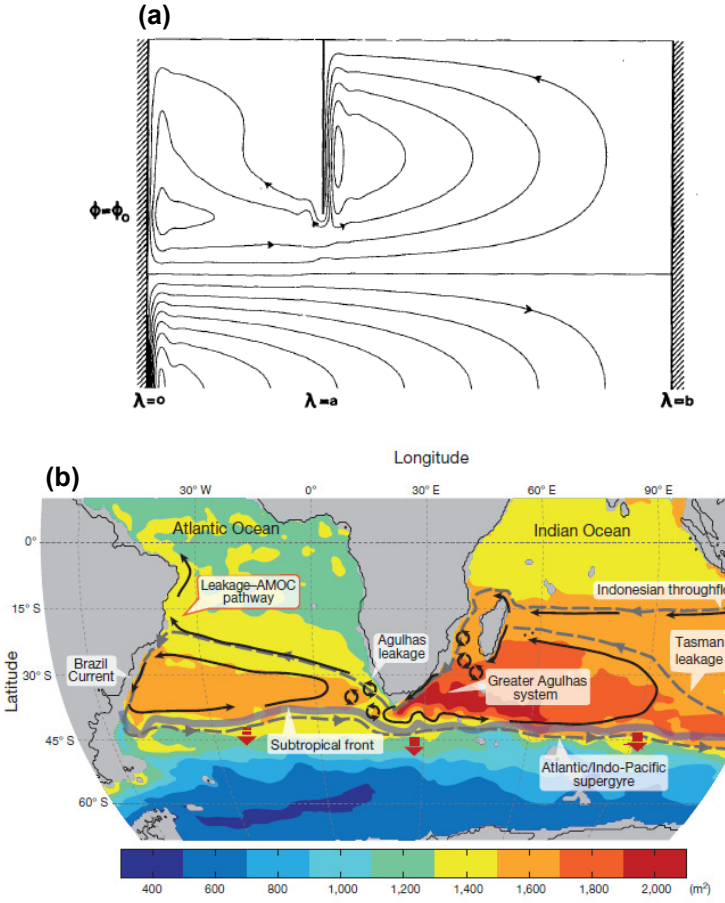

Figure 1.6: (a) Transport streamfunction leading to interaction between the subtropical gyres of the Atlantic and Indian ocean basins [panel/caption from the original de Ruijter (1982)]. (b) Sketch of the Southern Hemisphere Supergyre (gray dashed line) and interocean connections. Background colours indicate the mean subtropical gyre circulation, depicted by climatological dynamic height integrated between the surface and 2000 dbar [panel/caption from the original Beal et al. (2011)].

1.5 OUTLINE AND OPEN QUESTIONS

In view of the preceding discussion and from an observational perspective, this work intends to investigate different aspects of the WBC systems off eastern Madagascar (Chapters 2, 3 and 4) and off southeastern Brazil (Chapter 5), to inspect whether or not there is a teleconnection between the western boundaries in the Indian and Atlantic Oceans (also Chapter 5) and its possible impact on the Brazil Current variability. Finally, the relation between the South Indian tropical gyre and Indonesian Throughflow is investigated (Chapter 6). The motivation and the associated open questions addressed by this thesis are listed chapter by chapter in the next paragraphs.

Chapter 2:

As mentioned above, the flow in the MC and the EMC are the upstream sources of the AC and make an important connection between the near equatorial region with the South West Indian Ocean. For more than a decade [2003-2014] the flow through the MC has been monitored by a line of moorings deployed by the “Royal Netherlands Institute for Sea Research" (NIOZ) in the narrowest part of the channel (Harlander et al., 2009; Ridderinkhof et al., 2010; Ullgren et al., 2012). Previous to the work described in this thesis, similar monitoring of the EMC system was lacking and the few *in situ* data regarding this current system was restricted to works based on quasi-synoptic surveys (Nauw et al., 2008) or to direct measurements with a restricted set of instruments covering less than one year (Schott et al., 1988). To fill in this gap, from 7 October 2010 to 12 March 2013, NIOZ deployed an array with 5 vertical lines of moorings, carrying a total of 16 instruments. Supported by these *in situ* observations and by long-term altimeter data, remotely-sensed from satellites, Chapter 2 aims to answer the following questions:

> *On average, what is the volume of water carried by the East Madagascar Current? Is this transport marked by a band of variability? If so, what is its forcing?*

Chapter 3:

Below the EMC, and hugging the continental slope, an equatorward counterflow is found. This East Madagascar Undercurrent was first reported by Nauw et al. (2008) in terms of quasi-synoptic vertical profiling of velocities. Thus,

Is the East Madagascar Undercurrent a recurrent oceanographic feature? What is its volume transport and variability?

Chapter 4:

At surface level, the bifurcation of the SEC upon arrival at the Madagascar coast gives rise to the poleward EMC and the equatorward NMC (Schott et al., 1988). In the previous chapter we studied the equatorward EMUC beneath and opposite the EMC (Ponsoni et al., 2015a). Such undercurrents are also found below the Agulhas Current (Beal and Bryden, 1997) and in the Mozambique Channel (de Ruijter et al., 2002). However, nothing is know about a subsurface reversal in the North Madagascar Current system. In this sense, the main questions addressed in Chapter 4 are:

Is there an oppositely directed poleward North Madagascar Undercurrent flowing beneath the North Madagascar Current? If so, is there a candidate mechanism for forcing this undercurrent?

Chapter 5:

If the AC (Beal et al., 2015), the flow in the MC (Harlander et al., 2009; Ridderinkhof et al., 2010) and now the EMC (Ponsoni et al., 2015a, 2016) are well studied current systems with regards to long-term *in situ* observations of velocities, we can not say the same of the South Atlantic WBC, the Brazil Current. Only very few studies hinge on *in situ* observations of velocities, most of them by means of quasi-synoptic surveys (e.g. da Silveira et al., 2004; Biló et al., 2014), and even less by means of continuous (short-term) measurements (Rocha et al., 2014).

As a consequence, the BC is likely the least studied WBC regarding its velocity and variability patterns. Since in the previous chapters we acquired the experience of combining *in situ* measurements and long-term satellite data, we take advantage of this fact and extrapolate our analysis to the BC in Chapter 5. More than that, we look for a possible connection between the dynamics near the western boundaries of the Indian and South Atlantic Oceans, via the highly energetic Agulhas retroflection. Chapter 5 is built on the following questions:

What are the dominant bands of variability, and their respective forcings, of the Brazil Current at the Santos Basin? Does the Agulhas retroflection somehow affect the WBC in the South Atlantic Ocean?

Chapter 6:

The SEC is the northern branch of the subtropical gyre, but at the same time it can also be seen as the southern branch of the South Indian tropical gyre. As we mentioned before, this current plays an important role in redistributing waters from the Indonesian Throughflow towards the western boundary (Woodberry et al., 1989; Gordon et al., 1997; Yokoi et al., 2008; Le Bars et al., 2013). Nevertheless, although effort has already been directed to study the tropical South Indian Ocean (Schott and McCreary Jr., 2001; Schott et al., 2009), it is still not well understood how the Indonesian Throughflow interacts with the South Indian tropical gyre. Aiming to cover this gap, Chapter 6 is devoted to answering the following questions:

How does the Indonesian Throughflow interact with the annual cycle of the South Indian tropical gyre? And, what are the major forcings modulating the South Indian tropical gyre?

In the final Chapter 7, we come back to the points here presented and we highlight some recommendations to new questions raised or not addressed by this thesis, which require further investigation.

1.6 DATASETS AND OBSERVATIONAL PERSPECTIVE OF THIS STUDY

In this study we make use of a large range of observational data collected both *in situ* and by means of remote-sensing. Regarding the *in situ* observations, continuous measurements of velocities were taken by two monitoring programs: “Circulação Oceânica da Região Oeste do Atlântico Sul" (COROAS 3) and “INdian-ATlantic EXchange in present and past climate" (INATEX).

The velocity data from the COROAS program were sampled by a mooring deployed near the Brazil Current core at 25.5°S and span from 01/Jan/1993 to 16/03/1994 (Rocha et al., 2014). This dataset is explored in Chapter 5.

The INATEX is a multidisciplinary program consisting of four main subjects: *in situ* measurements of velocities in the Mozambique Channel (data processing is underway) and in the EMC domain (this thesis, Ponsoni et al., 2015a,

2016); tracing of Indo-Atlantic ocean exchange in sedimentary records (Steinhardt et al., 2014, 2015; Kasper et al., 2015); modeling of the Agulhas leakage dynamics (Le Bars et al., 2012, 2013, 2014); and air-sea coupled modeling of teleconnections and their tropical sources (Manola et al., 2013a,b, 2014). Regarding the part related to this thesis, a line with five moorings was deployed off the southeastern coast of Madagascar, at about 23°S, during the period from 07/Oct/2010 to 12/Mar/2013. The data processing and analysis are discussed in Chapters 2 and 3.

Quasi-synoptic profiles of temperature and salinity are used in Chapters 2 and 4, the former were sampled during the oceanographic cruises of deployment and redeployment of the INATEX moorings, and the latter were carried out on 30 March 2001 as part of the "Dutch-South African Agulhas Current Sources Experiment" (ACSEX 3). In this latter case, we also use velocities profiled by a Lowered Acoustic Doppler Current Profiler. Additionally, a large amount of *in situ* vertical profiles of temperature and salinity from the global array of free-drifting Argo floats are employed in Chapters 3 and 6. Also derived from *in situ* observations, the ANDRO database provides horizontal velocities (near 1000 m depth) estimated by the horizontal displacements of Argo floats (Chapter 3).

As remotely-sensed data from satellites, four different altimeter products are applied to support our analysis: absolute dynamic topography, absolute geostrophic velocity, sea level anomaly and geostrophic velocity anomaly (Chapters 2, 3, 5 and 6). And, also from satellite, Chapters 4 and 6 contain wind data from the NASA's Quick Scatterometer (QuikSCAT) satellite.

In Chapters 5, we apply the newly developed Faghmous' global database of ocean eddies identification (Faghmous et al., 2015a,b). Finally, a Sverdrup streamfunction dataset computed with the NCEP reanalysis winds and climatological thermohaline data from the CSIRO (Commonwealth Scientific and Industrial Research Organisation) Atlas of Regional Seas (CARS09) are used in Chapters 5 and 6.

In summary, this work is built on data from two monitoring (mooring) programs, quasi-synoptic data from two oceanographic cruises, hundreds of vertical profiles and horizontal displacements of Argo floats, two climatological and reanalysis-based datasets, five different satellite products, and an ocean eddy identification database. A detailed description of all datasets and their data processing are presented in the respective chapters.

1.7 SHORT GUIDANCE TO THE READER

The body of this thesis is composed of four published papers (Chapters 2, 3, 4 and 6) plus another manuscript in preparation for submission to a peer-reviewed journal (Chapter 5). We keep the thesis chapters as they were published so that they can be read independently. The price for that is that some repetition is found throughout the chapters. For making it easier to the reader, acronyms are redefined in each chapter.

2

THE EAST MADAGASCAR CURRENT

ABSTRACT

This study provides a long-term description of the poleward East Madagascar Current (EMC) in terms of its observed velocities, estimated volume transport and variability based on both ∼2.5 years of continuous *in situ* measurements and ∼21 years of satellite altimeter data. An array of five moorings was deployed at 23°S off eastern Madagascar as part of the "INdian-ATlantic EXchange in present and past climate" (INATEX) observational program. On average, the EMC has a width of about 60–100 km, and is found from the surface to about 1000 m depth. Its time-averaged core is positioned at the surface, at approximately 20 km from the coast, with velocity of 79(±21) cm s^{-1}. The EMC mean volume transport is estimated to be 18.3(±8.4) Sv. During the strongest events, maximum velocities and transport reach up to 170 cm s^{-1} and 50 Sv, respectively. A good agreement is found between the *in situ* transport estimated over the first 8-m of water column (0.32±0.13 Sv) with the altimetry-derived volume transport (0.28±0.09 Sv). Results from wavelet analysis display a dominant nearly bi-monthly (45–85 days) frequency band of transport variability, which explains about 41% of the transport variance. Altimeter data suggest that this band of variability is induced by the arrival of westward-propagating sea level anomalies, which in turn are likely represented by mesoscale cyclonic and anticyclonic eddies. Annual averages of the altimeter-derived surface transport suggest that interannual variabilities also play a role in the EMC system.

This chapter has been published as:
Ponsoni, L., B. Aguiar-González, H. Ridderinkhof and L.R.M. Maas, 2015. The East Madagascar Current: volume transport and variability based on long-term observations. *J. Phys. Oceanogr.* 46, 1045–1065.

2.1 INTRODUCTION

In the last decades the ocean circulation in the South-West Indian Ocean (SWIO) has drawn increasing attention from the scientific community. The main reason lies in the fact that the SWIO is a key region for the global overturning circulation and, therefore, to the climate system due to the interocean exchange between Indian and Atlantic Oceans. There, large amounts of relatively warm and salty water leak from the Indian to the Atlantic through the rings released by the Agulhas Current (AC) during its retroflection off the southern tip of Africa (Olson and Evans, 1986; Gordon et al., 1992; de Ruijter et al., 1999; Lutjeharms, 2006; Beal et al., 2011).

In addition to its importance in the climate system, the geostrophic circulation in the SWIO comprises one of the most intriguing western boundary current systems of all subtropical gyres. Unlike other western boundaries, the presence of Madagascar Island imposes a partitioning of the poleward flow into two components: one along the Mozambique Channel (MC) and another along the east Madagascar coast. In the MC the flow is dominated by southward-propagating anticyclonic eddies that fill almost the whole channel, both in depth and in width (de Ruijter et al., 2002; Ridderinkhof and de Ruijter, 2003; Ridderinkhof et al., 2010; Ullgren et al., 2012). On the other hand, off east Madagascar, the poleward flow is organized as a typical western boundary current (Duncan, 1970; Lutjeharms et al., 1981; Schott et al., 1988), the East Madagascar Current (EMC). We note here that the EMC is also referred to as Southeast Madagascar Current in the literature (e.g., Schott et al., 2009).

The main aim of this paper is to provide a long-term description of the EMC in terms of its observed velocities, estimated volume transport and variability, based on both ∼2.5 years of continuous *in situ* measurements and ∼21 years of satellite altimeter data.

The origin of the EMC is linked to the northern boundary of the South Indian subtropical gyre, represented by the South Equatorial Current (SEC). As the westward SEC approaches and crosses the Mascarene Plateau, near 60°E, it splits into northern and southern cores. The former carries 25 Sv between 10 and 14°S, whereas the latter transports about 20–25 Sv between 17 and 20°S (New et al., 2007). Farther west, the southern SEC core bifurcates towards the east coast of Madagascar into two branches: the poleward EMC and the equatorward North Madagascar Current (NMC, also know as Northeast Madagascar Current), which in turn joins the northern SEC core near the northern tip of the island (Schott et al., 1988; Swallow et al., 1988; Chapman et al., 2003; Siedler et al., 2006). According to Chen et al. (2014), the bifurcation of the southern SEC core, integrated over the upper thermocline depth, occurs on average at

18°S, varying throughout a year by about 1°, with its northernmost and southernmost positions found in November/December and June/July, respectively.

Downstream, the EMC seems to break up into a series of nearly symmetric dipolar vortex pairs off the southern tip of Madagascar. De Ruijter et al. (2004) and Ridderinkhof et al. (2013) suggest that the detachment of strong dipolar structures leads to events of early (easternmost) AC retroflection. Other suggestions have been presented in the literature on how the EMC contributes with source waters to the AC, such as by means of a retroflection regime characterized by cast-off eddies and fragments feeding into the AC system (Lutjeharms et al., 1981), through a minimized contribution due to a complete EMC retroflection (Lutjeharms, 1988), or in the form of a direct southwestward flow to the upstream Agulhas region (Grundlingh, 1993).

Most of the previous transport estimates for the EMC have been computed through geostrophic calculations based on *Expendable Bathythermograph* (XBT) and *Conductivity, Temperature, and Depth* (CTD) vertical profiling. Therefore, a computation of the geostrophic velocity field and its associated transport (e.g., Fomin, 1964) depends on the choice of a velocity reference level (and salinity estimates in the XBT case). Additionally, factors as time variability, geographical location and differences in the horizontal and vertical scales involved in the geostrophic calculations also contributed to the disparities in the EMC volume transport found in the literature: 20–24 Sv (Wyrtki, 1971); 35 Sv (Harris, 1972); 41 Sv (Lutjeharms et al., 1981); 35 Sv (Stramma and Lutjeharms, 1997). The reference level problem has been minimized by Swallow et al. (1988), who found 20.6 Sv of alongshore transport by using a reference level (1170 db) estimated from *in situ* velocities.

The EMC volume transport has also been inspected by numerical modelling. A 12-year modeled mean transport of 30 Sv has been found by Matano et al. (2002) in a meridional transect off southern Madagascar. Quartly et al. (2006) showed a downstream strengthening of the EMC transport, with mean alongshore transports of 7.9 Sv and 14.8 Sv at zonal transects off 22°S and 24°S, respectively. They also found 29.1 Sv at a meridional transect close to the transect previously inspected by Matano et al. (2002).

Only a few studies hinge on direct observations of velocity. Through a quasi-synoptic survey, where velocities were sampled by Lowered Acoustic Doppler Current Profiler (L-ADCP), Nauw et al. (2008) found a volume transport of 30 Sv at 25°S. Schott et al. (1988) analyzed 11 months of continuous observations, from three vertical lines of moorings, longitudinally aligned off 23°S, and found a mean (standard deviation) transport of 20.3(±6.6) Sv.

Since time series of *in situ* velocities are scarce, not much is known about the EMC variability. Schott et al. (1988) suggested that the most important varia-

tions occur in the 40 to 55-day-period-band, but such fluctuations contributed only with 15% to the total variance. These authors did not explore the forcing of such period of variability, since their main focus was on explaining why an annual cycle was not detected in the volume transport time series, despite the wind showing an important annual signal.

Warren et al. (2002), analyzing data from current meters deployed at 20°S in deep waters of the Mascarene Basin, found a bi-monthly undulation which propagates westward at 7 cm s^{-1} (6 km day^{-1}). The authors attributed this variability to barotropic Rossby waves forced by local wind-stress curl at one of the resonant frequencies of the Basin. Weijer (2008) determined the free oscillatory modes for the same region, by performing normal mode analysis, and reinforced that the mode that agrees best with the bi-monthly fluctuations can also be interpreted as a barotropic Rossby basin mode. However, while Warren et al. (2002) argued that such undulation is driven by mode-2, Weijer (2008) found the mode-1 resonance period as the source of this variability.

According to de Ruijter et al. (2005), strong variability around the intraseasonal scale is not just a local phenomenon in the SWIO, but it can also be associated to the basin and global scale circulations and their respective variabilities, which propagate sea surface height anomalies westward (Schouten et al., 2002a). Also, eddies reaching the region with frequencies of around five per year have been connected with the equatorial region (Schouten et al., 2002b; Palastanga et al., 2006) and with baroclinic instability of the South Indian Ocean Countercurrent (SICC) (Palastanga et al., 2007).

Regarding the vertical structure of the EMC system, at intermediate depths (around 1300 m), beneath the surface current and hugging the continental slope, an equatorward undercurrent was first reported by Nauw et al. (2008). More recently, a detailed study of this East Madagascar Undercurrent (EMUC) estimated a mean equatorward volume transport of 1.33($\pm$1.41) Sv, with maxima up to 6 Sv (Ponsoni et al., 2015a). An equatorward undercurrent has also been reported in the AC system (Beal and Bryden, 1997, 1999; Beal, 2009) and in the MC (de Ruijter et al., 2002; DiMarco et al., 2002; van Aken et al., 2004), while a poleward undercurrent was reported to occur below and opposite to the northward NMC (Ponsoni et al., 2015b).

In this context, the flow through the MC and off eastern Madagascar are important players of the climate system not only as sources of the AC but also due to their contribution to the upstream control of the AC retroflection. For more than a decade the flow through the MC has been observed with an array of moorings deployed and maintained by the Royal Netherlands Institute for Sea Research (NIOZ) (Ridderinkhof et al., 2010; Ullgren et al., 2012). Such long-term direct observations of the EMC system were still lacking and the

following sections intend to describe the EMC synoptic flow and the variability associated to this western boundary current.

This paper is organized as follows: the dataset description and data processing are addressed in Section 2; the EMC is described in terms of its mean flow, observed velocities, volume transport and variability in Section 3; a 21-year altimeter-based time series of surface geostrophic velocity is explored in Section 4; and, lastly, Section 5 presents the discussion and conclusions obtained by this study.

2.2 DATA AND DATA PROCESSING

2.2.1 *INATEX moorings: instrumentation and data return*

In early October 2010 an array of five moorings was deployed across the continental slope off the southeastern coast of Madagascar (Fig. 2.1), immediately north of 23°S, in the scope of the project "INdian-ATlantic EXchange in present and past climate" (INATEX). From inshore to offshore the moorings are named EMC1 to EMC5. The distances from the coast for every deployment are 6.3 (EMC1), 18.6 (EMC2), 44.8 (EMC3), 58.7 (EMC4) and 110.8 km (EMC5). The location of the INATEX array is near to the mooring array deployed, and maintained from October 1984 to September 1985, by Schott et al. (1988).

A sketch of the mooring array is presented in Fig. 2.2a. All five moorings carried an upward-looking Acoustic Doppler Current Profiler (ADCP) mounted in the top buoy, intended to sit at 500 m below the surface, to measure currents in this depth range where the flow is normally strongest and markedly sheared. Additionally, two moorings (EMC2 and EMC3) on the shoremost side of the array were equipped with an upward-looking ADCP in a frame positioned at about 13 m above the seabed.

The moorings EMC3, EMC4 and EMC5 were also equipped with Recording Current Meters (RCM) placed inline along the mooring cables at the nominal depths of 1000 and 1500 m, supplying point measurements of current velocity. In addition, EMC4 had RCMs at depths around 2000 and 3000 m (at 800 m above the seabed), while EMC5 was equipped with RCMs at depths around 2000 and 4000 m (near to the seabed).

RCM and ADCP sample rates were set to 20 and 30 minutes, respectively. RCM devices remained operational until the middle of March 2013, except for the RCMs at EMC3 at 1500 m and at EMC4 at 2000 m, which worked properly until the end of September 2012. The upper ADCP at EMC3 failed for the whole period, because of leakage and internal damage caused by the acid

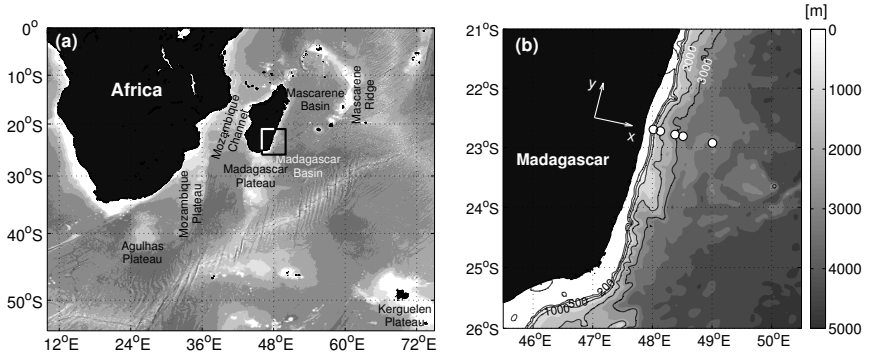

Figure 2.1: (a) Map of the South-West Indian Ocean. The main geomorphological features are highlighted in the plot. (b) Zoom of the area of study demarcated by the square drawn in (a). Bathymetric contours are drawn in shades of gray (depth indicated in meters). The white circles represent the geographical location of the INATEX moorings (EMC1–EMC5, from inshore to offshore). The plotted axes indicates the rotation of the coordinate system in alongshore (y) and cross-shore (x) directions.

from the batteries, while all the other ADCPs sampled continuously from the deployment until the mooring recovery in April 2013. Therefore, time series from 16 instruments (6 ADCPs and 10 RCMs) are used in this study.

2.2.2 *Mooring data processing*

Subsequent to the removal of bad-quality data, the series were synchronized and truncated from 7 October 2010 to 12 March 2013, accumulating approximately 2.5 years (888 days) of data. This is except for the two RCMs that worked only until September 2012, from whereon we treat the mooring array without these two instruments.

With the aim to remove tidal and near-inertial motions from the time series, all current velocity records went through low pass filtering (forward–backward Butterworth filter), with a 3.5 day cut-off period, as suggested in the literature (Ridderinkhof et al., 2010; Ullgren et al., 2012). The data were subsampled daily at noon. Meridional and zonal velocities were oriented, respectively, parallel (v) and perpendicular (u) to the coast after a clockwise rotation of 12.9° from North (Fig. 2.1b). By convention, negative and positive values of

the alongshore v-component represent a poleward and equatorward flow, respectively.

Velocity data from the upper layer (approximately from 50 m depth to the surface, illustrated by the red shaded region in Fig. 2.2a) are missed due to limited instrument resolution and near-surface loss typically presented by upward-looking ADCPs. To fill in this gap, velocity data were vertically extrapolated towards the surface onto 8 m cells (ADCP vertical resolution), at standard depth levels (0, 8, 16, etc), through an interactive process. For this, the mean vertical shear from the four uppermost sampled depth levels is extrapolated to fill in the next upper grid point and the process is repeated until the uppermost bin is reached. The method is applied at every time span and individually for all mooring positions, except at EMC3 where the uppermost measurement is around 1000 m. This method was motivated by the geostrophic velocity calculated from the thermohaline field observed during the deployment and redeployment cruises, which shows the velocity to be increasing in magnitude towards the surface (Fig. 2.2b).

We compare the velocity time series from different depths and moorings in order to guide spatial interpolation (Ridderinkhof et al., 2010). To do so, cross-correlations are calculated and the hypothesis of no correlation is tested by use of the p-value test (Fig. 2.2c). Each p-value represents the probability of getting a true correlation (p-value $= 0$) by random chance. The correlations are significant, for a 95% confidence interval, when the p-value is smaller than 0.05. Overall, high and significant positive correlations are obtained amongst series from the same mooring (pairs highlighted by white circles in Fig. 2.2c). Due to this strong vertical correlation, the time-synchronized data from ADCPs and RCMs were first linearly interpolated vertically onto 8 m bins.

An important exception to this good vertical correlation is seen at EMC2, since the series from the ADCP placed at 1600 m (Fig. 2.2c, red star and black dashed area) captured a flow reversal associated to the equatorward EMUC (Ponsoni et al., 2015a). However, velocities are also linearly interpolated between the two ADCPs in this mooring line because we noticed that velocities at the uppermost bin from EMC2–1600 both decay to zero and slightly increase their correlation with the lowest measurements from EMC2–0500.

Strong positive correlations are also found between pairs of series extracted from the region near the EMC core (highlighted by black circles in Fig. 2.2c). Green and yellow dashed areas in Fig. 2.2c show that the instruments placed at EMC5 have good correlation only amongst themselves, suggesting that the mooring array was well designed to capture the EMC flow, since this mooring was placed offshore the EMC domain during most of the time.

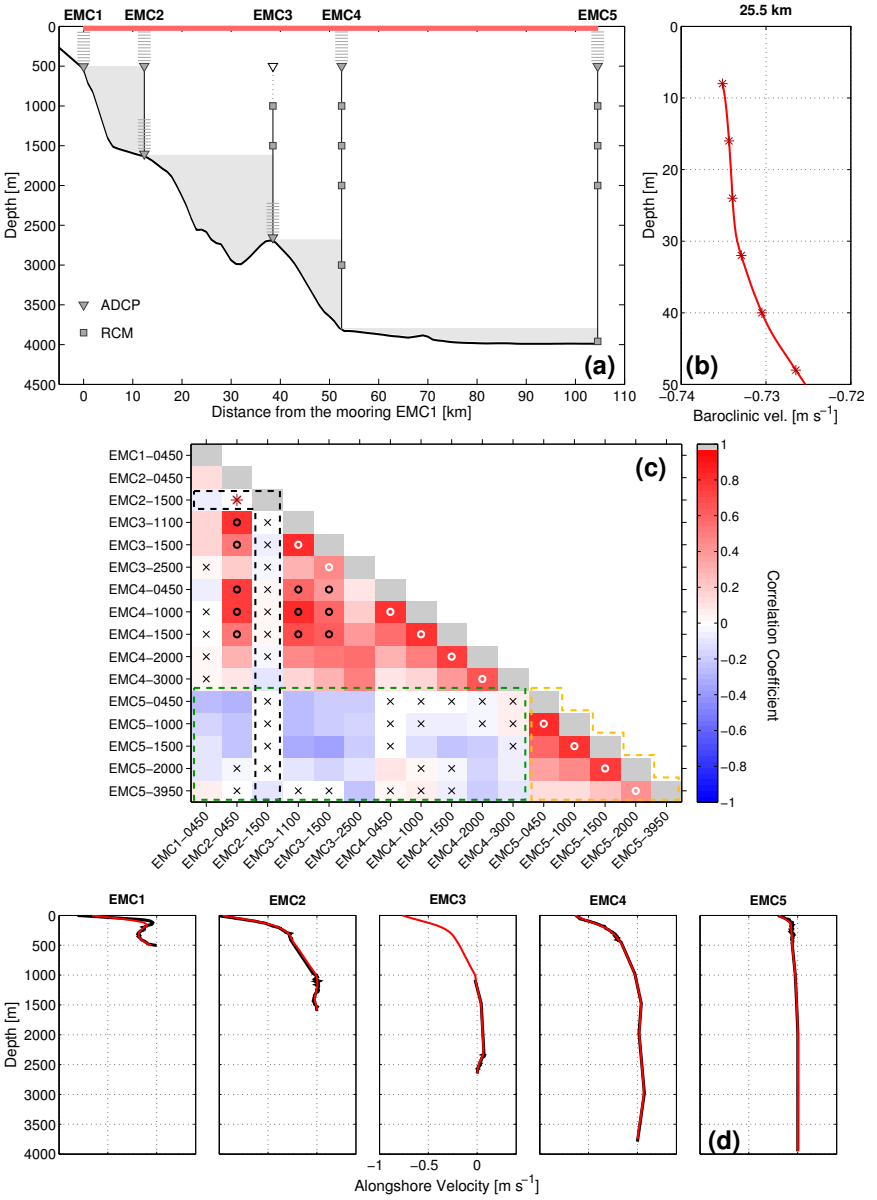

Figure 2.2: (a) Sketch of the INATEX moorings where ADCPs and RCMs are represented by triangles and squares, respectively. The small horizontal lines over the triangles represent the upward-looking range of the ADCPs and the empty triangle at EMC3 shows the faulty instrument. The gray shaded *(continue)*

Figure 2.2 : *(continuation)* areas (near the slope) and the red area (near the surface) show regions where extrapolation is applied. (b) Geostrophic velocity estimated in between EMC2 and EMC3 (at 25.5 km from EMC1) with *in situ* thermohaline profiles used to guide extrapolations towards the surface (red area in (a)). (c) Correlation matrix between pairs of velocity time series from all instruments. White and black circles highlight high correlation between time series from vertically adjacent instruments and time series from instruments near the EMC core, respectively. Black crosses display not significant correlation. Regions highlighted by yellow and green dashed lines indicate low (or not significant) correlation between time series from EMC5 and the time series from the other moorings. Black dashed line and red star indicate the low (or not significant) correlation between the velocity from EMC2-1500 and the other instruments due to the reversal of the flow associated with the EMUC. (d) Time average profiles of alongshore velocity achieved with full-slip (black) and optimal extrapolations (red).

Subsequently, the data from the moorings are horizontally merged by linear interpolation applied for each standardized 8-m depth level onto a horizontal grid of 1 km. Notice that this interpolation also fills in the empty region created by the malfunctioning of the faulty ADCP at EMC3 (Fig. 2.2a). Other methods of interpolation were attempted to fill in this gap, as for instance the tapered linear interpolation scheme suggested by Ridderinkhof et al. (2010), but our simple horizontal interpolation presented better results with respect to preserving spatial gradients. Hence, the final cross-shore grid resolution is 1 km (distance) $\times$ 8 m (depth).

Next, bottom extrapolation was performed to fill in empty data regions created between every pair of neighboring moorings and the bathymetry below the shallowest station of this pair (Fig. 2.2a, gray shaded areas). Initially, two opposite options are considered: (i) assume that velocities decrease linearly to zero at the continental slope, obeying a no-slip boundary condition; (ii) extrapolate horizontally the nearest measurement up to the continental slope, accomplishing a full-slip boundary condition (Beal and Bryden, 1997; Nauw et al., 2008; Beal, 2009). For the sake of completeness, we apply both boundary conditions to our observations, as well as a third method where empty regions are gridded with an (iii) optimal interpolation scheme (Carter and Robinson, 1987; da Silveira et al., 2004). The reader is referred to Ponsoni et al. (2015a) for a detailed description of (iii) applied to our data. Later in Section 2.3.2, the results will show that this extrapolation step has minor impact on the computation of the EMC transport, although it deserves special attention in the study of the EMUC, as explored by Ponsoni et al. (2015a). Fig. 2.2d shows the

time-averaged profiles of alongshore velocity, at every mooring, achieved with full-slip and optimal extrapolation.

2.2.3 *Supplementary data sources*

We noticed during the deployment cruise that the bottom topography strongly differed from the bathymetry databases. Thus, bathymetry values were time-recorded from the onboard echosounder every 5 minutes (see bathymetric contour in Fig. 2.2a).

As mentioned above, in order to guide extrapolations of velocities sampled by the 500-m upward-looking ADCPs from their maximum reach (minimum depth) until the surface (approximately the upper 50 m of water column), a vertical profile of geostrophic velocity was calculated in between EMC2-EMC3 (Fig. 2.2b) based on the thermohaline structure sampled by CTD, during the deployment and redeployment cruises, at the position of the moorings EMC2 and EMC3.

At daily resolution, a ∼21-year (from 01 January 1993 to 31 May 2014) altimeter-based time series of Absolute Dynamic Topography (ADT), Sea Level Anomaly (SLA) and surface absolute and anomaly geostrophic velocities estimated from both ADT and SLA, respectively, are used in this work. The altimeter products were produced by Ssalto/Duacs and distributed by Aviso (`http://www.aviso.altimetry.fr/duacs/`), with support from Cnes. Here we use the daily data from the "all sat merged" series of the delayed-time altimeter product, which is provided with a spatial resolution of 0.25°. The ADT product results in adding SLA to the New Mean Dynamic Topography (MDT-CNES-CLS13) produced by the CLS Space Oceanography Division as an estimate of the ocean sea surface height above the geoid for the 1993-2012 period (Rio et al., 2014).

2.3 IN SITU OBSERVATIONS OF THE EAST MADAGASCAR CURRENT

2.3.1 *Observed velocities, mean flow and mesoscale activity*

The *in situ* measurements from the INATEX moorings indicate a strong western boundary current with some meandering activity, as represented by the stick plot of velocities in Fig. 2.3. A reversal of the flow is observed near the surface at EMC2 (Fig. 2.3a) only twice, and for different reasons (see explanation below): around the transition December 2010–January 2011 and at the beginning of July 2011.

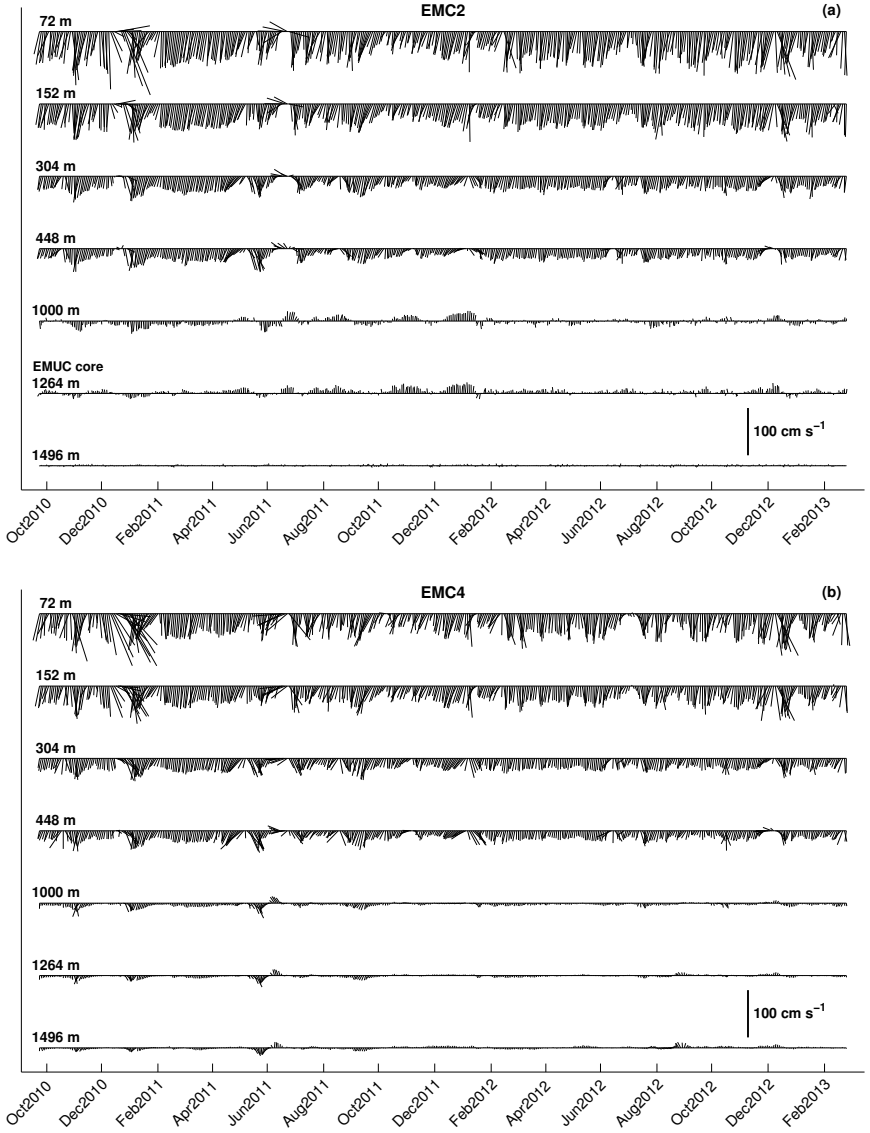

Figure 2.3: Velocity vectors from moorings (a) EMC2 and (b) EMC4 at depths of 72, 152, 304, 448, 1000, 1264 and 1496 m, plotted every 2 days. Ticks on the x-axis are placed at noon on the 15th day of the respective month. The vectors are rotated in cross-shore – alongshore coordinates.

The current is crossing the transect slightly inclined towards the coast at EMC2, while the flow is more perpendicular to the transect at EMC4 (Fig. 2.3b). Statistics displayed in Table 2.1 indicate that the mean velocities of the alongshore component (-55.0 and -42.3 cm s^{-1}, at EMC2 and EMC4) are more than eight times stronger than the mean cross-shore component (-6.4 and -3.5 cm s^{-1}) near the surface. Large differences are also found at other depths (Table 2.1).

Table 2.1: Mean velocities and standard deviations (cm s^{-1}) of the EMC at the EMC2 and EMC4 moorings at several depths (m). Alongshore and cross-shore velocity components are represented by v and u, respectively. The alongshore axis is rotated 12.9° from North. The statistics are based on a total of 888 days.

	EMC2 (v)		EMC4 (v)		EMC2 (u)		EMC4 (u)	
Depth	mean	std	mean	std	mean	std	mean	std
72	-54.99	20.43	-42.30	17.50	-6.41	10.50	-3.55	13.76
152	-42.24	14.13	-34.97	12.87	-6.22	7.34	-4.35	9.71
304	-25.78	9.10	-23.11	7.50	-4.55	6.14	-3.80	7.70
448	-19.34	9.28	-18.54	8.34	-3.94	6.55	-3.72	8.83
1000	-2.04	8.13	-4.45	4.76	-0.24	1.32	-1.38	3.19
1264	3.93	6.24	-2.04	4.08	-0.42	1.45	-0.75	2.52
1496	0.70	1.70	-0.08	3.79	0.23	1.12	-0.23	2.41

The vertical shear shown in Fig. 2.3 and Table 2.1 highlights the velocity decay from the surface to approximately 1000 m, where the velocity field is close to its mean level of no motion (0 cm s^{-1} isotach in Fig. 2.4a). In the vicinity of 1260 m at EMC2 (Fig. 2.3a), up on the continental slope, there is a reversal in the flow associated with the equatorward EMUC.

Hereafter the grid point where the EMC has its strongest velocity value will be referred to as core. The real current core at every moment is likely missed due to the horizontal spacing between neighboring moorings. The global maximum velocity was measured on 23 December 2010, when the EMC core presented speeds up to -172 cm s^{-1} at the EMC2 location. However, this value is an exception since velocities stronger than -150 cm s^{-1} were rarely observed: during 6 of 888 days. Velocities stronger than -100 cm s^{-1} were sampled on

119 days (∼13% of the whole time span), while most of the core values lie in the range of -50 and -100 cm s^{-1} (698 days, ∼79% of the whole time span).

The EMC presents a mean core with a velocity of -79(±21) cm s^{-1}, which is found close to the surface at EMC2 (Fig. 2.4a). Only on a few occasions the EMC core was sampled offshore in moorings EMC4 or EMC5 (for instance, Fig. 2.4b), during 24 and 17 days, respectively.

Fig. 2.4b and Fig. 2.4c display the two moments when a reversal of the flow is registered in Fig. 2.3. The daily sequence of plots (not presented) shows the equatorward flow related to the first event growing from the coast and vanishing at depths greater than 500 m, at the same moment as the EMC migrates offshore. However, we do not have a clear explanation of the forcing of this reversal. The second reversal is more pronounced and an equatorward flow is observed over the entire water column. It results from the passage of a cyclonic eddy coming from the EMC upstream region. In Section 2.4 we will discuss the impact of cyclonic eddies arriving from the east to the offshore edge of this western boundary current.

An outstanding contribution of the baroclinic component to the geostrophy of the EMC system is suggested in Fig. 2.4d–f. For instance, in Fig. 2.4e a strong poleward surface current appears concomitantly with a strong equatorward undercurrent, while in Figs. 2.4d and 2.4f a weak surface and a weak undercurrent coexist. Additionally, Fig. 2.4f shows an occasion when the EMC flow was exceptionally weak and, consequently, the integrated volume transport through the INATEX transect was nearly zero (see Section 2.3.2).

However, this scenario is not always observed, since there are moments when the baroclinic contribution is weaker, while the barotropic component increases, as suggested in Figs. 2.4g–i. At these moments, when a robust poleward barotropic flow contributes to an increasing volume transport, the EMC migrates deep into the water column, masking the equatorward flow at intermediate levels. Therefore, the EMUC is virtually absent in the velocity time series at these moments (Ponsoni et al., 2015a). Notice that the -10 cm s^{-1} isotach reaches down to about 1500 m in Figs. 2.4g–i.

Fig. 2.4g highlights an unusual scenario where the EMC core is not found close to the surface but is rather shifted to around 450 m depth. Only on nine other days the EMC core was found deeper than 50 m. This figure also stresses a deep excursion of the entire EMC structure. For instance, the -10 cm s^{-1} isotach reached 2500 m depth at EMC3.

Fig. 2.4h and Fig. 2.4i show the cross-shore transects in which the EMC attained maximum transport over our time series. In both cases maximum observed velocity was around -98 cm s^{-1}. However, besides this similarity, the

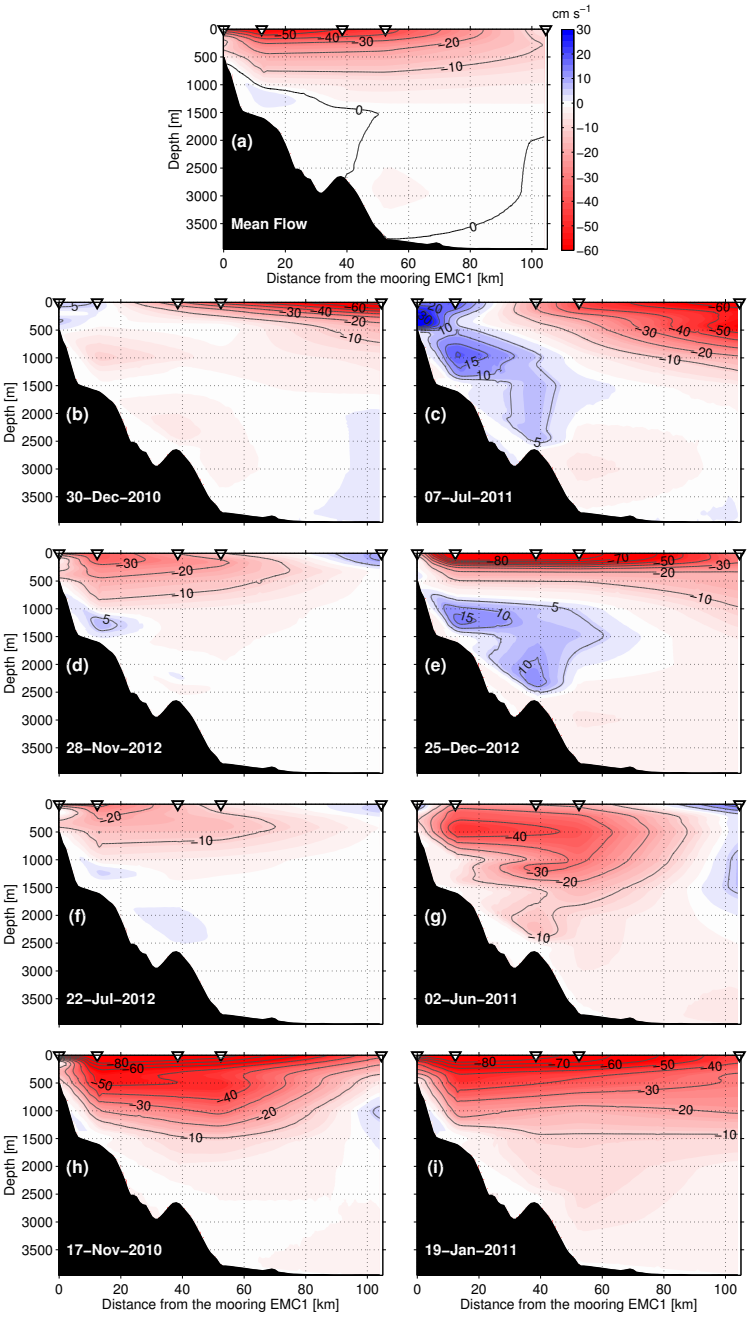

Figure 2.4: (a) Alongshore mean flow and (b-i) alongshore velocities observed at eight different moments. Notice that the panels are not placed in chronological order, but according to the sequence that they are discussed in the text.

computed EMC transport was 5 Sv stronger on 19 January 2011 (Fig. 2.4i), since at this occasion the EMC was wider than on 17 November 2010 (Fig. 2.4h) as indicated by the isotachs in both panels.

2.3.2 *Volume transport*

In order to calculate the volume transport two methodological issues have to be addressed. First, extrapolations are necessary to fill in empty data regions highlighted by the gray shades in Fig. 2.2a, as already detailed in Section 2.2.2. Second, we have to select the grid points, at every time span, in which velocity values will be computed for the transport calculations.

Regarding the first issue, the results indicate that the chosen method (no-slip, full-slip or optimal interpolation) for gridding empty areas has minor impact on the volume transport calculations, since most of the flow related to the EMC is not crossing those regions (compare Fig. 2.2a with Fig. 2.4). Notice in Table 2.2 that the average errors from different methods are smaller than 0.5 Sv. We use the velocity fields extrapolated through optimal interpolation to plot figures and for further discussions in this paper.

Table 2.2: Volume transport (Sv) calculated from different extrapolation methods (No-Slip (NS), Full-Slip (FS), Optimal Interpolation (OI)) and different integration criterion (Net Volume Transport (NVT) and Isotach-Delimited Volume Transport (IDVT)).

	NS	**FS**	**OI**
NVT: bottom–surface	-18.3(±8.5)	-18.6(±8.9)	-18.3(±8.4)
NVT: 1500 m–surface	-17.8(±6.8)	-18.1(±7.0)	-17.8(±6.8)
IDVT: 0 cm s^{-1} isotach	-20.6(±7.6)	-21.2(±7.9)	-20.5(±7.5)
IDVT: 10 cm s^{-1} isotach	-16.0(±6.8)	-16.4(±7.0)	-16.0(±6.8)

Regarding the second issue, we adopted two general options to guide the selection of points that will be used to compute the volume transport: (i) Net Volume Transport (NVT), where both positive and negative velocity values integrated from a certain depth to the surface are considered; and (ii) Isotach-Delimited Volume Transport (IDVT), where only grid points with negative values (poleward flow), enclosed by a specific isotach, are computed. The motivation for this latter choice is that this may represent a flow having different water mass properties.

Fig. 2.5a shows the mean NVT integrated from different depths. For instance, the black and red stars indicate a poleward (therefore, negative) mean NVT of -17.8(±6.8) Sv and -18.3(±)8.4 Sv for the upper 1500 m and for the whole water column, respectively. Fig. 2.5b shows a mean IDVT of -16.0±6.8 Sv and -20.5±7.5 Sv calculated with the isotachs of -10 cm s^{-1} (blue star) and 0 cm s^{-1} (green star) as limits, respectively.

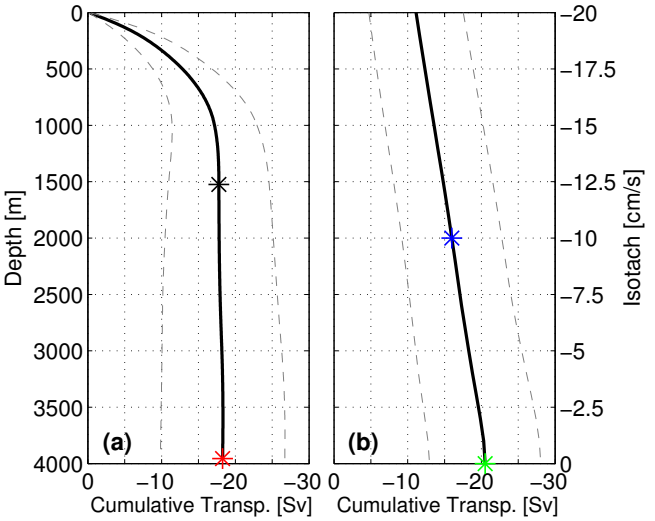

Figure 2.5: Mean EMC volume transport calculated with two methods. (a) Net Volume Transport (NVT), where both negative (poleward) and positive (equatorward) values of velocity are computed in the transport calculation. The black curve represents the cumulative mean transport from the surface to a certain depth (y-axis). (b) Isotach-Delimited Volume Transport (IDVT), where only grid points with negative values (poleward flow) enclosed by a specific isotach (y-axis) are computed in the transport calculation. Gray dashed lines represent the standard deviation. The stars highlight the mean values of the time series plotted in Fig. 2.6.

Fig. 2.6 shows the complete transport time series calculated for the four different cases discussed in the previous paragraph and highlighted with the stars in the mean scenario, shown in Fig. 2.5 and Table 2.2. Notice that besides the differences in the transport values, all time series have the same pattern of variability.

During three short periods the EMC is marked by a large volume transport: around 17 November 2010, 19 January 2011 and 30 September 2011 the EMC

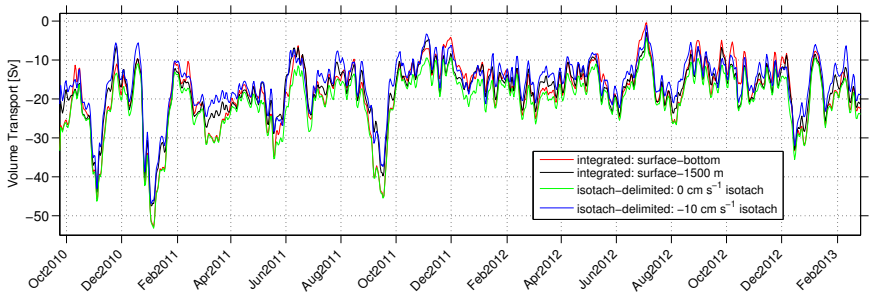

Figure 2.6: Volume transport time series: integrated volume transport from the bottom (red) and 1500 m (black) to the surface estimated with both negative (poleward) and positive (equatorward) values of velocity; isotach-delimited volume transport estimated through the poleward flow (only negative values of velocity) delimited by the isotachs of -10 (blue) and 0 cm s^{-1} (green). Ticks on the x-axis are placed at noon on the 15th day of the respective month.

transport reached up to -45.6, -52.8 and -45.2 Sv, respectively (NVT, integrated from bottom to surface, red line in Fig. 2.6). In the strongest event the EMC transported over 50 Sv from 12 January 2011 to 20 January 2011. Such strong volume transports, reaching up to -40 Sv, are unusual and occur only during 3% (26 of 888 days) of the entire time span. Transport values in the intervals of (-40,-30), (-30,-20), (-20,-10) and (-10,0) Sv were sampled during 51, 211, 488 and 112 days, respectively.

A notable minimum poleward transport of 0.4 Sv was observed on 18 July 2012. From 14 to 19 July 2012 the transport values were reduced to less than 3 Sv. The reduced transport around this period is effectively a consequence of a weak current, rather than an artifact of the EMC meandering offshore the INATEX moorings (Fig. 2.4f). Such small transport was not observed again from October 2010 to March 2013.

2.3.3 *Transport variability*

Wavelet analysis (Fig. 2.7b) of the EMC transport time series (Fig. 2.7a) reveals a clear nearly bi-monthly period band of variability, which dominates the global spectrum when integrated over time (Fig. 2.7c). This period is centered at 66 days (frequency 5.5 year^{-1}), but is also significant over the band from 45 to 85 days, corresponding to a frequency band of 4.3 to 8.1 peaks per year.

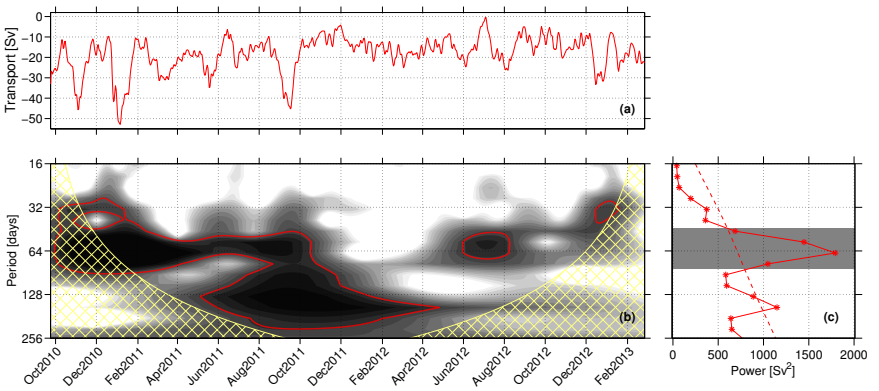

Figure 2.7: (a) Volume transport time series (same as red line in Fig. 2.6). (b) Wavelet power spectrum of the normalized volume transport time series. The red contours denote the 95% significance levels above a red noise background spectrum, while the cross-hatched areas indicate the “cone of influence" where edge effects become important. For all cases the mother wavelet is Morlet wavelet (see Torrence and Compo (1998) for details). (c) Time-integrated power spectrum from the wavelet analysis, where the dashed area corresponds to the 95% significance level. The nearly bi-monthly period (45–85 days) is represented by the horizontal gray bar.

As an additional analysis, we estimate the NVT for every 8-m vertical layer (see mean values per layer in Fig. 2.8a) and so apply the wavelet analysis for the individual time series. Fig. 2.8b indicates that the bi-monthly signal is surface-intensified, but still significant in the upper 1000–1500 m depth.

This dominant band of variability differs from that of the EMUC, which presents stronger variability near the semi-annual period band (132–187 days), likely related to some internal mode of variability of the system (Ponsoni et al., 2015a). The EMC transport presented only a slightly significant nearly semi-annual peak centered at 155 days (Fig. 2.7c).

After applying a band pass filter (forward–backward Butterworth filter) adjusted for the bi-monthly period (45 to 85 days), we found that 41% of the variance of the transport time series can be explained by this band. However, although strong, this variability is not persistent over the whole time series. From the beginning of November 2011 to the middle of June 2012, the bi-monthly band does not appear significant in the wavelet spectrum (Fig. 2.7a and Fig. 2.7b). During this period of time (here computed from 01 November 2011 to 15 June 2012) the EMC transport time series reduced both on aver-

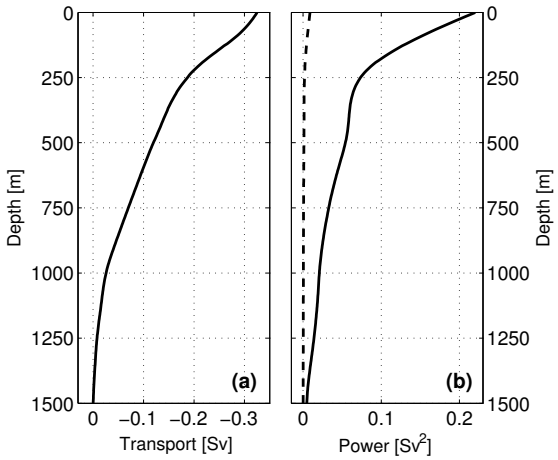

Figure 2.8: (a) Time-averaged NVT calculated for every 8-m depth interval perpendicular to the INATEX transect. (b) Power density for the 66-day signal (full line) from the wavelet analysis (same as in Fig. 2.7c) and its respective 95% significance level (dashed line) for every 8-m vertical bin.

age as well as in standard deviation (-14.4±4.3 Sv) when compared to the full record (-18.3±8.4 Sv).

The forcing of the nearly bi-monthly period, as well as an explanation for the absence of this variability in the time span mentioned above are discussed in Section 2.4.1.

2.4 ALTIMETER OBSERVATIONS OF THE EAST MADAGASCAR CURRENT

To the knowledge of the authors, the INATEX time series represent the longest continuous *in situ* measurements of the EMC system. This dataset also provides unique horizontal and vertical resolution of the current velocities. Nevertheless, it presents some limitations. For instance, the spatial coverage of the measurements is restricted to the mooring array, which makes answering questions as "what is the forcing of the nearly bi-monthly variability?" hard to assess. In this respect, satellite altimeter observations at ocean basin scale may contribute to our understanding of the EMC system.

2.4.1 *Forcing of the nearly bi-monthly variability*

The combined analysis of altimeter data and *in situ* observations reveals that the nearly bi-monthly variability is strongly related to the SLA field (Fig. 2.9). Overall, the peaks seen in both the geostrophic velocity estimated from ADT (Fig. 2.9b) and the *in situ* velocities (Fig. 2.9c) and, therefore, in the EMC transport (Fig. 2.9d), are observed concomitantly with high positive anomalies in the sea level (Fig. 2.9a).

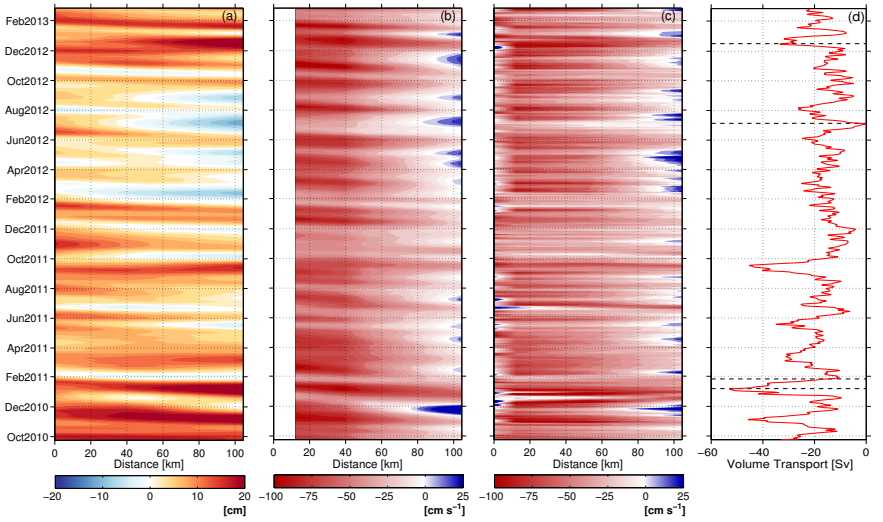

Figure 2.9: Distance/time diagrams: (a) Sea Level Anomaly (SLA); (b) alongshore geostrophic velocity estimated from Absolute Dynamic Topography (ADT); (c) Alongshore observed velocities at 75 m from the INATEX moorings. (d) Volume transport time series (same as red line in Figs. 2.6 and 2.7a) from INATEX velocity measurements. Horizontal black dashed lines indicate the moments when the horizontal fields of Sea Level Anomaly are shown in Fig. 2.10. In the three first panels, the horizontal scale displayed on the x-axis is the distance from EMC1 to EMC5.

In dynamic terms, these domes in SLA are represented by Anticyclonic Eddies (AE). The poleward flow on their landward side potentially increases the EMC flow. On top of this, the presence of the coast creates a mirror image vortex (Shi and Nof, 1993, 1994; Kundu and Cohen, 2008) which drives the core of the AE poleward. The converse is true for negative anomalies (Cyclonic Eddies, CE), which induce an attenuation in the EMC transport (Fig. 2.9). Again

this is due to the landward side of the CE flowing equatorward, while its mirror vortex, due to the presence of the coast, tends to drive the CE also equatorward.

Fig. 2.10 shows fields of SLAs plotted at four different moments, indicated by black dashed lines in Fig. 2.9d. On 20 January 2011 (Fig. 2.10a), a strong positive anomaly is intensifying the EMC transport to its maximum observed during the INATEX program. This event is particularly strong because such a feature is resulting from the merging of two AEs (for the daily sequence of images, the reader is referred to the animations in the supplemental material). On 09 February 2011 (Fig. 2.10b), right after the passage of the previous AE, a negative anomaly (CE) is attenuating the EMC transport. On 19 July 2012 (Fig. 2.10c), a CE is inducing the EMC transport to its minimum observed during the INATEX program. Notice that at this moment the whole region shown in the map presents reduced SLA values. On 30 December 2012 (Fig. 2.10d), another AE increases the EMC transport.

Remarkably, for about 3.5 months, from 16 February to 29 May 2012, a large CE maintained its landward branch over the mooring array. During this period the EMC did not present intense events, since this branch of the eddy was attenuating the EMC and the arrival of AEs was blocked by the quasi-standing CE. This is the reason why the bi-monthly variability is absent in the EMC transport (Fig. 2.7).

The remote origin of the reported quasi-standing CE was found farther east (62°E, 24°S) at the beginning of August 2011 (Fig. 2.11). From its origin to Reunion Island (55.6°E, 23.4°S, on 29 November 2011) the eddy travelled with a mean velocity of 6.2 km day^{-1}. After passing the Reunion Island the eddy became stronger and travelled with a mean velocity of 9 km day^{-1} towards the Madagascar coast until it parked near 50°E on 16 February 2012. Fig. 2.11 presents the track of the CE from its origin to the parking region, where it disappeared.

Fig. 2.12a shows the alongshore velocities observed at the EMC5 mooring highlighting the period when the quasi-standing CE was strong enough to induce a reversal of the flow at this location. Fig. 2.12b and Fig. 2.12c show such a cyclonic eddy on 23 February 2012 and on 18 May 2012, respectively.

In order to investigate the pathway of sea level anomalies which induce the nearly bi-monthly variability in the EMC, we calculate the wavelet spectra of SLA time series over the south Indian Ocean and compute the mean power spectra within the defined band (45–85 days, see Fig. 2.7c). The map plotted in Fig. 2.13 shows that, to the east of the Mascarene Ridge (longitudes to the east of 60°E), the westward-propagating anomalies travel preferentially in a cor-

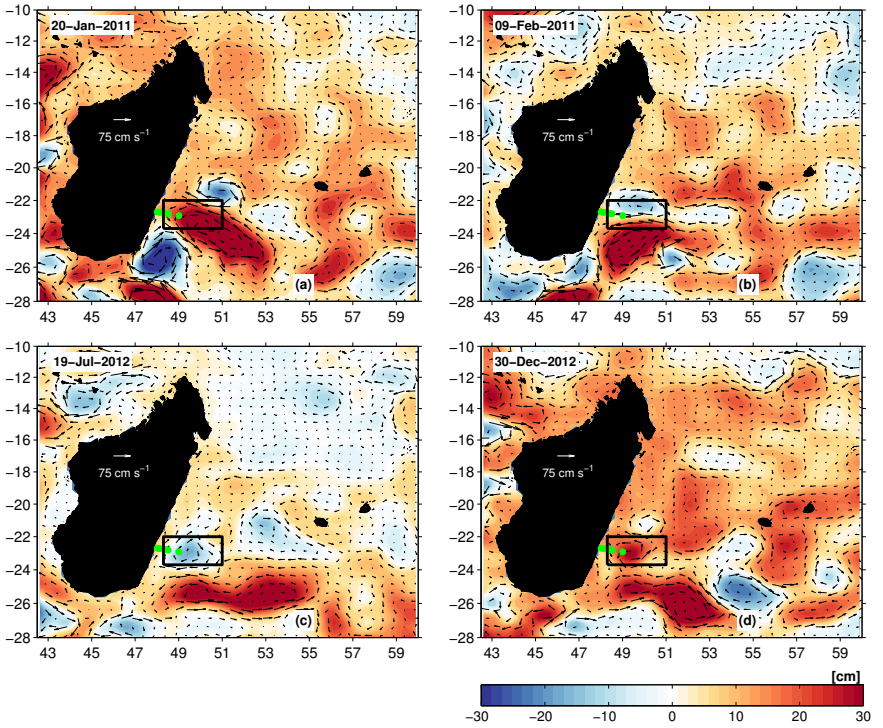

Figure 2.10: Sea Level Anomaly (SLA) from satellite altimeter data plotted at four different moments: (a) On 20/Jan/2011 when a strong positive anomaly (anticyclonic eddy) is intensifying the EMC transport to its maximum observed during the INATEX program; (b) On 09/Feb/2011 when, right after the passage of the anticyclonic eddy shown in (a), a negative anomaly (cyclonic eddy) is attenuating the EMC transport; (c) On 19/Jul/2012 when a cyclonic eddy is inducing the EMC transport to its minimum observed during the INATEX program; (d) and on 30/Dec/2012 when another anticyclonic eddy increases the EMC transport. The green points indicate the position of the INATEX moorings. The black box is discussed in Section 2.4.3 and used as reference to calculate the SLA averages plotted in Fig. 2.15.

ridor approximately defined by the latitudinal range of 18°S–24°S. However, the nearly bi-monthly period is strongly intensified in the Mascarene Basin, in between the Mascarene Ridge and the southern part of Madagascar Island (Fig. 2.13). This phenomenon is also visible in the animations provided as supplemental material to this paper.

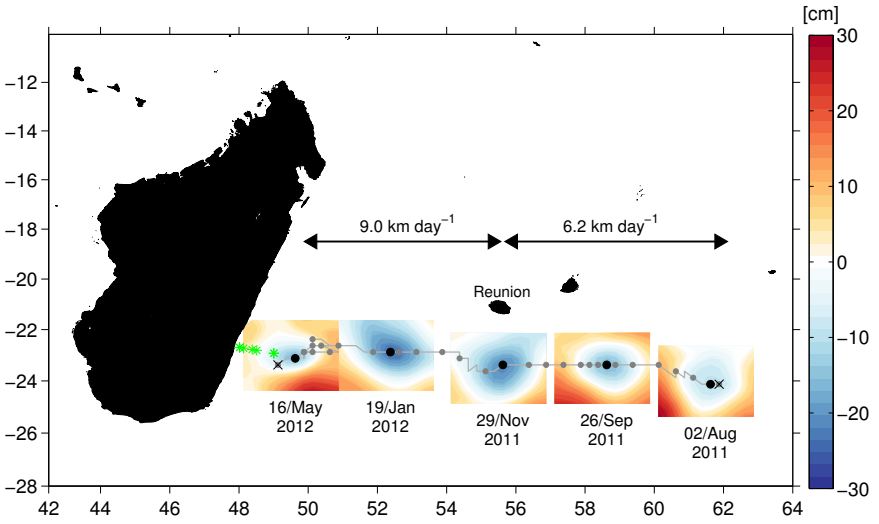

Figure 2.11: Origin and track of cyclonic eddy propagating towards Madagascar coast seen through values of Sea Level Anomaly (SLA). The cyclonic was observed standing offshore the INATEX moorings for about 3.5 months before being dissipated (see Fig. 2.12). Crosses display the regions of origin (∼62°E and 24°S, on 01/Aug/2011) and ending (∼49°E and 23°S, on 31/May/2012) of the eddy. Gray line shows the path of the CE, while small gray circles indicate the center of the eddy every 5 days. Black circles represent the cyclonic core at the moments when the contours of SLA are also plotted in the figure. The arrows indicate that the eddy travelled with mean speed of 6.2 km day^{-1} and 9.0 km day^{-1} along the track from the origin to Reunion Island and from Reunion Island to its parking location, respectively. The green stars indicate the position of the INATEX moorings.

2.4.2 *21 years of altimeter-based surface volume transport estimates*

In this section we evaluate how good the match is between the *in situ* velocities and the absolute geostrophic velocities measured from satellite, and then we derive a long-term altimeter-based time series of surface volume transport. To do so, first we spatially interpolate the altimeter-derived absolute geostrophic velocities to the horizontal INATEX grid positions and, subsequently, decompose these velocities in the same fashion as done for the *in situ* velocities (Section 2.2.2) in order to find the alongshore component.

Second, we calculate the volume transport, from EMC2 to EMC5, assuming that these velocities are uniform over the first 8 m of water column so that the grid resolution is equal to the one used for the sampled data (1 km (distance)

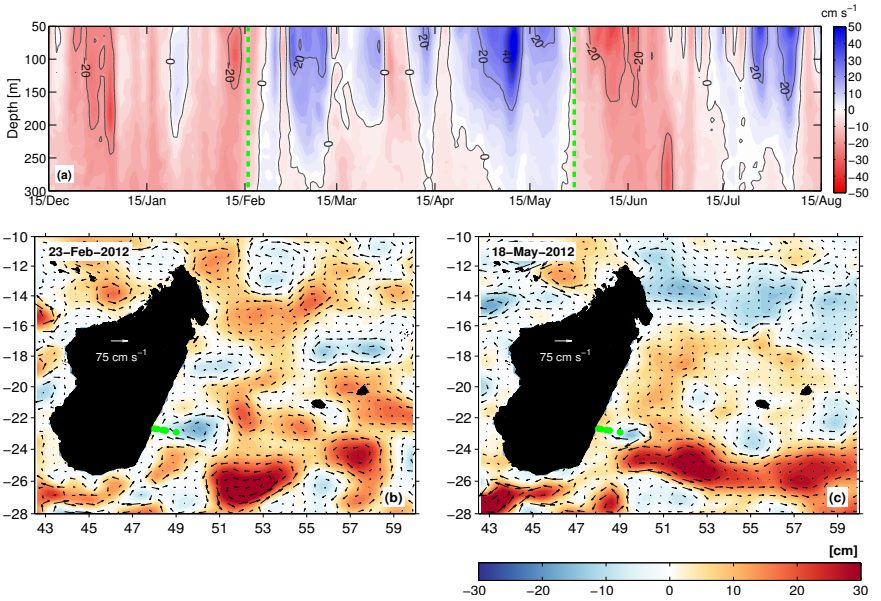

Figure 2.12: (a) Alongshore velocities observed at the EMC5 mooring highlighting the period (enclosed by the green dashed lines) when it is possible to observe the quasi-standing cyclonic eddy which stayed in the vicinity of the INATEX moorings for about 3.5 months (from 16/Feb/2012 to 29/May/2012, approximately). (b) Sea Level Anomaly (SLA) from satellite altimetry plotted on 23/Feb/2012 and (c) on 18/May/2012 showing the quasi-standing CE in the region of the INATEX moorings. The green stars indicate the position of the INATEX moorings.

$\times$ 8 m (depth)). We disregard the data inshore of EMC2, since close to the coast the altimeter performance is affected by the land mass and, therefore, errors of the altimeter-based geostrophic velocities are typically higher.

Fig. 2.14 shows the surface volume transport calculated from the altimeter-based geostrophic velocities (black line, from Oct/2010 to Mar/2013) and from the *in situ* velocities (red line) over the first 8-m bin. Overall there is a high correlation between both time series, with correlation coefficient of 0.72 (significant for a p-value test). The mean absolute error, $\frac{1}{n}\sum_{i=1}^{n}|e_i|$, where the daily error $e_i(i = 1, 2, ..., 888)$ is defined by the difference between both variables, is equal to 0.07 Sv. The average (standard deviation) of the poleward surface volume transport from the INATEX *in situ* observations is -0.32($\pm$0.13) Sv,

while the surface transport estimated over the same time span from the altimeter-derived geostrophic velocities presents values of -0.28(±0.09) Sv.

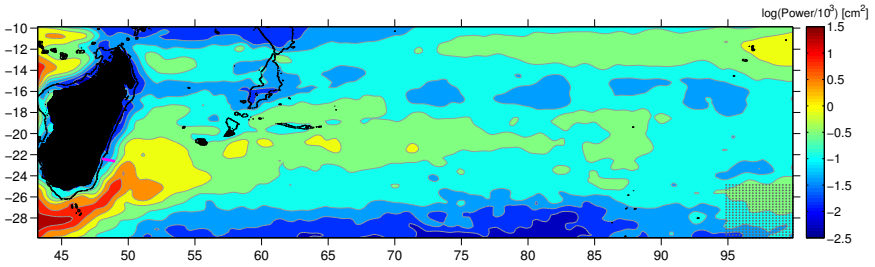

Figure 2.13: Power density (plotted on logarithmic scale) averaged over the 45–85 days period (band shown in Fig. 7c). The values are estimated from the wavelet analysis applied to the normalized (by standard deviation) time series of Sea Level Anomaly (SLA) at every point of the Aviso grid. For the entire domain (all time series) the spectra show values over the 95% significance level at the nearly bi-monthly period. The magenta line off eastern Madagascar indicates the position of the INATEX array, while black contours indicate the isobath of 1000 m plotted to highlight the location of the Mascarene Ridge at approximately 60°E. The points in the lower right corner illustrate the spatial resolution (0.25°) of the Aviso grid.

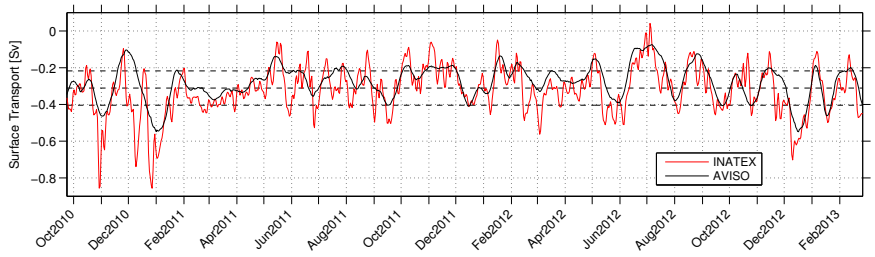

Figure 2.14: Volume transport estimated for the surface layer (first 8 meters of the water column), in between the moorings EMC2 and EMC5. The transport represented by the red line is based on *in situ* velocities from the INATEX moorings, while the transport represented by the black line is based on geostrophic velocities estimated from Absolute Dynamic Topography (ADT). For every horizontal grid point the velocity is assumed constant in the first 8 meters of the water column. The black dashed lines indicate the mean and the standard deviation of the 21-year altimeter-based volume transport.

For the 21 years, the surface transport estimated from the altimeter data exhibits a mean and standard deviation of -0.31±0.09 Sv (black full and dashed lines in Fig. 2.15). The nearly bi-monthly variability also shows up in the wavelet spectrum (not shown) of this time series, although there is a strong concentration of energy in the low frequency band (interannual, < 1 cycle per year).

The band pass filtered time series (forward–backward Butterworth filter) reveals that the interannual and bi-monthly variabilities explain about 16% and 31%, respectively, of the variance found in the 21-year altimeter-based transport. Therefore, both bands together explain almost half (47%) of the total variability. If we take into account only the period when the moorings were deployed, the bi-monthly band explains about 40% of the variance presented by the altimeter-based transport. This is in good agreement with the amount of variance of the *in situ* transport time series explained by the bi-monthly variabilities (41%, Section 2.3.3).

2.4.3 *On the interaction of the eddies with the EMC*

Since the most prominent fluctuations in the EMC transport occur due to the arrival of westward-propagating eddies, we select a region close to the western boundary, where these features are potentially interacting with the EMC, to better comprehend the effects of this interaction. The region is defined by a zonal rectangle delimited by 22–23.7°S and 48.3–51°E (see black rectangle in Fig. 2.10). The zonal orientation of the rectangle is justified by the fact that most of eddies are observed traveling in a nearly zonal trajectory (e.g., Fig. 2.11).

Fig. 2.15 compares the time series of the mean SLA from the selected region with the altimeter-derived EMC transport. Overall, the figure reinforces that pronounced positive and negative anomalies in the sea level drive strong and weak EMC transport, respectively. Fig. 2.16 shows the scatter plot for the mean SLA *versus* the surface volume transport estimated from satellite (Fig. 2.16a) and *in situ* (Fig. 2.16b) observations. A significant correlation is found in both diagrams with coefficient of -0.46.

Notice in Fig. 2.15 that only at two occasions an equatorward reversal of the surface transport is observed: from 23 January to 02 February 1993 and from 18 to 23 December 1995. Both reversals are associated to the passage of a strong CE.

The sequence of plots of the SLA fields (and also Fig. 2.15) shows that the intensification (EMC-AE interaction) or attenuation (EMC-CE interaction) of the

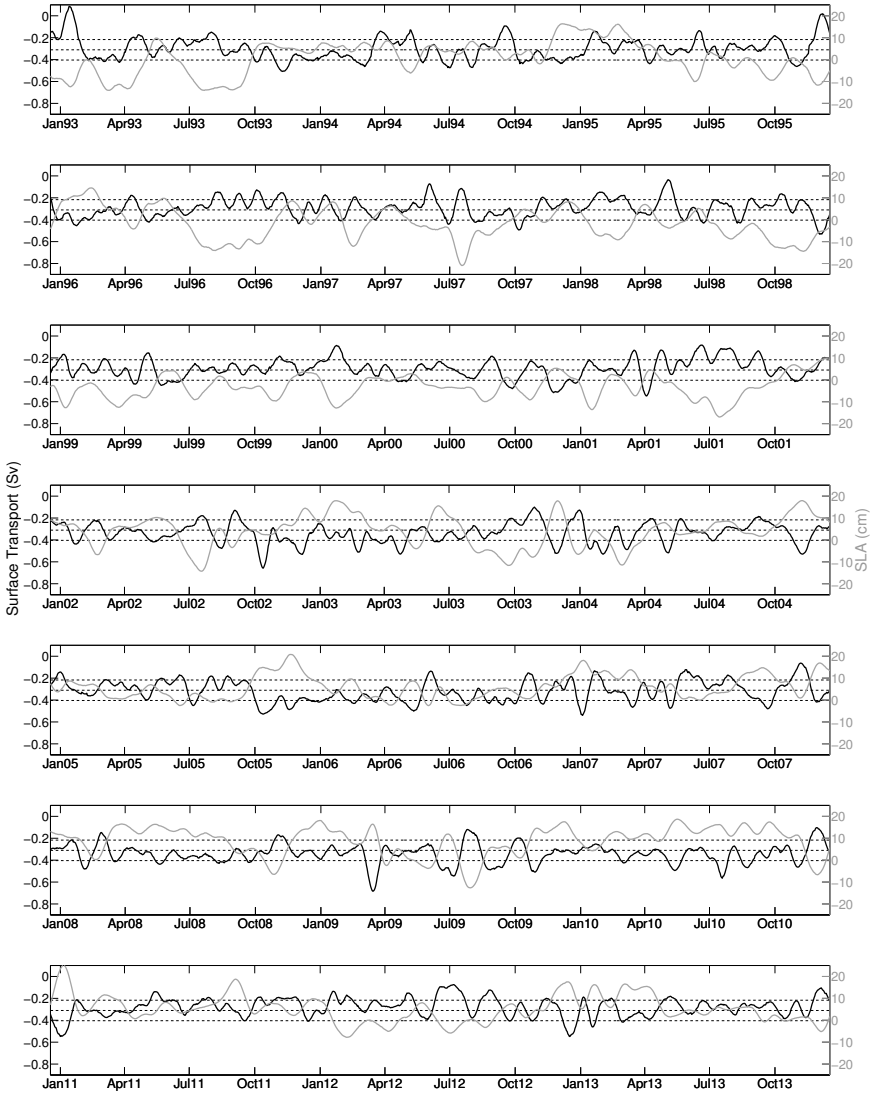

Figure 2.15: Volume transport (left y-axis, black line) calculated within the surface layer (first 8 meters of the water column) based on altimeter-derived geostrophic velocities. The black dashed lines represent the average and one standard deviation from the average. The gray line (right y-axis) represents the mean Sea Level Anomaly calculated for the region highlighted by the black rectangle in Fig. 2.10.

EMC transport by mesoscale eddies depend on different factors, as for instance, proximity to the current, residence time, size and amplitude of the anomalies.

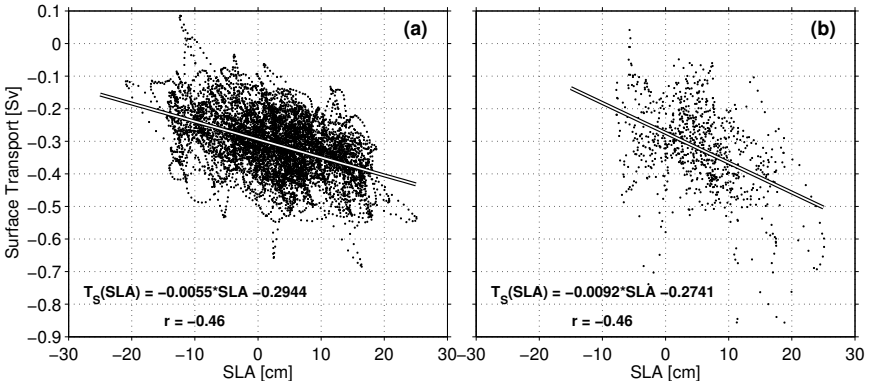

Figure 2.16: Scatter plot of the surface volume transport, estimated from altimeter (a) and *in situ* (b) observations *versus* the mean Sea Level Anomaly calculated for the region highlighted by the black rectangle in Fig. 2.10. T_S(SLA) represents the first-order polynomial fit, while r indicates the correlation coefficient between both parameters.

Fig. 2.17 indicates how the arrival of the eddies influences the vertical structure of the EMC. During outstanding events of EMC-AE interactions, here distinguished by the moments when the surface volume transport is stronger than one standard deviation away from its average (Fig. 2.15), the current migrates deep in the water column, its core is wider and stronger, and the EMUC virtually disappears (Fig. 2.17a). The opposite occurs during EMC-CE interactions (Fig. 2.17b).

2.4.4 *Interannual variability*

Besides the remarkable nearly bi-monthly signal, annual averages of the long-term surface transport suggest that interannual variabilities also play a role in the EMC system. For instance, the annual time series show a minimum and maximum poleward transport of 0.26 Sv (2012) and 0.35 Sv (2009), respectively. Fig. 2.18 suggests three distinct moments. First, from 1993 to 2001 when a reduced transport is observed, with exception of 1994. Second, from 2002 to 2010, the volume transport is stronger compared to the previous period (exceptions are 2005 and 2007). Finally, the third period covers 2011–2013, when the transport dropped again. Taking the averages over each of these periods of

years, poleward transports of 0.30 Sv (1993-2001), 0.33 Sv (2002-2010) and 0.25 Sv (2011-2013) are found.

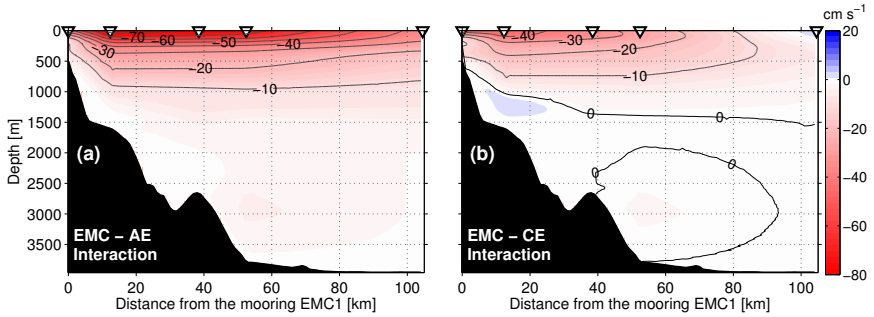

Figure 2.17: Alongshore velocities averaged for all moments when an outstanding Eddy-EMC interaction takes place between Oct/2010 and Mar/2013. (a) AE-EMC interactions, distinguished by the moments when the surface volume transport is less than one standard deviation away from the mean represented in Fig. 2.15. (b) CE-EMC interactions, distinguished by the moments when the surface volume transport is more than one standard deviation away from the mean represented in Fig. 2.15.

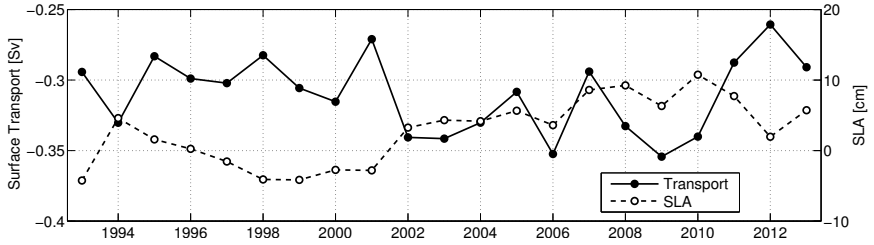

Figure 2.18: Annual averages of altimeter-based volume transport (left y-axis) and mean Sea Level Anomaly (right y-axis) calculated for the region highlighted by the black rectangle in Fig. 2.10.

2.5 DISCUSSION AND CONCLUSIONS

Based on both ∼2.5 years of continuous *in situ* measurements, from a 5-moorings array deployed nominally at 23°S off eastern Madagascar, and ∼21 years of satellite altimeter data, this paper provides a study of the East Madagascar

Current (EMC) in terms of its observed velocities, estimated volume transport and variability.

On average, the *in situ* observations reveal a poleward EMC between 60 and 100 km wide, from the surface to about 1000 m depth. Its mean core is found about 20 km away from the coast, with velocities of 79(±21) cm s^{-1}. Events with velocities stronger than 150 cm s^{-1} were sampled during a few days, while the global peak reached up to 170 cm s^{-1}.

The velocity time series (Fig. 2.3) show a well organized western boundary current at surface levels. At intermediate levels (∼1260 m) and attached to the continental slope, a reversal of the flow indicates the presence of an equatorward undercurrent, the East Madagascar Undercurrent (EMUC) (Ponsoni et al., 2015a). Fig. 2.3 also shows the EMC crossing the transect more inclined towards the coast at the mooring EMC2 than at EMC4. A potential explanation for this is that the boundary currents tend to flow along the isobaths to conserve potential vorticity and the EMC2 mooring is placed over the continental slope, where the isobaths immediately upstream the mooring array are also inclined towards the coast (see 200, 500, 1000 and 2000 m isobaths, between ∼22–28°S, in Fig. 2.1b). This interaction with the bottom is reduced offshore, at EMC4, where the cross-shore gradient of depth is reduced and the local depth is about 3800 m.

The mean transport of the EMC, estimated with the *in situ* velocities, amounts to 18.3 (±8.4) Sv. This is in good agreement with the transport of 20.3(±6.6) Sv estimated by Schott et al. (1988), who analyzed 11 months of continuous observations from three vertical lines of moorings longitudinally deployed slightly north of our moorings. In the strongest event, measured from 12 to 20 January 2011, the EMC presented a transport over 50 Sv. The deeper and oppositely directed EMUC has a mean volume transport much weaker than the overhead flow (<1.4 Sv, Ponsoni et al. (2015a)).

If indeed the entire volume transport of the EMC participates in building up the Agulhas Current (AC), the EMC contributes with about 26.5% to the AC transport, which is estimated to be 77(±5) Sv at 32°S (Beal et al., 2015). Likewise, the flow from the Mozambique Channel would contribute with about 22%, since its mean poleward transport is 16.7(±3.1) Sv (Ridderinkhof et al., 2010). It is important to mention that a large part of the AC transport is due to the contribution of the AC's recirculation (Stramma and Lutjeharms, 1997). Nevertheless, these percentages present crude estimates since the calculations are based on mean values.

The wavelet spectrum (Fig. 2.7) indicates a nearly bi-monthly period (45–85 days) as the most prominent band of variability in the EMC transport, which explained 41% of the total variance. Schott et al. (1988) found similar variability

of 40 to 55 days, but explaining only 15% of the total variance. A potential explanation for this disparity is the fact that the results from Schott et al. (1988) are based on a shorter time series (11 months), and in this work we showed (Section 2.4.1) that the nearly bi-monthly fluctuations can be interrupted over time, as for instance, when a quasi-standing cyclonic eddy was observed in the vicinity of the INATEX moorings for a time span of about 3.5 months.

Altimeter data indicate that the bi-monthly variability is induced by the arrival of westward-propagating sea level anomalies (SLA). In this paper we treat these features as Anticyclonic Eddies (AE, positive SLA) and Cyclonic Eddies (CE, negative SLA), since most of the anomalies are nearly circular as might be expected for vortical eddies, rather than being elongated meridionally which would characterize wavefronts (Quartly et al., 2005). However, we are aware about the ongoing discussion in the literature whether or not these entities are "Lagrangian coherent structures" that trap fluid and material (Haller, 2002, 2005; Beron-Vera et al., 2008; Samelson, 2012). Here, we follow other works (e.g., Faghmous et al., 2015a) and treat these nearly circular SLAs as eddies, independent of their trapping ability.

Upon approach of the Madagascar coast, the eddies interact with the western boundary and, depending on the rotation of the vortical structure, the current is intensified or attenuated. During EMC-AE interactions, the poleward flow at the shoremost side of the eddy adds to the current, while the opposite is observed when EMC-CE interactions take place.

The behavior of the eddies is intriguing once the interaction with the current is established. Some eddies propagate downstream, others remain quasi-steady interacting with the EMC for a long period (as the instance reported above) and some dissipate in the western boundary. Related to the last case, Zhai et al. (2010) showed that there is a significant sink of ocean-eddy energy near western boundaries.

According to Shi and Nof (1994) three mechanisms influence the alongshore migration of the eddies when they reach the western boundary coast: (i) the image or mirror effect (Shi and Nof, 1993; Kundu and Cohen, 2008), when the collision of an eddy with the coast creates a mirror of the vortex with opposite signal and, consequently, the parent eddy migrates along the wall, and is drifted forward by its own image; (ii) the rocket force, which occurs due to the fluid that leaks from the interior of the eddy and forms a thin jet advecting the eddy in the direction opposite to the leakage; and (iii) β-induced force, due to differences in the Coriolis force in both hemispheres of the eddy. Azevedo et al. (2012) presented a detailed sketch of these forces influencing the migration of an eddy along a continental wall (their Fig. 3). The balance among these three forces determines the direction of the eddy migration along

the wall. For instance, an AE (CE) in the Southern Hemisphere is forced poleward (equatorward) by mechanisms (i) and (ii) and equatorward (poleward) by (iii). Overall, the AE tends to drift poleward since mechanisms (i) and (ii) are stronger than (iii) (Shi and Nof, 1994). In this context, for the case where CEs were observed standing offshore the INATEX moorings, we can speculate that somehow at these moments the mechanisms (i) and (ii) that would induce the equatorward propagation of the cyclonic structure were counterbalanced by the poleward EMC.

Some important questions still need to be better investigated, as for instance: How much does the EMC transport account for the build up of the AC? Why do some of the CEs arriving near the coast maintain their position for longer than three months, while other vortical features disappear or propagate southward, as soon as they interact with the EMC? Do the westward-propagating eddies which modulate the EMC variability ride on Rossby waves (e.g., Polito and Sato, 2015)? These topics should be addressed in detail in future work.

3

THE EAST MADAGASCAR UNDERCURRENT

ABSTRACT

An array of five moorings was deployed at 23°S off eastern Madagascar and maintained for about 2.5 years as part of the “INdian-ATlantic EXchange in present and past climate" (INATEX) experiment. The observations reveal a recurrent equatorward undercurrent (during 692 of 888 days), the East Madagascar Undercurrent (EMUC), flowing below the poleward surface East Madagascar Current (EMC). The average core of the undercurrent was found near the continental slope, at a depth of 1260 m and at an approximate distance of 29 km from the coast, with mean velocities of 6.4 ($\pm$ 4.8) cm s^{-1}. Maximum speeds reach 20 cm s^{-1}. The mean equatorward volume transport is estimated to be 1.33 ($\pm$1.41) Sv with maxima up to 6 Sv. The baroclinic/barotropic partitioning of the geostrophic flow shows a persistent equatorward baroclinic velocity in the undercurrent core, which is sometimes inhibited by a stronger poleward barotropic contribution. The wavelet spectrum analysis of the transport time series displays two dominant frequency bands: (i) nearly bi-monthly (46–79 days), previously observed in the surface EMC, and attributed to the forcing of barotropic waves generated in the Mascarene Basin; and, (ii) nearly semi-annual (132–187 days), which seems related to the semi-annual cycle in the equatorial winds near the Indian Ocean eastern boundary. A historical dataset of temperature–salinity Argo profiles was used to investigate the spatial variability of the thermohaline properties at intermediate levels. Lastly, Argo-derived velocities suggest an undercurrent flowing upstream until approximately 17°S.

This chapter has been published as:
Ponsoni, L., B. Aguiar-González, L.R.M. Maas, H.M. van Aken and H. Ridderinkhof, 2015. Long-term observations of the East Madagascar Undercurrent. *Deep-Sea Res. I* 100, 64–78.

3.1 INTRODUCTION

An equatorward undercurrent flowing opposite and beneath a surface current is a recurring oceanographic feature in western boundary current systems. Such a feature has been universally observed at ocean western boundaries. For instance, the Luzon Undercurrent in the North Pacific (Hu and Cui, 1991; Hu et al., 2013); the East Australian Undercurrent in the South Pacific (Godfrey et al., 1980; Schiller et al., 2008); the Intermediate Western Boundary Current in the South Atlantic (Evans and Signorini, 1985; da Silveira et al., 2004); and, in the South Indian Ocean, the Agulhas Undercurrent (Beal and Bryden, 1997), the Mozambique Undercurrent (de Ruijter et al., 2002; van Aken et al., 2004) and the East Madagascar Undercurrent (Nauw et al., 2008), which the study of its vertical structure, transport and variability composes the main scope of this paper.

Historically, the interface between the undercurrents and the poleward-directed surface currents has been largely employed as a reference level (e.g., Swallow and Worthington, 1961) for estimating absolute geostrophic velocities via thermohaline properties and the dynamic method, especially when and where direct velocity measurements are scarce (Fomin, 1964). Also, undercurrents might play a role in the heat and salt budget (Bryden and Beal, 2001) and, consequently, be related with the world's climate. Bryden and Beal (2001) showed that the Agulhas Undercurrent reduces the Agulhas Current transport by about 15 Sv, attenuating its poleward heat transport.

In terms of global climate, the South-West Indian Ocean (SWIO) has a crucial contribution to the meridional overturning circulation, since in this region an interocean exchange occurs where large amounts of relatively warm and salty water leak from the Indian to the Atlantic Ocean through the Agulhas Current (Olson and Evans, 1986; Gordon et al., 1992; de Ruijter et al., 1999; Lutjeharms, 2006; Beal et al., 2011).

In turn, the surface poleward-directed Agulhas Current is fed upstream by the flows from the Mozambique Channel and the East Madagascar Current. Such a connection does not seem straightforward between the equatorward-directed undercurrents. Supported by numerical simulations, Biastoch et al. (2009) stated that there is no direct connection between the Agulhas Undercurrent and the undercurrents in the Mozambique Channel and east of Madagascar.

Nauw et al. (2008) described an East Madagascar Undercurrent (EMUC) 50–90 km wide flowing below and opposite to the poleward East Madagascar Current (EMC), with its core hugging the continental slope at depths of about 1300 m. Its description is based on *in situ* measurements of velocity and water

mass analysis (hydrographic, nutrients and oxygen data) carried out at four quasi-synoptic vertical cross-shore transects around the south of Madagascar. Velocities of the undercurrent core reached over 20 cm s^{-1}, yielding an equatorward volume transport of 2.8 ($\pm$ 1.4) Sv. Water mass analysis suggested that the EMUC core was mostly composed of diluted Red Sea Water (RSW) from the Mozambique Channel.

Nevertheless, since Nauw et al's (2008) work is based only on a few snapshots, issues related to the EMUC persistence, temporal variability of its velocity and volume transport, variations in its vertical structure, its mean flow, thermohaline characteristics of surrounding waters, amongst others, still need to be addressed. The present study provides further insight on those issues based on 2.5 years of continuous velocity measurements.

The paper is organized as follows: the dataset description and basic treatment are covered in Section 3.2; the mean flow, volume transport and dominant bands of variability are addressed in Section 3.3; considerations on the EMUC baroclinic/barotropic partitioning are presented in Section 3.4; the upstream extension of the EMUC and the spiciness of intermediate waters around Madagascar Island are investigated in Section 3.5; and, finally, Section 3.6 presents a discussion and draws some conclusions about the principal results.

3.2 DATA AND DATA PROCESSING

As a basis for this study we use a five-mooring array of velocity observations. The mooring line was deployed on the southeastern coast off Madagascar, nominally at 23°S, across the continental slope and perpendicular to the shoreline (and isobaths), as a part of the "INdian-ATlantic EXchange in present and past climate" (INATEX) project (Fig. 3.1). Offshore distances from the coast for each deployment are, respectively, 6.3 (EMC1), 28.6 (EMC2), 54.8 (EMC3), 68.7 (EMC4) and 120.8 km (EMC5).

All the moorings were equipped with upward-looking Acoustic Doppler Current Profilers (ADCP – RDI Workhorse Long Ranger 75 kHz with profiling range of about 500 m) and Recording Current Meters (RCM – Aanderaa RCM 11) placed in-line along the mooring cables (Fig. 3.2a). RCM and ADCP sample rates were set to 20 and 30 minutes, respectively. From here on, every individual instrument will be called EMC*X*–*Y*, where *X* represents the mooring number and *Y* the nominal depth (example: EMC2–1600 for the instrument in the mooring EMC2 at nominally 1600 m depth).

The INATEX deployment cruise (ALGOA179, named after the oceanographic vessel) took place in October 2010, while the recovery cruise (ALGOA197) was

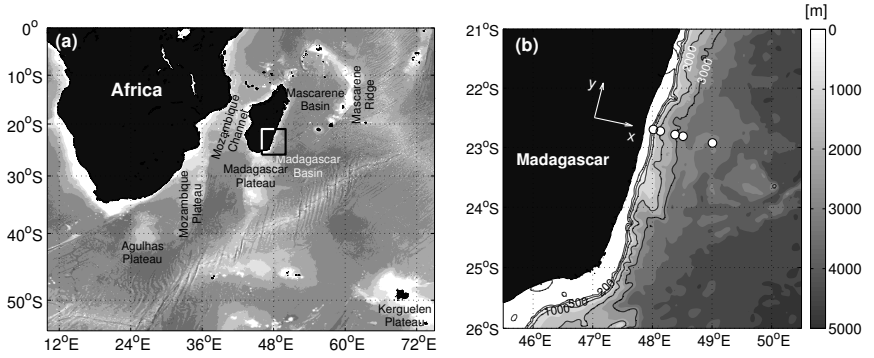

Figure 3.1: (a) Bathymetric map of the South-West Indian Ocean (SWIO). (b) Zoom of the area of study indicated by the square drawn in (a). White circles represent the locations of the INATEX moorings. Isobaths of 200, 500, 1000, 2000 and 3000 m are plotted in the map.

carried out on April 2013. All the ADCPs sampled continuously from deployment until recovery, except the upper ADCP at EMC3 which failed for the whole period due to leakage and internal damage caused by acid from the batteries. RCM devices remained operational until the middle of March 2013, except EMC3-1500 and EMC4-2000, which worked properly until the end of September 2012, from whereon we considered the line mooring composition without those two instruments. After the first basic data treatment removed bad quality data and addressed blow-down corrections, the time series were synchronized and truncated from 7 Oct 2010 to 12 Mar 2013 (91% of daily data return), accumulating approximately 2.5 years of continuous data.

All current velocity records went through low pass filtering (forward–backward Butterworth filter), with a 3.5 day cut-off period, in order to remove tidal and near-inertial motions from the time series (Ridderinkhof et al., 2010; Ullgren et al., 2012), since this study is focused on the mesoscale geostrophic circulation. The data were subsampled daily at noon. Meridional and zonal velocities were rotated clockwise 12.9° from north, so that the flow components are oriented parallel/perpendicular to the coast. These velocity components are referred to as alongshore (v) and cross-shore (u) components.

Following Ridderinkhof et al. (2010), cross-correlations among the instruments were determined to support spatial interpolations. These authors found stronger correlations between velocity time series from the same mooring,

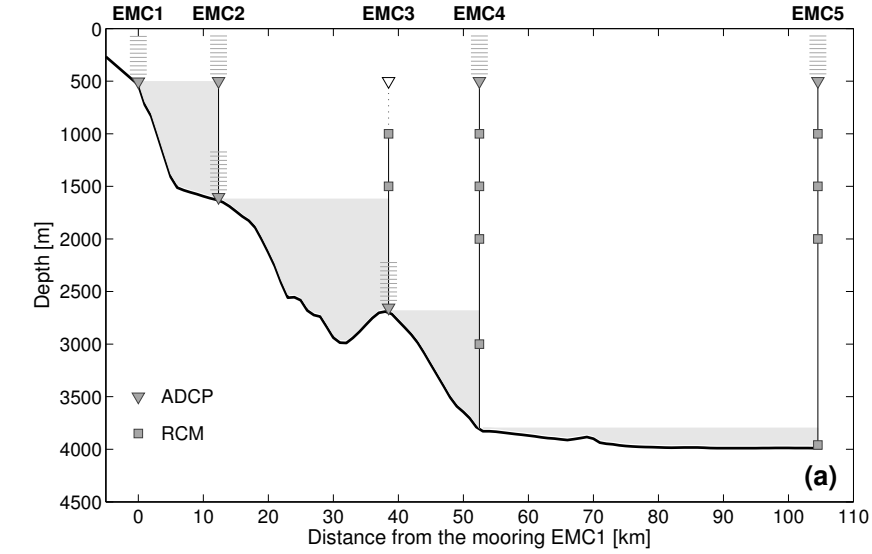

(b)

	EMC1–0500	EMC2–0500	EMC2–1260	EMC2–1500	EMC3–1000	EMC3–1500	EMC3–2500	EMC4–0500	EMC4–1000	EMC4–1500	EMC4–2000	EMC4–3000
EMC1–0500	**1.00**											
EMC2–0500	**0.16**	**1.00**										
EMC2–1260	**0.14**	**0.50**	**1.00**									
EMC2–1500	**–0.07**	0.03	**0.15**	**1.00**								
EMC3–1000	**0.11**	**0.77**	**0.78**	**0.07**	**1.00**							
EMC3–1500	**0.14**	**0.54**	**0.66**	0.05	**0.73**	**1.00**						
EMC3–2500	0.04	**0.22**	**0.24**	–0.02	**0.34**	**0.42**	**1.00**					
EMC4–0500	–0.05	**0.76**	**0.33**	0.05	**0.64**	**0.38**	**0.10**	**1.00**				
EMC4–1000	0.00	**0.75**	**0.50**	**0.08**	**0.85**	**0.56**	**0.20**	**0.82**	**1.00**			
EMC4–1500	0.02	**0.55**	**0.43**	**0.08**	**0.74**	**0.56**	**0.41**	**0.58**	**0.81**	**1.00**		
EMC4–2000	0.05	**0.33**	**0.32**	0.02	**0.54**	**0.46**	**0.62**	**0.33**	**0.51**	**0.78**	**1.00**	
EMC4–3000	0.06	**0.12**	**0.08**	**–0.09**	**0.21**	**0.20**	**0.52**	**0.10**	**0.17**	**0.40**	**0.66**	**1.00**

Figure 3.2: (a) Vertical sketch of the INATEX moorings where RCMs are represented by squares and ADCPs by triangles and small horizontal lines, which indicate the upward-looking range of the ADCP. The empty triangle in EMC3 shows the faulty instrument. The gray shaded areas show the regions where extrapolation is applied. (b) Correlation coefficients calculated in between different pairs of time series (instruments). Values in bold are significant (p-value test, testing the hypothesis of no correlation) for a 95% confidence interval.

mainly over vertical separations of 500 m. The INATEX data also present strong correlations between time series from vertically adjacent instruments, although some good horizontal correlations are also observed (Fig. 3.2b). Horizontal correlations are drastically affected if time series from any mooring are combined with EMC5, since this mooring was deployed near the offshore front of the EMC system. But still, even in EMC5 the vertical correlations are strong (not shown).

Time synchronized data from ADCPs and RCMs were linearly merged, first vertically onto 8 m bins (ADCP vertical resolution) at standard depth levels, and subsequently horizontally, by linear interpolation applied for each standardized depth level onto a horizontal grid of 1 km. Therefore, the cross-shore grid resolution utilized for further transport calculations is 1 km (distance) × 8 m (depth).

Before computing volume transport estimates, an essential step concerns the choice of the extrapolation method used to fill in empty data regions. These empty areas are created between every pair of neighboring moorings and the bathymetry below the shallowest station of this pair (gray shaded areas in Fig. 3.2a). This choice presents an infamous problem, especially pressing in regions near a steep continental slope.

Observations from the near-bottom ADCP at EMC2 suggest speed attenuation towards the seafloor. Since the first measurement from this instrument took place at ∼20 m from the bottom, it is difficult to infer whether or not the current speed decreases to zero right above the seafloor. On the other hand, some studies have shown that under certain conditions an undercurrent core near the bottom can create a slippery boundary layer for itself (MacCready and Rhines, 1993) and eventually reduce (or eliminate) bottom friction effects (Chapman and Lentz, 1997).

For the sake of completeness, we apply the two extreme boundary conditions (no-slip and full-slip) following previous works (Beal and Bryden, 1997; Nauw et al., 2008), as well as a third alternative method based on optimal interpolation (Carter and Robinson, 1987; da Silveira et al., 2004). In this way a global overview of the EMUC transport is attempted, from underestimated (no-slip condition) to overestimated (full-slip condition) values.

The optimal interpolation has been performed as introduced by Carter and Robinson (1987) for oceanographic data gridding purposes, where a classical Gaussian correlation function $C(x,z)$ is used as follows:

$$C(x,z) = (1-\epsilon)e^{\left(-\frac{x^2}{L_x^2}-\frac{z^2}{L_z^2}\right)}, \tag{3.1}$$

where x and z are horizontal and vertical grid points, respectively, $\epsilon = 0.1$ is the random sampling error variance, and $L_x = 50$ km and $L_z = 500$ m represent the horizontal and vertical correlation lengths. L_x and ϵ were estimated from the fit by non-linear regression to the theoretical one-dimensional (horizontal) form of the Eq. 3.1. This method consists in the best fitting of the Gaussian shape to the horizontal correlation pairs from all velocity series around the EMUC depths. L_z was chosen as a typical scale for the EMUC resulting from the strongly sheared velocity profiles observed at EMC2 (assumed as the core's location of the EMUC, see Section 3.3). A reduced number of well equidistantly time series in EMC2 prohibited the estimation of L_z in the same way as L_x was estimated.

Absolute dynamic topography (η) sampled from satellite is used to compare the cross-shore gradients of this property with the EMUC velocities. To achieve this, we linearly interpolate a time series of η collocated onto the positions of the moorings. The original data for this analysis contains daily η, which is the sum of sea level anomaly and mean dynamic topography. The altimeter products were produced by Ssalto/Duacs and distributed by Aviso (`http://www.aviso.altimetry.fr/duacs/`), with support from Cnes (Rio et al., 2011). Here we use the "all sat merged" series of the delayed-time altimeter product, which is provided with a spatial resolution of 0.25°.

Water mass properties carried by the undercurrent were investigated using a subset of potential temperature (θ) and salinity (S) profiles from the global array of free-drifting Argo floats. The Argo database consists of a collection of profiling floats which monitor the upper 2000 dbar of the ocean at regular 10-day intervals. All Argo profiles shown in this study were downloaded on July 2014 from the Global Argo Data Repository of the National Oceanographic Data Center (NODC). To ensure robustness of the results, only profiles in delayed mode after passing the quality control were used. Additionally, all profiles were visually inspected with their neighbouring counterparts. Floats with suspicious profiles either in temperature or salinity, or in the Argo gray list, were discarded. Also, profiles shallower than 1000 m depth were discarded as they are not deep enough to capture the intermediate waters at which the undercurrent is flowing. As a result, a total of 1776 profiles distributed from Sep/2001 to Dec/2013 are used. The span of 12 years of data and wide spatial coverage provides support that our analysis describes long-term θ-S patterns.

Finally, we use the ANDRO (Ollitrault and Rannou, 2013) current velocities deduced at surface and near 1000 m depth ("parking" depth) from Argo float displacements to assist discussion on the location of Argo floats sampling the undercurrent.

3.3 THE EAST MADAGASCAR UNDERCURRENT

3.3.1 *Observed velocities and mean flow*

Considering the geostrophic nature of the EMC system, one might expect an undercurrent strongly aligned to the shoreline and isobaths given its tendency to conserve potential vorticity. Fig. 3.3a shows the standard deviation ellipses and the mean vectors of the velocity component decomposed along the principal axis. Notice that the mean flow along the major axis is stronger at EMC2, which is rotated 13° from north. This angle is consistent with the alongshore rotation described in the previous section (12.9° from north).

Fig. 3.3b shows the alongshore velocity gridded in the vertical transect and averaged over the whole time span. An undercurrent core near EMC2 at depths around 1260 m is suggested by the figure. A poleward integrated transport of -18.4 Sv is computed from this mean velocity field. When calculated only in the area enclosed by the 0 cm s^{-1} isotach (green line), the mean velocity field generates an equatorward transport of 0.24 Sv.

In this section, the description of the velocity time series in the EMUC domain is focused on measurements recorded by EMC2–1600, EMC3–1500 and EMC3–2600. Also, an interpolated position in between the last two (referred to as EMC2–2000) is explored, so we have a point near the uppermost measurements from the ADCP profiler EMC3–2600 and, at the same time, we can inspect the performed vertical gridding. Table 3.1 summarizes some velocity statistics, such as mean, maximum and variance of both alongshore and cross-shore velocity components. Despite the focus on those time series, the other neighboring instruments will be important to account for the EMUC transport in cases of a spread-out undercurrent or, for instance, in the case of EMC2–0500, to define the sheared interface EMC–EMUC.

Fig. 3.4 shows the time series of alongshore velocity at the selected positions. Equatorward currents sampled by EMC2–1600 were generally stronger than those observed at other instruments. The global maximum velocity was observed to be 27.3 cm s^{-1}, on 21 Jan 2012 at 1100 m (black star in Fig. 3.4a). Fig. 3.4b presents the velocity time series extracted from EMC2-1600 at 1260 m. Strong velocities over 20 cm s^{-1} were found only on a few occasions (1% of the whole time span, 9 days), with a peak velocity of 23.8 cm s^{-1}. 13.5% (121 days) of this same time series were dominated by velocities between 10 to 20 cm s^{-1}, and 63.5% (562 days) between 0 to 10 cm s^{-1}. The remaining 22% (196 days) were marked by a reversal to poleward flow. For the other three

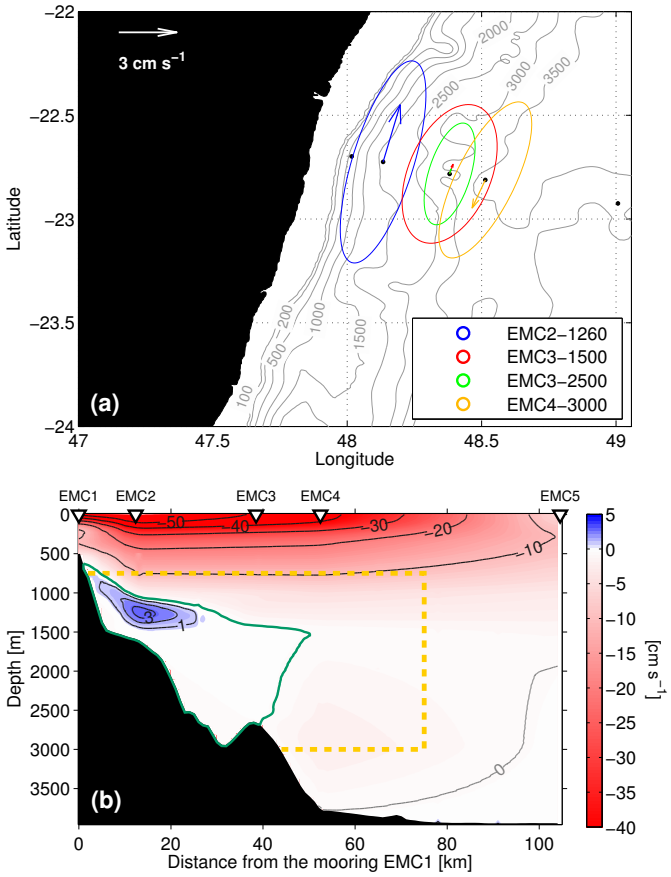

Figure 3.3: (a) Standard deviation ellipses and mean vectors of the velocity component decomposed along the principal axis from the EMC2-1260, EMC3-1500, EMC3-2500 and EMC4-3000 time series. The main axis for each time series (rotated clockwise 13, 15.1, 12.6 and 19.9° from north, respectively) is defined as the angle in which the sum of the squares of the zonal and meridional velocities relative to the mean flow are maximal. (b) Alongshore mean flow of the EMC system averaged over the whole time series. Optimal interpolation is applied as extrapolation method. EMUC (EMC) mean flow is shown in shades of blue (red). Dashed yellow rectangle encloses the area where the Equatorward Volume Transport (EVT) is calculated (see Section 3.3.2). The green contour represents the 0 cm s^{-1} isotach, and it encloses the area where the Net Volume Transport (NVT) is calculated (see Section 3.3.3).

Table 3.1: Properties of the EMUC sampled at the instruments EMC2–1600, EMC3–1500, EMC3–2600, as well as at the interpolated position (EMC3–2000). Alongshore and cross-shore velocity components are represented by v and u, respectively. The alongshore axis is rotated 12.9° degrees from north. The statistics are based on a total of 888 days.

Instrument	EMC2–1600	EMC3–1500	EMC3–2000	EMC3–2600
Depth (m)	1260[a]	1500	2000	2500[b]
Height above bottom (m)	304	1150	650	150
v, mean velocity (cm s^{-1})	4.1	0.7	0.6	0.4
v, velocity variance (cm^2 s^{-2})	39.9	19.0	23.4	10.0
v, max velocity (cm s^{-1})	23.8	12.1	15.3	9.3
# days of $v > 0$ flow[c]	692	521	504	479
$v > 0$, mean velocity (cm s^{-1})[d]	6.4	3.5	4.1	2.76
u, mean velocity (cm s^{-1})	-0.4	0	0.1	-0.1
u, velocity variance (cm^2 s^{-2})	2.4	4.4	4.2	1.1
u, max velocity (cm s^{-1})	7.5	8.7	7.0	4.5

[a] Extracted from EMC2–1600 ADCP, representing the maximum mean velocity level.
[b] Arbitrary level from the EMC3–2600 ADCP.
[c] $v > 0$ represents equatorward flow.
[d] v must be positive, so they do not necessarily have Gaussian statistics.

positions (EMC3–1500, EMC3–2000 and EMC3–2600) velocities are typically weaker than 10 cm s^{-1} (Figs. 3.4c-f).

The EMUC core may not be at the location of EMC2, but taking into account the sharp horizontal decay of the undercurrent velocities between that mooring position and EMC3, as well as the relatively small distance between EMC2 and the continental slope (at the undercurrent depths), it is fair to consider that location as the core position of the EMUC, as previously suggested by the mean flow in Fig. 3.3b. In this sense, an average core at intermediate depths is estimated from the data sampled by EMC2–1600. The mean core is placed at around 1260 m depth, approximately 400 m from the seabed, and it exhibits an average (and standard deviation) velocity of 4.1 ($\pm$ 6.3) cm s^{-1}. If the average is taken only over the equatorward flow (positive values in Fig. 3.4b) this mean speed increases to 6.4 ($\pm$ 4.8) cm s^{-1}.

Note that velocities in EMC3-2000 (Fig. 3.4d) present variance and equatorward mean flow higher than the two adjacent EMC3-1500 and EMC3-2500 (Table 1). This fact occurs due to the shape of the undercurrent hugging the continental slope, so that EMC3-2000 is closer to the undercurrent core than EMC3-1500 and EMC3-2500.

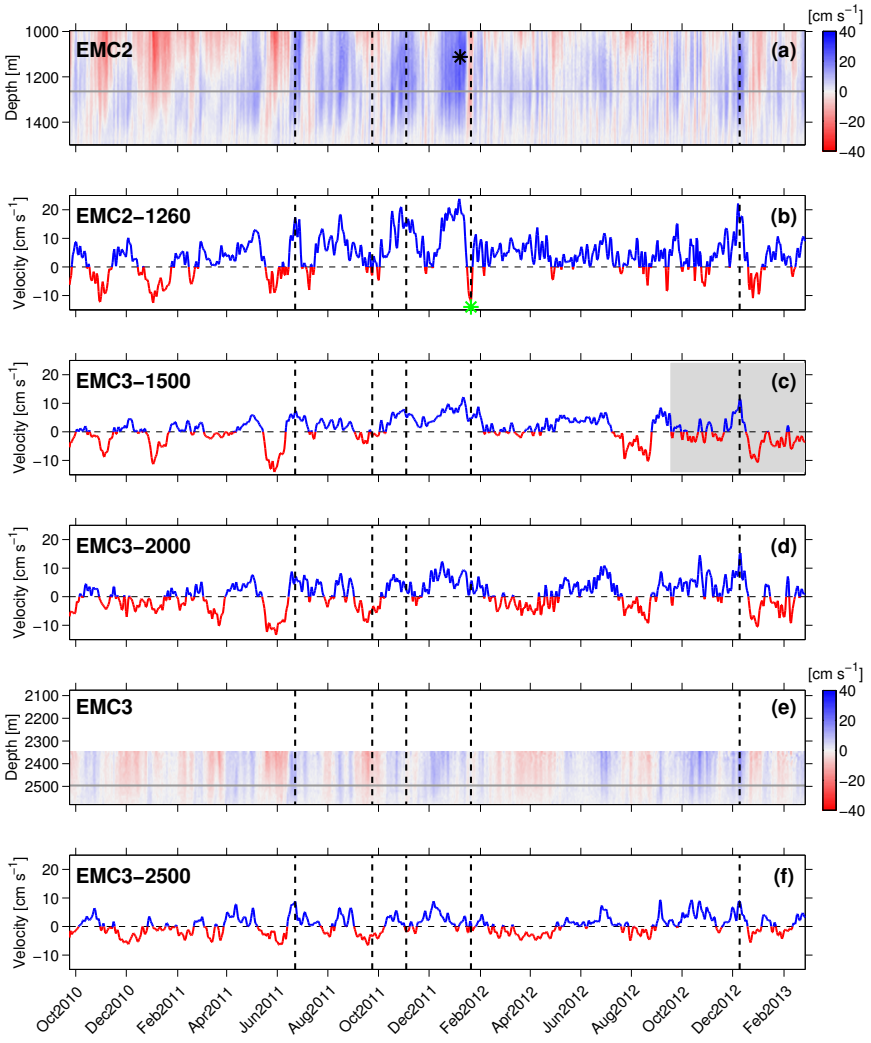

Figure 3.4: Alongshore (v) velocity time series from the instruments placed into the undercurrent mean domain. (a) and (e) represent the time series over the depth range sampled by the EMC2–1600 and EMC3-2600 ADCPs. (b), (c), (d) and (f) show the time series at single individual levels. Blue (red) colors represent equatorward (poleward) flow. Vertical black dashed lines indicate the moments when the vertical transects are shown in Fig. 3.5. Horizontal gray lines in (a) and (e) represent the level plotted in (b) and (f), respectively. The black star in (a) highlights the time and level with the velocity peak. Green star in (b) shows a strong flow reversal only at EMC2–1600. The gray shadow at the end of (c) shows the time span when velocity has been reconstructed (see Section 3.2). Ticks on the x-axis are placed at noon on the 15th day of the respective month.

Remarkably, only on a single occasion there was a strong reversal in the flow at EMC2–1600 that was not followed by the other instruments (green star in Fig. 3.4b). During this event, occurring at the beginning of February 2012, the undercurrent core seems to have shifted offshore, suggesting the presence of a secondary deeper core, as can be inferred due to the persistence of the equatorward flow recorded in the other instruments at the same moment (Figs. 3.4c-f). Besides the primary core in the vicinity of EMC2, at different moments the EMUC flow seems to contain a concomitant secondary deeper core below 2000 m. de Ruijter et al. (2002) and Beal (2009) also observed a secondary core in the Mozambique Undercurrent and in the Agulhas Undercurrent, respectively.

Fig. 3.5 shows five snapshots representing different EMUC velocity scenarios encountered. First, the undercurrent flow reinforced by a cyclonic eddy (06 Jul 2011; Fig. 3.5a). Second, the absence of any equatorward flow (07 Oct 2011; Fig. 3.5b). Third, an undercurrent flowing only with the primary intermediate core (17 Nov 2011; Fig. 3.5c). Fourth, when EMUC core is shifted offshore as mentioned in the previous paragraph (03 Feb 2012; Fig. 3.5d). And fifth, the EMUC with two cores at the moment when it has its maximum transport (23 Dec 2012; Fig. 3.5e).

The latter snapshot shows a strong equatorward undercurrent concomitant with a strong poleward surface current, suggesting an important baroclinic component of the geostrophic system, since a purely baroclinic structure must present a vertical compensation of the flow in order to have zero net transport. On the other hand, Fig. 3.5b suggests an important poleward barotropic contribution, since a flow reversal in the vertical is virtually absent.

3.3.2 *Equatorward volume transport*

The first challenge involved in the calculation of the EMUC volume transport is to define the extrapolation methods to fill in the empty data regions (Fig. 3.2a). As detailed in Section 3.2, we use two opposite boundary conditions (no-slip and full-slip), as well as optimal interpolation to address this issue.

Subsequently, we have to define the limits where the flow across the transect will be computed as an undercurrent. A first choice might be to consider the flow enclosed by the 0 m s^{-1} isotach found at every moment. However, such a choice is not practical because the EMUC does not always appear well organized as a single “package", but either the zero velocity contour is spread all over the whole transect, or the undercurrent is merged with a poleward flow of different nature (for instance, Fig. 3.5a).

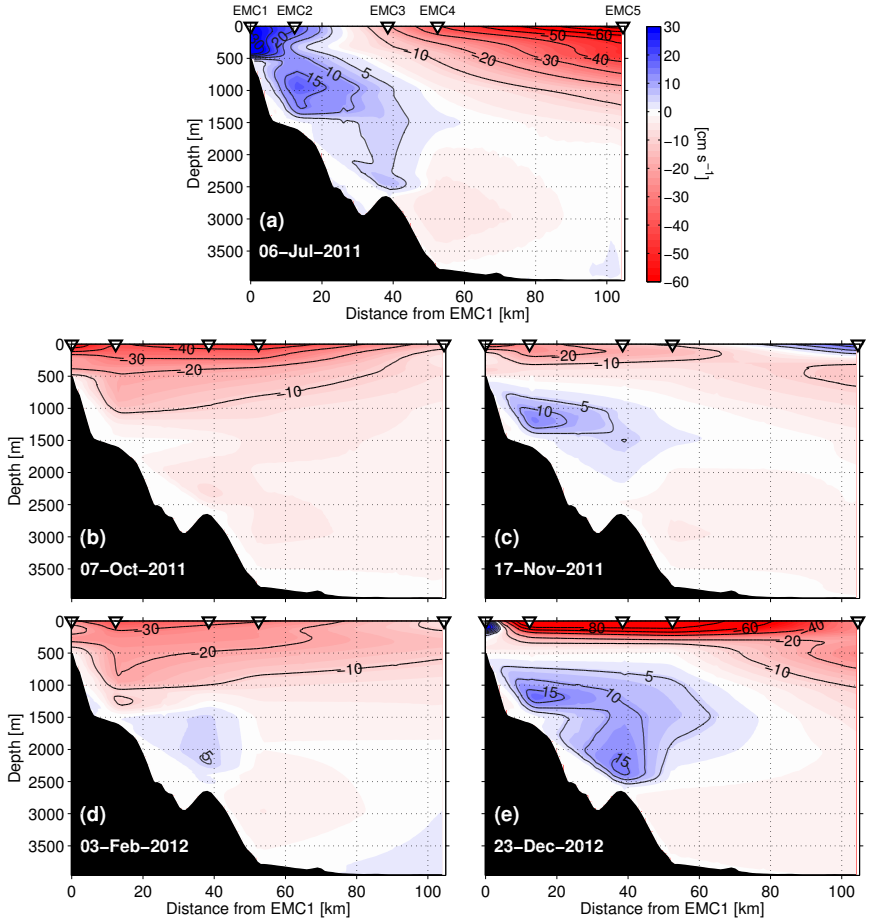

Figure 3.5: Alongshore velocities observed at five different moments: (a) EMUC flow reinforced by a cyclonic eddy (06 Jul 2011); (b) during the absence of equatorward flow (07 Oct 2011); (c) an undercurrent flowing with the primary intermediate core (17 Nov 2011); (d) occasion when only the secondary core is observed (03 Feb 2012), and (e) a strong EMUC (maximum transport), in which the flow exhibits the primary and deep secondary cores (23 Dec 2012). These snapshots are indicated in Fig. 3.4 by vertical dashed lines. Extrapolations to the coast were made through optimal interpolation.

In this study we propose two methods to provide the EMUC transport time series: Equatorward Volume Transport (EVT) and Net Volume Transport (NVT). The first (presented in this Section 3.3.2) aims to quantify exclusively the amount of water transported equatorward by the undercurrent, and therefore only grid cells with positive velocities are used for this computation. Notice that transport values must be positive, so they do not necessarily have Gaussian statistics. The second method is addressed to access the transport variability and it is described in Section 3.3.3.

In order to calculate the EVT we first defined a rectangle (yellow dashed line in Fig. 3.3b) within which only grid cells with equatorward transport were computed for the total transport. On the east, the rectangle is bounded at a horizontal distance of 75 km from EMC1, to the west by the continental slope, and vertically by the levels of 750 and 3000 m. To delimit these boundaries, we took into account the average flow (Fig. 3.3b), cases of deeper and offshore undercurrent excursions observed in the time series and the EMUC boundaries presented in the literature (Fig. 3 from Nauw et al. (2008)).

Fig. 3.6a exhibits the EVT independently calculated from the three different extrapolation methods. Average transports of 1.23, 1.54 and 1.23 Sv were found for no-slip, full-slip and optimal interpolation, respectively. If the mean of the three methods is taken, the transport amounts to 1.33 Sv. This value is equivalent to 7% of the EMC mean transport, estimated to be ∼18.5 Sv from our data or ∼20.5 Sv from the literature (Swallow et al., 1988; Schott et al., 1988). A peak in the EMUC transport higher than 6.5 Sv (6.86, 8.50 and 6.80 Sv, at the same extrapolation order) occurred in the transition spring–summer in 2012.

There are moments when the EVT dropped to zero due to poleward reversals of the flow. These “flats" (e.g. January 2011, Fig. 3.6a) affect the time series oscillations and consequently the periodogram analysis. In order to identify significant period bands, another way to access the transport is presented in the next section.

3.3.3 *Net volume transport*

Net Volume Transport has been computed taking into account both equatorward and poleward flows crossing a fixed area enclosed by the average 0 m s^{-1} isotach (green line in Fig. 3.3b). Note that this method is not appropriate to quantify the volume of water transported northward by the undercurrent (as proposed in the previous section), since it underestimates the transport in case of a spread-out undercurrent. Also, because poleward velocities are generally much stronger than equatorward velocities (compare the colorbar scale

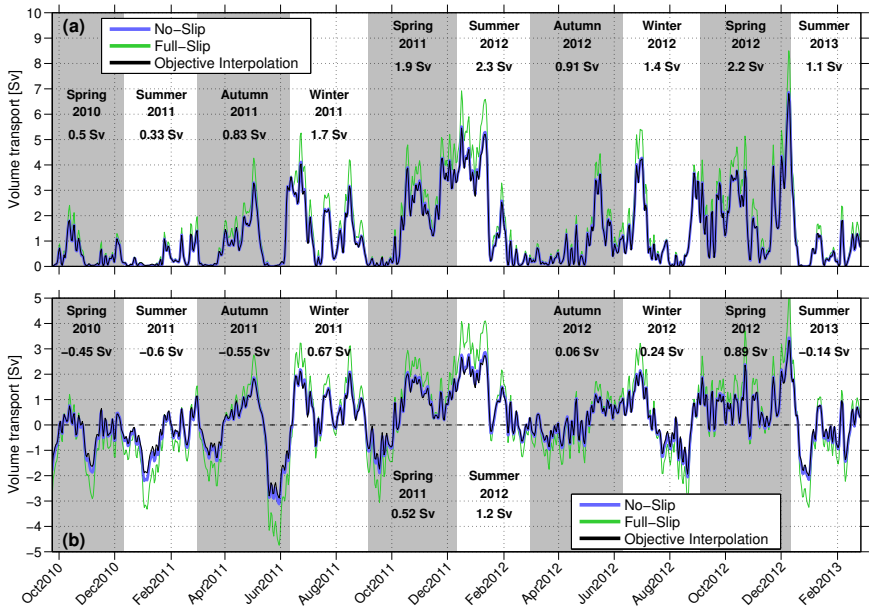

Figure 3.6: (a) Equatorward Volume Transport (EVT): only grid points with positive velocities from the area delimited by the yellow rectangle shown in Fig. 3.3b were computed. (b) Net Volume Transport (NVT): all values (positive and negative) at grid points inside the region enclosed by the average 0 m s^{-1} isotach (green line in Fig. 3.3b) were computed. In both cases the transport was estimated through three different gridding methods: no-slip (blue line), full-slip (green line) and optimal interpolation (black line). Note that blue and black lines almost overlap. The gray and white vertical bars display the mean volume transport in every season.

in Fig. 3.3b and Fig. 3.5), we could not use the same rectangle as defined in the previous section to calculate the NVT, otherwise the resulting transport in this region (rectangle) would be poleward and, consequently, the EMUC equatorward transport would be masked.

Fig. 3.6b shows the NVT time series, where the average value from the three extrapolation methods is 0.21 (±1.25) Sv, while the maximum is 3.93 Sv. Seasonal averages show that occasionally the transport was marked by poleward net transport, for instance, during Spring–2010, Summer–2011 and Autumn–2011 (vertical bars in Fig. 3.6b). But, this fact does not mean that there was a predominance of the poleward flow over time. For instance, in Spring–2010 there were more days with equatorward flow, but the mean is still negative

(poleward flow). This flow reversal is associated with a deep excursion of the EMC, in which velocities are much larger than in the EMUC.

Overall, both EVT and NVT time series present the same pattern of variability (Figs. 3.6a,b), except during events of reversal of the flow when the NVT also has negative values (Fig. 3.6b).

3.3.4 *Variability*

A large amount of variability about the mean occurs on different time scales, both in transport and velocity. Such variability may be induced by different factors: current meandering, actual reductions in the water volume carried by the current, eddy interactions and spatial amplification of the flow are some examples. Our time series reveal that the interaction of all these factors affects the EMUC. In the light of this, an important question emerges: is the EMUC variability dominated by particular frequency bands?

This question is answered affirmatively by means of wavelet analysis (Torrence and Compo, 1998), applied both to the velocity (Figs. 3.7a-d,f) and the NVT time series (Figs. 3.7e,g).

The velocity series from EMC3 (Figs. 3.7b-d) show a persistent nearly semi-annual period centered around 160 days (frequency of 2.3 year^{-1}), which dominates when integrated over time (Fig. 3.7f). In addition, for the same three EMC3 time series, secondary peaks around a nearly bi-monthly period band are identified, although they are not persistent over the entire time span. Different from that observed for the nearly semi-annual period, the nearly bi-monthly peaks are not positioned at exactly the same time-period (Fig. 3.7f).

The velocity time series near the EMUC core, extracted from the bottom ADCP moored at EMC2, revealed only a strong nearly bi-monthly period band centered around 66 days (frequency of 5.5 year^{-1}), although it is also non-persistent over the whole time span. For example, from March to October 2012, such a period was not significantly present. No trace has been found of the nearly semi-annual period in this time series (see red lines in Figs. 3.7a,f).

Considering the NVT time series, the wavelet analysis shows both nearly semi-annual (strongest) and nearly bi-monthly peaks (Figs. 3.7e,g).

To better define the nearly bi-monthly and nearly semi-annual band periods, we considered all points in the global power spectra in which the values are over the 95% significance level (part of the curve to the right of the corresponding dashed line in Fig. 3.7g). Results show intervals of 46–79 days and 132–187 days, respectively. These two band periods are highlighted by the gray horizontal bars in Figs. 3.7f-g.

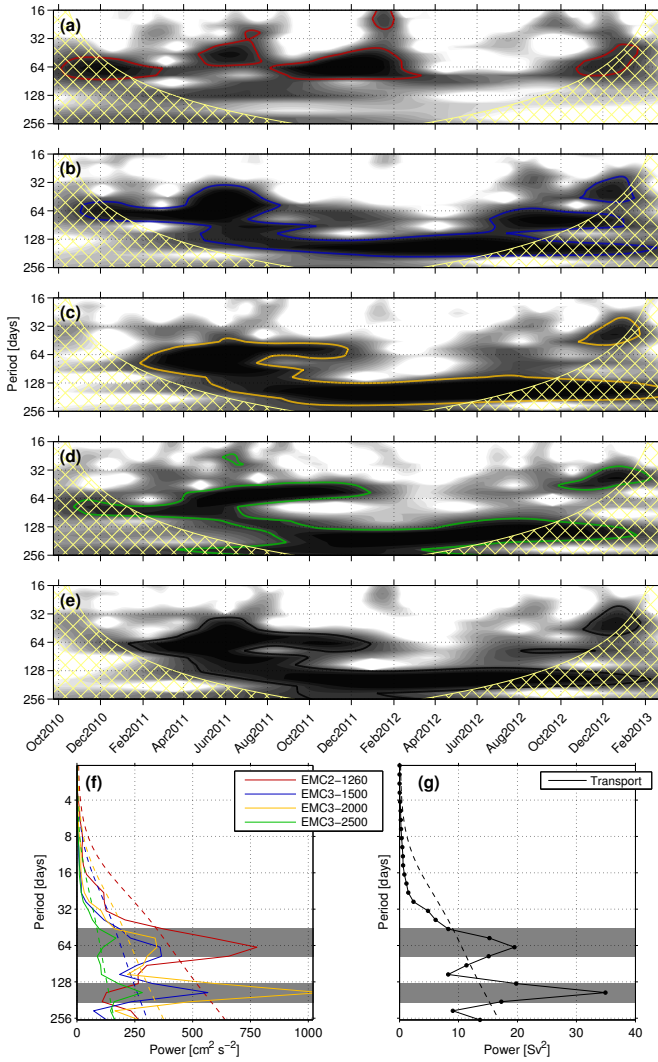

Figure 3.7: Wavelet power spectra of alongshore velocities and volume transport time series: (a) EMC2-1260; (b) EMC3–1500; (c) EMC3-2000; (d) EMC3–2500; (e) Net Volume Transport (NVT). The colored contours (red, blue, yellow, green and black, respectively) denote the 95% significance levels above a red noise background spectrum, while the cross-hatched areas indicate the "cone of influence" where edge effects become important. For all cases the mother wavelet is Morlet wavelet (see Torrence and Compo (1998) for details). Global power spectra for alongshore velocities (f) and NVT (g) time series. For every series, the dashed lines correspond to the 95% significance levels. Nearly bi-monthly period (46–79 days) and nearly semi-annual period (132–187 days) are represented by the horizontal gray bars.

Beal (2009) also found the nearly bi-monthly period for the Agulhas Undercurrent. This author related this frequency band to the same mode that dominates the main surface Agulhas Current variability, an assessment that we share and, analogously, link the EMUC nearly bi-monthly period to the surface EMC variability (Schott et al., 1988). Such a variability in the EMC domain is attributed to the barotropic mode, forced by local wind-stress curl over the Mascarene Basin (Matano et al., 2002; Warren et al., 2002; Weijer, 2008).

The origin of the nearly semi-annual cycle seems to be associated with the monsoon wind regime, which is pronounced over the eastern equatorial Indian Ocean, and marked by a strong semi-annual cycle. However, there is no clear understanding on how this signal propagates to the western boundary and manifest itself in the EMUC at 23°S.

Morrow and Birol (1998) showed that baroclinic Rossby waves are generated near the Indian Ocean eastern boundary, extending across the entire basin, between 20°S and 35°S, with characteristic timescales between 120 and 180 days. Such timescales are in a good agreement with the nearly semi-annual cycle (132–187 days) here defined.

Schouten (2001) and Schouten et al. (2002b) proposed an explanation for the adjustment of the western part of the basin to the monsoon regime. According to these authors, Kelvin waves generated in the equatorial region are observed to reach the west coast of Indonesia, after the reversal of monsoons, from where they propagate southward as coastal Kelvin waves, so that these waves work as a trigger for Rossby waves at midlatitudes. But, the authors also speculated that the reflection of semi-annual Rossby waves against the Maldives ridge, near the middle of the basin, are frequency doubled and then arrive at the western boundary with a frequency of 4 per year. Therefore, care should be taken in definitely relating monsoon regimes to EMUC semi-annual variability. Due to the regional focus of this paper, a detailed study of basin scale processes still has to be conducted to confirm (or reject) such a teleconnection.

Fig. 3.8 shows a bandpass filter (forward–backward Butterworth filter) of the NVT time series with the passband adjusted for the nearly semi-annual and nearly bi-monthly periods, conjointly to the sum of both, plotted together with the original transport time series. The nearly bi-monthly, nearly semi-annual and the composition of both explain, respectively, about 21%, 27% and 48% of the transport variance.

In order to illustrate whether or not some seasonal patterns appear in the volume transport, Table 3.2 summarizes the EVT in every season, as previ-

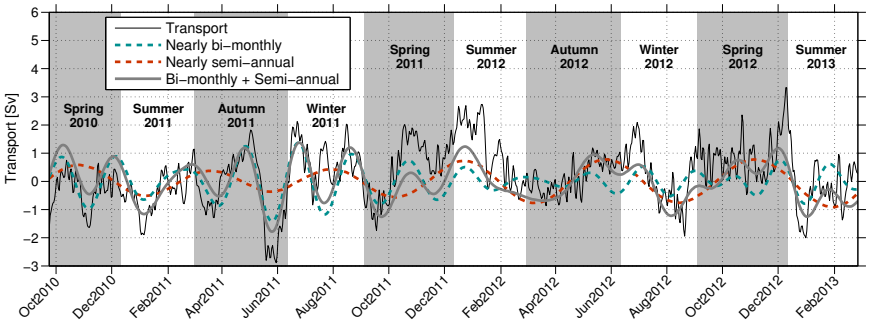

Figure 3.8: Bandpass filter of the detrended Net Volume Transport (NVT) time series (black solid line) considering the nearly bi-monthly (46–79 days, dashed blue line) and nearly semi-annual (132–187 days, dashed red line) periods. The gray line shows the composition of the two periods.

Table 3.2: Average seasonal Equatorward Volume Transport (EVT) and variance for every season and for two subsequent seasons. The averages are calculated through a mean between series from the three different extrapolation methods.

Period	# days	Mean transp. (Sv)	Variance (Sv^2)
Summer	260	1.24	2.88
Autumn	186	0.87	0.85
Winter	188	1.57	1.61
Spring	254	1.59	1.89
Spring–Summer	514	1.41	2.42
Summer–Autumn	446	1.09	2.06
Autumn–Winter	374	1.22	1.35
Winter–Spring	442	1.58	1.77

ously highlighted by the vertical bars in Fig. 3.6a. Averages of 1.24, 0.87, 1.57 and 1.59 Sv have been found for summer, autumn, winter and spring, respectively. A reduced mean transport occurred in autumn, while maxima occurred in spring and winter. But, the wavelet spectral analysis did not show a significant seasonal variability.

If averages of two subsequent seasons are considered, transports of 1.42 (spring–summer), 1.09 (summer–autumn), 1.22 (autumn–winter) and 1.58 Sv (winter–spring) suggest a stronger undercurrent during winter–spring compared to summer–autumn. But, this association must be interpreted with caution, since a longer time series must be considered.

There is a difference in the mean EVT between 2011 (1.2 Sv) and 2012 (1.7 Sv), suggesting also an interannual mode of variability of the system. Interannual variability has already been identified in the SWIO, for instance, inside the Mozambique Channel (Harlander et al., 2009; Ridderinkhof et al., 2010; Ullgren et al., 2012). Unfortunately, the length of our time series does not allow us to study this phenomenon in depth.

3.4 ON THE EMUC BAROCLINIC/BAROTROPIC PARTITIONING

The partitioning of velocity profiles in barotropic and baroclinic components is addressed in this section. We use a simple barotropic/baroclinic decomposition where the barotropic component is interpreted as the vertical average of the alongshore velocity profile, while the remaining sheared profile represents the baroclinic component (da Silveira et al., 2004; Meinen et al., 2013). Fig. 3.9 shows two examples where the alongshore velocity fields are decomposed in barotropic and baroclinic fields. Such a partitioning is applied to the entire time span, at each horizontal grid point and at every moment.

Fig. 3.9a shows a case where a robust poleward barotropic flow is extracted from the observed field. At this moment the EMC migrates deep into the water column (the -10 cm s^{-1} isotach reaches about 1500 m), inhibiting the equatorward flow at intermediate levels, and as consequence the undercurrent is not observed in the data at this moment, although its baroclinic signal is still present. Fig. 3.9b shows a situation when the barotropic influence is reduced, and therefore the baroclinic field is similar to the observed.

Considering that the barotropic pressure gradients are forced at the surface, we investigate the cross-shore gradients of absolute dynamic topography (η) from altimetry. While η comprises both baroclinic and barotropic effects (Gill and Niiler, 1973; Rintoul et al., 2002), the latter is straightforward and constant from the surface to the bottom. So, one might wonder whether or not

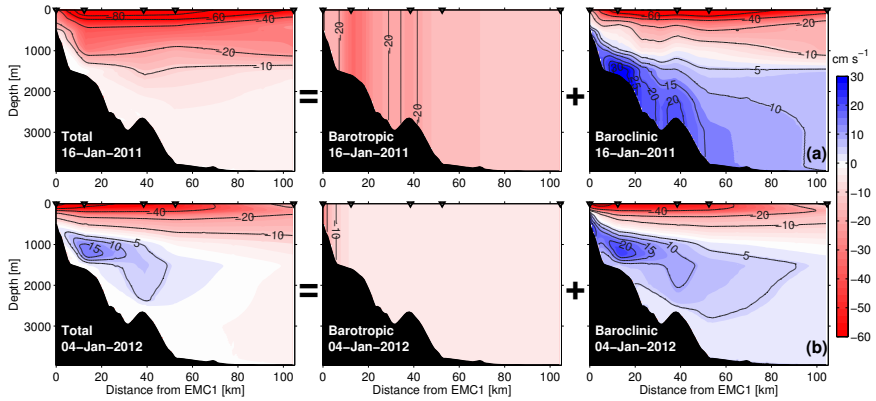

Figure 3.9: Observed alongshore velocity field (left), and its partitioning in barotropic (center) and baroclinic (right) fields, on (a) 16 Jan 2011 and (b) 04 Jan 2012.

strong (positive) cross-shore gradients of η ($\partial\eta/\partial x$) may correspond to a strong (negative) alongshore barotropic flow and, consequently, induce a weakening or reversal of the undercurrent speeds. Surface velocity is related with $\partial\eta/\partial x$ through geostrophy: $v = (g/f)(\partial\eta/\partial x)$, where g is the acceleration due to gravity and f is the Coriolis parameter (f <0 on Southern Hemisphere).

Distance-time diagrams of $\partial\eta/\partial x$, alongshore barotropic velocity (v_{BT}), alogshore observed velocity at 1260 m ($v(1260)$), and alongshore baroclinic velocity at 1260 m ($v_{BC}(1260)$) are shown in Figs. 3.10a-d. Notice that v_{BT} is persistently negative (Fig. 3.10b), forcing a flow against the EMUC. Its strong events are mainly associated with strong positive $\partial\eta/\partial x$. There is only one moment when a remarkable reversal of the barotropic flow is observed: during the reported cyclonic eddy (around 6 Jul 2011). On the other hand, the baroclinic signal at 1260 m is persistently equatorward (Fig. 3.10d), although it is superimposed by stronger barotropic events (Fig. 3.10c).

Time series extracted from the EMC2 location are plotted in Figs. 3.10e,f, while Table 3.3 exhibits the correlation coefficients calculated between every pair of variables throughout the whole time span. Overall, the results confirm that a strong negative v_{BT} is related with a strong positive $\partial\eta/\partial x$, leading to attenuation or reversal of the flow in the EMUC. But not always a strong $\partial\eta/\partial x$ leads to a strong v_{BT} (for instance, Jan/2012).

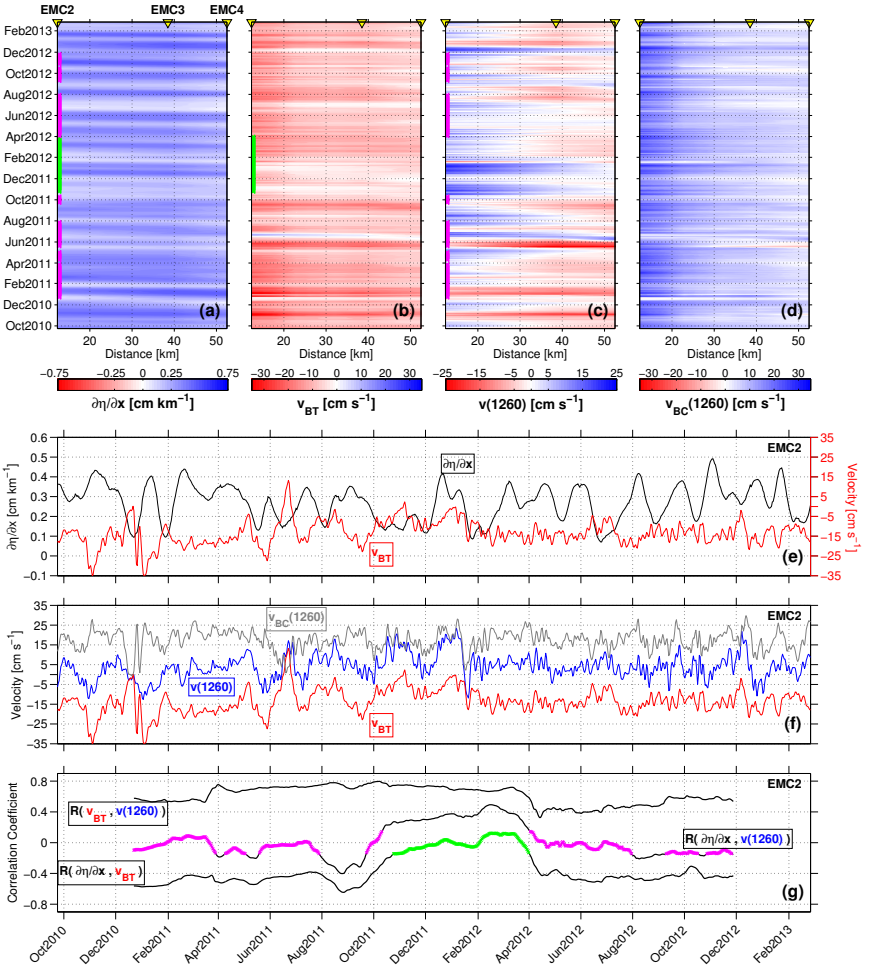

Figure 3.10: Distance/time diagrams: (a) horizontal gradients of absolute dynamic topography ($\partial\eta/\partial x$), interpreted in terms of a finite difference $\Delta\eta/\Delta x$; (b) alongshore barotropic velocity (v_{BT}) ; (c) alongshore observed velocity at 1260 m ($v(1260)$); and (d) alongshore baroclinic velocity at 1260 m ($v_{BC}(1260)$). (e) Time series at the EMC2 location of $\partial\eta/\partial x$ (black line and left y-axis) compared to v_{BT} (red line and right y-axis). (f) Time series at the EMC2 location of $v(1260)$ (blue line) and $v_{BC}(1260)$ (gray line) compared to v_{BT} (same than (d); red line). (g) Correlation coefficients (R) computed with a moving window of 180 days between $\partial\eta/\partial x$, v_{BT} and $v(1260)$ time series. The pink and green line segments highlight non-significant correlations (p-value test). These points are time-projected on the plots (a), (b) and (c).

Table 3.3: Correlation coefficients (R) computed at EMC2 location between every pair of the following variables: $\partial\eta/\partial x$, v_{BT}, $v(1260)$ $v_{BC}(1260)$. All correlations are significant (p-test value) for a 95% confidence level.

	$\partial\eta/\partial x$	v_{BT}	$v(1260)$	$v_{BC}(1260)$
$\partial\eta/\partial x$	1.00			
v_{BT}	-0.44	1.00		
$v(1260)$	-0.11	0.68	1.00	
$v_{BC}(1260)$	0.42	-0.41	0.40	1.00

We also computed the correlation coefficients with a moving window of 180 days (similar to the nearly semi-annual period). The results show that such a correspondence can be stronger or not significant (Fig. 3.10g), depending on the moments of the time series. For instance, in the period from Nov/2011 to Apr/2012 (green segment) the correlation between $\partial\eta/\partial x$ and v_{BT} is not significant.

Around Jan/2012, both EMUC ($v(1260)$) and $\partial\eta/\partial x$ are marked by strong events and, therefore, a significant positive correlation is observed between these two time series. We do not have a clear explanation for this observation.

3.5 SPATIAL EXTENT AND THERMOHALINE PROPERTIES FROM ARGO FLOATS

The time series studied in previous sections present results in the matter of continuous long-term observations of the EMUC. Nevertheless, the data are restricted to a certain latitude (∼23°S). Uncertainty about the extent of the undercurrent farther north and the spatial variation of the thermohaline properties in its domain could not be investigated with the INATEX data. In order to address those issues we use a historical dataset of Argo profiling floats.

3.5.1 *Spatial extent*

The origin of the EMUC seems to be placed at the continental slope near the southern tip of Madagascar (Nauw et al., 2008). These authors showed (in their Figure 3) four frames where the undercurrent transport is increasing from a meridional transect at 45°W, located slightly west to the southern tip of the island, to the southeastern coast of Madagascar.

In Figs. 3.11a,b, we show the vectors of horizontal velocity from the ANDRO database (Ollitrault and Rannou, 2013), derived at the surface and near 1000 m depth (Argo “parking" depth), respectively. Most of the floats north of 21°S and near the slope were captured by the equatorward undercurrent (Fig. 3.11b, blue vectors), even taking into account that their parking depth is near the region of the mean flow reversal (see 0 m s^{-1} isotach in Fig. 3.3b).

Farther downstream, Argo-derived velocities suggest an equatorward undercurrent flowing until approximately 17°S, the region where the South Equatorial Current bifurcates towards the Madagascar coast (Swallow et al., 1988; Chapman et al., 2003; Siedler et al., 2006). No floats were caught by the undercurrent south of 21°S, which might be due to upstream deepening of the undercurrent.

It is important to note that even floats with poleward displacements (red vectors in Figs. 3.11a,b) could have profiled the undercurrent south of 21°S, since these autonomous devices descend to 2000 m during the vertical profiling. Nevertheless, the blue vectors in Fig. 3.11b corroborate the results from the time series (see Fig. 3.3b) and indicate a region where the EMUC is expected to occur, in between the isobaths of 1000 and 3000 m.

3.5.2 *Thermohaline properties at intermediate levels*

In this section we investigate the thermohaline properties around Madagascar Island at intermediate levels. Intermediate waters are generically defined to lie in the isopycnal range of 26.9–27.7 kg m^{-3} in the SWIO (Donohue and Toole, 2003). The EMUC, in turn, has been found in between the isopycnals of 27.2 and 27.75 kg m^{-3} at 25°S (Nauw et al., 2008).

Based on thermohaline, oxygen and nutrient data, Nauw et al. (2008) conducted a water mass analysis that shows a contrast between a saline water mass near the EMUC core and a fresher one around the offshore border of the undercurrent. The fresher water was due to the strong contribution of Antarctic Intermediate Water (AAIW), which is marked by a minimum in salinity. On the other hand, these authors related the increase of salinity towards the continental slope to the influence of the poorly oxygenated Red Sea Water (RSW). However, these previous results are based on four quasi-synoptic transects around the southern tip of Madagascar and, hence, there is no information whether this cross-shore salinity gradient is persistent northward to 25°S, along the eastern margin of the island.

The RSW pathway tracked by those authors is the following: RSW emerging from the Gulf of Aden is partially diluted and transported southward at

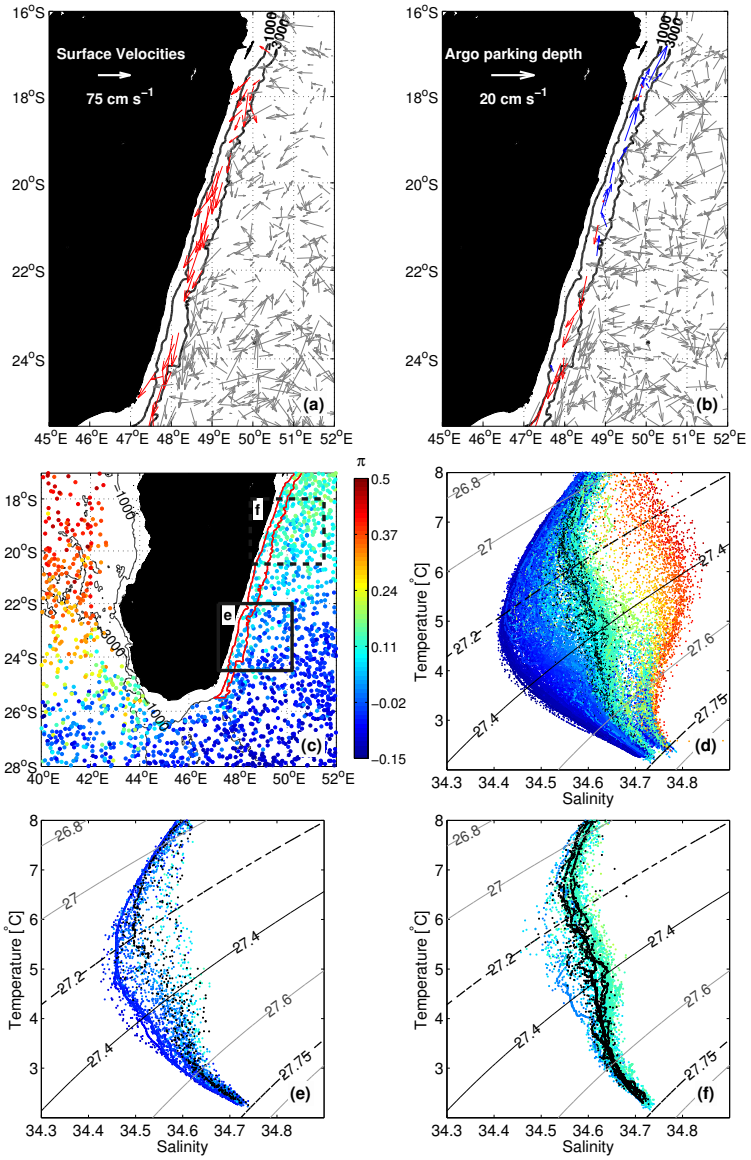

Figure 3.11: ANDRO current velocities deduced at (a) surface and (b) near the Argo parking depth (∼1000 m). (c) Spiciness (π) at the isopycnal level of 27.4 kg m^{-3} estimated from historical Argo profiles. (d) θ-S diagram corresponding to the Argo profiles used in (c). The same spiciness colors used in (c) are used in (d) so only to stress the geographical position of the profiles. Profiles sampled in the region enclosed by the red line along the slope (bounded by the 1000 and 3000 m isobaths) are plotted in black. (e-f) θ-S diagram for the profiles enclosed by the (e) solid and (f) dashed rectangles highlighted in (c), respectively. Black profiles represent the same as in (d).

intermediate levels inside the Mozambique Channel (Wyrtki, 1971; Beal et al., 2000). Somehow it contours the southern tip of Madagascar Island and, leaning on the continental slope, the diluted RSW forms the EMUC core. In turn, AAIW is known to spread northward after being injected in the southwestern portion of the basin, around 50–60°E, north of the Kerguelen Plateau ($\sim$ 50°S) (Park et al., 1993; Donohue and Toole, 2003).

Fig. 3.11c shows the spiciness (π) at the isopycnal level of 27.4 kg m^{-3} estimated from historical Argo profiles, according to the algorithm developed by Flament (2002). Spiciness is a state variable useful to characterize water mass, with largest (smallest) values corresponding to hot-and-warm (cold-and-fresh) waters. The results reproduce the pathway of the diluted RSW described above. Waters marked by high spiciness values are found in the north portion of the Mozambique Channel, while low spiciness waters are found offshore to the southeast of Madagascar.

Fig. 3.11d shows the θ-S diagram plotted with the same profiles used to estimate the spiciness displayed in Fig. 3.11c. We also use the same spiciness colors so only to distinguish the θ-S profiles according to their geographical position. Additionally, profiles sampled in the region where the EMUC is expected to occur (area bounded by the red line in Fig. 3.11c) are plotted in black.

Notice in Fig. 3.11e that the θ-S diagram, from the region off the southeastern coast (solid rectangle in Fig. 3.11c, northward-limited at 22°S), reinforces that waters in the EMUC region are saltier than waters offshore. On the other hand, this cross-shore salinity gradient is not observed in the θ-S diagram from the profiles sampled off the eastern coast (dashed rectangle in Fig. 3.11c, southward-limited at 20.5°S), as can be seen in Fig. 3.11f. These results suggest that the zonal gradient of salinity found by Nauw et al. (2008) at 25° S vanishes northward, while the influence of AAIW also vanishes in the same direction.

3.6 DISCUSSION AND CONCLUSIONS

As part of the Southern Hemisphere supergyre (de Ruijter, 1982), the western boundary current system in the South-West Indian Ocean (SWIO) is a remarkable component of the thermohaline circulation and global climate through the Indian-Atlantic interocean exchange (Beal et al., 2011). In this scenario, the East Madagascar Current (EMC) is one of the main sources of the Agulhas Current and seems to impact downstream the variability of the Agulhas retroflection via southward propagating dipoles (de Ruijter et al., 2004; Ridderinkhof et al., 2013).

The East Madagascar Current system itself is composed of the surface poleward EMC and an underlying flow at intermediate levels, near the continental slope, associated with the East Madagascar Undercurrent (EMUC). The existing information describing the EMUC is based on a few quasi-synoptic measurements (Nauw et al., 2008).

In this work, we extend previous results to a long-term description of the EMUC based on 2.5 years of velocity observations, along a line of 5 moorings deployed at 23° S, sampled in the scope of the "INdian-ATlantic EXchange in present and past climate" (INATEX) project. Furthermore, altimeter data and Argo data (temperature–salinity and horizontal velocity) were also used.

Direct velocity measurements from the INATEX moorings reveal a recurrent EMUC which was present 78% of the sampling time (692 from 888 days). Some of the reversal periods were directly associated with a strong barotropic component of the poleward western boundary current. The maximum equatorward velocity reached 27.3 cm s^{-1} in the mooring EMC2 (28.6 km from the coast) at a depth level of 1110 m, whereas maximum averaged velocity (4.1 cm s^{-1}) was identified at around 1260 m at the same mooring. Mesoscale activities such as meandering and passage of a cyclonic eddy were also observed.

In this study we propose two methods to provide the EMUC transport time series: Equatorward Volume Transport (EVT) and Net Volume Transport (NVT). The first (EVT) is more appropriated for estimating the amount of water transported equatorward by the EMUC, and it computes only positive velocities enclosed in the area indicated by the yellow dashed line in in Fig. 3.3b. On the other hand, the second (NVT) is more suitable to address the transport variability. It accounts for both positive and negative velocities in the region enclosed by the mean 0 m s^{-1} isotach (green line in Fig. 3.3b). For the EVT case, maximum values can reach up to 6 Sv while the mean was about 1.33 ($\pm$1.41) Sv. The NVT presents average values of 0.21 ($\pm$1.25) Sv and maxima of 3.93 Sv.

Variability in two period bands showed up in the wavelet spectra of the NVT time series: nearly bi-monthly (46–79 days) and nearly semi–annual (132-187 days), which explain about 21% and 27% of the EMUC transport variance, respectively.

The nearly bi-monthly period is connected to the same mode that dominates the main EMC (Schott et al., 1988). In the literature this cycle is attributed to the incidence of barotropic Rossby waves originated due to local wind-stress curl over the Mascarene Basin (Matano et al., 2002; Warren et al., 2002; Weijer, 2008). Considering the velocity time series, the nearly bi-monthly period also showed up in the entire water column at the moorings EMC2 and EMC3.

In turn, the nearly semi-annual cycle seems to be related to the monsoon wind regime over the eastern equatorial Indian Ocean. However, there is no theoretical understanding on how this signal propagates to the other side of the basin, and how it manifests itself in the EMUC at 23°S. A suggestion is proposed by Morrow and Birol (1998), who observed baroclinic Rossby waves to be generated near the Indian Ocean eastern boundary, with a timescale between 120 and 180 days, and propagating westward across the whole basin in the range from 20°S to 35°S.

Interannual variabilities could not be attempted due to the length of our time series, although a significant difference in transport was found between 2011 and 2012.

A partitioning of the alongshore velocity fields in barotropic and baroclinic contributions shows the baroclinic undercurrent as a persistent feature throughout time. But, sometimes the equatorward baroclinic component is masked by a relatively stronger barotropic flow, leading to reversals of the EMUC flow during these events. In turn, events of strong poleward barotropic velocities are often observed concomitantly with strong positive cross-shore gradients of absolute dynamic topography ($\partial\eta/\partial x$), although not always a strong $\partial\eta/\partial x$ represents an increase of the barotropic flow.

Horizontal velocities from the ANDRO database indicate the extent of the EMUC farther north along the continental slope, which reaches approximately 17°S.

An updated historical dataset of temperature–salinity Argo profiles was used to investigate the spatial variability of spiciness at intermediate levels, around the island of Madagascar. Results support previous observations reported by Nauw et al. (2008) at 25°S, where the undercurrent core was found saltier than offshore waters, due to the contribution of diluted Red Sea Water (RSW) from the Mozambique Channel. However, we also show that this zonal salinity gradient vanishes equatorward, since the contribution of Antartic Intermediate Water (AAIW) also vanishes in that direction.

Results suggest that further research is still needed to improve our understanding of the EMUC. Uncertainty about whether an upstream shallowing of the undercurrent takes place, and whether the undercurrent interacts with the Equatorial Current system, requires future work based on *in situ* velocity measurements at northern latitudes along the eastern margin of Madagascar. Also, long-term measurements of the thermohaline properties are necessary, so that the relationship between EMUC and water mass can be addressed synoptically.

4

FIRST OBSERVATIONAL EVIDENCE OF A NORTH MADAGASCAR UNDERCURRENT

ABSTRACT

In situ observations reveal a southeastward-directed North Madagascar Undercurrent (NMUC) below and opposite to the equatorward-directed North Madagascar Current (NMC) off Cape Amber, at the northern tip of Madagascar. Results show an undercurrent hugging the continental slope with its core at 460 m depth and velocities over 0.7 m s^{-1}. Its volume transport is estimated to be 3.1–3.8 Sv, depending on the velocity extrapolation methods used to fill in the data gaps near the slope (no-slip and full-slip, respectively). The thermohaline characteristics show a saltier and warmer NMUC, compared to the surrounding offshore waters, transporting mainly South Indian Central Water. Also, strong horizontal gradients of density are found in the NMUC domain. An inshore cell of coastal downwelling due to Ekman Transport toward the coast is identified, which can explain, at least in part, the strong baroclinic pressure gradients as well as the NMUC development and possible persistence.

This chapter has been published as:

Ponsoni, L., B. Aguiar-González, J.J. Nauw, H. Ridderinkhof and L.R.M. Maas, 2015. First observational evidence of a North Madagascar Undercurrent. *Dyn. Atmos. Oceans* 72, 12–20.

4.1 INTRODUCTION

The South-West Indian Ocean (SWIO) presents one of the most intriguing western boundary regions of all subtropical gyres. Unlike other regions, in the SWIO the Madagascar island imposes a physical barrier to the westward flowing South Equatorial Current (SEC), which reaches the Madagascar coast between 17°S and 20°S (Fig. 4.1a). At this location, the SEC bifurcates into two branches: the southward branch feeds into the East Madagascar Current (EMC), which farther south will feed the Agulhas Current (AC); on the other hand, the northward branch feeds into the North Madagascar Current (NMC; Swallow et al. (1988); Chapman et al. (2003); Siedler et al. (2006)), which turns around Cape Amber, at the northern tip of Madagascar, and continues westward toward the east coast of Africa (Swallow et al., 1988).

Besides the surface patterns of the boundary currents, an undercurrent flowing opposite and beneath the surface current appears to be a recurring feature near eastern and western ocean boundaries. At western boundaries, such a feature has been universally observed: the Luzon Undercurrent in the North Pacific (Hu et al., 2013), the East Australian Undercurrent in the South Pacific (Godfrey et al., 1980; Schiller et al., 2008), and the Intermediate Western Boundary Current in the South Atlantic (Evans and Signorini, 1985; da Silveira et al., 2004) are some examples.

In turn, three undercurrents have already been reported to occur in the SWIO: the Agulhas Undercurrent (AUC; Beal and Bryden (1997)), the Mozambique Undercurrent (MU; de Ruijter et al. (2002); van Aken et al. (2004)) and the East Madagascar Undercurrent (EMUC; Nauw et al. (2008); Ponsoni et al. (2015a)), all flowing equatorwards (Fig. 4.1b).

To the knowledge of the authors, this work presents the first observational evidence of a North Madagascar Undercurrent (NMUC) flowing below and opposite to the NMC. First estimates about its spatial extent, core velocity, volume transport and thermohaline properties are addressed. The importance of the wind stress and Ekman Transport in the region are also investigated.

4.2 THE ACSEX3 DATA SET

The results of this study are based on thermohaline and velocity observations carried out on 30 March 2001, as part of the “Dutch-South African Agulhas Current Sources Experiment" (ACSEX). The ACSEX program (de Ruijter et al., 2002) was accomplished by three oceanographic surveys around Madagascar on board the RV Pelagia. More precisely, in this paper we use Conductivity–

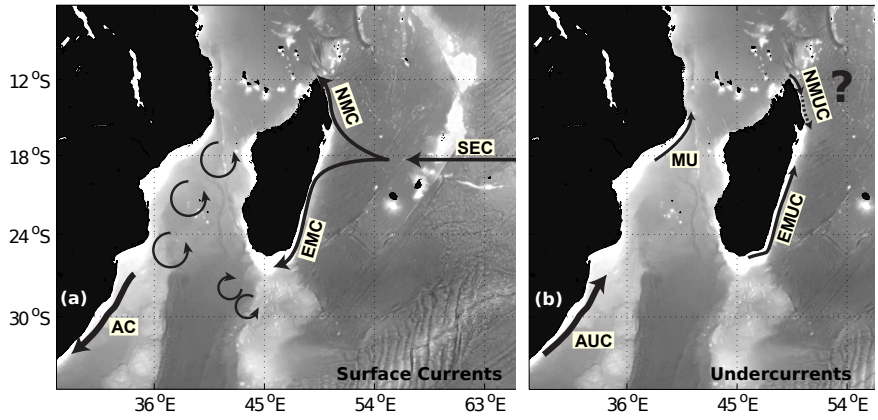

Figure 4.1: Sketch of the surface currents (a) and undercurrents (b) in the SWIO: South Equatorial Current (SEC), East Madagascar Current (EMC), North Madagascar Current (NMC), Agulhas Current (AC), Agulhas Undercurrent (AUC), East Madagascar Undercurrent (EMUC), Mozambique Undercurrent (MU) and North Madagascar Undercurrent (NMUC).

Temperature–Depth (CTD) and Lowered Acoustic Doppler Current Profiles (L-ADCP) from the six innermost stations (Sta18–Sta13) at Transect E1, located northeast of Cape Amber (ACSEX3 survey, Fig. 4.2). The deepest observation of each vertical profile (200, 580, 1060, 1040, 2520 and 3020 m, from Sta18–Sta13, respectively) is placed near the bottom, on average 17 m above the seafloor.

The CTD frame was equipped with two synchronized self-contained 300-kHz ADCPs. Vertical profiles of horizontal velocities were achieved either with an inverse solution method (Visbeck, 2002), if near-bottom data were available (stations shallower than 2400 m), or shear-based method (Fischer and Visbeck, 1993) for stations deeper than 2400 m. For a complete view of the ACSEX data processing the reader is referred to Nauw et al. (2008).

In addition, monthly fields (from July 1999 to November 2009) and an average field from 25 to 31 March 2001 of wind stress data from the SeaWinds scatterometer, coupled to the NASA's Quick Scatterometer (QuikSCAT) satellite, are analyzed in order to support our interpretations. We use the Version-4 (V4) data products produced by Remote Sensing System and available at `www.remss.com` (Ricciardulli and Wentz, 2011). The scatterometer spatial resolution is about 25 km. A full description of the SeaWinds is presented by Freilich et al. (1994).

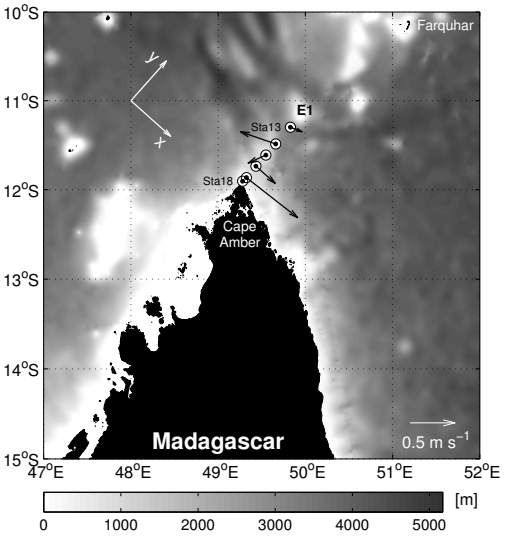

Figure 4.2: Map of the region of study indicating the oceanographic stations (circles) at transect E1 occupied during the ACSEX3 cruise. From inshore to offshore, the stations are named Sta18–Sta13. Bathymetric contours are drawn in shades of gray. The coordinate system is rotated 41.7 degrees from the north, and it is represented by along-stream (x) and cross-stream (y) components. Vectors show velocities from the L-ADCP, at the depth of 460 m (NMUC core). Notice that the coordinate axes are plotted only to show the orientation of the coordinate system, since their origins are set at Sta18.

4.3 VELOCITIES AND VOLUME TRANSPORT

The two measured components of current velocity were rotated into along-stream (x) and cross-stream (y) directions. The x component represents the main direction of the NMUC, since its flow is markedly perpendicular to Transect E1 (see arrows in Fig. 4.2). Horizontal extrapolations were performed to fill in the empty data regions created due to the depth difference between two neighboring stations. This is a typical problem, especially pressing in regions near a steep continental slope. For the sake of completeness, we apply two boundary conditions in order to compute the volume transport: no-slip and full-slip (Beal and Bryden, 1997; Nauw et al., 2008). The first condition assumes that velocity decreases linearly to zero at the continental slope, while in the second condition the velocity at the continental slope is assumed equal to the nearest measurement at the same depth.

Fig. 4.3a presents the vertical structure of the along-stream velocity. Negative values (dashed isotachs) represent the NMC flowing northwestward, while

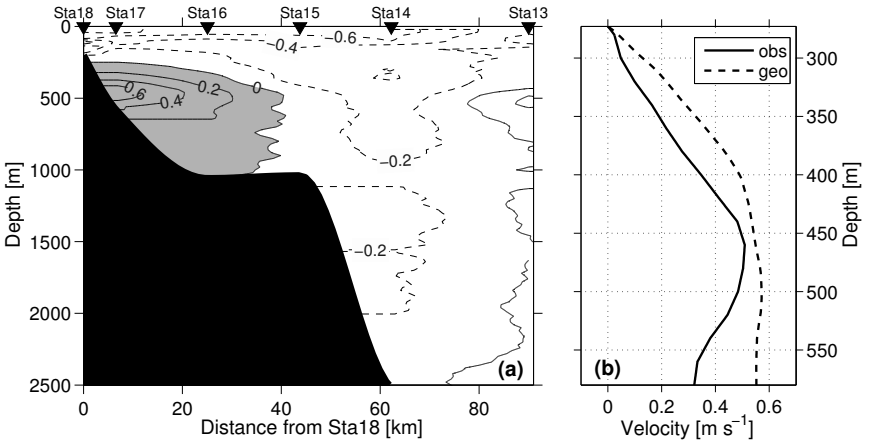

Figure 4.3: (a) Along-stream velocities in m s^{-1}. Full-slip extrapolation is applied in this figure. The gray shaded area highlights the NMUC domain. The bathymetry mask is drawn according to the deepest measured point at every station, which took place near the seafloor (about 17 m from the bottom). (b) Profile of along-stream velocity interpolated in between Sta17 and Sta16 (solid line) and geostrophic velocity estimated from the thermohaline profiles sampled at Sta17 and Sta16 (dashed line). The level of no motion (275 m) was selected according to the observed profile (solid line).

positive values on the upper part of the continental slope (solid isotachs, shaded) are related to the southeastward NMUC. The vertical reversal of the flow takes place at Sta17 and Sta16 at a depth of 250 and 320 m, respectively, where the strongly sheared profiles suggest an important baroclinic contribution to the total geostrophic flow.

Fig. 4.3b shows the vertical profile of geostrophic velocity estimated through the thermal wind relation and from the thermohaline properties (dashed line), for the location in between Sta17–Sta16, as well as the profile of observed velocity interpolated to the same location (solid line). Notice that there is a good agreement in the vertical shear of both profiles at the NMUC vertical range.

At the time of sampling, the total velocity field depicts a NMUC confined from 250 m depth to the seafloor (near 1060 m), hugging the continental slope with a well defined core in which the velocity exceeds 0.7 m s^{-1} at 460 m at the location of Sta17. Arrows in Fig. 4.2 show the velocity at this depth level. Notice that the NMUC maximum is comparable to the maximum speed found in the surface NMC (-0.7 m s^{-1}). The NMUC extends offshore between 25 km (Sta16) and 44 km (Sta15).

On the other hand, the NMC core is found at surface level, where the isotach of -0.6 m s^{-1} is spread from Sta18 to Sta14. At the locations of Sta15 and Sta14, the vertical profiles of velocity suggest a reduced baroclinic component compared to the profiles at Sta17 and Sta16.

Additionally, we plotted daily fields (from 25 March to 05 April 2001) of geostrophic velocity calculated from Absolute Dynamic Topography (ADT) and Sea Level Anomaly (SLA), measured from satellite, in order to investigate whether eddies were present or not in the region at the moment of the cruise. The results (not shown) pointed to the absence of eddies in the area of study during the sampling time.

Considering only the NMUC grid points, which are enclosed by the 0 m s^{-1} isotach (gray area in Fig. 4.3a), mean flows of 0.18 ($\pm$ 0.15) and 0.16 ($\pm$ 0.15) m s^{-1} are found for full-slip and no-slip extrapolation conditions, respectively.

The NMUC southeastward transport amounts to 3.8 Sv (1 Sv = 10^6 m^3 s^{-1}) and 3.1 Sv for full-slip and no-slip conditions. Taking into account the integrated transport in the E1 vertical transect (as plotted in Fig. 4.3a) the amount of -18.3 Sv (full-slip, or -17.4 Sv for no-slip) indicates a net northwestward transport. Swallow et al. (1988) and Schott et al. (1988) estimated the NMC volume transport to be -29.6 Sv and -26.9 Sv, respectively, based on geostrophic calculations and observed velocity data. These values represent an integration from surface to 1100 dbar out to 115 km, where their most inshore point is placed offshore of our Sta16 location.

4.4 THERMOHALINE STRUCTURE

The thermohaline and density structures are marked by strong horizontal gradients in temperature (T, Fig 4.4a), salinity (S, Fig 4.4b) and potential density anomaly (σ_θ, Fig 4.4c) which shows that the NMUC lies within the isopycnal range of 26.1–27.4 kg m^{-3}, while its core is found near the 26.75 kg m^{-3} isopycnal level (see solid lines in Fig 4.4d).

The inclination of the isolines towards the coast indicates a NMUC saltier and warmer than waters offshore. Vertical averages calculated in the range of 250–580 m, from the NMUC upper limit to the deepest sampled depth at Sta17, exhibit this difference (Table 4.1). Notice that horizontal gradients are stronger in between Sta17–Sta16 than in any other combination of neighboring stations. The results also show that the offshore gradients of density are governed mainly by offshore gradients of temperature.

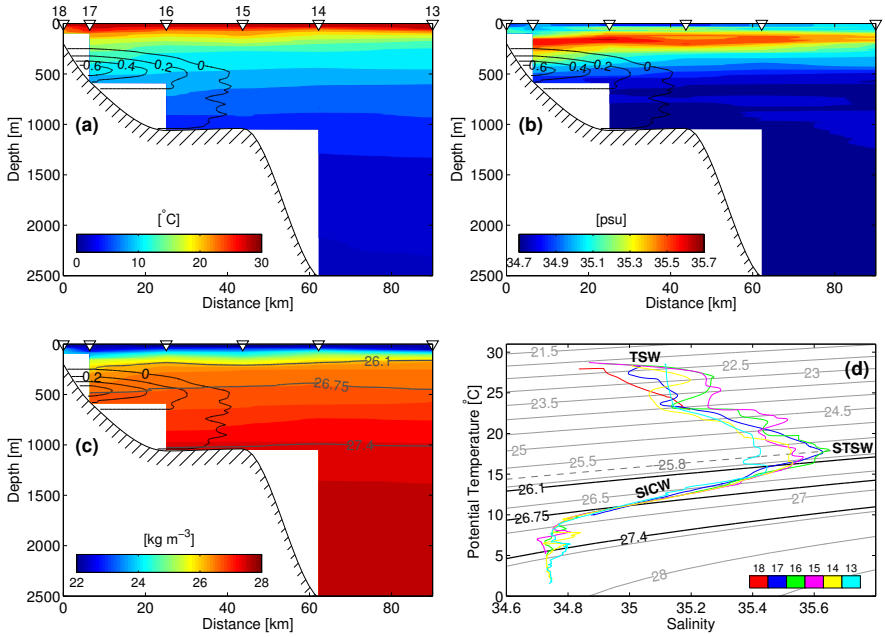

Figure 4.4: (a) Potential temperature, (b) salinity and (c) potential density anomaly along the E1 transect. The NMUC isotachs are also plotted (a–c). (d) θ–S diagram color-coding each E1 station. Abbreviations indicate water masses: Tropical Surface Water (TSW), Sub-Tropical Surface Water (STSW) and South Indian Central Water (SICW)

Fig 4.4d presents the θ–S diagram for all stations. At surface levels the Tropical Surface Water (TSW) covers the Sub-Tropical Surface Water (STSW), which has a core density of 25.8 kg m^{-3}. While TSW is formed in the tropics due to high precipitation and solar warming, STSW is created in the subtropics region due to an excess of evaporation over precipitation and, therefore, it is marked by a maximum in salinity. The lens of high salinity seen in Fig 4.4b, at subsurface levels, has characteristics of STSW (Wyrtki, 1973). Overlaid by STSW, South Indian Central Water (SICW, also known as Indian Central Water) is found in between the isopycnals of about 26.1 and 27.0 kg m^{-3}. This water mass is typified by a narrow θ–S relation (Emery and Meincke, 1986; Schott and McCreary Jr., 2001) which is expressed as a line in the diagram. The inflexion seen in the θ–S curve below the 27.0 kg m^{-3} isopycnal reflects an increase in salinity due to influence of Red Sea Water (RSW) (Schott and McCreary Jr., 2001) and marks the transition to intermediate water masses.

Table 4.1: Vertical (250–580 m) averages and standard deviations of potential temperature (θ), salinity (S) and potential density anomaly (σ_θ).

Station	Sta17	Sta16	Sta15	Sta14	Sta13
θ [°C]	12.46 (±1.85)	11.49 (±1.15)	11.17 (±1.04)	10.93 (±1.15)	10.85 (±1.23)
S [psu]	35.14 (±0.19)	35.04 (±0.15)	35.00 (±0.14)	34.98 (±0.15)	34.96 (±0.12)
σ_θ [kg m^{-3}]	26.59 (±0.22)	26.71 (±0.10)	26.74 (±0.09)	26.76 (±0.10)	26.76 (±0.12)

Ullgren et al. (2012) found similar θ–S curves in the narrowest part of the Mozambique Channel.

The results show a NMUC mainly carrying SICW, although this water mass also spreads across the offshore zone where the undercurrent is not observed. Also, the undercurrent is not distinguished by this single water mass, since its upper and deeper limits appear to carry waters influenced by STSW and RSW, respectively.

4.5 COASTAL DOWNWELLING

Undercurrents can be both remotely and locally forced. For instance, the Intermediate Western Boundary Current (the undercurrent opposite and underneath the Brazil Current) has a remote origin linked to the depth-dependent bifurcation of the South Equatorial Current towards the Brazilian coast, which occurs near 15°S at the surface and around 25–27°S at intermediate levels (Legeais et al., 2013; Soutelino et al., 2013; Rocha et al., 2014). On the other hand, off Northwest Africa, the alongshore undercurrent and an associated upwelling system are closely coupled to the alongshore component of the local wind (McCreary, 1981).

The development of alongshore undercurrents forced by local alongshore wind, and its associated cross-shore Ekman Transport, was proposed by Yoshida (1959) based on a theoretical model in response to an upwelling-favorable wind. Through a linear stratified ocean model of coastal undercurrents, which was forced with a uniform band of alongshore steady winds, McCreary (1981) and McCreary and Chao (1985) concluded that internal friction and an alongshore pressure gradient are needed for the existence of a realistic undercurrent. Supported by numerical model results, also forced with upwelling-favorable winds, Suginohara (1982) postulated that the development of an alongshore undercurrent is linked to the arrival of the first mode Coastal Trapped Wave (CTW). However, the undercurrent ceases to develop with the arrival of the

second mode. Suginohara and Kitamura (1984) also stated that the undercurrent disappeared after long time evolution of the upwelling cell. These authors argued that the upwelling system is insensitive to the absence or presence of bottom friction and, therefore, the bottom boundary layer has minor importance on the undercurrent dynamics.

Taking into account that in linear systems (McCreary, 1981; McCreary and Chao, 1985) upwelling and downwelling are symmetric, the same results described above are also expected for a region dominated by downwelling conditions. Indeed, using the Princeton Ocean Model, Middleton and Cirano (1999) complemented the results from Suginohara (1982), where during the first 10–20 days after the set up by the downwelling-favorable winds, the linear system was characterized by the first mode CTW. However, after this initial phase, Middleton and Cirano (1999) showed important differences. Unlike the upwelling scenario, where bottom drag is insignificant, ultimately, this mechanism promotes nonlinear advection of density within the bottom Ekman layer and an increase in the thermal wind shear in the downwelling system. Therefore, an undercurrent can be sustained by a steady downwelling-favorable wind.

We do not have enough *in situ* data to state whether the NMUC is steady and whether its origin is entirely explained by the mechanism proposed by Middleton and Cirano (1999). But, since our region of study is dominated by downwelling-favorable winds, with similar conditions encountered by these authors, we expect that the local alongshore winds contribute, at least in part, to the NMUC development and possibly to its persistence.

Fig. 4.5a shows the wind field, surrounding the E1 Transect, averaged from 25 to 31 March 2001 (the oceanographic cruise took place on 30 March 2001). Analogous winds were observed during almost the whole month of March 2001 (Fig. 4.5b) so that the wind pattern is persistent before and during the cruise and, therefore, the ocean had enough time to adjust to the Ekman dynamics. Middleton and Cirano (1999) showed that after the first 10 days of a steady downwelling-favorable wind the undercurrent starts to develop and by day 30 the undercurrent is well organized over the slope. Note that the vector scale ($0.1\ \mathrm{N\ m^{-2}}$) used as reference in Fig. 4.5 is equal to the wind stress used in the simulations carried out by Middleton and Cirano (1999). Also, the stratification from the ACSEX transect (Fig 4.4c) resembles the stratification found by these authors after the establishment of the undercurrent (their Fig. 4c and Fig. 4e) with the isopycnals curving down towards the continental slope.

Both mean wind fields shown in Fig. 4.5 present northwestward winds, perpendicular to the E1 Transect. So, considering that the Ekman Transport, integrated in the Ekman Layer, is 90° to the left of the wind stress on the Southern

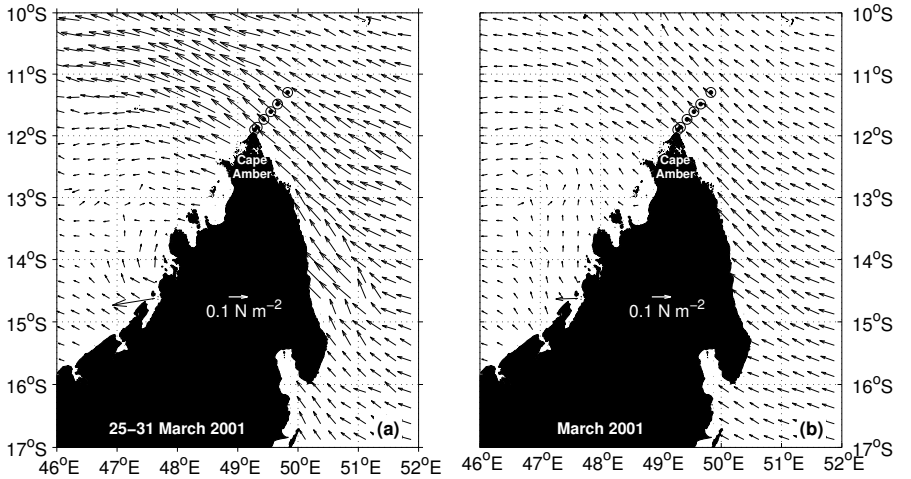

Figure 4.5: (a) Mean wind stress field for the week 25–31 March 2001. (b) Mean wind stress field for the month of March 2001.

Hemisphere, such a pattern is responsible for a piling up of water near the coast creating a downwelling system. Notice that the horizontal scale of depression of the thermocline (and pycnocline, Figs. 4.4a and 4.4c) towards the coast is similar to the first internal Rossby radius of deformation, estimated to be ∼45 km.

Fig. 4.6a shows the profile of cross-stream velocity from the L-ADCP data, averaged for Sta18–Sta13, while Fig. 4.6b displays the associated depth-integrated cross-stream Transport (T_{cs}). Negative values of velocity and transport represent a flow towards the coast. For instance, T_{cs} = -4.6 m^2 s^{-1} for the first 90 m of water column.

We also calculated the cross-stream Ekman Transport (V_y) at every oceanographic station based on the wind data, as follows:

$$V_y = -\frac{\tau_x}{\rho_w f}, \tag{4.1}$$

where f is the Coriolis parameter ($f < 0$ on the Southern Hemisphere), τ_x represents the along-stream wind stress and ρ_w=1024 kg m^{-3} is the seawater density, assumed constant. Fig. 4.7a shows the Ekman Transport estimated with ρ_w and the average wind for the period of the ACSEX cruise (Fig. 4.5a).

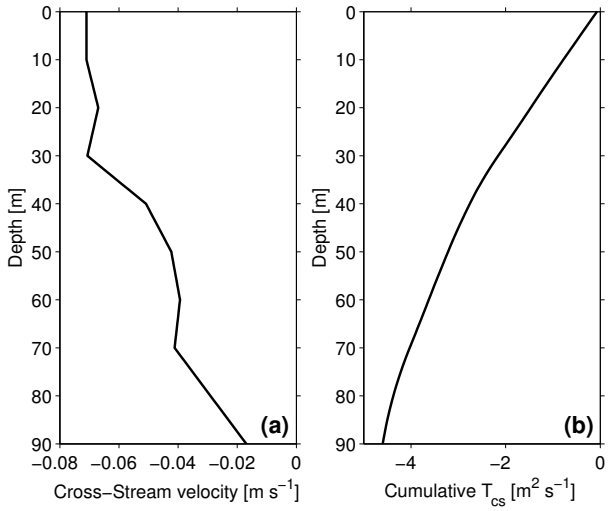

Figure 4.6: (a) Cross-stream velocity, from the L-ADCP data, averaged for Sta18–Sta13. (b) Cross-stream Transport (T_{cs}), per unit width, estimated by depth integrating the mean cross-stream velocity profile in (a).

From Sta18 to Sta13, V_y = -4.05, -4.07, -4.11, -3.94, -3.78 and -3.64 m^2 s^{-1}, respectively.

An estimation of the thickness of the Ekman Surface Layer is given by

$$H_E = \sqrt{\frac{2A_V}{|f|}}, \tag{4.2}$$

where A_V is the coefficient of turbulent viscosity, a poorly known quantity. For a typical choice of $A_V = 0.1$ m^2 s^{-1}, $H_E = 82$ m. This thickness is coherent with the layer suggested by Stewart (2008) for similar latitude and wind stress. Despite the fact that this is a coarse estimate, and even though such a thickness varies few dozens of meters, the values of T_{cs} in Fig. 4.6b are, at the very least, consistent with the values of V_y estimated for the period of the cruise (Fig. 4.7a). The Ekman drift is the most likely main contributor of the onshore flow in Fig. 4.6a.

The QuikSCAT monthly averages show that such a pattern of northwestward wind is persistent during almost the whole year, reinforced in the austral winter (July/August/September) when the winds are stronger, and with the exception of the austral summer (January/February/March) when the winds are

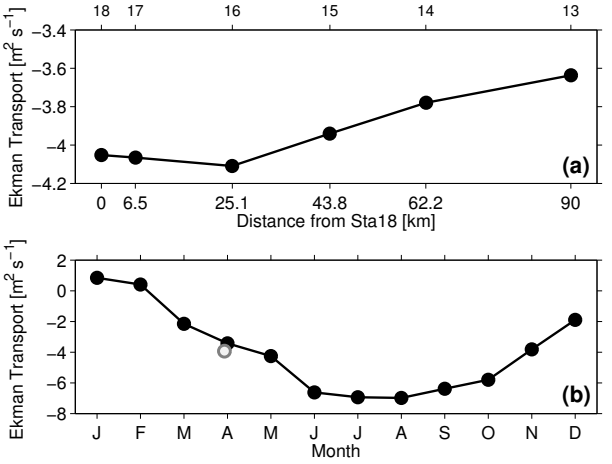

Figure 4.7: (a) Ekman Transport, per unit width, estimated with the wind stress from 25 to 31 March 2001, at every station. (b) Ekman Transport, per unit width, averaged for Sta18–Sta13 and calculated with the monthly climatological fields (2000-2009, black line and dots). The gray circle at the end of March represents an average of the values plotted in (a).

weaker. Fig. 4.7b shows the estimated monthly Ekman Transport (black line and black dots) compared to the mean Ekman Transport for the week from 25 to 31 March 2001 (gray circle). Mean values of -0.30 and -6.77 $m^2\ s^{-1}$ indicate reduced and strong Ekman transport during summer and winter, respectively. Autumn and spring present intermediate mean values of -4.76 and -3.83 $m^2\ s^{-1}$. Since downwelling-favorable winds are weaker in summer, one might also expect a reduced NMUC transport in this season.

4.6 DISCUSSION AND CONCLUSION

This paper presents the first observational evidence of a North Madagascar Undercurrent (NMUC). Our results describe a NMUC between 25 and 44 km wide, and at depths from around 300 to 1000 m limited by the bathymetry. Hugging the continental slope, the NMUC core is found with velocities higher than 0.7 m s^{-1}, at 460 m depth in the vicinity of Sta17 (about 13 km from the coast).

Its volume transport amounts to 3.8 Sv (3.1 Sv) for full-slip (no-slip) boundary condition. This value is comparable with the range of northward transport reported for the East Madagascar Undercurrent (see Fig. 4.1), which was estimated to be, on average, 1.33 (±1.41) Sv and with maxima up to 6 Sv (Pon-

soni et al., 2015a). However, the East Madagascar Undercurrent is found much deeper in the water column, since its core is placed at around 1300 m (Nauw et al., 2008; Ponsoni et al., 2015a), transporting intermediate waters (while the NMUC transports central waters). From their Transect T8, Nauw et al. (2008) showed an East Madagascar Undercurrent lying between the isopycnals of 27.2 and 27.75 kg m^{-3}, while the NMUC is enclosed by the isopycnals of 26.1 and 27.4 kg m^{-3}. Thermohaline properties reveal that the NMUC is mainly carrying South Indian Central Water.

Both temperature and salinity experience downwelling due to the Ekman Transport, which contribute to a NMUC being saltier and warmer than the surrounding offshore waters. Potential density increases in the offshore direction, while temperature and salinity decrease. Thus, density gradients are dominated by temperature gradients, while salinity gradients are playing an opposite role, attenuating the density gradients.

The velocity field indicates a strong baroclinic contribution to the NMUC (Sta17 and Sta16), while this geostrophic component appears weaker offshore (Sta15 and Sta14). Probably, this is because coastal processes such as downwelling attenuate farther offshore.

Results suggest that the alongshore winds participate in maintaining the density gradients and, consequently, the cross-shore baroclinic pressure gradient. Considering that the downwelling-favorable winds are markedly reduced in summer, one might expect a weaker (or perhaps absent) NMUC during this season. On the other hand, strong and persistent downwelling-favorable winds in winter, autumn and spring might indicate a well developed undercurrent.

Two other aspects of the hypothesis that the NMUC is driven by downwelling-favorable winds might be investigated in future observations. First, its southward extend, which should be limited to ∼15°S, the latitude equatorward of which the winds are downwelling-favorable (see Fig. 4.5). And, second, the presence of wind-forced anticlockwise propagating coastal trapped waves and the implied mean flow, which is the direction into which these waves propagate on the Southern Hemisphere and which should therefore be observable beyond Cape Amber, on the Western side of Madagascar (e.g., Middleton and Cirano (1999)).

This paper presents a new dynamical feature, the North Madagascar Undercurrent, through analysis of *in situ* data, in a poorly studied region. But, more important than these results are the new questions arising from this study. For instance, is the NMUC a persistent, or at least a recurrent undercurrent? What is its real spatial extent? Are there clear bands of spatio-temporal variability manifested in the NMUC? These questions have to be addressed in future work based on long term time series and finer spatial resolution.

5

BRAZIL CURRENT VARIABILITY: AN INDO-ATLANTIC TELECONNECTION

ABSTRACT

This chapter studies the variability of the Brazil Current (BC), as well as an energetic teleconnection between the western boundaries of the Indian and Atlantic Oceans. First, we validate a long-term altimeter-based time series of geostrophic velocity, by comparison with *in situ* measurements, for the BC. It presents a mean (standard deviation) alongshore velocity of -26.8(±12.8) cm s^{-1}, at surface levels. Two main bands of variability dominate the BC: (i) nearly annual, characterized by periods of 319–435 days, stronger near the BC core; (ii) nearly trimonthly (87–110 days), which dominates the offshore border of the current and has its origin linked to the Agulhas Current retroflection off Africa's southern tip.

In preparation, to be submitted to Geophys. Res. Lett.:
Ponsoni, L., I.C.A. da Silveira, B. Aguiar-González, B.M. de Castro and L.R.M. Maas, 2016. Brazil Current variability: a link with the Agulhas Current retroflection.

5.1 INTRODUCTION

The Agulhas Current (AC) is the strongest western boundary current of the southern hemisphere (Lutjeharms, 2006) and presents an important connection between Indian and Atlantic Oceans via its retroflection off Africa's southern tip, which releases anticyclonic eddies towards the Atlantic Ocean (Olson and Evans, 1986; Gordon et al., 1992). These eddies are named Agulhas Rings (ARs) and some of them migrate farther into the Atlantic Basin (Byrne et al., 1995).

While the AC is a well studied current with regards to long-term *in situ* observations of velocities (Beal et al., 2015), analogous studies of the South Atlantic western boundary flow, the Brazil Current (BC), are still lacking in literature. The BC is probably the least studied western boundary current regarding its velocity and variability patterns. Only a few studies hinge on *in situ* observations of velocity through quasi-synoptic surveys (e.g. da Silveira et al., 2004; Biló et al., 2014), and even less by means of continuous measurements (Rocha et al., 2014).

In this context, this study intends to cover two important aspects of the BC. First, we explore its main bands of variability based on ∼22 years of altimeter-derived geostrophic velocities, which are initially validated by one of the few time series of *in situ* measurements available for the BC. Second, we investigate whether the AC retroflection plays a role in the BC variability.

5.2 DATA AND METHODS

In this work we use a ∼22-year altimeter-based time series (from 01 January 1993 to 23 April 2015) of Absolute Dynamic Topography (ADT), Sea Level Anomaly (SLA), surface absolute geostrophic velocities and anomalies estimated from both ADT and SLA, respectively. These four variables are based on daily data from the "all sat merged" series of the delayed-time altimeter product, which is provided with a spatial resolution of 0.25°. The altimeter products were produced by Ssalto/Duacs and distributed by Aviso (`http://www.aviso.altimetry.fr/duacs/`), with support from Cnes. The ADT adds SLA to the New Mean Dynamic Topography (MDT-CNES-CLS13) produced by the CLS Space Oceanography Division as an estimate of the ocean sea surface height above the geoid for the 1993–2012 period (Rio et al., 2014).

The altimeter-based geostrophic velocities are validated for the BC, at the Santos Basin, by a time series of *in situ* measurements (Fig. 5.1) carried out in the scope of the project "Circulação Oceânica da Região Oeste do Atlântico Sul" (COROAS 3) (Campos et al., 1996, 2000). This time series spans from

Dec/1992 to Mar/1994 (with a gap between May/1993 to Jul/1993) and its processing is detailed in Rocha et al. (2014). Notice in Figs. 5.1c-d the good correspondence, quantified by a significant correlation coefficient of 0.64, between the altimeter-based absolute geostrophic velocity (gray line in Fig. 5.1d) and the *in situ* measurements (black line in Fig. 5.1d). For this cross-correlation, the hypothesis of no correlation was tested by use of the p-value test, where each p-value represents the probability of getting a true correlation (p-value = 0) by chance. The coefficient is significant, for a 95% confidence interval, when the p-value is smaller than 0.05.

The ARs released by the AC retroflection were tracked by using a newly developed global database in which ocean eddies are identified (Faghmous et al., 2015a,b). To assure that Faghmouth et al's algorithm is properly identifying the formation and propagation of ARs we made a composite analysis by inspecting every single day the conjointly plotted identified eddies and SLA field. Faghmous et al. (2015b) also provide the track of the eddies. However, we found some issues to use this dataset for our purpose, since at several instances the track of a single eddy breaks down and, consequently, distinct locations of origin and termination, as well as different tracks, are attributed to a single eddy. We also found this limitation in the eddy tracking dataset provided by Chelton. et al. (2011). To avoid this problem, we inspected individually the daily images at every time span. When the algorithm somehow misses the eddy, but the feature is still evident in the SLA field, we digitized the ring-like structure in order to keep the tracking. It is worth to mention that Faghmous et al's algorithm detects eddies independent of their water trapping ability. This is an important issue that will be discussed in Section 5.4.

Finally, a dataset of wind-driven global ocean circulation, computed by Shi et al. (2007), and presented in terms of Sverdrup stream function, is used in this work. These authors applied the Island Rule model (Godfrey, 1989) to monthly surface wind stress fields from NCEP reanalysis (Kalnay et al., 1996). This dataset is available at `http://eprints.usq.edu.au/1911/`.

5.3 RESULTS

5.3.1 *Velocities and variability of the Brazil Current*

The fact that the altimeter data are in good agreement with the *in situ* measurements (Figs. 5.1c-d) allows us to explore a long-term time series of remotely sensed data, in order to investigate the patterns of surface velocities and variability of the BC. It is worth to mention that, in the Santos Basin, the BC is a

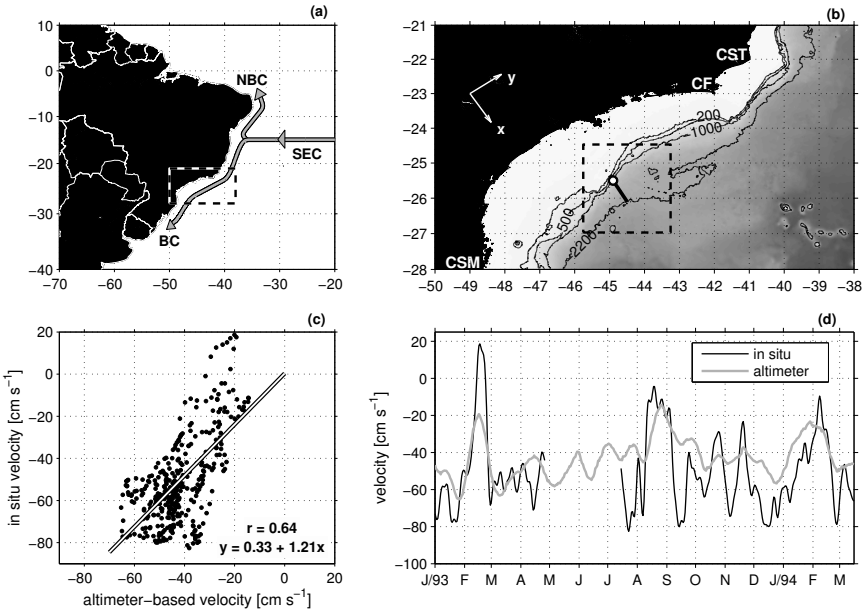

Figure 5.1: (a) Sketch of the surface western boundary currents off the Brazilian coast: Brazil Current (BC), North Brazil Current (NBC) and South Equatorial Current (SEC). (b) Region highlighted by the dashed square in panel (a). Acronyms indicate the geographical location of Cape of São Tomé (CST), Cape Frio (CF) and Cape of Santa Marta (CSM). The CF and CSM define the latitudinal limits of the Santos Basin. The white circle indicates the geographical location of the COROAS 3 mooring, while the black thick line represents a transect perpendicular to the isobaths/coast connecting the depths of 200 and 2200 m. The black dashed rectangle represents the area from where monthly averages of sea level anomalies are extracted (see Fig. 5.4a). (c) Scatter plot of the in situ *versus* the altimeter-based alongshore velocities, plotted in panel (d), for the period between Jan/1993 and Mar/1994. The correlation coefficient (r) and the best-fit line (and equation) are indicated. The alongshore component (v) is parallel to the y-axis, which is rotated clockwise 56° from North.

surface-intensified current, with level of no motion (0 cm s^{-1} isotach) at about 400 m (see Rocha et al. (2014), their Fig. 9a). Fig. 5.2 shows the long-term time series averaged over a cross-shore transect, connecting the isobaths of 200 and 2200 m (Fig. 5.1b), which represents a fair cross-shore scale for the BC in the Santos Basin (Rocha et al., 2014).

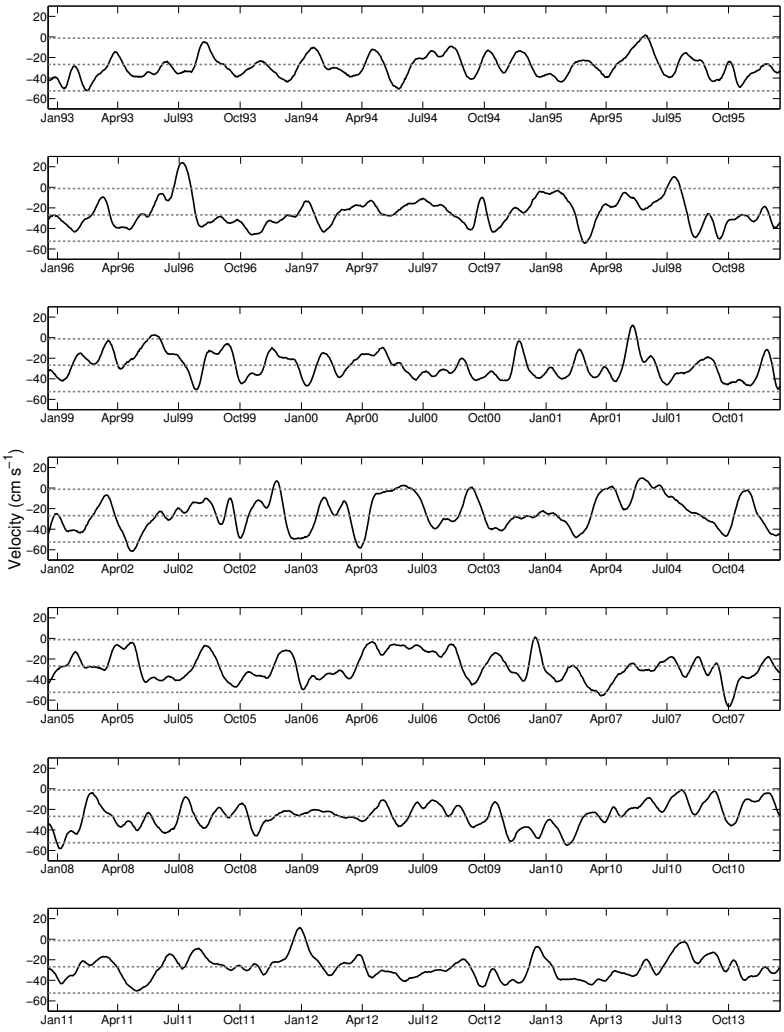

Figure 5.2: Alongshore geostrophic velocity based on altimeter observations and averaged over the transect highlighted in Fig. 1b, which is delimited by the isobaths of 200 and 2200 m. The dashed lines represent the average and two standard deviation from the average.

The long-term time series (8148 days) presents a mean (standard deviation) alongshore velocity of -26.8(±12.8) cm s^{-1}. The negative sign indicates poleward flow. The strongest velocities are registered around 15/Oct/2007, when the BC presents speeds up to -66.4 cm s^{-1}. Events of strong BC, for instance when the velocities are one (-39.6 cm s^{-1}) and two (-52.4 cm s^{-1}) standard deviations from the mean, are observed during 1205 and 119 days, respectively. Moments marked by a weak BC, also indicated by one (-14.0 cm s^{-1}) and two (-1.2 cm s^{-1}) standard deviations from the mean, are observed on 1353 and 217 days, respectively. On 178 days a reversal to equatorward flow is detected along the transect.

Overall, moments when the BC is strong are associated with the presence of anticyclonic eddies, since the poleward flow of their landward side increases the BC flow. The opposite is observed during the presence of cyclonic eddies, when the poleward flow is potentially attenuated or even reversed (Animation 5.1).

The spectral analyses applied to the altimeter-based geostrophic velocities, interpolated to every 1 km along the cross-shore transect, show an interesting pattern with a period of about one year dominating the inshore part of the current, while at its offshore border a nearly trimonthly period dominates (Fig. 5.3a). In Fig. 5.3b the spectral analysis is also applied to the transect-averaged time series, presented in Fig. 5.2.

From Fig. 5.3b, we define two remarkable spectral bands of variabilities (vertical gray bars): (i) nearly annual, comprised of periods of 319–435 days. This is selected as the power spectral band whose values are in excess of 7×10^3 cm^2 s^{-2} cpd^{-1}. (ii) nearly trimonthly, comprised of periods of 87–110 days and defined where the power spectral content is in excess of 3×10^3 cm^2 s^{-2} cpd^{-1}. A band pass filtered time series (forward-backward Butterworth filter) reveals that the combination of the annual (10%) and trimonthly (17%) periods explain about 27% of the total variance found for the 22-year altimeter-based velocities (Fig. 5.2).

5.3.2 *The annual period: regional eddies*

The monthly averages of absolute geostrophic velocity clearly highlight the BC's annual cycle, with a relatively stronger flow in austral summer compared to a weaker flow in winter (black line in Fig. 5.4a). From October to March (except December) absolute velocities are stronger than 29 cm s^{-1}. Weak poleward velocities are found from May to August (weaker than 24 cm s^{-1}), with a minimum in July when the BC has a speed of about 20 cm s^{-1}. If we take tri-

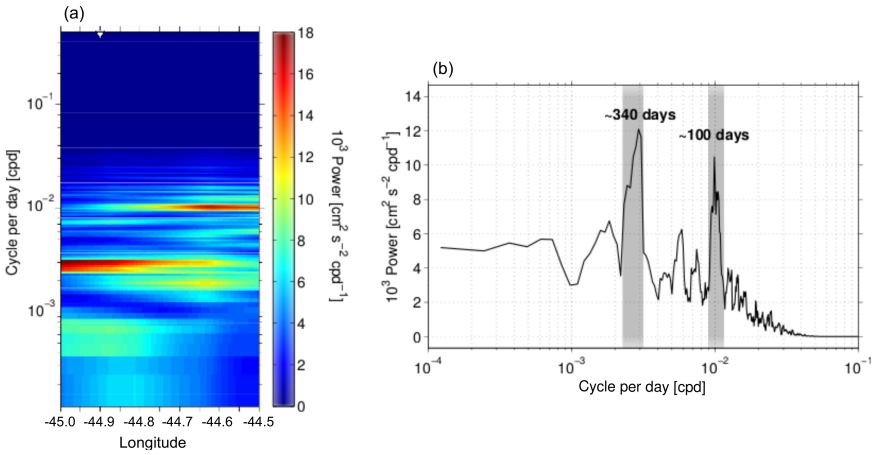

Figure 5.3: (a) Power spectral density of the altimeter-based geostrophic velocity interpolated along the transect plotted in Fig. 5.1b. (b) Same as (a), but applied to the altimeter-based geostrophic velocity averaged over the referred transect (time series presented in Fig. 5.2). The gray vertical bars highlight the nearly semi-annual period (318-435 days) and nearly trimonthly period (87-110 days). The power spectral densities were computed by a multitaper estimator (e.g., Percival and Walden (2006)).

monthly averages, representative for summer (Jan/Feb/Mar), autumn (Apr/-May/Jun), winter (Jul/Aug/Sep) and spring (Oct/Nov/Dec), the mean values are: -30.2, -24.3, -23.1 and -29.7 cm s^{-1}, respectively.

The gray line in Fig. 5.4a shows the monthly averages of SLA, calculated for the region highlighted by the dashed black rectangle in Fig. 5.1b, and roughly defined according to the scale of the eddies passing by our transect. This result reinforces the annual cycle with higher values of SLA from January to April, which implies stronger velocities, and smaller values from June to September. The seasonal averages are: 4.2 (summer), 3.4 (autumn), 1.2 (winter) and 2.9 cm (spring).

In the same vein, Fig. 5.4b shows a higher number of days when cyclonic eddies are identified by Faghmous et al. (2015b) within the defined region during austral winter, while a reduced number of anticyclonic eddies are observed in summer. For instance, for all months of June, July and August over the 22-year period, cyclonic and anticyclonic eddies are detected in the referred region on 1347 days and 911 days, respectively. However, during the months of December, January and February this difference reduces, and cyclonic and anticyclonic eddies are observed on 1195 and 1151 days, respectively. As suggested

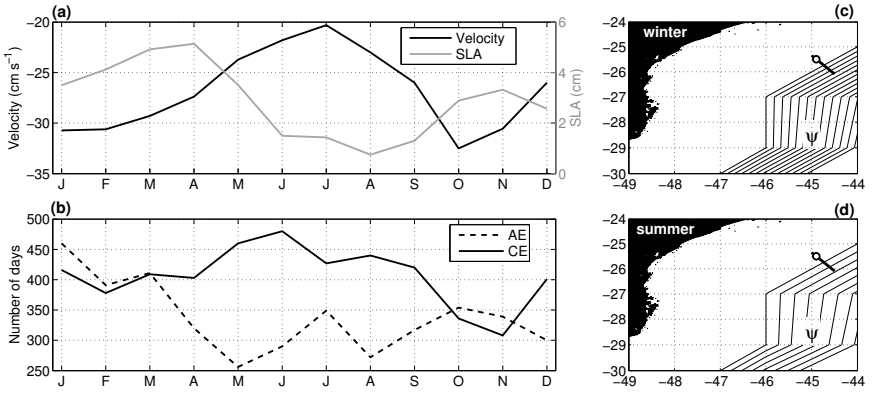

Figure 5.4: (a) Monthly average of the altimeter-based geostrophic velocity (black line) and monthly average of sea level anomaly extracted from the region demarcated by the dashed rectangle in Fig. 5.1b. (b) Total number of days per month when cyclonic (black full line) and anticyclonic (black dashed line) eddies were observed within the region delimited by the dashed rectangle plotted in Fig. 5.1b. (c–d) Isolines of Sverdrup stream function (ψ) from Shi et al. (2007) for winter (c) and summer (d), respectively. Both panels present the same spacing between two adjacent isolines.

in Animation 5.1 (supplemental material), the majority of the cyclonic eddies are generated regionally, upstream the Santos Basin, at the region of Cape of São Tomé (∼22°S) and Cape Frio (∼23°S), where the Brazilian coast changes its orientation from north–south to northeast–southwest (see Fig.5.1b).

The wind-driven circulation, represented by the maps of Sverdrup stream function (ψ) provided by Shi et al. (2007), also suggests an annual cycle. However, in contrast to the results presented above, the wind driven-circulation prescribes a BC that is stronger in austral winter (Fig. 5.4c) and weaker in summer (Fig. 5.4d). Notice in Fig. 5.4c-d that the cross-shore gradients of ψ are proportional to the intensity of the poleward alongshore flow ψ ($\frac{\partial \psi}{\partial x} = -v$).

5.3.3 *The trimonthly period: a link with the Agulhas Current retroflection*

The results show that the ∼100-day period has its origin in the region of retroflection of the AC (Fig. 5.5). Spectral analyses applied to the long-term time series of SLA (from the Aviso grid, 0.25°×0.25°) in the South Atlantic, averaged over the band of periods of 87–110 days (defined by the right vertical gray bar in Fig. 5.3b), show a clear westward oriented corridor of this band of variability (Fig. 5.5a), propagating its phase from the retroflection

area towards the Santos Basin near the Brazilian Coast (Fig. 5.5b). The phase propagation in Fig. 5.5b, represented by a cyclic color scale, indicates a repetition and hence a zonal length scale of approximately 450 km. Notice the decay in phase coherency, especially to the south of the corridor.

The AC retroflection and the release of ARs is a rather complex oceanographic phenomenon at its origin (Goni et al., 1997; van Aken et al., 2003). Through the animations presented as supplemental material (Animation 5.2) to this paper, it is possible to notice that after detaching from the AC, some anticyclonic rings propagate westward, while others remain quasi-steady, merging with other rings, or are reincorporated into the retroflection and, eventually, are released again westward.

Fig. 5.5c shows the track of the ARs identified by Faghmous et al. (2015b), which detached from the retroflection and followed a westward course, crossing the 0° meridian. From Jan/1993 to Apr/2014, the Faghmous et al.'s data reveal about 85 rings crossing this longitude, representing an average of ∼4 ARs year^{-1}. Notice also that the eddies travel within the highly energetic corridor displayed in Fig. 5.5a.

Fig. 5.5d indicates that the rings lose strength and dissipate as ring-like features on their way to the South Atlantic western boundary.

5.4 DISCUSSION AND CONCLUSIONS

The results presented in this paper show a good match between *in situ* velocity and altimeter-based absolute geostrophic velocity derived from satellite. This is in agreement with recent results for the South Indian western boundary current at similar latitudes, the East Madagascar Current (EMC), presented by Ponsoni et al. (2016). Based on 2.5 years of mooring observations, these authors also found a correspondence between *in situ* and altimeter data, which allowed them to explore the variability of the EMC through the long-term altimeter data.

A marked difference between the BC and EMC is related to the arrival of cyclonic eddies. In both cases this vortical structure attenuates the flow of the currents. At several moments the BC flow reverses and becomes equatorward (12 moments in 22 years), while this scenario is not often observed in the EMC (only 2 short periods in 21 years, Fig. 15 from Ponsoni et al. (2016)). There are two potential explanations for recurrent reversals in the BC due to the arrival of cyclonic features. First, because of the strength of the "newborn" eddies impinging on the current at the Santos Basin, which have their origin relatively close to our region of study (see Fig. 5.1b), around Cape Frio (∼23°)

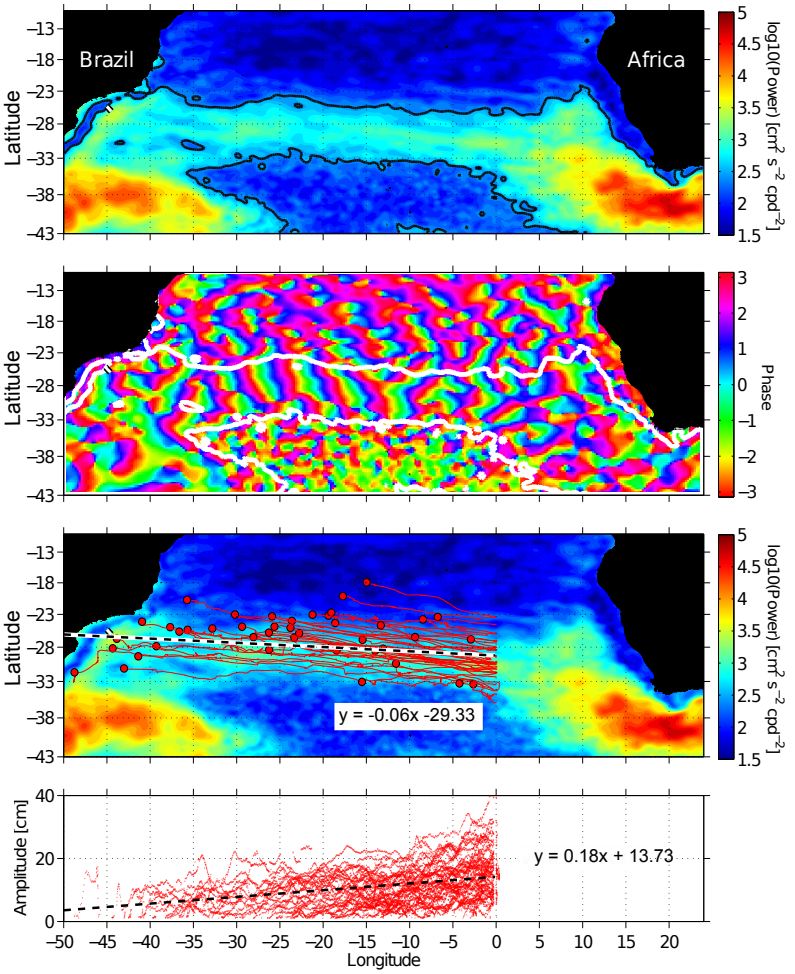

Figure 5.5: (a) Power density applied to every (0.25°×0.25°) time series of SLA (normalized by the mean and detrended) and averaged over the nearly trimonthly period (87–110 days). The black contour highlights the region in which the mean power spectral density is higher than $\log_{10}(\text{Power}) = 2.5$. (b) Phase (represented by cyclic color scale) extracted from the spectral density analysis for the period of 100 days. The white contour is the same as the black contour in (a). (c) Tracking of the ARs (identified by Faghmous et al. (2015b)) towards the South Atlantic western boundary. For clarity, we plotted only the eddies tracked in the period between between Jan/1993 and Jun/2004. (d) Amplitude of the ARs, plotted in (c), at different longitudes. Equations presented in (c) and (d) indicates the linear regression of the tracks' latitudes and amplitudes (y) in terms of longitude (x), respectively.

and Cape of São Tomé (∼22°S) (Calado et al., 2006; da Silveira et al., 2008). Second, because the BC is a relatively shallow and weak western boundary current compared to its analogs in the South Indian. Its weakness is evident from the fact that the level of no motion between the BC and the counterflow imposed by the Intermediate Western Boundary Current (Boebel et al., 1999; Legeais et al., 2013) is found around 400 m in the Santos Basin. By contrast, in the South Indian Ocean this transitional level between surface currents and undercurrents, represented by the interfaces EMC–East Madagascar Undercurrent (Ponsoni et al., 2015a) and AC–Agulhas Undercurrent (Beal, 2009), are found deeper in the water column, at about 1000 m.

The spectral analysis of the surface geostrophic velocity suggests two main bands of variabilities in the BC (Fig. 5.3): (i) nearly annual, defined by periods of 319–435 days; and (ii) nearly trimonthly, characterized by periods of 87–110 days.

Taking into account that the wind field also presents a marked annual cycle over the Atlantic Basin (Hellerman and Rosenstein, 1983), this forcing is the first candidate to explain this band of variability in the BC, due to the return flow of the Sverdrup circulation. In this sense, Mayer and Weisberg (1993) described the nature of the Atlantic Ocean wind-driven circulation and also found a marked annual cycle, but with Sverdrup return flow stronger in austral winter. This result is in agreement with the stronger cross-shore gradients in the Sverdrup stream function computed by Shi et al. (2007) (Figs. 5.4c-d). Additionally, our further analysis, by applying Stommel's model to Hellerman and Rosenstein's climatology, also suggests a stronger BC in winter (not shown). Surprisingly, the altimeter data reveal the opposite, i.e., a stronger BC in summer. Again, the likely explanation for this difference is related to the larger number of cyclonic eddies passing by the Santos Basin during winter (Fig. 5.4b), attenuating the BC flow. Further work is necessary to understand why there are more cyclonic eddies arriving at the Santos Basin in austral winter compared to summer.

Our tracking of Agulhas Rings shows that ∼4 year^{-1} of these features cross to the western part of the South Atlantic, suggesting a possible link with the trimonthly period identified in the BC.

The ARs lose strength on their trip towards the South Atlantic western boundary (Byrne et al. (1995)). Although the ARs rarely collide with the BC domain as a ring-like structure, the anomalies in sea level generated during the Agulhas retroflection follow their trip to the western boundary in a well-defined, highly energetic corridor of variability (Fig. 5.5a-c), and they play an important role in the bands of oscillations of the Brazil Current as suggested above, modulating at a nearly trimonthly period. Notice in Fig. 5.5a that this variabil-

ity seems to be more prominent farther west, up to the offshore border of the BC, reinforcing the results shown in Fig. 5.3a.

As already pointed out by Chelton et al. (2007), not specifically to the Agulhas Rings but based on global observations of large oceanic eddies, the anticyclonic eddies tend to deflect towards the equator while they migrate westward at approximately the phase speed of nondispersive baroclinic Rossby waves. For a wave length of $\lambda = 450$ km, the dispersion expected for nondivergent westward propagating Rossby waves is about $\omega \approx -\beta/k = -1.42\times10^{-6}$ s^{-1} [$\mathcal{O}(10^{-6})$]. If we calculate the frequency resulting from the $T = 100$ days period (Fig. 5.5b), $2\pi/T$, a similar absolute value of 7.2×10^{-7} s^{-1}, also $\mathcal{O}(10^{-6})$, is found. In addition, the length scale of the rings is close to a typical internal Rossby deformation radius, estimated to be ~35 km for a two-layer ocean (with density difference of 1.5 kg m^{-3} and upper layer depth of 500 m) along the corridor of trimonthly variability (Fig. 5.5a). This radius is in agreement with the values proposed by Houry et al. (1987).

Nevertheless, distinguishing Rossby waves from eddies is a complicated task which requires both *in situ* and satellite measurements. It has already been shown that some ARs are entities which transport relatively warm and salt waters from the Indian to the Atlantic Ocean, establishing an important link to the global overturning circulation (e.g. Gordon et al., 1992; van Aken et al., 2003). On the other hand, it has also been shown that many of the so-called “eddies" in the global ocean do not truly qualify as Lagrangian coherent structures (Beron-Vera et al., 2008; Samelson, 2012), since they are not invariant to addition of a background flow and do not have water trapping ability, and hence they can not be expected to represent a water mass transport mechanism.

Indeed, based on a geodesic transport theory applied to altimeter-derived velocities, Beron-Vera et al. (2013) have shown some ARs preserving their material coherence for months, effectively trapping and transporting water. According to these authors, by contrast, other ARs “candidates" spotted by SLA-based algorithms of eddies identification (e.g. Faghmous et al., 2015a) do not behave as a Lagrangian coherent structure. As a consequence, Beron-Vera et al. (2013) suggested that the Agulhas leakage is actually overestimated by one order of magnitude.

Therefore, taking into account our results and the discussion above, this study raises the question whether ARs (or most of them), identified from the SLA fields, are not simply part of a (nearly) westward propagating Rossby wave? In other words, is the corridor, instead of acting as a mass-conveyor, in fact perhaps operating mainly as an energetic pathway for Rossby waves that are forced by periodic oscillatory motions of the retroflecting AC and that are traversing the Atlantic and impinging on the BC? Or are we looking at a

mixture? Do ARs (or at least some of them) ride on Rossby waves? (Polito and Sato, 2015). These topics will be addressed in detail in future work.

6

SOUTH INDIAN TROPICAL GYRE: AN INDO-PACIFIC TELECONNECTION

ABSTRACT

Based on satellite altimeter data and global atlases of temperature, salinity, wind stress and wind-driven circulation we investigate the seasonal variation of the South Indian tropical gyre and its associated open-ocean upwelling system, known as the Seychelles–Chagos Thermocline Ridge (SCTR). Results show a year-round, altimeter-derived cyclonic gyre where the upwelling regime appears closely related to seasonality of the ocean gyre, a relationship that has not been previously explored in this region. An analysis of major forcing mechanisms suggests that the thermocline ridge results from the constructive interaction of basin-scale wind stress curl, local-scale wind stress forcing and remote forcing driven by Rossby waves of different periodicity: semi-annual in the west, under the strong influence of monsoonal winds; and, annual in the east, where the southeasterlies prevail. One exception occurs during winter, when the well-known westward intensification of the upwelling core, the Seychelles Dome, is shown to be largely a response of the wind-driven circulation. At basin-scale, the most outstanding feature is the seasonal shrinkage of the ocean gyre and the SCTR. From late autumn to spring, the eastward South Equatorial Countercurrent (SECC) recirculates early in the east on feeding the westward South Equatorial Current, therefore closing the gyre before arrival to Sumatra. We find this recirculation longitude migrates over 20° and collocates with the westward advance of a zonal thermohaline front emerging from the encounter between (upwelled) Indian Equatorial Water and relatively warmer and fresher Indonesian Throughflow Water. We suggest this front, which we call the Indonesian Throughflow Front, plays an important role as remote forcing to the tropical gyre, generating southward geostrophic flows that contribute to the early recirculation of the SECC.

This chapter has been published as:
B. Aguiar-González, **L. Ponsoni**, H. Ridderinkhof, H.M. van Aken, W.P.M. de Ruijter and L.R.M. Maas, 2016. Seasonal variation of the South Indian tropical gyre. *Deep-Sea Res. I* 110, 123–140.

6.1 INTRODUCTION

The South Indian tropical gyre is of special importance as it receives and redistributes water masses from the Indonesian Throughflow (ITF), a remote source of Pacific Ocean water that represents a key component in global ocean circulation as the only low-latitude connector between the world oceans (de Ruijter et al., 1999; Gordon, 2001; Valsala and Ikeda, 2007; Le Bars et al., 2013).

Nevertheless, although much effort has been devoted to the seasonal variability of the Tropical South Indian Ocean (TSIO), this tropical gyre is still not well understood. The South Indian tropical gyre expands south of the equator, and down to 18°S, from the eastern coast of Africa to the western coasts of Sumatra and Java (Fig. 6.1). Its complexity is mainly a response to its unique location. On the one hand, the TSIO is influenced by the semi-annual Indian monsoon between the Equator and 12°S, and by the persistent southeasterly trades between 12°S and 16°S (see Schott and McCreary Jr. (2001) & Schott et al. (2009) for a review); on the other hand, it is fed by an annual inflow of remote origin, the ITF (Woodberry et al., 1989; Gordon et al., 1997; Yokoi et al., 2008; Le Bars et al., 2013).

Concomitant with a large-scale cyclonic circulation, an upwelling regime is in most cases found, where the upward displacement of the isotherms sustains an associated geostrophic flow. In the southwest TSIO, the presence of an upwelling region was first reported in model data by Woodberry et al. (1989) and McCreary et al. (1993), who attributed the large-scale upwelling to dominant negative wind stress curl present throughout the year. Later, Donguy and Meyers (1995) observed that the eastward South Equatorial Countercurrent (SECC) and the westward South Equatorial Current (SEC) flow cyclonically around a low in surface dynamic height at about 50°E–65°E, 7°S–8°S in the western basin, hence connecting the surface cyclonic circulation to a dome-like feature in the thermocline.

More observations and model studies have been added supporting the existence of this dome centered in the west, known as the Seychelles Dome (SD). On occasions this dome extends eastward as a ridge, where it gets connected to another minimum in the thermocline depth at about 90°E, 11°S (Masumoto and Meyers, 1998; Feng and Meyers, 2003; Saji et al., 2006). Owing to its elongated shape and location, Hermes and Reason (2008) termed this feature the Seychelles–Chagos Thermocline Ridge (SCTR). In their modelling simulations, Hermes and Reason (2008) found that this thermocline ridge is present throughout the year, although it is more well-defined and stronger during cer-

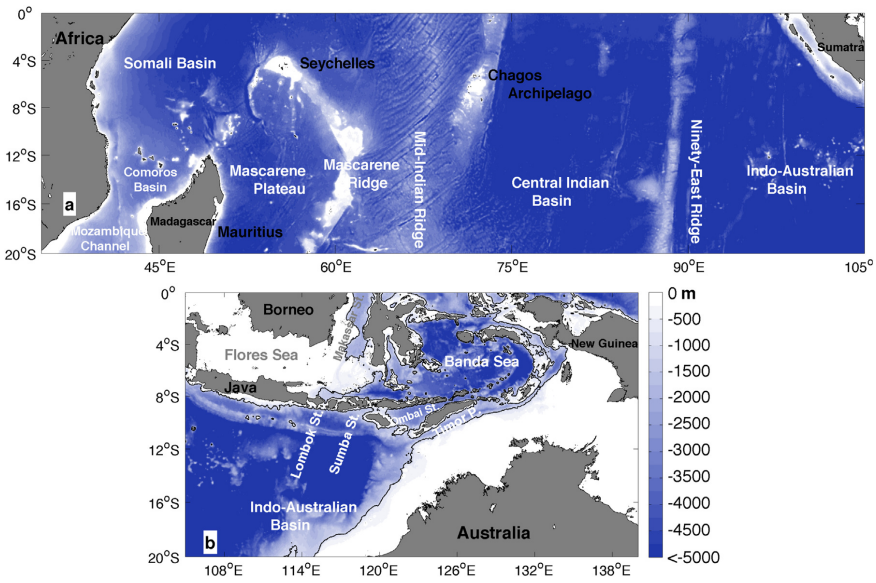

Figure 6.1: Ocean bathymetry in meters depth with labels indicating major topographic features and islands in (a) the tropical South Indian Ocean and (b) the Indonesian Seas. Bathymetry is derived from the ETOPO1 topography data set (Amante and Eakins, 2009).

tain periods (March–August) with a noticeable intensification in the west, especially from June to August.

Several authors have also noted that, locally, there are areas of strong upwelling which do not coincide with regions of strong negative wind curl (Woodberry et al., 1989; McCreary et al., 1993; Masumoto and Meyers, 1998), suggesting that other forcing mechanisms must be contributing to the rise and descend of the thermocline. Masumoto and Meyers (1998) suggested that the large-scale wind stress curl interacts with Rossby waves radiating from the east and that these waves modify the local wind-driven upwelling. Based on modelling results, Hermes and Reason (2008) postulate that the depth of the thermocline ridge appears to result from a more complex interaction among basin-wide wind stress curl, local-scale wind stress forcing, annual Rossby waves and the variation of the speed of these waves with latitude. Nevertheless, one dominant feature of the SCTR remains unresolved, namely its weakening throughout the year as a thermocline ridge, evolving to a western-intensified dome during winter. Concerning this, Xie et al. (2002) imply that the upwelling site is mainly focused in the west owing to a western intensification of the ocean

gyre. However it has not been shown yet whether or not the wind-driven Sverdrup circulation would account for this feature. We will address this issue here.

Another striking pattern exists regarding the upper circulation of the tropical gyre. Modelling studies show that the eastward SECC vanishes at the surface during austral winter (McCreary et al., 1993; Song et al., 2004; Hermes and Reason, 2008; Schott et al., 2009), even though the upwelling is reported to be active meanwhile (Hermes and Reason, 2008). It is argued that during this season the SECC is subsurface, masked by overlying westward Ekman currents, hence leading to the view of a non-persistent ocean gyre at the surface. Within this context, the recent improvement on the estimates of altimeter-derived equatorial semi-geostrophic velocities (SSALTO/DUACS, 2015) combined with a global atlas of ocean temperature and salinity, provides us with an unprecedented opportunity to study the upwelling ridge and the overlying (semi-)geostrophic circulation of the ocean gyre based on long-term observations.

Along the eastern boundary of the tropical gyre, the inflow of Pacific water rises as one of the most intriguing players. Beyond feeding the westward SEC with source waters (Gordon et al., 1997; Le Bars et al., 2013), and partially recirculating into the eastward Eastern Gyral Current (EGC) (Menezes et al., 2013), not much is known about the immediate impact that buoyancy fluxes, introduced by low density throughflow waters, may have on the recirculation regime of the ocean gyre. While Woodberry et al. (1989) already suggested that the circulation in the eastern basin is most likely affected by the ITF, Yokoi et al. (2008) explicitly included and discussed in their modelling study the remote forcing that throughflow waters exert over the upwelling system. These authors found that the annual contribution of the ITF always promotes downward vertical velocities, although the amplitude of the seasonal cycle was shown to be smaller compared to that of Ekman vertical velocities. Following these results, Yokoi et al. (2008) postulate that if the ITF were shut down, one could expect that the Seychelles Dome would become even shallower (cf. Hirst and Godfrey (1993); Lee et al. (2002)). Accordingly, one may reasonably think that the ITF contribution may become stronger over the eastern part of the gyre, close to the exit of Pacific Ocean water. However, to the knowledge of the authors, this has not been further investigated from observations.

The two main goals of this study are (1) to provide a comprehensive, modern view of the seasonal upper circulation of the South Indian tropical gyre; (2) to assess the relative contribution of the basin-scale, local and remote forcing to observed modes of variability of the South Indian tropical gyre and its associated upwelling system. To achieve these goals we use open access data sets: the atlas Scatterometer Climatology of Ocean Winds (SCOW) by Risien

and Chelton (2008); a wind-driven ocean circulation atlas of the Sverdrup Streamfunction computed by Shi et al. (2007) using the island rule; 22 years of satellite altimeter observations (1993–2014) (SSALTO/DUACS, 2015); and, a global atlas of temperature and salinity (CARS09) (Ridgway et al., 2002; Condie and Dunn, 2006).

The paper is organised as follows. Data sets and methodology are presented in Section 6.2. In Section 6.3, the seasonal variation of the South Indian tropical gyre is analyzed based on the basin-scale wind stress curl, the barotropic wind-driven circulation and the altimeter-derived geostrophic circulation. Throughout this section, seasonality of the Seychelles–Chagos Thermocline Ridge is shown to be related to seasonality of the ocean gyre. In subsequent sections, driving forces different from the basin-scale wind stress curl are explored. Section 6.4 analyzes the local wind stress forcing. Sections 6.5 and 6.6 investigate the impact of Rossby waves and the Indonesian Throughflow as remote forcing, respectively. A discussion of main findings and conclusions are presented in Section 6.7.

6.2 DATA AND METHODS

6.2.1 *Wind data*

6.2.1.1 *Wind stress and wind stress curl*

Seasonal climatologies of the wind circulation are based on monthly wind stress and wind stress curl fields estimated from the 8-year record (September 1999–August 2007) of wind measurements by the NASA Quick Scatterometer (QuikSCAT). These fields are provided as part of the atlas Scatterometer Climatology of Ocean Winds (SCOW) at `http://cioss.coas.oregonstate.edu/scow/`. For details on the processing of the QuikSCAT wind fields, the reader is referred to Risien and Chelton (2008).

Because the monsoon regime, a dominant feature of the wind circulation in the Northern Hemisphere, is also noticeable in tropical latitudes of the Southern Hemisphere (Tchernia, 1980; Schott and McCreary Jr., 2001), we define austral seasons for all data sets used in this work with semi-equivalence to the monsoon regime such as (1) summer or northeast monsoon (January–February–March); (2) autumn or southwest intermonsoon (April–May–June); (3) winter or southwest monsoon (July–August–September); and (4) spring or northeast intermonsoon (October–November–December).

6.2.1.2 *Wind-driven Sverdrup circulation*

The strength, shape and location of the ocean gyre is investigated based on the atlas of the barotropic Sverdrup Streamfunction computed by Shi et al. (2007) from the NCEP Reanalysis winds, with the Indonesian Throughflow Passage open in a quasi-realistic topographic setting. The dataset is available at the TPAC (Tasmanian Partnership for Advanced Computing) website.

For the interior ocean, the stream function ψ is determined by the Sverdrup relationship:

$$\beta \frac{\partial \psi}{\partial x} = \frac{curl \boldsymbol{\tau}}{\rho_0}, \tag{6.1}$$

where the planetary vorticity, β, is the meridional gradient of the Coriolis parameter ($\beta = \partial f / \partial y$); $curl\boldsymbol{\tau}$, is the vertical component of the curl of the wind stress vector, $\boldsymbol{\tau} = (\tau_x, \tau_y)$, such that $curl\boldsymbol{\tau} = (\partial \tau_y / \partial x) - (\partial \tau_x / \partial y)$; x and y are the eastward and northward spatial coordinates, respectively; and, ρ_0 is the mean water density. The flow along the western boundary, where the Sverdrup relationship breaks down, is calculated using the island rule for flows around an island (Godfrey, 1989; Pedlosky et al., 1997). There, the island transport stream function ψ_0 is determined by the pressure head between the island's northern and southern extremities, and follows the integral of the wind stress along a closed path c as

$$\psi_0 = \frac{1}{f_n - f_s} \oint_c \frac{\boldsymbol{\tau}.\, \boldsymbol{t}}{\rho_0} dc, \tag{6.2}$$

where f_n and f_s are the Coriolis parameters at the northern and southern tips of the island, $\boldsymbol{t}$ is a unit vector parallel to the integration path, c. For the Madagascar case, the closed integration path, c, is from the eastern boundary of the Indian Ocean basin (west coast of Australia), westwards along the latitude of the northern tip of Madagascar, down the island's west coast, then eastward across the basin at the southern latitude of the island (reaching again the west coast of Australia) and up the eastern margin to the starting point.

6.2.1.3 *Ekman vertical velocity*

The contribution from the local wind stress is evaluated with a set of seasonal climatologies of the vertical velocity driven by the wind stress forcing, referred

to as Ekman vertical velocity, w_E. At the base of the surface Ekman layer, w_E is computed following

$$w_E = \frac{1}{\rho_0}\, curl\left(\frac{\boldsymbol{\tau}}{f}\right) = \frac{1}{\rho_0 f}\, curl\boldsymbol{\tau} + \frac{\beta}{f^2}\tau_x, \tag{6.3}$$

where w_E is caused by two wind forcing terms: one contribution that is proportional to the wind stress curl (first term on the right-hand side); and, the other contribution that is proportional to the planetary vorticity and the zonal wind stress, τ_x (second term on the right-hand side). For brevity in the text, we refer to the former as the $curl$ contribution and to the latter as the β contribution. Positive (negative) w_E indicate upward (downward) velocities.

The Ekman model breaks down close to the equator, where f approaches zero. Therefore estimates of Ekman vertical velocity closer to the equator than 5°S must be interpreted carefully. However, in order to have a qualitative hint as close as possible to the equator, we only mask here values of w_E between the equator and 3°S.

6.2.2 *Satellite altimeter data*

The Absolute Dynamic Topography (ADT) data used in this study are the latest version (Duacs 2014, v15.0 version) of merged and gridded satellite altimeter observations for the period 1993–2014 produced by SSALTO/DUACS and distributed by AVISO with support from CNES. The ADT is the result of adding Sea Level Anomaly (SLA) to the New Mean Dynamic Topography (MDT_CNES-CLS13; Rio et al. (2014)) produced by the CLS Space Oceanography Division as an estimate of the ocean sea surface height above the geoid for the 1993–2012 period. We use the 'All sat merged' Series of ADT, which consist of a data set of daily maps on a $1/4°$ Cartesian grid where all missions available are considered and observations from up to four satellites at a given time are merged (Ducet et al., 2000).

6.2.2.1 *Altimeter-derived geostrophic and semi-geostrophic velocities*

Altimeter-derived velocities are based on the assumption of a geostrophic balance, i.e. a balance between Coriolis force and pressure gradient force. Sur-

face geostrophic velocities are then computed from maps of ADT following the geostrophic relation:

$$u = -\frac{g}{f}\frac{\partial h}{\partial y}, \qquad v = \frac{g}{f}\frac{\partial h}{\partial x}, \tag{6.4}$$

where u is the zonal velocity (positive in the eastward direction); v is the meridional velocity (positive in the northward direction); h, is the ADT; and, g, the gravitational acceleration.

A novel aspect in the present analysis is the inclusion of equatorial current systems, covering a geographical area traditionally avoided in the literature of altimeter-based studies. Within (5°N–5°S), the estimation of geostrophic velocities requires a special treatment as the Coriolis force vanishes at the Equator ($f = 0$). Previous theoretical and observational works (Moore and Philander, 1977; Lukas and Firing, 1984; Picaut et al., 1989) suggest that the equatorial β-plane approximation provides estimates of equatorial semi-geostrophic velocities which are in good agreement with measured velocities. In former altimeter-derived products, the numerical scheme used to solve the derivatives in the (semi-) geostrophic equations introduced a sharp transition near the Equator, where equatorial semi-geostrophic velocities were discontinuous with off-equatorial geostrophic velocities due to the impact of the anisotropy on the grid resolution. This problem often ended with a mask over the Equator in most of the altimetry-based studies. The AVISO altimeter products released in April of 2014 (SSALTO/DUACS, 2015) apply a new technique presented in Lagerloef et al. (1999), which smoothes the previous discontinuity observed between equatorial and off-equatorial velocities, and improves the consistency between altimeter products and drifter observations.

For discussion in this work, climatologies of altimeter-derived horizontal velocity fields (u, v) are presented as their seasonal averages over the period 1993–2014.

6.2.2.2 *Altimeter-derived geostrophic volume transport*

The annual cycle of the ITF geostrophic transport is computed from two different data sets. First, the annual cycle is obtained from monthly averages of 22 years of satellite altimeter measurements assuming that derived surface geostrophic velocities can be considered constant over at least the first 10 m of the water column. And, second, the annual cycle is computed from geostrophic velocities referenced to a level of no motion using the thermal wind relation and a global atlas of temperature and salinity. The latter approach is detailed

in the next section. In both cases, the annual cycle is presented in terms of monthly zonal geostrophic transport. As will be shown, results support each other.

In a meridional section, the zonal geostrophic transport carried by the ITF in the upper 10 m is computed as

$$U(x_i) = \int_{y2}^{y1} \int_{z_2}^{z_1} u \, dz dy, \tag{6.5}$$

where U is the geostrophic volume transport in Sverdrups (1 Sv $= 10^6\ m^3\ s^{-1}$); $y_1 = 10.25°$S and $y_2 = 14.5°$S are the latitudinal boundaries of integration; $z_1 = 0\ m$ and $z_2 = -10\ m$ set the vertical range of integration; and, x_i (i=1,2,3,4) are the longitudes of the meridional transects T1–T4 used for computation and spatial average of the ITF geostrophic transport, positioned at $x_1 = 117.5°E$, $x_2 = 118°E$, $x_3 = 118.5°E$, $x_4 = 119°E$ (indicated in Fig. 6.4c).

In order to prevent masking the variability of the ITF geostrophic transport, special attention is given to the meridional extent of T1–T4 due to spatial closeness to the eastward Eastern Gyral Current. For this reason, T1–T4 do not cross the Indo-Australian Basin entirely but end at about the latitude where a flow reversal is observed between the westward ITF and the eastward Eastern Gyral Current. Furthermore, the latitude of flow reversal selected here as southern boundary for volume transport integration ($y_2 = 14.5°$S) agrees well with observational results obtained by Wijffels et al. (2008) for a similar meridional transect, the IX22 line in the Indo-Australian Basin.

6.2.3 *Global atlas of temperature and salinity*

For the study of the thermohaline distribution of the tropical gyre, the annual cycle of the thermocline depth, and the impact of buoyancy fluxes introduced by the Indonesian Throughflow, we use a temperature and salinity annual mean and seasonal atlas, the CSIRO (Commonwealth Scientific and Industrial Research Organisation) Atlas of Regional Seas (CARS09) version 2011.1.0 (Ridgway et al., 2002; Condie and Dunn, 2006).

CARS09 is based on a set of quality-controlled vertical profiles of in situ measured ocean water properties (temperature (T), practical salinity (S), oxygen, nitrate, silicate, and phosphate) which originate from different sources, including: the Argo global archives up to May 2009; the World Ocean Database 2005; the WOCE (World Ocean Circulation Experiment) hydrographic data;

the profiles from TAO/TRITON (Tropical Atmosphere Ocean/Triangle Trans-Ocean Buoy Network) Array moorings; the CSIRO Marine and Atmospheric Research and the New Zealand National Institute of Water and Atmospheric Research archives (Condie and Dunn, 2006). Most of these data were collected between 1950 and 2008.

The gridded fields have a horizontal grid resolution of $1/2^\circ \times 1/2^\circ$ at 79 standard depths from the sea surface to 5500 m, covering the region 0°E and 360°E and 75°S and 90°N. Annual harmonics are defined down to 1800 m and the semi-annual down to 1000 m.

6.2.3.1 *Referenced geostrophic velocities*

We investigate ocean currents at thermocline depths by computing geostrophic velocities referenced to a level of no motion using the thermal wind relationship,

$$\frac{\partial u}{\partial z} = \frac{g}{f}\frac{\partial \rho}{\partial y}, \qquad \frac{\partial v}{\partial z} = -\frac{g}{f}\frac{\partial \rho}{\partial x} \tag{6.6}$$

where the vertical shear of geostrophic velocities are related to horizontal gradients of density, ρ, and so to the horizontal gradients of temperature and salinity. Subsequently, the horizontal velocity field $(u(z),\ v(z))$ is computed by integrating Eq. (6.6) upward from a reference level of assumed no motion (z_{ref}). In this work we use $z_{ref} = -1800$ m.

Based on water mass properties, Stramma and Lutjeharms (1997) found that density surface σ_2=36.94 (depth range 1500–2500 m) in the Indian Ocean is an adequate reference level, z_{ref}, for the geostrophic computation in the subtropical region, north of 40°S. This surface lies below the oxygen minimum layer and above the Circumpolar Deep Water (Stramma and Lutjeharms, 1997). Concerning this, Menezes et al. (2014) found a good correspondence between estimates of referenced geostrophic velocities at the surface, based on different levels of no motion (at 1000 db, 1500 db, 1950 db and 3000 db), and altimeter-derived geostrophic velocities within 10°S–35°S.

Our region of interest extends here farther north, to the tropical South Indian Ocean. Nevertheless, computation of referenced geostrophic velocities performed with z_{ref} at different levels within the range of depths of discussion provides similar results (not shown) also for the remaining region of the TSIO, i.e. 2°S–10°S. Thus, the choice of z_{ref} in the discussed depth range appears not to affect the analysis presented in this work.

We use here z_{ref}=-1800 m, being the deepest common level which allows us to sample meridional transects crossing the Indonesian Throughflow without interference of topographic features shallower than 1800 m depth. As will be discussed, comparison of the altimeter-derived surface circulation and the referenced geostrophic circulation show encouraging results, suggesting that our choice of z_{ref} is appropriate for the upper ocean circulation throughout much of the study area.

6.2.3.2 *Referenced geostrophic volume transport*

The ITF transports Pacific water into the eastern Indian Ocean mostly within the upper ocean (<400 m), being dominantly composed of North Pacific water from the Mindanao Current (Gordon, 2005), although throughflow waters also have a subsurface core at intermediate depths, most of which comes from the South Pacific (Gordon, 2005; McCreary et al., 2007; van Sebille et al., 2014). In this work, the focus is on the upper core of the ITF, as it is this core which largely interacts with the upper ocean circulation of the tropical gyre.

We compute the annual cycle of the ITF from the monthly referenced geostrophic velocity fields using two different depths of integration in Eq. (6.5). First, for comparison with geostrophic transport estimates from altimeter-derived velocities, we use $z_2 = -10\ m$. And, second, for a rough estimate of the actual geostrophic volume transport interacting with the upper tropical gyre, we use $z_2 = -400\ m$. The latter choice is based on the above-discussed observations by Gordon (2005) and McCreary et al. (2007).

6.3 SEASONALITY OF THE SOUTH INDIAN TROPICAL GYRE

6.3.1 *The Sverdrupian tropical gyre*

A key player in the seasonal South Indian tropical gyre corresponds to the wind-driven circulation of the Sverdrupian tropical gyre. This is shown in Fig. 6.2 with overlaid large-scale wind stress forcing.

Two features stand out. First, the southern location of a relatively weak Sverdrupian tropical gyre during summer, when the southeasterlies are replaced by northeasterlies over the band 0–8°S (Fig. 6.2a). This replacement brings along, on the one hand, positive curl driving a Sverdrupian anticyclonic cell north of the tropical gyre; and, on the other hand, the southward displacement of the negative curl sustaining the tropical gyre.

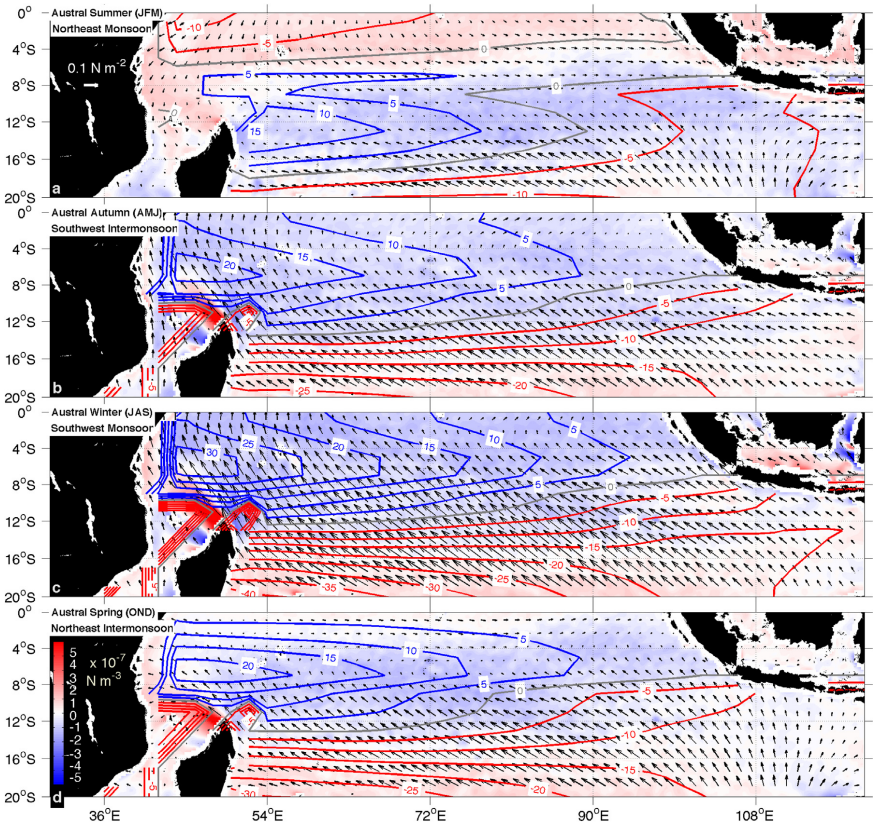

Figure 6.2: Climatology of wind stress (N m^{-2}), as a vector field, and wind-stress curl ($\times$ 10^{-7} N m^{-3}), as shades of colors, from global SCOW fields during (a) summer (January-February-March), (b) autumn (April-May-June), (c) winter (July-August-September) and (d) spring (October-November-December). Solid contours in the background show the seasonally-averaged Sverdrup Streamfunction, ψ [m^2 s^{-1}] computed by Shi et al. (2007) using the island rule. Blue (red) contours indicate cyclonic (anticyclonic) circulation.

Second, the strengthening of the tropical gyre in the west during winter as a response to the enhancement of negative curl driven by the southeasterly trades (Fig. 6.2c). From autumn to spring, the southeasterlies, prevailing over the full domain of tropical latitudes, drive a Sverdrupian tropical gyre which extends accordingly up to the Equator (Fig. 6.2b–d).

6.3.2 *Absolute dynamic topography and geostrophic circulation of the tropical gyre*

Complementary to the seasonal barotropic Sverdrup circulation, we investigate the seasonal ADT (Fig. 6.3) and ADT-based geostrophic circulation (Fig. 6.4) of the South Indian tropical gyre. These fields relate to each other according to Eq. (6.4). A prominent low in ADT is suggestive of a cyclonic geostrophic circulation, and therefore of an upward displacement of the isopycnals leading to an upwelling site. The opposite occurs when a prominent high in ADT is found, pointing to an anticyclonic circulation which promotes the downward displacement of the isopycnals (downwelling).

To ease discussion, three isolines are highlighted as black contours in Fig. 6.3. The 80 cm and 65 cm isolines delimit the surface expression of the Seychelles–Chagos Thermocline Ridge and the Seychelles Dome, respectively. The ITF lies along the northern flank of the 100 cm high in ADT, departing from the Indo-Australian Basin. A fourth isoline, while not emphasized, must also be noted which contours the secondary dome in the east near the Chagos Archipelago, a low of 70 cm in ADT. This feature is hereafter referred to as the Chagos Dome (CD), owing to its geographical location, and is well-defined only during summer.

In summer, the Seychelles Dome in the west (50°E–65°E) and the Chagos Dome in the east (75°E–90°E) are observed zonally aligned and embedded within the low of 80 cm in ADT, i.e. the SCTR (Fig. 6.3a). Compared with other seasons, the SD appears weak and on its easternmost location, as does the Sverdrupian gyre and its center in ψ (Fig. 6.2a). During autumn, the CD merges zonally with the outer isoline of the SD, weakening as a 'dome-like' structure. From autumn to winter, the SD strengthens around a deeper low in ADT (60 cm isoline) and migrates towards the west, as does the 80 cm isoline defining the SCTR. Meanwhile, the CD virtually vanishes in the east (Fig. 6.3b and c). The pattern observed from autumn to winter resembles that of the Sverdrupian tropical gyre in Fig. 6.2c, with a noticeable western intensification during winter.

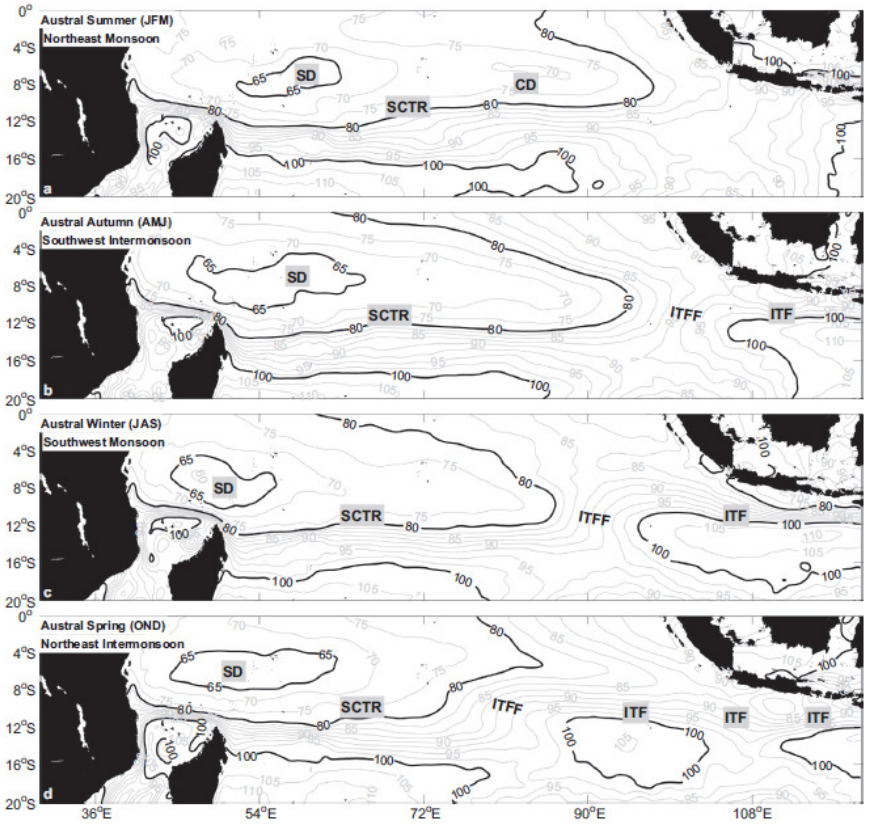

Figure 6.3: Climatology of absolute dynamic topography (cm) during (a) summer (January–February–March), (b) autumn (April–May–June), (c) winter (July–August–September) and (d) spring (October–November–December). Labels indicate the location of the Seychelles Dome (SD), the Chagos Dome (CD), the Seychelles–Chagos Thermocline Ridge (SCTR), the Indonesian Throughflow (ITF) and the Indonesian Throughflow Front (ITFF). The 65, 80 and 100 cm isolines are highlighted in black to ease discussion on the seasonal distribution of the SD, the SCTR and the ITF, respectively.

In the Indo-Australian Basin, the absence of ADT meridional gradients during summer points to the weakness of zonal flows exiting the Indonesian passages. From autumn to spring, the high of 100 cm in ADT expands westwards, between 10°S and 18°S, reaching its westernmost location as far as 85°E late in the year (Fig. 6.3d). The strong meridional gradients along the northern flank of this high in ADT steer the westward spread of the ITF. Noticeably, a zonal front emerges along the western flank of the 100 cm high in ADT as this propagates westward and approaches the SCTR. Hereafter, we refer to this zonal front as the Indonesian Throughflow Front (ITFF), which will be revealed throughout this paper as an important player of the TSIO.

Following the ADT distribution, a year-round basin-wide cyclonic gyre emerges in Fig. 6.4. To the best of our knowledge, this is the first time that a full view of the seasonal South Indian tropical gyre is investigated from an ADT-based geostrophic circulation.

The ocean gyre appears bounded to the north by the eastward SECC, and to the south by the westward SEC and the North Madagascar Current (NMC). The NMC originates after the SEC arrives to 60°E and crosses an extensive range of islands and banks, the Mascarene Ridge (Fig. 6.1). Over this region, the SEC is channeled into two main surface-enhanced cores (New et al., 2007), which on reaching Madagascar form, respectively, the NMC and the poleward East Madagascar Current (EMC) (Schott et al., 1988; Swallow et al., 1988; Nauw et al., 2008; Ponsoni et al., 2015a). The latter, situated farther south of our framework is part of the subtropical gyre.

To visualize the spatial domain of the tropical gyre, a black box has been added to each panel of Fig. 6.4, assuming the seasonal bifurcation latitude of the SEC as the southern boundary of the tropical gyre. This southern boundary is based on values obtained by Chen et al. (2014) with its southernmost position in June/July (∼17.6°S) and its northernmost position in November/December (∼16.1°S). Remarkably, we find the eastern boundary of the tropical gyre also varies seasonally. This boundary corresponds to the longitude where the SECC is observed to recirculate southwestward, feeding the SEC and closing the gyre.

From summer to autumn, the tropical gyre extends from 45°E to 100°E, reaching the west coast of Sumatra (Fig. 6.4a and b). During winter, the recirculation longitude of the SECC shifts westward approaching 90°E. This occurs concomitant to the entrance of a noticeable pulse of ITF in the eastern Indian basin (Fig. 6.4c). During spring, the tropical gyre shrinks most while the spreading of the former pulse of ITF is clearly visible as a continuous westward flow exiting the Indonesian passages and extending up to 80°E. During this season,

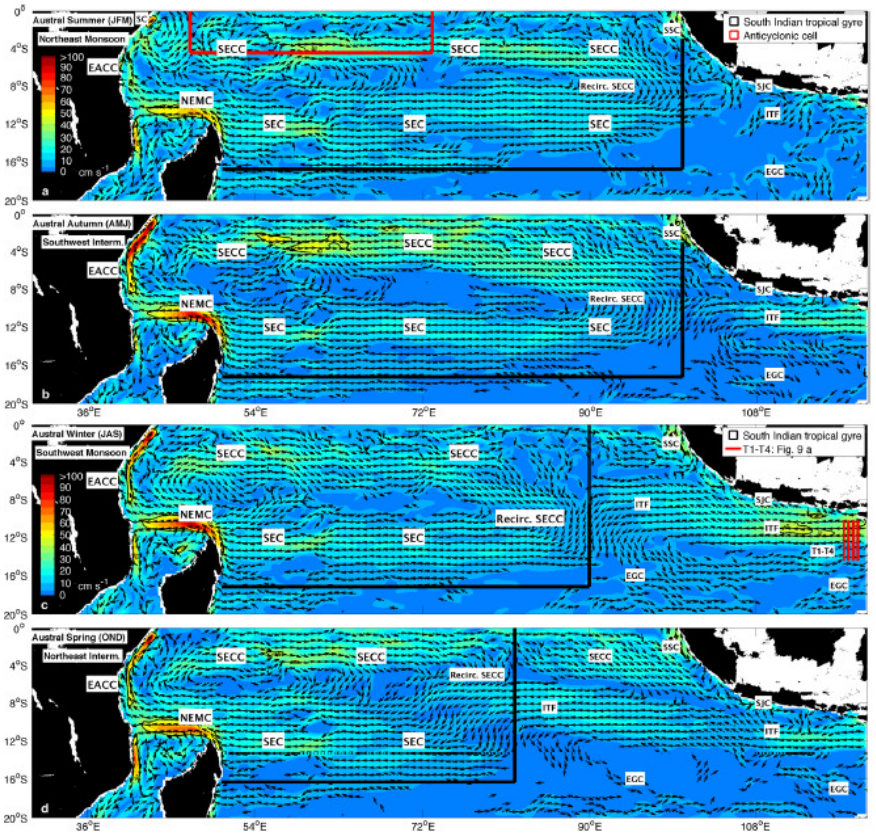

Figure 6.4: Climatology of the altimeter-derived geostrophic surface circulation during (a) summer (January–February–March), (b) autumn (April–May–June), (c) winter (July–August–September) and (d) spring (October–November–December). Shades of colors are speed in units of cm s^{-1}. Arrows represent unit vectors parallel to the vector velocity field (only arrows with speed values above 4 cm s^{-1} are plotted). In (c), the meridional transects T1–T4 in the exit of the Indonesian passages indicate where sampling of altimeter measurements has been performed to investigate the mean annual cycle of the ITF (Fig. 6.9a). Labels indicate major currents: the westward Indonesian Throughflow (ITF); the eastward Eastern Gyral Current (EGC); the southeastward South Sumatra Current (SSC), the South Java Current (SJC), reversing seasonally (see text); the eastward South Equatorial Countercurrent (SECC); the westward South Equatorial Current (SEC); the westward North Madagascar Current (NMC); the northward East African Coastal Current (EACC); and, the Somali Current (SC), which reverses southward during summer. The year-round components of the South Indian tropical gyre, i.e. the EACC, the SECC, the recirculation of the SECC, the SEC and the NMC, are highlighted within the black box delimiting the seasonality of the gyre.

the more southern location of the ITF seems to promote the split of the SECC in two branches: the southern branch, which recirculates when encountering the ITF; and, the northern branch, which does not confront the ITF and continues its route towards Sumatra (Fig. 6.4d). As the annual cycle of the ITF evolves, this pulse of Pacific water relaxes in the Indo-Australian Basin (summer and autumn), and the tropical gyre newly extends basin-wide.

These results suggest that, although the ITF represents a continuous source of Pacific water, the shift in the recirculation longitude of the SECC occurs when new pulses of ITF strongly confront the SECC, hence forming the zonal Indonesian Throughflow Front noted from the ADT climatologies (Fig. 6.3b-d). Compared with the altimeter-derived geostrophic circulation, the large-scale shrinkage of the tropical gyre is absent in the barotropic, wind-driven Sverdrup circulation (Fig. 6.2). Remarkably, we find no previous works reporting this feature.

Additionally, the 'SECC-ITF' encounter collocates with the longitude where the ITF partially recirculates on feeding the eastward Eastern Gyral Current (EGC). The latter flows along the southern meridional gradients of the 100 cm high in ADT exiting the Indonesian passages (Fig. 6.3). Menezes et al. (2013) postulate that the EGC, flowing opposite to classical theories of wind-driven circulation, is maintained by the strong meridional salinity front existing at thermocline depths near 14°S. This front is formed between fresh Indonesian Throughflow Water (ITW; salinities from 34.4 to 34.6 psu) and saltier Subtropical Water (STW; 35.4 psu). These authors show that if the meridional salinity gradient is neglected in the calculation of geostrophic currents, the EGC vanishes. Importantly, we observe in Fig. 6.4 that the zonal domain of the EGC is in accordance with the westward advance of the Indonesian Throughflow Front. This feature suggests that the ITFF may be also responsible for setting the longitude at which the ITF recirculates towards the EGC.

South of the Equator, during summer, an anticyclonic cell stands out in the western Indian Basin (red box in Fig. 6.4a), with the initial path of the SECC as its southern branch. This counterclockwise circulation agrees well with the presence of the Sverdrupian anticyclonic cell observed north of the tropical gyre in Fig. 6.2a.

Along the western boundary, a year-round contributor of source waters to the SECC is revealed in the ADT-based geostrophic circulation: northeastward recirculating flows departing from the NMC. We find these recirculating flows to arise along the western flank of the SD and note they strengthen concomitantly to the intensification of the dome from winter to spring (cf. Fig. 6.3c and d). Similarly, the intensification of the SD might also be responsible for

the southwestward recirculating flows found along the eastern flank of the SD, therefore departing from the SECC and feeding back into the NMC. This adds to the well-known source waters coming from the northward East African Coastal Current (EACC), which converges with the (summertime) southward Somali Current (SC), jointly feeding the SECC between 2°S and 4°S (Schott and McCreary Jr., 2001).

Although out of the scope of the present study, it is worth while to mention that seasonality of eastern boundary flows in Fig. 6.4 is in agreement with previous studies. The South Sumatra Current (SSC) is shown as a year-round southeastward flow (Clarke and Liu, 1993; Shenoi et al., 1999), contouring the western coast of Sumatra as an apparent extension of the SECC when the tropical gyre is basin-wide (summer and autumn). Southward, seasonality of the South Java Current (SJC) also agrees well with existing knowledge, flowing northwestward from autumn to winter and reversing as a southeastward flow from spring to summer (Wyrtki, 1961; Quadfasel and Cresswell, 1992; Sprintall et al., 1999).

6.3.3 *The Seychelles–Chagos Thermocline Ridge*

The temperature and salinity fields in Fig. 6.5 extend our view of the seasonal tropical gyre and its associated upwelling system at thermocline depths, where z=-100 m.

The Seychelles–Chagos Thermocline Ridge stands out as an elongated feature of relatively cold (upwelled) water, contoured by the 20°C isotherm, and encapsulating the Seychelles and Chagos Domes, contoured by the 18°C isotherm (black contours in left panels of Fig. 6.5). The SCTR collocates seasonally with the zonal low of 80 cm in the ADT fields (Fig. 6.3), and with the corresponding ADT-based circulation of the tropical gyre (Fig. 6.4), supporting the dynamical relationship between the upwelling system and the ocean gyre. Also, the SD and the CD, as shown in the temperature field, collocate seasonally with the local lows of 65 cm and 70 cm in ADT.

From summer to autumn, the SD and the CD evolve from being two well-defined features to their merger forming the so-called zonal ridge. In winter, the western intensification of the SCTR over the SD follows. This intensification in the west expands eastward during spring, while the domain of the SCTR continues to shrink westward. Interestingly, the seasonal shrinkage of the tropical gyre (black box), as described in previous section, is captured here by the 20°C isotherm defining the SCTR.

The arrival of Indonesian Throughflow Water is visible in the salinity fields as the westward spread of fresh water (34.6 psu isohaline) exiting the Indone-

sian Seas (right panels in Fig. 6.5). In the temperature fields, the ITW presents a negative meridional temperature gradient while embedded in the 34.6 psu isohaline. This negative gradient is in agreement with values of transport-weighted temperature reported by Wijffels et al. (2008) for the major outflow straits contributing to the ITF, showing distinct temperature signals for outflows of different origin. At 100 m depth, we find to the north, cooler water of about 20–22°C predominantly exiting the Lombok, Sumba and Ombai Straits; and, to the south, warmer water mostly exiting the Timor Passage of about 23–24°C.

During winter, the Indonesian Throughflow Front emerges here at the encounter of ITW with the eastern Seychelles–Chagos Thermocline Ridge, formed of relatively cool and salty Indian Equatorial Water (IEW: 0–500 m, 8–23°C, 34.6–35 psu; Emery and Meincke (1986); Emery (2001)) of about 20°C and 35 psu at 100 m depth. In the temperature fields, the formation and advance of the ITFF is noticeable following the warm pool of ITW, mostly exiting the Timor Passage (23°C isotherm). Synchronized with the resizing of the SCTR from winter to spring, the westward advance of the ITFF suggests that the front may be exerting a thermohaline forcing to the geostrophic vertical shear at thermocline depths, which leads to the early recirculation of the SECC, closing the tropical gyre before arrival to Sumatra.

During spring, source waters leaving the Indonesian Seas diminish, while the ITFF continues travelling across the Central Indian Basin. As time evolves, the ITW mixes along its route (Gordon et al., 1997), leaving a weaker freshwater signal in its wake (Fig. 6.5e and f).

6.4 LOCAL-SCALE WIND STRESS FORCING: EKMAN UPWELLING

The basin-scale wind stress curl plays a major role in sustaining the ocean gyre, and hence the upwelling regime; however, it is reasonable to think that local wind stress forcing may also impact seasonality of the SCTR, as has been discussed in previous modelling studies (Hermes and Reason, 2008; Yokoi et al., 2008). An analogous observational-based approach, which will be presented here, is nevertheless absent in the existing literature.

First, we investigate horizontal maps of Ekman vertical velocity, w_E, over the entire domain of the Seychelles–Chagos Thermocline Ridge. Second, we analyze the monthly evolution of w_E, ADT and the thermocline depth through a novel partitioning of the thermocline ridge, performing spatial averages over the Seychelles Dome and the Chagos Dome, separately.

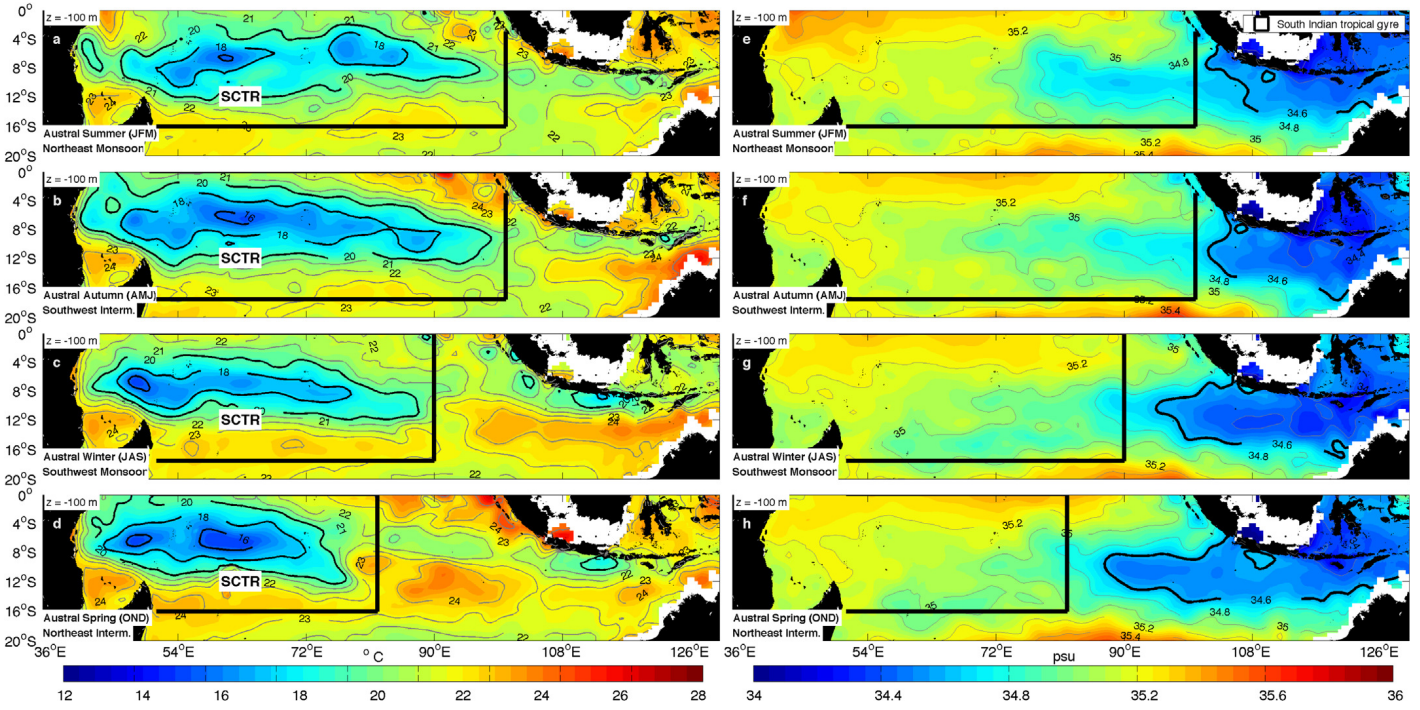

Figure 6.5: Climatology of potential temperature (°C) (left panels) and salinity (psu) (right panels) at 100 m depth from a global atlas of temperature and salinity (CARS09) for (a, e) summer (January–February–March), (b, f) autumn (April–May–June), (c, g) winter (July–August–September) and (d, h) spring (October–November–December). The black boxes indicate the domain of the seasonal South Indian tropical gyre as shown in Fig. 6.4.

6.4.1 *The Seychelles–Chagos Thermocline Ridge*

Ekman vertical velocity (Fig. 6.6) is caused by two wind forcing contributions (see Eq. (6.3)), namely due to the $curl$ contribution and the β contribution. As a result, the Ekman vertical velocity in the open-ocean upwelling region (black box) appears mostly driven by the wind stress curl contribution from spring to autumn, reaching upward velocities over 30 cm day^{-1} (shades of blue). The existence during summer of an anticyclonic cell north of the South Indian tropical gyre, as observed from the wind-driven Sverdrup circulation (Fig. 6.2a) and the ADT-based geostrophic circulation (Fig. 6.4a), is promoted here by downward velocities stronger than -30 cm day^{-1} (shades of red).

A striking phenomenon occurs during winter (Fig. 6.6c). One could expect that the western intensification of the SCTR over the SD might be promoted by an enhancement of upward w_E. Nevertheless, the strengthening of the south-easterly trades (Fig. 6.2c) drives strong downward w_E due to the β contribution, which overcomes the positive vertical velocities induced by the $curl$ contribution. This leads to low $w_E \approx 0$ over the central and southern flank of the tropical gyre, showing patches of negative w_E of about 15 cm s^{-1} over both the SD and the CD. At this point we must also note the presence of a small-scale curl dipole northwest of Madagascar's northern tip, near 48°E, 12°S (see Fig. 6.2b-c). This dipole, firstly reported by Chelton et al. (2004), is associated with island-induced wind shadows and its positive curl lobe (shades of red) counteracts an upwelling dome. The above scenario strongly supports that the western intensification of the SCTR during winter, rather than being caused by local wind-driven upwelling, is likely the response to the western intensification of the wind-driven Sverdrup tropical gyre (Fig. 6.2c).

6.4.2 *Seychelles and Chagos Domes*

Because the core of the Seychelles Dome falls within the region of the curl dipole only during winter, we present its spatial averages excluding the area of the curl dipole. Otherwise, the persistent downward effect of the curl dipole would partially mask the monthly contribution of w_E to the open ocean dome. The domains selected for spatial averages over the SD (50°E–65°E; 5°S–10°S) and the CD (75°E–90°E; 5°S–10°S) are shown as brown boxes in Fig. 6.6).

To be consistent with Hermes and Reason (2008) and Yokoi et al. (2008), we use the 20°C isotherm depth, D_{20}, as reference of the thermocline depth. D_{20} follows z-coordinates, and is thus negative in the downward direction. When comparing the monthly evolution of ADT and D_{20} (Fig. 6.7a and b),

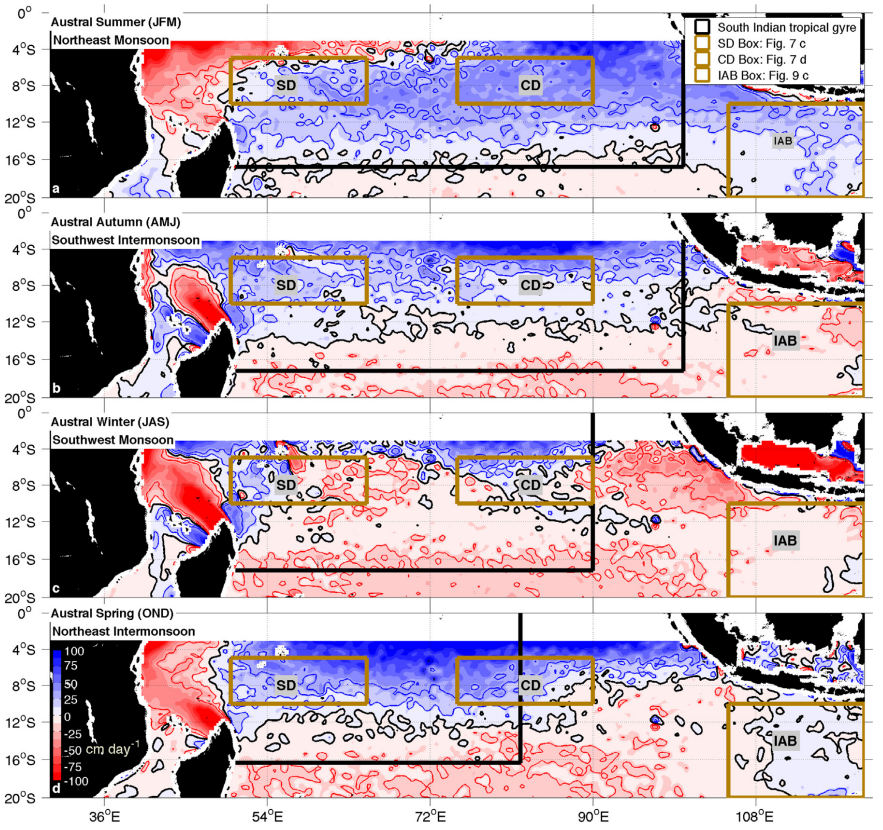

Figure 6.6: Climatology of Ekman vertical velocity, w_E (cm day^{-1}), computed from the global SCOW fields for (a) summer (January–February–March), (b) autumn (April–May–June), (c) winter (July–August–September) and (d) spring (October–November–December). Solid contours in black correspond to zero isotachs. Solid contours in blue and red correspond, respectively, to positive (upward) and negative (downward) velocity magnitudes of 15 cm day^{-1} and 30 cm day^{-1}. The black boxes indicate the domain of the seasonal South Indian tropical gyre as shown in Fig. 6.4. The brown boxes show domains for the analysis of w_E over the Seychelles Dome, the Chagos Dome and the Indo-Australian Basin (IAB). The number of the corresponding figure is listed in the inset.

the interpretation is as follows. A low in ADT relates to a high of D_{20}, as a geostrophic cyclonic circulation generally relates to the upward displacement of the isotherms. Conversely, a high in ADT follows the relaxation of the upwelling site, corresponding to a low of D_{20}.

A clear semi-annual cycle dominates the monthly evolution of the ADT and the D_{20} over the SD. This is in agreement with calculations presented by Hermes and Reason (2008) and Yokoi et al. (2008) over a greater region covering the entire Seychelles–Chagos Thermocline Ridge (45°E–75°E; 5°S–10°S). The SD strengthens during June and December, when D_{20} rises up to 69 m depth, and weakens during March and September, when D_{20} deepens down to 88 m depth. By contrast, an annual cycle governs the ADT and the D_{20} evolution of the CD in the east. Thus, D_{20} rises up to 78 m depth during April and deepens down to 117 m during November. The latter cycle reveals why the CD vanishes as a well-defined feature after autumn.

In Fig. 6.7c and d, the time derivative of D_{20} provides an estimate of the actual vertical velocity, w. As for w_E, positive (negative) w indicates upward (downward) vertical velocity. Results show maximum upward values of w about 40 cm day^{-1} over both the SD and the CD; while maximum downward velocities are found to be weaker over the CD, about -30 cm day^{-1}, than over the SD, about -35 cm day^{-1}. w_E follows a similar pattern as w, a semi-annual cycle over the SD and an annual cycle over the CD, although over both regions w_E presents a narrower range of variability. The resemblance between the mode of oscillation of w and w_E highlights the constructive contribution of the local wind forcing to the ascend and descend of the thermocline.

The different cycles of w_E over the SD and the CD are due to different $curl$ contributions, as both domes present β contributions that resemble each other with a distinct annual cycle (Fig. 6.7c and d). The β contribution drives negative vertical velocities from April to November, with a maximum downward velocity in August due to the basin-scale strengthening of the southeasterly trades (Fig. 6.2c). From December to March, this contribution reverses to upward velocities with the arrival of the northeasterlies. The semi-annual signal of w_E emerges then from the $curl$ contribution, which over the SD presents a strong semi-annual mode of oscillation in comparison to the weaker and nearly annual cycle over the CD. We attribute this difference to the stronger influence of (semi-annual) monsoonal winds over the SD (Fig. 6.2a). In this regard, the SD and the CD differ the most from December to March, when the $curl$ contribution reverses sign from upward to downward velocities over the western Indian Ocean, i.e. over the SD.

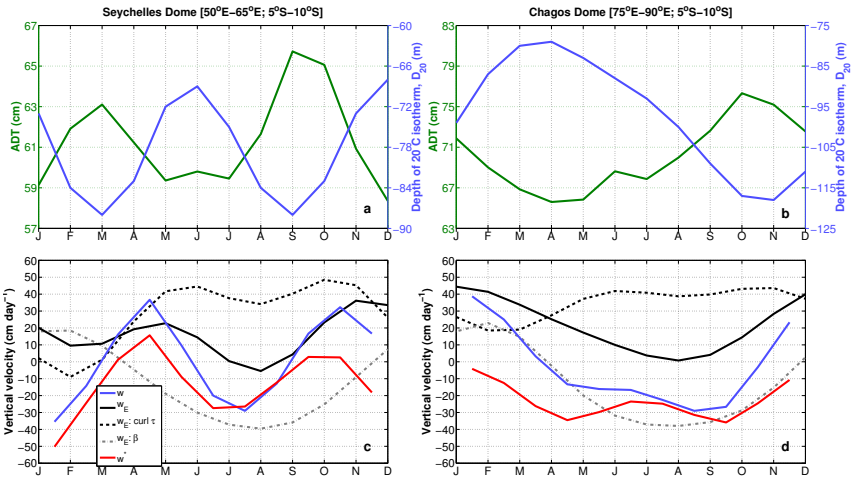

Figure 6.7: Spatial averages of the monthly evolution of the Seychelles Dome (left panels) and the Chagos Dome (right panels). (a, b) Absolute Dynamic Topography (cm) and depth of the 20°C isotherm (m) taken as a reference of the thermocline depth. (c, d) Actual vertical velocity (w); Ekman vertical velocity (w_E) and its $curl$ and β contributions; and, vertical velocity forced by additional forcings (w^*). Positive (negative) values indicate upward (downward) velocities in units of cm day^{-1}.

The difference vertical velocity, $w^* = w - w_E$, provides an estimate of forcings other than Ekman upwelling (Fig. 6.7c and d). w^* is particularly important over the SD and the CD during winter (July to September), when the spatially averaged Ekman component is small. We suggest that w^* downward velocities and deepening of D_{20}, occurring during this season within the box selected for the SD, are due to the westward migration of the Sverdrupian tropical gyre, strengthening west of the domain used for spatial averaging (see Figs. 6.2c and 6.5c). The decrease of w^* downward velocities obtained for July to September is, therefore, related to the progressive disappearance of this westward migration of the upwelling site. Over the CD, the forcing promoting an increase of w^* downward velocities during winter, from -20 cm day^{-1} to -30 cm day^{-1}, relates to the westward propagation of ITW flowing over the eastern part of the SCTR, as will be accounted for Section 6.6.2.

Lastly, it is worth noting that w^* displays a semi-annual cycle at both sites, although these are out of phase with respect to each other. Over the SD, the semi-annual cycle of w_E and w^* suggests that the latter works constructively to the former during the rise and sinking of the thermocline. This constructive

interaction occurs over the CD only from spring to summer, when the increase and decrease of w^* follows the respective increase and decrease of w_E.

In the next section we further investigate the nature of w^* and explore the role that Rossby waves and the Indonesian Throughflow may be playing as remote forcing to seasonality of the South Indian tropical gyre and its associated upwelling regime.

6.5 REMOTE FORCING: ROSSBY WAVES

Previous studies investigated the role of oceanic Rossby waves in the tropical and subtropical South Indian Ocean (Périgaud and Delecluse, 1992; Masumoto and Meyers, 1998; Morrow and Birol, 1998; Wang et al., 2001; Matano et al., 2002; Schouten et al., 2002a; Jury and Huang, 2004; Hermes and Reason, 2008, 2009). In their modelling study, Hermes and Reason (2009) found that the southern and eastern regions of the SCTR are dominated by annual harmonics, while the northwest part of the ridge is dominated by semi-annual harmonics.

To investigate the role of Rossby waves as remote forcing in the SCTR based on observations, we use a set of longitude-time plots of SLA averaged over eight different latitude bands (Fig. 6.8). Results are in agreement with previous modeling studies (Hermes and Reason, 2008, 2009), although basin-wide longitude-time plots presented here may provide a more comprehensive view on the spatial pattern of Rossby waves affecting the SCTR.

The propagation of Rossby waves in Fig. 6.8 is clearly seen in the form of elongated features travelling westward, slower with increasing latitudes from (a) to (h). Between 4°S and 8°S, we find three different domains according to the prevalence of either annual or semi-annual harmonics (Fig. 6.8a and b). Semi-annual harmonics appear in the far eastern and western parts of the basin, while annual harmonics are seen over the Central Indian Basin.

The above zonal asymmetry may be promoted by the semi-annual forcing of the Indian monsoon, especially strong in the western TSIO (Fig. 6.2). Crossing the equator and reaching down to 8°S, the monsoonal reversal might emerge as a mid-ocean source of semi-annual Rossby waves from 40°E to 75°E, while east of this region, in the Central Indian Basin, the annual Rossby waves dominate. The situation differs again along the easternmost margin, where semi-annual harmonics prevail contouring the western coasts of Sumatra and Java, disappearing offshore. We attribute this semi-annual dominance in the east as resulting from eastward-propagating equatorial Kelvin waves, forced remotely during the monsoon breaks (Sprintall et al., 1999) and evolving as poleward-

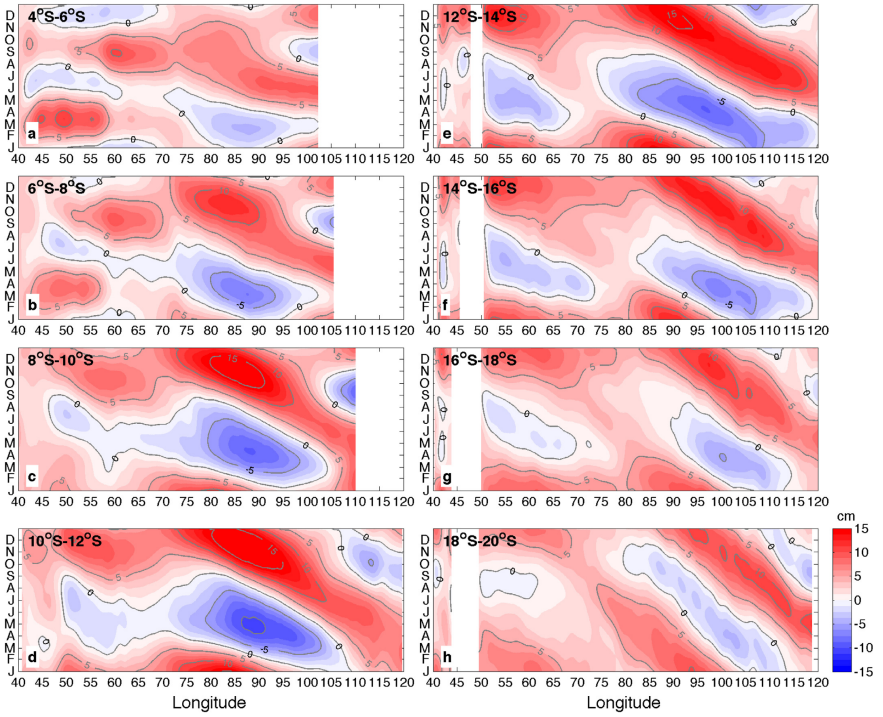

Figure 6.8: Time-longitude plots of Sea Level Anomaly (cm) averaged over eight different latitude bands of the TSIO for the period 1993–2014: (a) 4°S–6°S; (b) 6°S–8°S; (c) 8°S–10°S; (d) 10°S–12°S; (e) 12°S–14°S; (f) 14°S–16°S; (g) 16°S–18°S; (h) 18°S–20°S. Before time-averaging daily data, frequencies higher than semi-annual have been low-pass filtered using a Butterworth filter of order 4. Land areas and Indonesian Seas are masked in white.

propagating coastal Kelvin waves at their arrival to Sumatra. Supporting this hypothesis, we note that south of 8°S, where the meridional extent of Java's coast ends, semi-annual harmonics vanish.

Between 8°S and 20°S (Fig. 6.8c–h), annual Rossby waves dominate along the entire length of the tropical gyre, likely related to the prevalence of the annual southeasterly trades (see Fig. 6.2). The source of annual Rossby waves between 4°S and 8°S in the Central Indian Basin is, nevertheless, still unclear.

This complex pattern accounts for the different cycles exhibited by the Seychelles Dome (semi-annual cycle) and the Chagos Dome (annual cycle) in Fig. 6.7a and b. Furthermore, the arrival of upwelling Rossby waves (negative SLA) and downwelling Rossby waves (positive SLA) appear concomitant to, respectively, the rise and descend of the thermocline over both sites. This points

to Rossby waves forcing contributing to the w^* vertical velocity in Fig. 6.7c and d.

Between 60°E and 80°E, and within the latitude bands enclosing 10°S–18°S, an apparent mid-ocean breakdown of the westward phase propagation of annual Rossby waves is also noticeable (Fig. 6.8d–g). This feature is shown by two local maxima separated by a mid-ocean minimum that, with increasing latitude, shifts eastward. The eastward shift is observed between 60°E and 65°E at 10°S–12°S, and between 80°E and 85°E at 16°S–18°S.

Using altimeter data, a Levitus climatology and a linear reduced-gravity model, Wang et al. (2001) investigated this apparent mid-ocean disruption of Rossby waves. These authors postulate the breakdown is due to the destructive masking of the westward-propagating annual Rossby waves by the wind-driven localized response; while the two maxima simply result from the constructive interference between the localized response and the Rossby waves. Complementary, Hermes and Reason (2009) found the breakdown is more apparent in a regional ocean modelling system (ROMS) when using a high resolution wind stress field, as opposed to a coarser version. Bottom topography was also found not to play a role in the appearance of this feature. The above results jointly suggest that the arrival of westward-propagating annual Rossby waves interacting with localized wind stress forcing may be a determining factor in triggering this feature.

6.6 REMOTE FORCING: THE INDONESIAN THROUGHFLOW

Observational results on the seasonal cycle of the upper ITF exiting the Indo-Australian Basin are still scarce and mostly indirect, although these generally agree with modelling studies in suggesting that the maximum throughflow occurs in June–July and the minimum in February (see Schott and McCreary Jr. (2001); Schott et al. (2009) for a review).

In order to assess the impact that the ITF may have on the seasonality of the tropical gyre, we first present in Section 6.6.1 a detailed analysis of the annual cycle and westward propagation of the ITF geostrophic transport entering the Indo-Australian Basin and interacting with the eastern tropical gyre. Next, in Section 6.6.2, we analyze the potential role of the Indonesian Throughflow Front in the seasonal resizing of the tropical gyre.

6.6.1 *Annual cycle and westward propagation*

One important exception to the persistent southeasterly trades in the region 8°S–16°S is found in the Indo-Australian Basin, where the wind stress changes direction during spring to reverse as southwesterlies during summer. This change of the zonal wind stress occurs concurrent to the seasonal exit and farther westward spread of the ITF (cf. Figs. 6.2–6.4), suggesting that geostrophic currents in this region may be promoted by a baroclinic response to the local wind stress forcing on inducing Ekman downwellling/upwelling. Motivated by this observation, we explore the concurrence of the monthly mean of ITF geostrophic transport along transects T1–T4 in Fig. 6.4c (red solid lines) and Ekman vertical velocity in the Indo-Australian Basin (Fig. 6.9a-c). For details on the computation of ITF geostrophic transport the reader is referred to Sections 6.2.2.2 and 6.2.3.2.

The annual cycle of ITF geostrophic transport computed from altimeter-derived velocities and referenced geostrophic velocities in the upper 10 m agrees well with that displayed for the upper 400 m (Fig. 6.9a and b). In all cases, a distinctive annual cycle arises. The ITF geostrophic transport for the upper 400 m (10 m) peaks during austral winter with about 14 Sv (1 Sv), and weakens from spring to summer, reaching a minimum of about 3 Sv (0.2 Sv) in February. The annual mean is 8 Sv for the upper 400 m, and about 0.6 Sv for both altimeter-derived and referenced geostrophic velocities in the upper 10 m. These results support that the adopted level of no motion for referenced geostrophic velocities achieves comparable ITF geostrophic transports in the upper 10 m. Also, we note that the annual mean of 8 Sv falls within the range of existing estimates when adding up the two main sources of ITW feeding transects T1–T4, i.e. water from the Timor Passage: 3.4–5.3 Sv (Molcard et al., 1996); and, water from the Ombai Strait, 4–6 Sv (Molcard et al., 2001).

According to this, the annual cycle of Ekman vertical velocity in Fig. 6.9c suggests that, throughout the year, seasonal variations of ITW exiting the Indonesian Seas might be enhanced by the local wind stress forcing, with the β contribution playing a major role. The connection develops as follows. Ekman downwelling conditions appear to set up in the upper ocean an anticyclonic circulation that promotes the exit of ITW (see the ADT field and corresponding geostrophic circulation in Figs. 6.3b–d and 6.4b–d). We speculate the opposite would occur if Ekman upwelling conditions dominate. Thus, the decrease of positive w_E observed from February to June agrees well with the concurrent increase of ITF geostrophic transport from 3 Sv to about 14 Sv in Fig. 6.9b. From April to June, w_E becomes negative and reaches maximum downward veloci-

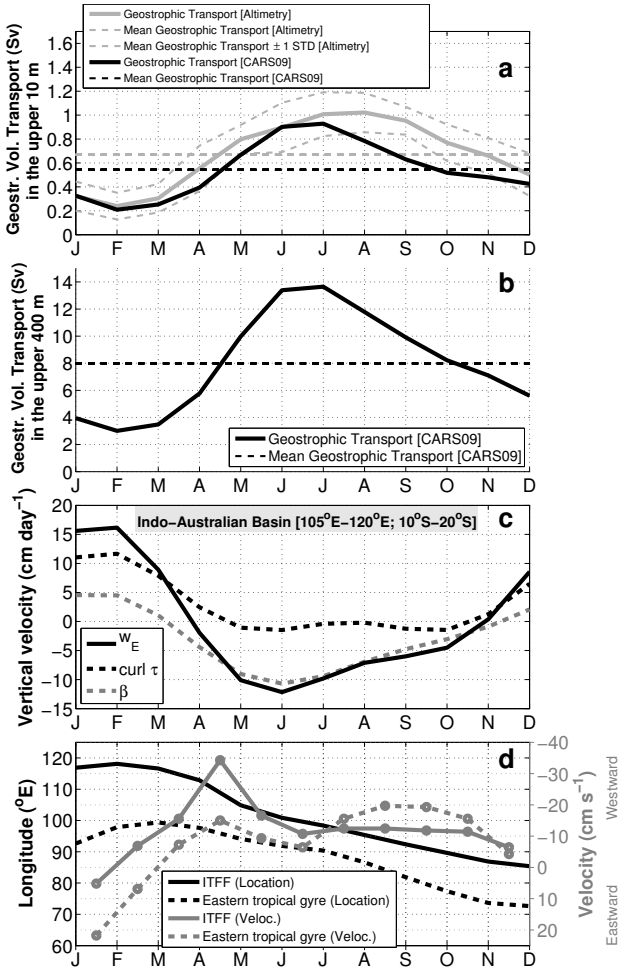

Figure 6.9: (a) Monthly mean of the upper 10 m of ITF geostrophic volume transport (Sv) computed along transects T1–T4 (see Fig. 6.4c) from altimeter-derived (black line) and referenced (grey line) geostrophic velocities. (b) Same as (a) but computed from referenced geostrophic velocities for the upper 400 m. In (a,b) only westward transports (positive values) were accounted. (c) Spatial averages of Ekman vertical velocity (w_E) and its $curl$ and β contributions within the Indo-Australian Basin. Positive (negative) values indicate upward (downward) velocities in units of cm day^{-1}. (d) Longitude (°E) of the ITFF and the eastern tropical gyre, namely the recirculation of the SECC. Corresponding velocities of propagation are shown in units of cm s^{-1}. Negative (positive) values indicate westward (eastward) velocities.

ties, coinciding with a maximum increase of ITW (up to 4 Sv of difference between April and May). From June to February, downward w_E decreases, weakening the downwelling conditions that enhance the exit of ITW. As expected, the ITF geostrophic transport follows a parallel decrease.

Here we provide support for the notion that the westward propagation of ITW may be contributing to the early recirculation of the SECC. Because the Indonesian Throughflow Front moves slightly slanted, from southeast to northwest, we track the advance of ITW and of the eastern tropical gyre selecting two fixed zonal transects over which respective characteristic isolines in ADT are searched. The ITFF is tracked following the western flank of the 100 cm high in ADT along 13°S. The eastern flank of the tropical gyre is tracked following the low of 80 cm in ADT along 9°S. One must note here that the eastern flank of the tropical gyre in ADT can also be interpreted as its dynamic surface expression, namely the recirculation of the SECC.

Following the increase of geostrophic transport since February (Fig. 6.9b), a consequent westward advance of the ITFF is observed (solid black line in Fig. 6.9d). However, it is not until one month later that the ITFF exits the Indo-Australian Basin and the eastern flank of the tropical gyre (dashed black line) confronts the arrival of Pacific water, therefore starting to jointly migrate westward. From March to December, both the ITFF and the eastern tropical gyre move westward synchronously enhanced by the advance of ITW.

As expected, velocities of propagation of the ITFF (solid gray line) and the eastern tropical gyre (dashed gray line) in Fig. 6.9d follow a parallel evolution where the former leads the latter throughout the year except from July to November, when the shrinkage of the gyre accelerates with respect to the ITFF. In principle, one could think that this involves a discrepancy with the suggestion that the ITFF may be forcing the westward displacement of the eastern tropical gyre. However, the wind-driven Sverdrup circulation shown in Fig. 6.2 indicates that a western intensification of the ocean gyre occurs during winter. We suggest that the wind-driven circulation is responsible for an additional westward motion of the eastern tropical gyre from July to October, hence propagating westward faster than the ITFF. During November, westward velocities of the ITFF and the eastern tropical gyre drop to zero with the weakening of the ITFF as a distinctive feature, which is now advected by the tropical gyre flowing along its southern branch as the South Equatorial Current.

Noticeably, the maximum westward speed of 35 cm s^{-1} estimated for the advance of the ITFF during April coincides with the maximum increase of geostrophic volume transport (about 4 Sv) throughout the year (Fig. 6.9b). This peak also agrees well with a concurrent local maximum of 15 cm s^{-1} of westward speed in the shrinkage of the tropical gyre.

During January, the cycle starts again. The lower ITF geostrophic transport exiting the Indo-Australian Basin leads the return of the ITFF to its initial position in the east. A new input of ITW is now far from interacting with the gyre, which expands eastward until February. Between December and January velocities of propagation have not been computed since the phenomenon described here represents a closed cycle that restarts each year in the Indo-Australian Basin with new ITW exiting the Indonesian Seas.

6.6.2 *The Indonesian Throughflow Front*

Geostrophic currents are also related to horizontal gradients of density, and so to the horizontal gradients of temperature and salinity, by the thermal wind relation (Eq. (6.6)). Given the nature of the Indonesian Throughflow Front, confronting cold and salty Indian Equatorial Water from the SCTR with relatively warmer and fresher Indonesian Throughflow Water, it is reasonable to think that the westward propagation of such a zonal front may force in turn an associated meridional flow.

To investigate this, Fig. 6.10 presents a seasonal climatology of the referenced geostrophic surface circulation derived from a temperature and salinity atlas, CARS09 (see Section 6.2.3.1). When compared to the ADT-based climatology (Fig. 6.4), circulation patterns agree on major seasonal features, validating at a basin-scale the election of a reference level of no motion at 1800 m depth. Importantly, the westward shrinkage of the tropical gyre is well captured. From winter to spring the relatively cooler and saltier SECC largely recirculates southward on feeding the SEC over the region where the former confronts the warmer and fresher ITF (cf. Fig. 6.5 and 6.10).

An in-depth view of the bimonthly 'SCTR–ITFF' interaction illustrates how the westward advance of the ITFF may be forcing the geostrophic vertical shear of the eastern tropical gyre, leading to the early recirculation of the SECC before arrival to Sumatra (Fig. 6.11). The large scale of this phenomenon requires the use of meridional averages over a large range of latitudes. We average seven nearly basin-wide zonal transects at regular spatial distance (0.5°) from 5.5°S down to 11.5°S. As a side effect, seasonality of local features like the SD and CD is averaged out.

In February and April, first and second rows in Fig. 6.11, potential temperature fields show the SCTR as a basin-wide feature. In the salinity fields, the ITW spreads westward as a shallow freshwater layer from the surface down to 50-60 m depth. During these months, the ITW reaches the western margin of the basin leading to a weakened surface front in density.

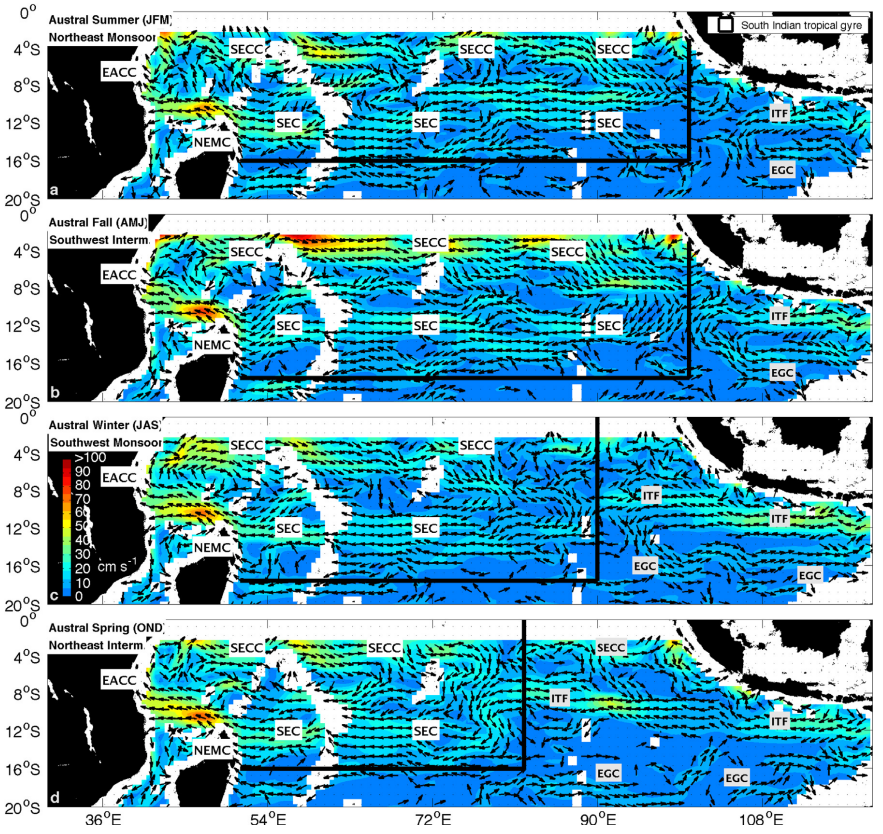

Figure 6.10: Climatology of the referenced geostrophic surface circulation (cm s^{-1}) derived from a global atlas of temperature and salinity (CARS09) for (a) summer (January–February–March), (b) autumn (April–May–June), (c) winter (July–August–September) and (d) spring (October–November–December). Shades of colors are speed in units of cm s^{-1}. Arrows represent unit vectors parallel to the vector velocity field (only arrows with speed values above 4 cm s^{-1} are plotted). Regions shallower than the reference level of no motion (z_{ref} = -1800 m) have been masked in white. Labels indicate major currents as in Fig. 6.4. The black boxes indicate the domain of the seasonal South Indian tropical gyre in agreement with Fig. 6.4.

In June, third row in Fig. 6.11, a new input of warm and fresh ITW enters in the eastern basin while its signal in the west becomes more diffuse. From June to December, third to sixth rows in Fig. 6.11, the encounter of recently discharged ITW with the cooler and saltier upwelled IEW leads the appearance of the Indonesian Throughflow Front with a clear expression in the density field.

The eastern part of the SCTR relaxes by deepening of D_{20} as the ITFF advances westward. This phenomenon may be enhanced during winter by the western intensification of the Sverdrupian tropical gyre. These results suggest the westward propagation of ITW may also contribute as remote forcing to the deepening of the thermocline as it flows over the Seychelles–Chagos Thermocline Ridge, leading to downward vertical velocities. This scenario agrees well with the increase of downward vertical velocities occurring during winter in the east via w^* (see Fig. 6.7d). Complementary, the weakening of the ITW input as a shallower and hence lighter overlying plume may induce a weakening of downward vertical velocities.

From the geostrophic surface circulation in Figs. 6.4 and 6.10 we observe that southward recirculating flows departing from the SECC and feeding the SEC exist all along the extent of the tropical gyre. In agreement with this, panels along the last column of Fig. 6.11 highlight a broad range of southward flows (black contours) which feed the SEC with core velocities ranging from 5 to 10 cm s^{-1}, and reaching down to 120 m. Most importantly, from June to December, these results confirm that the easternmost southward flows collocate with the westward advance of the ITFF, in agreement with the longitudes where the SECC closes seasonally the tropical gyre in the geostrophic surface circulation.

In the last column of Fig. 6.11 the zonal Turner angle, T_u (Turner, 1973; Tippins and Tomczak, 2003) is used to evaluate temperature and salinity contributions to density gradients leading to meridional geostrophic flows. The interpretation is straightforward. A density compensation occurs when $|T_u|=45°$ (white color). Salinity gradients dominate density variations when $|T_u| \ll 45°$ (blue shades), and temperature gradients when $|T_u| \gg 45°$ (red shades). In this manner we find that southward geostrophic velocities labelled at the recirculation longitudes of the SECC are mostly driven by temperature gradients of the ITFF, both at shallow and deep levels, although patches of greater salinity gradient contributions also emerge at shallow levels leading to southward flows.

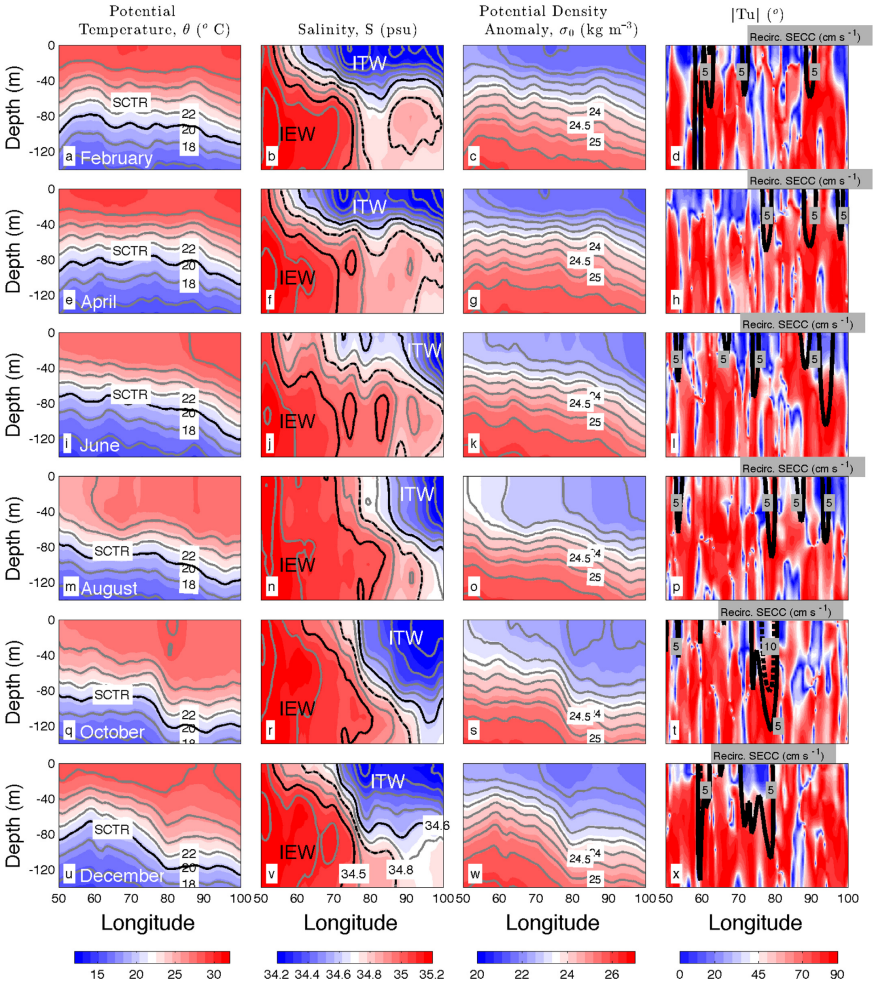

Figure 6.11: Meridionally-averaged zonal section of potential temperature (°C) (first column), salinity (psu) (second column), potential density anomaly (kg m^{-3}) (third column) and zonal Turner angle (°) (fourth column) showing the monthly evolution of the Seychelles–Chagos Thermocline Ridge and the Indonesian Throughflow (thermohaline) Front over 5.5°S–11.5°S. From top to bottom monthly means are presented for February, April, June, August, October and December. Labels indicate the Seychelles–Chagos Thermocline Ridge (SCTR), the Indonesian Throughflow Front (ITFF), Indian Equatorial Water (IEW), Indonesian Throughflow Water (ITW) and the recirculation of the SECC. Panels in the fourth column show solid (dashed) black contours, representing southward geostrophic velocities of 5 cm s^{-1} (10 cm s^{-1}).

6.7 DISCUSSION AND CONCLUSIONS

The South Indian tropical gyre is the only low-latitude gyre in interaction with a gateway between two ocean basins, hence emerging as an important player in the redistribution of water masses in the global ocean circulation.

Throughout this paper two novel large-scale features governing the upper geostrophic circulation of the South Indian tropical gyre are revealed. First, the seasonal shrinkage of the ocean gyre. This occurs when the SECC recirculates before arrival to Sumatra from winter to spring, in apparent synchronization with the annual cycle of the ITF. Second, the open-ocean upwelling is found to vary following seasonality of the overlying geostrophic ocean gyre, a relationship that has not been previously shown for this region.

The reason why these features have remained unknown until now might be related to the central role that the South Equatorial Countercurrent plays in the upper geostrophic circulation of the tropical gyre, as described in this work. Given the nature of the SECC, an open ocean basin-wide current flowing within the equatorial belt, a robust observational picture of this current was not attainable in the past due to scarcity of high resolution, synoptic observations. This circumstance led the scientific community to strongly rely on modeling results and on classical theories of wind-driven circulation, which masked the role of the geostrophic SECC, flowing at the surface only during summer and masked by opposing overlying Ekman currents during winter (see e.g. McCreary et al. (1993); Schott and McCreary Jr. (2001); Schott et al. (2009)). Additionally, little attention was given to interseasonal periods, and often the South Indian Ocean is represented bimodally, focusing on the northeast (austral summer) and southwest (austral winter) monsoons. Following the view of a non-persistent ocean gyre at the surface, the dynamical connection between the open-ocean upwelling ridge and the overlying gyre remained hidden.

The South Indian Countercurrent (Palastanga et al., 2007; Huhn et al., 2012), flowing opposite to classical theories of wind-driven circulation, is one of those cases by which the use of satellite altimeter data has uncovered open ocean dynamics that force us to update our view of the ocean circulation. To the authors' knowledge, the present study represents the first investigation of the geostrophic circulation of the tropical gyre based on synoptic long-term observations. Results are coherent in expressing a close relationship between the upwelling ridge and the overlying cyclonic geostrophic circulation.

Consistent with previous works, the SCTR is shown to be largely a response to the negative wind stress curl between the southeasterly trades and equatorial westerlies (Woodberry et al., 1989; McCreary et al., 1993; Donguy and Meyers, 1995; Masumoto and Meyers, 1998; Xie et al., 2002; Hermes and Rea-

son, 2008; Yokoi et al., 2008). Nevertheless, we also provide evidence that the western intensification over the Seychelles Dome during winter is mainly driven by the westward strengthening of the Sverdrupian tropical gyre, rather than by localized wind stress forcing. This result confirms a former suggestion by Xie et al. (2002), pointing to the basin-scale wind-driven circulation as accounting for the intensification of the upwelling in the west.

The partitioning of the upwelling ridge into two different domains, the Seychelles Dome and the Chagos Dome, provides further insight in the upwelling response to localized wind stress forcing. In the west, the SD follows a semi-annual cycle, while in the east an annual cycle dominates the rise of the CD. We attribute this difference to the stronger influence of the monsoon winds in the western basin, and the prevalence of the persistent southeasterly trades in the eastern basin. In addition to this novel partitioning, we find that westward-propagating upwelling and downwelling Rossby waves appear to work constructively as remote forcing to the SD and the CD. More intriguing is the source of this asymmetry: annual Rossby waves in the east and semi-annual Rossby waves in the west, geographically separated by a mid-ocean disruption which migrates eastward with increasing latitudes (Wang et al., 2001; Hermes and Reason, 2009). We speculate this asymmetry may be forced by the analogous asymmetry governing the wind stress field of the TSIO but also stress that further research is required to confirm this suggestion. Also the role that the breakdown may be playing in the downstream propagation of wind-forced anomalies through the SEC, westward-flowing within the latitudes of discussion, is unknown and may be worth exploring in future work.

Along the eastern boundary of the upwelling ridge, the arrival of ITW flowing westward while overlying IEW agrees well with downward vertical velocities captured in our analysis as forcing of the CD via w^*.

Broadly speaking, the seasonal shrinkage of the ocean gyre (and the SCTR) is the one feature that differs most when the geostrophic circulation (Figs. 6.4 and 6.10) is compared to the barotropic, wind-driven Sverdrup circulation (Fig. 6.2). Results indicate that discrepancy is due to the seasonal westward propagation of a density front, the Indonesian Throughflow Front. This drives baroclinic, southward geostrophic currents promoting the recirculation of the SECC at longitudes more westward than predicted from the barotropic wind-driven circulation.

Given the above scenario, one may reasonably question whether interannual and interdecadal variability affecting the size of the ITF geostrophic transport (England and Huang, 2005; Potemra and Schneider, 2007; Valsala et al., 2010) may change to some extent the seasonal resizing and circulation patterns described here. Because our findings are based on time-averaged sea-

sonal fields from 22 years of satellite altimeter data and from about 60 years of non-systematic sampling of ocean temperature and salinity data (CARS09), we stress the importance of further study on the possibility that changes in the seasonal ITF may cause changes in the seasonal resizing of the ocean gyre and its associated upwelling ridge. As highlighted in Hermes and Reason (2009), gaps of in situ observations in the historically data-sparse Indian Ocean hamper better understanding of the SCTR region, and by extension, of the ocean gyre.

Modeling efforts have already addressed the interannual variability of the SCTR. Using a coupled climate model, Santoso et al. (2010) analyzed the heat budget components of the Indian Ocean and found that advection and entrainment play an important role in the generation and maintenance of mixed layer temperature anomalies over the SCTR at seasonal and interannual scales. These authors found that warm meridional Ekman advection driven by the winds dominates the heat budget of the SCTR in austral winter–spring, when entrainment becomes small and the thermocline deepens. Additionally Santoso et al. (2010) noted this occurs around the time when the ITF is at a maximum, contributing to the warming primarily to the southeast of the region. These modeling results suggest that our novel description of the upper ocean dynamics of the South Indian tropical gyre (and underlying SCTR) in interaction with the ITF might be suitable for further study at interannual scales with the current state-of-the-art of numerical modeling.

Within the context of the long-term variability, Dilmahamod et al. (2016) have already modelled the biological variability of the SCTR at interannual scales (Dilmahamod et al., 2016). Their analyses show that the SCTR cannot be investigated as a single homogeneous region due to its large spatial distribution and different response mechanisms to climate events. These findings agree well with our observational description of the seasonal South Indian tropical gyre and the SCTR, highlighting the heterogeneity of this sensitive region which lacks on observational studies exploring further the interannual variability of the SCTR and the overlying ocean gyre.

Finally, it must be emphasized that our study of the South Indian tropical gyre is based on its geostrophic and wind-driven Sverdrup circulation patterns. In this regard we stress that a long-term mooring array crossing meridionally the surface tropical gyre would greatly improve our understanding of the upper ocean dynamics, especially along the route of the SECC where predicted Ekman currents oppose geostrophic currents and, hence, a comprehensive view of the total surface circulation demands in situ observations.

7

GENERAL CONCLUSIONS

As mentioned in Chapter 1, our main goal was to improve our understanding of the Western Boundary Current (WBC) system in the Indian Ocean as presently depicted in the literature. To do so, we used a range of observational data sampled *in situ* and remotely from satellites.

With the "know-how" acquired in the first part of this work, Chapters 2–4, we extended our analysis to the poorly studied Brazil Current, the South Atlantic's WBC (Chapter 5). We showed that there is a teleconnection between the dynamics of these two western ocean boundaries which takes place via a highly energetic corridor, forced by fluctuations in the Agulhas Current (AC) retroflection. Another interocean connection, between the Pacific and Indian Oceans, via the Indonesian Throughflow, modulating a seasonal cycle in the South Indian tropical gyre, was studied in Chapter 6.

7.1 ANSWERING THE OPEN QUESTIONS

Each chapter of this thesis was built on the open questions posed in Chapter 1. Now, it is time to recapitulate those questions, summarizing their answers chapter by chapter.

Chapter 2:

> *On average, what is the volume of water carried by the East Madagascar Current? Is this transport marked by a band of variability? If so, what is its forcing?*

The mean velocity and volume transport of the East Madagascar Current (EMC) are estimated to be 79(±21) cm s^{-1} and 18.3(±8.4) Sv, respectively. Both the *in situ* and satellite observations point to a persistent and well organized poleward WBC, i.e. having reduced meandering activity. The events

of intensification and attenuation of the flow are associated with the arrival of anticyclonic and cyclonic eddy-like features from the east. The latter are also responsible for promoting some rare events of equatorward reversal of the flow. The arrival of eddies modulates a dominant, nearly bi-monthly (45–85 days) frequency band of transport variability, which explains about 41% of the transport variance. However, *in situ* observations show that this cycle can be interrupted over time when cyclonic eddies are trapped for a long period at nearly the same location.

Chapter 3:

> *Is the East Madagascar Undercurrent a recurrent oceanographic feature? What is its volume transport and variability?*

The *in situ* data indicate a recurrent East Madagascar Undercurrent (EMUC), observed during 692 of 888 days, hugging the continental slope with a core at an average depth of 1260 m. However, the EMUC can be masked during moments when the EMC appears strong and deep in the water column due to interactions with vigorous anticyclonic eddies. Average velocity and equatorward volume transport are 6.4 ($\pm$4.8) cm s^{-1} and 1.33 ($\pm$1.41) Sv, respectively. Maximum transports reach 6 Sv. The transport time series is marked by two bands of variability: nearly bi-monthly (46–79 days), also observed in the surface EMC, and nearly semi-annual (132–187 days), likely related to the semi-annual cycle in the equatorial winds near the Indian Ocean eastern boundary. The nearly bi-monthly and nearly semi-annual cycles explain about 21% and 27% of the transport variance.

Chapter 4:

> *Is there an oppositely directed poleward North Madagascar Undercurrent flowing beneath the North Madagascar Current? If so, is there a candidate mechanism for forcing this undercurrent?*

A quasi-synoptic transect of horizontal velocities, vertically profiled off northeastern Madagascar, shows the first observational evidence of a North Madagascar Undercurrent (NMUC), which appears with velocities over 0.7 m s^{-1} and volume transport higher than 3 Sv. A cell of coastal downwelling due to Ekman Transport towards the coast has the requirements to force the NMUC

development and its possible persistence, through the mechanism explained by Middleton and Cirano (1999).

Chapter 5:

> *What are the dominant bands of variability, and their respective forcings, of the Brazil Current at the Santos Basin? Does the Agulhas retroflection somehow affect the WBC in the South Atlantic Ocean?*

Two main bands of variability dominate the velocities of the Brazil Current (BC): nearly annual, defined by periods of 319–435 days, and nearly trimonthly, characterized by periods of 87–110 days. The annual period is related to the larger number of cyclonic eddies passing by the Santos Basin during winter, attenuating the BC in this season. On the other hand, less cyclonic eddies interact with the BC in summer, when this current is more intense. Concerning the second question, a highly energetic corridor of trimonthly variability was also found extending from the Agulhas retroflection area towards the Brazilian coast. Within this corridor, phase of altimeter-derived Sea Level Anomaly (SLA) is observed propagating westward. This westward propagation of energy stimulates the trimonthly period observed in the Brazil Current.

Chapter 6:

> *How does the Indonesian Throughflow interact with the annual cycle of the South Indian tropical gyre? And, what are the major forcings modulating the South Indian tropical gyre?*

Our results reveal that besides the basin-scale wind stress curl and the westward propagation of Rossby waves of different periodicity, variability in the South Indian tropical gyre is also largely modulated by the influence of Pacific Ocean waters. In this regard, a prominent zonal shrinkage of the South Indian tropical gyre is found in apparent synchronization with the annual cycle of the Indonesian Throughflow. This occurs as the South Equatorial Countercurrent (SECC), forming the northern boundary of the tropical gyre, recirculates before its arrival to the basin's eastern boundary from winter to spring. This early recirculation of the SECC is due to the seasonal westward propagation of the Indonesian Throughflow Front. This imposes a southward baroclinic geostrophic flow to the SECC, forcing the loop of recirculation at longitudes more westward than expected for the barotropic wind-driven circulation.

7.2 RECOMMENDATIONS

Even though important results were achieved, it is worth to emphasize that our study covers only a few topics while many others were either not addressed or only popped up in passing during the course of this study. This motivates summarizing here topics for future research that were previously posed in the discussion and conclusion sections of the individual chapters. For ease of reference, we will link these recommendations to the corresponding chapter(s) of the thesis, as follows:

Chapter 2:

Both the flow in the Mozambique Channel (MC) and the EMC contribute with water sources to the AC. The AC recirculation itself can also be seen as a third contributor for generating the strongest WBC of the southern hemisphere (Stramma and Lutjeharms, 1997), see Fig. 1.5a. With the ongoing processing of the velocity data from the MC (Section 1.6), also sampled in the INATEX program, it will be possible to quantify the relative contribution of the two upstream sources (MC flow and EMC) to the AC. This comparison can be further improved with support of long-term altimeter-derived geostrophic velocities, by extending the time series and by providing an estimation of the third contributor, the AC recirculation. It has been shown that this product provides a good representation of *in situ* surface velocities of the EMC (Ponsoni et al., 2016) and AC (Krug and Tournadre, 2012). A validation of this product is still lacking for the flow in the MC and AC recirculation.

As mentioned above, there is a good agreement between *in situ* surface velocity and altimeter-based geostrophic velocity. Can we take advantage of this correspondence in order to provide a transport proxy for the EMC covering the entire water column? A first attempt could be made by applying the concepts of "feature models" (FMs) (e.g., Robinson et al., 1988, 1989; Calado et al., 2008; Gangopadhyay et al., 2011). The FMs represent a simple mathematical parameterization of oceanographic features, which can be reconstructed by estimating some parameters in the governing equations. This concept is mostly used for initialization and assimilation in numerical models. For instance, Calado et al. (2008) and Calado et al. (2010) applied this technique, using sea surface data as parameters, to reconstruct the Brazil Current and the upwelling system off southeastern Brazilian coast, respectively, and so assimilate the fields in numerical models. In our case a FM could provide a proxy of the vertical (two dimensional) structure of the EMC by using altimeter-based geostrophic velocity (Fig. 2.14) and the Sea Level Anomaly (Fig. 2.15), which correlate sufficiently well with *in situ* data, to "plug" them into the relevant equations.

Some questions remained open from Ponsoni et al. (2016). For instance: Why do some of the cyclonic eddies arriving near the coast maintain their position for longer than three months, interrupting the EMC's bi-monthly variability, while other vortical features disappear or propagate southward as soon as they interact with the WBC? Do the eddies, which modulate the EMC variability, qualify as "Lagrangian coherent structures", having water trapping ability (Haller, 2002, 2005; Beron-Vera et al., 2008; Samelson, 2012)? Do they "ride" on Rossby waves (Polito and Sato, 2015)? These are important topics that should be addressed in detail in future research.

Chapters 2 and 3:

The results presented in Chapters 2 and 3 show significant variations in the vertical structure of the EMC system. Now, it would be interesting to go deeper into the study of the EMC–EMUC vertical structure and its variability. For future research, it will be relevant, for instance, to analyze the partitioning into barotropic and baroclinic modes over time, as well as to provide a quantitative account of the different vertical modes.

Chapter 3 suggests an upstream shallowing of the EMUC, that can also be perceived as a downstream thickening of the EMC. This suggestion is in agreement with the quasi-synoptic transects presented by Nauw et al. (2008). Additionally, this phenomenon was also reported for the Brazil Current (Rocha et al., 2014), where it occurs due to the depth-dependent bifurcation of the South Equatorial Current (SEC) towards the South Atlantic western boundary (Boebel et al., 1999; Legeais et al., 2013). Chen et al. (2014) argued that in the Indian Ocean the SEC is confined to the upper 400 m and its bifurcation off Madagascar also exhibits a poleward tilting with increasing depth, where the bifurcation, situated at the surface at 17.5°S, shifts to 400 m at 19°S. Since these results are achieved by means of smooth climatological fields, in our opinion a more detailed study of the depth-dependent bifurcation of the SEC off Madagascar, based on (quasi-)synoptic data, is required to answer the question whether the downstream thickening of the EMC and upstream shallowing of the EMUC is indeed related to the SEC bifurcation tilting with increasing depth.

Chapter 4:

Even though we reported the first observational evidence of a NMUC and a potential candidate (downwelling system) for forcing this undercurrent, its persistence and a definitive understanding of its origin can only be confirmed through a study based on continuous *in situ* measurements. This may also lead to a better understanding of the surface North Madagascar Current (NMC),

which also suffers from the lack of a monitoring program. The only continuous *in situ* measurements were performed by Schott et al. (1988), but with a restricted set of instruments, spanning only a few months.

Chapter 5:

In Chapter 5 we showed that there is a teleconnection, via a highly energetic corridor of trimonthly variability, between the western boundaries of the Indian and Atlantic Oceans. Sea Level Anomalies generated during the Agulhas retroflection travel westward and cause the trimonthly cycle observed in the Brazil Current. At their origin, most of the anomalies are characterized as ring-like features, in the literature identified as Agulhas Rings (ARs). The large majority of these anomalies lose their ring-like characteristics before arrival at the BC domain. Additionally, an ongoing discussion in the literature suggests that not all ring-like features (candidate ARs) are water-trapping coherent structures (Beron-Vera et al., 2013). This discussion raises the question whether ARs (or most of them), identified from the SLA fields, are not simply part of a westward propagating Rossby wave? Does the corridor, instead of acting as a mass-conveyor, operate mainly as an energetic pathway for Rossby waves that are forced by periodic, oscillatory motions of the retroflecting AC and that are traversing the Atlantic and impinging on the BC? In that case, the predominant anticyclonic nature of these "ARs" might be due to the background zonal shear flow, perhaps reducing cyclones and amplifying anticyclones. Or are we looking at a mixture of genuine ARs and Rossby waves?

Related to the BC's annual variability, it is not yet clear why in austral winter there are more cyclonic eddies being released at Cape of São Tomé ($\sim$22° S) and Cape Frio ($\sim$22° S), arriving downstream at the Santos Basin, compared to summer. This phenomenon induces a weaker BC in winter.

Chapter 6: Is the South Indian tropical gyre also marked by interannual variability? The answer is: "Yes, it is". Preliminary results are under investigation and the manuscript will be submitted to a peer-reviewed journal (Aguiar-González et al., in preparation).

Chapters 2, 3 and 6:

In Chapter 3 we showed that the semi-annual cycle plays a role in the EMUC variability. When this chapter was published (Ponsoni et al., 2015a) we speculated that this band of variability could be linked to the monsoon wind regime, pronounced over the eastern equatorial Indian Ocean. At that moment, there was not a clear understanding on how this signal propagates to the western boundary and manifests itself in the EMUC. Afterwards, in Section 6 (Aguiar-

González et al., 2016), we explained how the monsoon winds, the Indonesian Throughflow and the South Indian tropical gyre interact and influence the South Indian western boundary. However, further investigation is still needed to understand how this signal manifests itself at subsurface level in the EMUC domain.

Another intriguing point for future research it is to understand why this nearly semi-annual period appears pronounced both subsurface, in the EMUC (Ponsoni et al., 2015a), as well as upstream at surface level, in the NMC (Aguiar-González et al., 2016), while it is not present in the EMC.

7.3 FINAL REMARK: AN ENERGETIC SOUTHERN HEMISPHERE SUPERGYRE

In the General Introduction of this thesis we raised a discussion about the "intriguingly beautiful" interocean teleconnections, which leads to the concept of a Southern Hemisphere Supergyre (Section 1.4). Important connections occur via the Agulhas leakage, Indonesian Throughflow and Tasman leakage, the latter not addressed by this study.

While it is clear that interocean exchanges of water mass occur via the mentioned connections (e.g. Beron-Vera et al., 2013; Aguiar-González et al., 2016), and the Southern Hemisphere Supergyre is somehow embedded in the Meridional Overturning Circulation (Speich et al., 2007), our results strongly suggest that connectivities also occur beyond, as an energetic remote system. For instance, the Indonesian Throughflow modulates the variability of the South Indian tropical gyre (Aguiar-González et al., 2016), which influences the Indian Ocean western boundary, and this in turn also modulates the variability of the Brazil Current, the WBC of the South Atlantic Ocean (Chapter 5).

We close this thesis raising the question: "Is there an *Energetic Southern Hemisphere Supergyre*?" In our perception, the answer is: "Yes, there is". But, as we mentioned in the Introduction, these "intriguingly beautiful" teleconnections are still far from being fully understood.

BIBLIOGRAPHY

Aguiar-González, B., L. Ponsoni, H. Ridderinkhof, H. M. van Aken, W. P. M. de Ruijter, and L. R. M. Maas, 2016: Seasonal variation of the South Indian tropical gyre. *Deep-Sea Res. I*, **in press**.

Amante, C., and B. W. Eakins, 2009: ETOPO1 1 Arc-Minute Global Relief Model: Procedures, Data Sources and Analysis. *NOAA Technical Memorandum NESDIS NGDC-24. National Geophysical Data Center, NOAA. doi:10.7289/V5C8276M*.

Azevedo, J. L. L., D. Nof, and M. M. Mata, 2012: Eddy-Train Encounters with a Continental Boundary: A South Atlantic Case Study. *J. Phys. Oceanogr.*, **42**, 1548–1565.

Beal, L. M., 2009: A time series of Agulhas Undercurrent transport. *J. Phys. Oceanogr.*, **39**, 2436–2450.

Beal, L. M., and H. L. Bryden, 1997: Observations of an Agulhas Undercurrent. *Deep-Sea Res. I*, **44 (9–10)**, 1715–1724.

Beal, L. M., and H. L. Bryden, 1999: The velocity and vorticity structure of the Agulhas Current at 32°s. *J. Geophys. Res.*, **104 (C3)**, 5151–5176.

Beal, L. M., W. P. M. de Ruijter, A. Biastoch, and R. Zahn, 2011: On the role of the Agulhas system in ocean circulation and climate. *Nature*, **472**, 429–436.

Beal, L. M., S. Elipot, A. Houk, and G. M. Leber, 2015: Capturing the Transport Variability of a Western Boundary Jet: Results from the Agulhas Current Time-Series Experiment (ACT). *J. Phys. Oceanogr.*, **45**, 1302–1324.

Beal, L. M., A. Ffield, and A. L. Gordon, 2000: Spreading of Red Sea Overflow Waters in the Indian Ocean. *J. Geophys. Res.*, **105 (C4)**, 8549–8564.

Beron-Vera, F. J., M. J. Olascoaga, and G. J. Goni, 2008: Oceanic mesoscale eddies as revealed by Lagrangian coherent structures. *Geophys. Res. Lett*, **35**, 1–7.

Beron-Vera, F. J., Y. Wang, M. J. Olascoaga, G. J. Goni, and G. Haller, 2013: Objective Detection of Oceanic Eddies and the Agulhas Leakage. *J. Phys. Oceanogr.*, **43**, 1426–1438.

Biastoch, A., L. M. Beal, J. R. E. Lutjeharms, and T. G. D. Casal, 2009: Variability and coherence of the Agulhas Undercurrent in a high-resolution ocean general circulation model. *J. Phys. Oceanogr.*, **39**, 2417–2435.

Biló, T. C., I. C. A. da Silveira, W. C. Belo, B. M. de Castro, and A. R. Piola, 2014: Methods for estimating the velocities of the Brazil Current in the pre-salt reservoir area off southeast Brazil (23° S–26°S). *Ocean Dynam.*, **64**, 1431–1446.

Boebel, O., R. E. Davis, M. Ollitrault, R. G. Peterson, P. L. Richardson, C. Schmid, and W. Zenk, 1999: The intermediate depth circulation of the western South Atlantic. *Geophys. Res. Lett.*, **26 (21)**, 3329–3332.

Bryden, H. L., and L. M. Beal, 2001: Role of the Agulhas Current in Indian Ocean circulation and associated heat and freshwater fluxes. *Deep-Sea Res. I*, **48**, 1821–1845.

Byrne, D. A., A. L. Gordon, and W. F. Haxby, 1995: Agulhas Eddies: A synoptic view using geosat ERM data. *J. Phys. Oceanogr.*, **25**, 902–917.

Calado, L., I. C. A. da Silveira, A. Gangopadhyay, and B. M. de Castro, 2010: Eddy-induced upwelling off Cape São Tomé. *Cont. Shelf Res.*, **30**, 1181–1188.

Calado, L., A. Gangopadhyay, and I. C. A. da Silveira, 2006: A parametric model for the Brazil Current meanders and eddies off southeastern Brazil. *Geophys. Res. Lett.*, **33**, 1–5.

Calado, L., A. Gangopadhyay, and I. C. A. da Silveira, 2008: Feature-oriented regional modeling and simulations (forms) for the western South Atlantic: Southeastern Brazil region. *Ocean Model.*, **25**, 48–64.

Campos, E. J. D., Y. Ikeda, B. M. Castro, S. A. Gaeta, J. A. Lorenzetti, and R. Stevenson, 1996: Experiment studies circulation in the Western South Atlantic. *EOS Trans. AGU*, **27**, 253–259.

Campos, E. J. D., D. Velhote, and I. C. A. da Silveira, 2000: Shelf break upwelling driven by Brazil Current Cyclonic Meanders. *Geophys. Res. Lett.*, **27**, 751–754.

Carter, E. F., and A. R. Robinson, 1987: Analysis models for the estimation of oceanic fields. *J. Atmos. Oceanic Tech.*, **4**, 49–74.

Chapman, D. C., and S. J. Lentz, 1997: Adjustment of stratified flow over a sloping bottom. *J. Phys. Oceanogr.*, **27**, 340–356.

Chapman, P., S. F. DiMarco, R. E. Davis, and A. C. Coward, 2003: Flow at intermediate depths around Madagascar based on ALACE float trajectories. *Deep-Sea Res. II*, **50**, 1957–1986.

Chelton., D., M. G. Schlax, and R. M. Samelson, 2011: Global observations of nonlinear mesoscale eddies. *Prog. Oceanogr.*, **91**, 167–216.

Chelton, D. B., M. G. Schlax, M. H. Freilich, and R. F. Milliff, 2004: Satellite radar measurements reveal short-scale features in the wind stress field over the world ocean. *Science*, **303**, 978–983.

Chelton, D. B., M. G. Schlax, R. M. Samelson, and R. A. de Szoeke, 2007: Global observations of large oceanic eddies. *Geophys. Res. Lett.*, **34**, 1–5.

Chen, Z., L. Wu, B. Qiu, S. Sun, and F. Jia, 2014: Seasonal Variation of the South Equatorial Current Bifurcation off Madagascar. *J. Phys. Oceanogr.*, **44**, 618–631.

Clarke, A. J., and X. Liu, 1993: Observations and dynamics of semiannual and annual sea levels near the eastern equatorial Indian Ocean boundary. *J. Phys. Oceanogr.*, **23**, 386–399.

Condie, S. A., and J. R. Dunn, 2006: Seasonal characteristics of the surface mixed layer in the Australasian region: implications for primary production regimes and biogeography. *Mar. Freshwater Res.*, **57**, 569–590.

Cushman-Roisin, B., and J.-M. Beckers, 2011: *Introduction to Geophysical Fluid Dynamics: Physical and Numerical Aspects*. 2nd ed., Academic Press.

da Silveira, I. C. A., L. Calado, B. M. Castro, M. Cirano, J. A. M. Lima, and A. S. Mascarenhas, 2004: On the baroclinic structure of the Brazil Current–Intermediate Western Boundary Current system at 22°–23°s. *Geophys. Res. Lett.*, **31 (L14308)**, 1–5.

da Silveira, I. C. A., J. A. M. Lima, A. C. K. Schimdt, W. Ceccopieri, A. Sartori, C. P. F. Francisco, and R. F. C. Fontes, 2008: Is the meander growth in the Brazil Current System off Southeast Brazil due to baroclinic instability? *Dyn. Atmos. Oceans*, **45**, 187–207.

de Ruijter, W., 1982: Asymptotic analysis of the Agulhas and Brazil current systems. *J. Phys. Oceanogr.*, **12**, 361–373.

de Ruijter, W. P. M., A. Biastoch, S. S. Drijfhout, J. R. E. Lutjeharms, R. P. Matano, T. Pichevin, P. J. van Leeuwen, and W. Weijer, 1999: Indian-Atlantic interocean exchange: Dynamics, estimation, and impact. *J. Geophys. Res.*, **104 (C9)**, 20 885–20 910.

de Ruijter, W. P. M., H. Ridderinkhof, J. R. E. Lutjeharms, M. W. Schouten, and C. Veth, 2002: Observations of the flow in the Mozambique Channel. *Geophys. Res. Lett.*, **29**, 140–1–140–3.

de Ruijter, W. P. M., H. Ridderinkhof, and M. W. Schouten, 2005: Variability of the southwest Indian Ocean. *Phil. Trans. R. Soc. A*, **363**, 63–76.

de Ruijter, W. P. M., H. M. van Aken, E. J. Beier, J. R. E. Lutjeharms, R. P. Matano, and M. W. Schouten, 2004: Eddies and dipoles around south Madagascar: formation, pathways and large-scale impact. *Deep-Sea Res. I*, **51**, 383–400.

Dilmahamod, A. F., J. C. Hermes, and C. J. C. Reason, 2016: Chlorophyll-a variability in the Seychelles–Chagos Thermocline Ridge: Analysis of a coupled biophysical model. *J. Mar. Syst.*, **154**, 220–232.

DiMarco, S. F., P. Chapman, W. D. Nowlin Jr., P. Hacker, K. Donohue, M. Luther, G. C. Johnson, and J. Toole, 2002: Volume transport and property distributions of the Mozambique Channel. *Deep-Sea Res. II*, **49**, 1481–1511.

Donguy, J. R., and G. Meyers, 1995: Observations of geostrophic transport variability in the western tropical Indian Ocean. *Deep-Sea Res. I*, **42**, 1007–1028.

Donohue, K. A., and J. M. Toole, 2003: A near-synoptic survey of the southwest Indian Ocean. *Deep-Sea Res. II*, **50**, 1893–1931.

Ducet, N., P.-Y. Le Traon, and G. Reverdin, 2000: Global high-resolution mapping of ocean circulation from TOPEX/Poseidon and ERS-1 and-2. *J. Geophys. Res.*, **105**, 19 477–19 498.

Duncan, C. P., 1970: The Agulhas Current. Ph.D. thesis, University of Hawaii, 76 pp.

Emery, W. J., 2001: Water Types and Water Masses. *Encycl. Ocean Sci.*, **6**, 3179–3187.

Emery, W. J., and J. Meincke, 1986: Global water masses: summary and review. *Oceanol. Acta*, **9 (4)**, 383–391.

England, M. H., and F. Huang, 2005: On the interannual variability of the Indonesian Throughflow and its linkage with ENSO. *J. Clim.*, **18**, 1435–1444.

Evans, D. L., and S. S. Signorini, 1985: Vertical structure of the Brazil Current. *Nature*, **315**, 48–50.

Faghmous, J. H., I. Frenger, Y. Yao, R. Warmka, A. Lindell, and V. Kumar, 2015a: A daily global mesoscale ocean eddy dataset from satellite altimetry. *Scientific Data*, **2**, 150 028.

Faghmous, J. H., I. Frenger, Y. Yao, R. Warmka, A. Lindell, and V. Kumar, 2015b: A daily global mesoscale ocean eddy dataset from satellite altimetry. *Dryad Digital Repository*.

Feng, M., and G. Meyers, 2003: Interannual variability in the tropical Indian Ocean: a two-year time-scale of Indian Ocean Dipole. *Deep-Sea Res. II*, **50**, 2263–2284.

Fischer, J., and M. Visbeck, 1993: Deep Velocity Profiling with Self-contained ADCPs. *J. Atmos. Oceanic Tech.*, **10**, 764–773.

Flament, P., 2002: A state variable for characterizing water masses an their diffusive stability: spiciness. *Prog. Oceanogr.*, **54**, 493–501.

Fomin, L. M., 1964: *The Dynamic Method in Oceanography*. Elsevier Publishing Company, Amsterdam, London and New York.

Freilich, M. H., D. G. Long, and M. W. Spencer, 1994: Seawinds: a scanning scatterometer for ADEOS-II-science overview. *In Geoscience and Remote Sensing Symposium, 1994. IGARSS'94. Surface and Atmospheric Remote Sensing: Technologies, Data Analysis and Interpretation., International. IEEE.*, **2**, 960–963.

Gangopadhyay, A., P. F. J. Lermusiaux, L. Rosenfeld, A. R. Robinson, L. Calado, H. S. Kimf, and P. J. H. W. G. Leslie, 2011: The California Current System: A multiscale overview and the development of a feature-oriented regional modeling system (FORMS). *Dynam. Atmos. Oceans*, **52**, 131–169.

Gill, A. E., and P. P. Niiler, 1973: The theory of the seasonal variability in the ocean. *Deep-Sea Res.*, **20**, 141–177.

Godfrey, J. S., 1989: A sverdrup model of the depth-integrated flow for the world ocean allowing for island circulations. *Geophys. Astrophys. Fluid Dynam.*, **45**, 89–112.

Godfrey, J. S., G. R. Cresswell, and F. M. Boland, 1980: Observations of low Richardson numbers and undercurrents near a front in the East Australian Current. *J. Phys. Oceanogr.*, **10**, 301–307.

Goni, G. J., S. L. Garzoli, A. J. Roubicek, D. B. Olson, B. Donald, and O. B. Brown, 1997: Agulhas ring dynamics from TOPEX/POSEIDON satellite altimeter data. *J. Mar. Res.*, **55**, 861–883.

Gordon, A. L., 2001: Interocean Exchange. *Ocean Circulation and Climate: Observing and Modelling the Global Ocean*, Columbia University Academic Commons, 303–314.

Gordon, A. L., 2005: Oceanography of the Indonesian Seas. *Oceanography*, **18**, 14–27.

Gordon, A. L., S. Ma, D. B. Olson, P. Hacker, A. Ffield, L. D. Talley, D. Wilson, and M. Baringer, 1997: Advection and diffusion of Indonesian throughflow water within the Indian Ocean South Equatorial. *Geophys. Res. Lett.*, **24**, 2573–2576.

Gordon, A. L., R. F. Weiss, W. M. Smethie Jr., and M. J. Warner, 1992: Thermocline and intermediate water communication between the south Atlantic and Indian Oceans. *J. Geophys. Res.*, **69**, 97 (C5).

Grundlingh, M. L., 1993: On the winter flow in the southern Mozambique channel. *Deep-Sea Res. I*, **40**, 409–418.

Haller, G., 2002: Lagrangian coherent structures from approximate velocity data. *Phys. Fluids*, **14**, 1851–1861.

Haller, G., 2005: An objective definition of a vortex. *J. Fluid Mech.*, **525**, 1–26.

Harlander, U., H. Ridderinkhof, M. W. Schouten, and W. P. M. de Ruijter, 2009: Longâterm observations of transport, eddies, and Rossby waves in the Mozambique Channel. *J. Geophys. Res.*, **114 (C02003)**, 1–15.

Harris, T. F. W., 1972: Sources of the Agulhas current in the spring of 1964. *Deep-Sea Res. Part A*, **19**, 633–650.

Hellerman, S., and M. Rosenstein, 1983: Normal Monthly Wind Stress Over the World Ocean with Error Estimates. *J. Phys. Oceanogr.*, **13**, 1093–1104.

Hermes, J. C., and C. J. C. Reason, 2008: Annual cycle of the South Indian Ocean (Seychelles–Chagos) thermocline ridge in a regional ocean model. *J. Geophys. Res.*, **113**, C04 035.

Hermes, J. C., and C. J. C. Reason, 2009: The sensitivity of the Seychelles–Chagos thermocline ridge to large-scale wind anomalies. *ICES J. Mar. Sci.*, **66**, 1455–1466.

Hirst, A. C., and J. S. Godfrey, 1993: The role of Indonesian throughflow in a global ocean GCM. *J. Phys. Oceanogr.*, **23**, 1057–1086.

Houry, S., E. Dombrowsky, P. De Mey, and J.-F. Minster, 1987: Brunt-Vaisala and Rossby radii in the South Atlantic. *J. Phys. Oceanogr.*, **17**, 1619–1626.

Hu, D., and M. Cui, 1991: The western boundary current of the Pacific and its role in the climate. *Chin. J. Oceanol. Limnol.*, **9**, 1–14.

Hu, D., and Coauthors, 2013: Direct measurements of the Luzon Undercurrent. *J. Phys. Oceanogr.*, **43**, 1417–1425.

Huhn, F., A. Kameke, V. Pérez-Muñuzuri, M. J. Olascoaga, and F. J. Beron-Vera, 2012: The impact of advective transport by the South Indian Ocean Countercurrent on the Madagascar plankton bloom. *Geophys. Res. Lett.*, **39**, L06 602.

Jury, M. R., and B. Huang, 2004: The Rossby wave as a key mechanism of Indian Ocean climate variability. *Deep-Sea Res. I*, **51**, 2123–2136.

Kalnay, E., and Coauthors, 1996: The NCEP/NCAR 40-Year Reanalysis Project. *Bull. Amer. Meteor. Soc.*, **77**, 437–471.

Kasper, S., M. T. J. van der Meer, I. S. C. neda, R. Tjallingii, G.-J. Brummer, J. S. Sinninghe Damsté, and S. Schouten, 2015: Testing the alkenone d/h ratio as a paleo indicator of sea surface salinity in a coastal ocean margin (mozambique channel). *Org. Geochem.*, **78**, 62–68.

Krug, M., and J. Tournadre, 2012: Satellite observations of an annual cycle in the Agulhas Current. *Geophys. Res. Lett.*, **39**, L15 607.

Kuhlbrodt, T., A. Griesel, M. Montoya, A. Levermann, M. Hofmann, and S. Rahmstorf, 2007: On the driving processes of the Atlantic meridional overturning circulation. *Rev. Geophys.*, **45**, RG2001.

Kundu, P. K., and I. M. Cohen, 2008: *Fuid Mechanics*. Academic Press, Florida.

Lagerloef, G. S. E., G. T. Mitchum, R. B. Lukas, and P. P. Niiler, 1999: Tropical Pacific near-surface currents estimated from altimeter, wind, and drifter data. *J. Geophys. Res.*, **104**, 23 313–23 326.

Le Bars, D., W. P. M. de Ruijter, and H. A. Dijkstra, 2012: A New Regime of the Agulhas Current Retroflection: Turbulent Choking of IndianâAtlantic leakage. *J. Phys. Oceanogr.*, **42**, 1158–1172.

Le Bars, D., H. A. Dijkstra, and W. P. M. de Ruijter, 2013: Impact of the Indonesian Throughflow on Agulhas leakage. *Ocean Sci.*, **9**, 773–785.

Le Bars, D., J. V. Durgadoo, H. A. Dijkstra, A. Biastoch, and W. P. M. de Ruijter, 2014: An observed 20-year time series of Agulhas leakage. *Ocean Sci.*, **10**, 601–609.

Lee, T., I. Fukumori, D. Menemenlis, Z. Xing, and L.-L. Fu, 2002: Effects of the Indonesian throughflow on the Pacific and Indian Oceans. *J. Phys. Oceanogr.*, **32**, 1404–1429.

Legeais, J. F., M. Ollitrault, and M. Arhan, 2013: Lagrangian observations in the Intermediate Western Boundary Current of the South Atlantic. *Deep-Sea Res. II*, **85**, 109–126.

Lukas, R., and E. Firing, 1984: The geostrophic balance of the Pacific Equatorial Undercurrent. *Deep-Sea Res. Part A*, **31**, 61–66.

Lutjeharms, J. R. E., 1988: Remote sensing corroboration of retroflection of the East Madagascar Current. *Deep-Sea Res. Part A*, **35**, 2045–2050.

Lutjeharms, J. R. E., 2006: *The Agulhas Current*. Springer, Berlin.

Lutjeharms, J. R. E., N. D. Bang, and C. P. Duncan, 1981: Characteristics of the currents east and south of Madagascar. *Deep-Sea Res. Part A*, **28**, 879–899.

MacCready, P., and P. B. Rhines, 1993: Slippery bottom boundary layers on a slope. *J. Phys. Oceanogr.*, **23**, 5–22.

Manola, I., F. M. Selten, W. P. M. de Ruijter, and W. Hazeleger, 2014: The ocean-atmosphere response to wind-induced Thermocline changes in the tropical South Western Indian Ocean. *Climate Dynam.*, **45**, 989–1007.

Manola, I., F. M. Selten, H. de Vries, and W. Hazeleger, 2013a: Waveguidability of idealized jets. *J. Geophys. Res.*, **118**, 10,432–10,440.

Manola, I., F. M. Selten, H. de Vries, and W. Hazeleger, 2013b: Drivers of North Atlantic Oscillation Events. *Tellus A*, **65**, 19 741.

Masumoto, Y., and G. Meyers, 1998: Forced Rossby waves in the southern tropical Indian Ocean. *J. Geophys. Res.*, **103**, 27 589–27 602.

Matano, R. P., E. J. Beier, P. T. Strub, and R. Tokmakian, 2002: Large-scale forcing of the Agulhas variability: the seasonal cycle. *J. Phys. Oceanogr.*, **32**, 1228–1241.

Mayer, D. A., and R. H. Weisberg, 1993: A Description of COADS Surface Meteorological Fields and the Implied Sverdrup Transports for the Atlantic Ocean from 30°S to 60°SN. *J. Phys. Oceanogr.*, **23**, 2201–2211.

McCreary, J. P., 1981: A linear stratified ocean model of the coastal undercurrent. *Phil. Trans. R. Soc. Lond.*, **302 (1469)**, 385–413.

McCreary, J. P., and S. Y. Chao, 1985: Three-dimensional shelf circulation along an eastern ocean boundary. *J. Mar. Res.*, **43**, 13–36.

McCreary, J. P., P. K. Kundu, and R. L. Molinari, 1993: A numerical investigation of dynamics, thermodynamics and mixed-layer processes in the Indian Ocean. *Prog. Oceanogr.*, **31**, 181–244.

McCreary, J. P., T. Miyama, R. Furue, T. Jensen, H. W. Kang, B. Bang, and T. Qu, 2007: Interactions between the Indonesian Throughflow and circulations in the Indian and Pacific Oceans. *Prog. Oceanogr.*, **75**, 70–114.

Meinen, C. S., W. E. Johns, S. L. Garzoli, E. van Sebille, D. Rayner, T. Kanzow, and M. O. Baringer, 2013: Variability of the Deep Western Boundary Current at 26.5°N during 2004–2009. *Deep-Sea Res. II*, **85**, 154–168.

Menezes, V. V., H. E. Phillips, A. Schiller, N. L. Bindoff, C. M. Domingues, and M. L. Vianna, 2014: South Indian Countercurrent and associated fronts. *J. Geophys. Res.*, **119**, 6763–6791.

Menezes, V. V., H. E. Phillips, A. Schiller, C. M. Domingues, and N. L. Bindoff, 2013: Salinity dominance on the Indian Ocean Eastern Gyral current. *Geophys. Res. Lett.*, **40**, 5716–5721.

Middleton, J. F., and M. Cirano, 1999: Wind-Forced Downwelling Slope Currents: A Numerical Study. *J. Phys. Oceanogr.*, **29 (8)**, 1723–1743.

Molcard, R., M. Fieux, and A. G. Ilahude, 1996: The Indo-Pacific throughflow in the Timor Passage. *J. Geophys. Res.*, **101**, 12 411–12 420.

Molcard, R., M. Fieux, and F. Syamsudin, 2001: The throughflow within Ombai Strait. *Deep-Sea Res. I*, **48**, 1237–1253.

Moore, D. W., and S. G. H. Philander, 1977: Modeling of the tropical oceanic circulation. *The sea*, **6**.

Morrow, R., and F. Birol, 1998: Variability in the southeast Indian Ocean from altimetry: Forcing mechanisms for the Leeuwin Current. *J. Geophys. Res.*, **103 (C9)**, 18 529–18 544.

Munk, W. H., 1950: On the wind driven ocean circulation. *J. Meteor.*, **7**, 79–93.

Nauw, J. J., H. M. van Aken, A. Webb, J. R. E. Lutjeharms, and W. P. M. de Ruijter, 2008: Observations of the southern East Madagascar Current and undercurrent and countercurrent system. *J. Geophys. Res.*, **113**, 1–15.

New, A. L., S. G. Anderson, D. A. Smeed, and K. L. Stansfield, 2007: On the circulation of water masses across the Mascarene Plateau in the South Indian Ocean. *Deep-Sea Res. I*, **54**, 42–74.

Ollitrault, M., and J. P. Rannou, 2013: ANDRO: An Argo-based deep displacement dataset. *J. Atmos. Oceanic Tech.*, **30**, 759–788.

Olson, D. B., and R. H. Evans, 1986: Rings of the Agulhas Current. *Deep-Sea Res. I*, **33**, 27–42.

Palastanga, V., P. J. van Leeuwen, and W. P. M. de Ruijter, 2006: A link between low-frequency mesoscale eddy variability around Madagascar and the large-scale Indian Ocean variability. *J. Geophys. Res.*, **111**, 1–15.

Palastanga, V., P. J. van Leeuwen, M. W. Schouten, and W. P. M. de Ruijter, 2007: Flow structure and variability in the subtropical Indian Ocean: Instability of the South Indian Ocean Countercurrent. *J. Geophys. Res.*, **112**, 1–11.

Park, Y. H., L. Gamberoni, and E. Charriaud, 1993: Frontal structure, water masses, and circulation in the Crozet Basin. *J. Geophys. Res.*, **C7**, 12 361–12 385.

Pedlosky, J., L. J. Pratt, M. Spall, and K. R. Helfrich, 1997: Circulation around islands and ridges. *J. Mar. Res.*, **55**, 1199–1251.

Percival, D. B., and A. T. Walden, 2006: *Spectral Analysis for Physical Applications*. Cambridge University Press.

Périgaud, C., and P. Delecluse, 1992: Annual sea level variations in the southern tropical Indian Ocean from Geosat and shallow-water simulations. *J. Geophys. Res.*, **97**, 20 169–20 178.

Picaut, J., S. P. Hayes, and M. J. McPhaden, 1989: Use of the geostrophic approximation to estimate time-varying zonal currents at the equator. *J. Geophys. Res.*, **94**, 3228–3236.

Polito, P. S., and O. Sato, 2015: Do eddies ride on Rossby waves? *J. Geophys. Res.*, **120**, 5417–5435.

Ponsoni, L., B. Aguiar-González, L. R. M. Maas, H. M. van Aken, and H. Ridderinkhof, 2015a: Long-term observations of the East Madagascar Undercurrent. *Deep-Sea Res. I*, **100**, 64–78.

Ponsoni, L., B. Aguiar-González, J. J. Nauw, H. Ridderinkhof, and L. R. M. Maas, 2015b: First observational evidence of a North Madagascar Undercurrent. *Dyn. Atmos. Oceans*, **72**, 12–20.

Ponsoni, L., B. Aguiar-González, H. Ridderinkhof, and L. R. M. Maas, 2016: The East Madagascar Current: volume transport and variability based on long-term observations. *J. Phys. Oceanogr.*, **in press**.

Potemra, J. T., and N. Schneider, 2007: Interannual variations of the Indonesian throughflow. *J. Geophys. Res.*, **112**, C05 035.

Quadfasel, D., and G. R. Cresswell, 1992: A note on the seasonal variability of the South Java Current. *J. Geophys. Res.*, **97**, 3685–3688.

Quartly, G. D., J. J. H. Buck, and M. A. Srokosz, 2005: Eddy variability east of Madagascar. *Phil. Trans. R. Soc. A*, **363**, 77–79.

Quartly, G. D., J. J. H. Buck, M. A. Srokosz, and A. C. Coward, 2006: Eddies around Madagascar – The retroflection re-considered. *J. Mar. Syst.*, **63**, 115–129.

Ricciardulli, L., and F. Wentz, 2011: Reprocessed QuikSCAT (V04) Wind Vectors with Ku-2011 Geophysical Model Function, Technical Report 043011. *Remote Sensing Systems, Santa Rosa, CA*, p. 8.

Ridderinkhof, H., and W. P. M. de Ruijter, 2003: Moored current observations in the Mozambique Channel. *Deep-Sea Res. II*, **50**, 1933–1955.

Ridderinkhof, H., P. M. van der Werf, J. E. Ullgren, H. M. van Aken, P. J. van Leeuwen, and W. P. M. de Ruijter, 2010: Seasonal and interannual variability in the Mozambique Channel from moored current observations. *J. Geophys. Res.*, **115 (C06010)**, 1–18.

Ridderinkhof, W., D. Le Bars, A. S. von der Heydt, and W. P. M. de Ruijter, 2013: Dipoles of the South East Madagascar Current. *Geophys. Res. Lett.*, **40**, 558–562.

Ridgway, K. R., and J. R. Dunn, 2007: Observational evidence for a Southern Hemisphere oceanic supergyre. *Geophys. Res. Lett.*, **34**, L13 612.

Ridgway, K. R., J. R. Dunn, and J. L. Wilkin, 2002: Ocean interpolation by four-dimensional weighted least squares-application to the waters around Australasia. *J. Atmos. Oceanic Tech.*, **19**, 1357–1375.

Rintoul, S. R., S. Sokolov, and J. Church, 2002: A 6 year record of baroclinic transport variability of the Atartic Circumpolar Current at 140°E derived from expandable bathythermograph and altimeter measurements. *J. Geophys. Res.*, **107 (C10)**, 19–1–19–22).

Rio, M. H., S. Guinehut, and G. Larnicol, 2011: New CNES–CLS09 global mean dynamic topography computed from the combination of GRACE data, altimetry, and in situ measurements. *J. Geophys. Res.*, **116**, 1–25.

Rio, M. H., S. Mulet, and N. Picot, 2014: Beyond GOCE for the ocean circulation estimate: Synergetic use of altimetry, gravimetry, and in situ data provides new insight into geostrophic and Ekman currents. *Geophys. Res. Lett.*, **41**, 8918–8925.

Risien, C. M., and D. B. Chelton, 2008: A global climatology of surface wind and wind stress fields from eight years of QuikSCAT scatterometer data. *J. Phys. Oceanogr.*, **38 (11)**, 2379–2413.

Robinson, A., M. A. Spall, and N. Pinardi, 1988: Gulf stream simulations and the dynamics of ring and meander processes. *J. Phys. Oceanogr.*, **18**, 1811–1853.

Robinson, A., M. A. Spall, L. J. Walstad, and W. G. Leslie, 1989: Data assimilation and dynamical interpolation in GULFCAST experiments. *Dynam. Atmos. Oceans*, **13**, 301–316.

Rocha, C. B., I. C. A. da Silveira, B. C. Castro, and J. . M. Lima, 2014: Vertical structure, energetics, and dynamics of the Brazil Current System at 22°S–28°S. *J. Geophys. Res.*, **119**, 52–69.

Saji, N. H., S.-P. Xie, and C.-Y. Tam, 2006: Satellite observations of intense intraseasonal cooling events in the tropical south Indian Ocean. *Geophys. Res. Lett.*, **33**, L14 704.

Samelson, R. M., 2012: Lagrangian Motion, Coherent Structures, and Lines of Persistent Material Strain. *Ann. Rev. Mar. Sci.*, **5**, 137–163.

Santoso, A., A. Sen Gupta, and M. H. England, 2010: Genesis of Indian Ocean mixed layer temperature anomalies: A heat budget analysis. *J. Clim.*, **23**, 5375–5403.

Schiller, A., P. R. Oke, G. Brassington, M. Entel, R. Fiedler, D. A. Griffin, and J. V. Mansbridge, 2008: Eddy-resolving ocean circulation in the Asian–Australian region inferred from an ocean reanalysis effort. *Prog. Oceanogr.*, **76**, 334–365.

Schott, F., M. Fieux, J. Swallow, and R. Zantopp, 1988: The boundary currents east and north of Madagascar 2. Direct measurements and model comparisons. *J. Geophys. Res.*, **93 (C5)**, 4963–4974.

Schott, F. A., and J. P. McCreary Jr., 2001: The monsoon circulation of the Indian Ocean. *Prog. Oceanogr.*, **51 (1)**, 1–123.

Schott, F. A., S.-P. Xie, and J. P. M. Jr., 2009: Indian Ocean circulation and climate variability. *Rev. Geophys.*, **47**, 1–46.

Schouten, M., 2001: Indian–Atlantic interocean exchange: variability and controls. Ph.D. thesis, Utrecht University.

Schouten, M. W., W. P. M. de Ruijter, and P. J. van Leeuwen, 2002a: Upstream control of Agulhas Ring shedding. *J. Geophys. Res.*, **107**, 23–1–23–11.

Schouten, M. W., W. P. M. de Ruijter, P. J. van Leeuwen, and H. A. Dijkstra, 2002b: An oceanic teleconection between the equatorial and southern Indian Ocean. *Geophys. Res. Lett.*, **29**, 59–1–59–4.

Shenoi, S. S. C., P. K. Saji, and A. M. Almeida, 1999: Near-surface circulation and kinetic energy in the tropical Indian Ocean derived from Lagrangian drifters. *J. Mar. Res.*, **57**, 885–907.

Shi, C., and D. Nof, 1993: The splitting of eddies along boundaries. *J. Mar. Res.*, **51**, 771–795.

Shi, C., and D. Nof, 1994: The Destruction of Lenses and Generation of Wodons. *J. Phys. Oceanogr.*, **24**, 1120–1136.

Shi, S., J. Ribbe, T. Cowan, and W. Cai, 2007: A dataset of the wind-driven global ocean circulation for climate research. *In: 14th National Conference of the Australian Meteorological and Oceanographic Society, 5-8 Feb 2007, Adelaide, Australia.*, URL http://eprints.usq.edu.au/id/eprint/1914.

Siedler, G., M. Rouault, and J. R. E. Lutjeharms, 2006: Structure and origin of the subtropical South Indian Ocean Countercurrent. *Geophys. Res. Lett.*, **33**, 1–5.

Song, Q., A. L. Gordon, and M. Visbeck, 2004: Spreading of the Indonesian Throughflow in the Indian Ocean. *J. Phys. Oceanogr.*, **34**, 772–792.

Soutelino, R. G., A. Gangopadhyay, and I. C. A. da Silveira, 2013: The roles of vertical shear and topography on the eddy formation near the site of origin of the Brazil Current. *Cont. Shelf Res.*, **70**, 46–60.

Speich, S., B. Blanke, and W. Cai, 2007: Atlantic meridional overturning circulation and the Southern Hemisphere supergyre. *Geophys. Res. Lett.*, **34**, L23 614.

Sprintall, J., J. Chong, F. Syamsudin, W. Morawitz, S. Hautala, N. Bray, and S. Wijffels, 1999: Dynamics of the South Java Current in the Indo-Australian Basin. *Geophys. Res. Lett.*, **26**, 2493–2496.

SSALTO/DUACS, 2015: SSALTO/DUACS User Handbook: (M)SLA and (M)ADT Near-Real Time and Delayed Time Products CLS-DOS-NT-06-034. Tech. Rep. 4.4, SALP-MU-P-EA-21065-CLS.

Steinhardt, J., C. Cléroux, L. J. de Nooijer, G.-J. Brummer, R. Zahn, G. Ganssen, and G.-J. Reichart, 2015: Reconciling single-chamber Mg/Ca with whole-shell δ 18O in surface to deep-dwelling planktonic foraminifera from the Mozambique Channel. *Biogeosciences*, **12**, 2411–2429.

Steinhardt, J., C. Cléroux, J. Ullgren, L. de Nooijer, J. V. Durgadoo, G.-J. Brummer, and G.-J. Reichart, 2014: Anti-cyclonic eddy imprint on calcite geochemistry of several planktonic foraminiferal species in the Mozambique Channel. *Mar. Micropaleontol.*, **113**, 20–33.

Stewart, R. H., 2008: *Introduction to Physical Oceanography*. Orange Grove Texts Plus, Florida.

Stommel, H., 1948: The westward intensification of wind-driven ocean currents. *Eos Trans. AGU*, **29**, 202–206.

Stommel, H., 1958: The abyssal circulation. *Deep-Sea Res.*, **5**, 80–82.

Stramma, L., and J. R. E. Lutjeharms, 1997: The flow field of the subtropical gyre of the South Indian Ocean. *J. Geophys. Res.*, **102**, 5513–5530.

Suginohara, N., 1982: Coastal Upwelling: Onshore–Offshore Circulation, Equatorward Coastal Jet and Poleward Undercurrent over a Continental Shelf-Slope. *J. Phys. Oceanogr.*, **12**, 272–284.

Suginohara, N., and Y. Kitamura, 1984: Long-Term Coastal Upwelling over a Continental Shelf-Slope. *J. Phys. Oceanogr.*, **14 (6)**, 1095–1104.

Sverdrup, H. U., 1947: Wind-Driven Currents in a Baroclinic Ocean; with Application to the Equatorial Currents of the Eastern Pacific. *Proc Natl Acad Sci U S A.*, **5**, 318–326.

Swallow, J., M. Fieux, and F. Schott, 1988: The boundary currents east and north of Madagascar 1. Geostrophic currents and transports. *J. Geophys. Res.*, **93 (C5)**, 4951–4962.

Swallow, J. C., and L. V. Worthington, 1961: An observation of a deep countercurrent in the Western North Atlantic. *Deep-Sea Res.*, **8**, 1–19.

Tchernia, P., 1980: *Descriptive Regional Oceanography*, Vol. 1. Pergamon.

Tilburg, C. E., H. E. Hurlburt, J. J. O'Brien, and J. F. Shriver, 2001: The dynamics of the East Australian Current system: The Tasman Front, the East Auckland Current, and the East Cape Current. *J. Phys. Oceanogr.*, **31**, 2917–2943.

Tippins, D., and M. Tomczak, 2003: Meridional Turner angles and density compensation in the upper ocean. *Ocean Dyn.*, **53**, 332–342.

Tomczak, M., and J. S. Godfrey, 2003: *Regional Oceanography: an Introduction*. 2nd ed., Daya Publishing House.

Torrence, C., and G. P. Compo, 1998: A practical guide to wavelet analysis. *Bull. Am. Meteorol. Soc.*, **79 (1)**, 61–78.

Turner, J. S., 1973: *Buoyancy effects in fluids*. Cambridge University Press, 368 pp.

Ullgren, J. E., H. M. van Aken, H. Ridderinkhof, and W. P. M. de Ruijter, 2012: The hydrography of the Mozambique Channel from six years of continuous temperature, salinity, and velocity observations. *Deep-Sea Res. I*, **69**, 36–50.

Vallis, G. K., 2006: *Atmospheric and Oceanic Fluid Dynamics*. Cambridge University Press, Berlin.

Valsala, V., S. Maksyutov, and R. Murtugudde, 2010: Possible interannual to interdecadal variabilities of the Indonesian throughflow water pathways in the Indian Ocean. *J. Geophys. Res.*, **115**, C10 016.

Valsala, V. K., and M. Ikeda, 2007: Pathways and effects of the Indonesian Throughflow water in the Indian Ocean using particle trajectory and tracers in an OGCM. *J. Clim.*, **20**, 2994–3017.

van Aken, H. M., 2007: *The Oceanic Thermohaline Circulation: An Introduction*. Springer, New York.

van Aken, H. M., H. Ridderinkhof, and W. P. M. de Ruijter, 2004: North Atlantic Deep Water in the south-western Indian Ocean. *Deep-Sea Res. I*, **51**, 755–776.

van Aken, H. M., A. K. van Veldhoven, C. Veth, W. P. M. de Ruijter, P. J. van Leeuwen, S. S. Drijfhout, C. P. Whittle, and M. Rouault, 2003: Observations of a young Agulhas ring, Astrid, during MARE in March 2000. *Deep-Sea Res. II*, **50**, 167–195.

van Sebille, E., J. Sprintall, F. U. Schwarzkopf, A. Sen Gupta, A. Santoso, M. H. England, A. Biastoch, and C. W. Böning, 2014: Pacific-to-Indian Ocean connectivity: Tasman leakage, Indonesian Throughflow, and the role of ENSO. *J. Geophys. Res.*, **119**, 1365–1382.

Visbeck, M., 2002: Deep Velocity Profiling Ising Lowered Acoustic Doppler Current Profiler: Bottom Track and Inverse Solutions. *J. Atmos. Oceanic Tech.*, **19 (5)**, 794–807.

Wang, L., C. J. Koblinsky, and S. Howden, 2001: Annual Rossby wave in the southern Indian Ocean: Why does it "appear" to break down in the middle ocean? *J. Phys. Oceanogr.*, **31**, 54–74.

Warren, B. A., T. W. III, and J. H. LaCasce, 2002: Forced resonant undulation in the deep Mascarene Basin. *Deep-Sea Res. II*, **49**, 1513–1526.

Weijer, W., 2008: Normal modes of the Mascarene Basin. *Deep-Sea Res. I*, **55 (1)**, 128–136.

Wijffels, S. E., G. Meyers, and S. Godfrey, 2008: A 20-Yr Average of the Indonesian Throughflow: Regional Currents and the Interbasin Exchange. *J. Phys. Oceanogr.*, **38**, 1965–1978.

Woodberry, K. E., M. E. Luther, and J. J. O'Brien, 1989: The wind-driven seasonal circulation in the southern tropical Indian Ocean. *J. Geophys. Res.*, **94**, 17 985–18 002.

Wyrtki, K., 1961: Scientific results of marine investigations of the South China Sea and the Gulf of Thailand 1959–1961. *NAGA report, vol. 2*, **2**.

Wyrtki, K., 1971: *Oceanographic Atlas of the International Indian Ocean Expedition*. National Science Foundation, Washington, D.C.

Wyrtki, K., 1973: Physical Oceanography of the Indian Ocean. In: Zeitzschel, B., Gerlach, S.A. (Eds), The Biology of the Indian Ocean. *Ecol. Stud.*, **3**, 18–36.

Xie, S.-P., H. Annamalai, F. A. Schott, and J. P. McCreary Jr., 2002: Structure and Mechanisms of South Indian Ocean Climate Variability. *J. Clim.*, **15**, 864–878.

Yokoi, T., T. Tozuka, and T. Yamagata, 2008: Seasonal variation of the Seychelles Dome. *J. Clim.*, **21**, 3740–3754.

Yoshida, K., 1959: A Theory of Cromwell Current (the Equatorial Undercurrent) and of the Equatorial Upwelling – An Interpretation in a Similarity to a Costal Circulation. *J. Oceanogr. Soc. Japan*, **15 (4)**, 159–170.

Zhai, X., H. L. Johnson, and D. P. Marshall, 2010: Significant sink of ocean-eddy energy near western boundaries. *Nature Geosci.*, **3**, 608–621.

ACKNOWLEDGMENTS

It's been three years since I started my PhD at NIOZ and Utrecht University under the guidance of Prof. Leo Maas. It was quite an intense experience, but really worth and pleasant as well. Mainly, thanks to my supervisor. I could list hundreds of reasons why I am grateful to Leo, but I would run out of space so that better to stick to only few of them. Leo accepted to guide me after I had a bad experience in another university, when I was obliged to quit and restart a new PhD with a very limited fellowship-time. During these years he has been always available and managed somehow to keep me motivated since my first day at NIOZ. His prompt corrections, critical suggestions, scientific rigor and insightful ideas were inspiring and crucial for making this thesis a reality.

At the same time, working close to Borja also made things much easier. Doubtless, our almost daily discussions and mutual colaboration substantially improved and strengthen the final version of this document.

I would like to thank Herman Ridderinkhof for trusting me with the data processing/analysis of the INATEX moorings, for making possible my participation in the Ocean Sciences Meeting 2014 and in an oceanographic cruise on board the R.V. Algoa. Thanks to Hendrik van Aken for his advices, as well as to Jenny Ullgren for the tips on the data processing, at the very beginning of this journey. Will de Ruijter was always a source of inspiration during our meetings at IMAU.

I am twice grateful to Taco de Bruin. First, because he was the one who suggested me to contact Leo when I was looking for a new PhD program. Second, because he offered me an one-year job at the Data Management Group – NIOZ when my scholarship finished in Nov/2014. Without this position things would be much harder. Thanks to Theo Gerkema for the two months (Jan and Feb/2015) contract with the Physical Oceanography Department – NIOZ. Thanks to Geert-Jan Brummer for the great time during the ASCA cruise. I also want to express my gratitude to Janine Nauw for teaching me a bit more about coastal oceanography and opening new possibilities for my carrier.

I have been living in big cities almost my whole life and suddenly moving to Texel was an enjoyable experience. I had a lot of fun on this pretty island in the North Sea. There, I met many nice people. For all the coffee breaks, lunches at the canteen, dinners, beers, escapes to the beach, cycling in the forest, soccer and volleyball matches, thanks to Allert, Andrea, Andres,

Anna, Carol, Carola, Cathy, Costanza, Eelke, Eric, Felipe, Femke, Fred, Ingmar, Irene, Isabela, Jan Dirk, Jan Nieuwenhuis, Jan van Gils, Jenny, Jie, Jolanda, Jurra, Karlos, Kristina, Laura, Marlies, Marten Tacoma, Martina, Matias, Maxi, Meinard, Olga, Rick, Rodrigo, Rudolf, Thomas Richter, Roald, Ronald de Koster, Roeland, Paolo, Sander, Sarina, Sérgio, Stéfani, Sven, Wil Sistermans and many others who made my stay on Texel unforgettable.

I could not fail to mention my former colleagues/friends in Belgium: Jo Randall, Qunyan Ren and Olivier Carrière. They were great company and really supportive. Also in Belgium, a big thanks to my Brazilian and Greek friends: Ari, Bruno, Dudu, Matina, Miriam, Pablo, Paco, Pavlo, Vaia and Vassilis.

It may sounds ridiculous, but one of the most loyal company during these years was a small sweet/angry Australian budgie called Kiwi, so it is fair to mention her here as well.

In Brazil, I would like to thank my former supervisor Ilson Silveira. He was the first, even before me, to realize that it was about time to leave from my previous PhD program. I almost killed him in a car accident, but he insisted on being my friend. I am suspicious that he will deny new rides. Thanks to Leandro Calado and Paulo Polito who supported my scholarship application.

I am the luckiest person to have the family I have. Even living thousands of kilometers away, they have never let me feel alone. Thanks mom, dad, grandma, Adriana, Rogério, Cidinha, Belli and Miguel.

Finally, I have no words to express my gratitude to Aliki. BY FAR, she was the best part of this journey.

This document was typeset using an adapted version of `classicthesis` developed by André Miede.

Final Version as of 30th May 2016 at 9:59.

CURRICULUM VITAE

Leandro Ponsoni was born in São Paulo, Brazil, on the 1st of March 1980. He doesn't remember exactly why but since an early age his dream was to become an oceanographer. Maybe due to the trips to Caraguatatuba (a beautiful city on the coast of São Paulo state), influenced by Jacques Cousteau expeditions or even amazed by Amyr Klink adventures. Notwithstanding, sometimes life goes in another direction. At the age of 16 he started to work at the juridical department of "Porto Seguro Cia. de Seguros Gerais", a Brazilian insurance company, and stayed there for 6 years. Concomitantly, in 2000, he started a bachelor degree in Law. However, that old idea didn't disappear and few years later he decided to pursue his dream. He then dropped the job and the studies in Law to start the bachelor in Oceanography at the University of São Paulo (USP) in 2003. From this year until 2010 he remained at the Oceanographic Institute of USP, concluding the bachelor degree and Master thesis in Physical Oceanography, as well as participating in several oceanographic cruises, research projects and stages in different fields of this multidisciplinary science. In 2005 Leandro was the founder of the "Projeto Descobrindo o Mar". This still ongoing volunteer project shares oceanographic knowledge with students from elementary school in Brazil with the aim of empowering them as 'Ocean Literate' citizens. This project already reached more than 50000 students. In 2009, during his master thesis, Leandro had the opportunity to visit the "Servicio de Hidrografía Naval" from the Argentinian Navy, in Buenos Aires, for about one year. After, in the last days of 2010 he moved to Belgium in order to start a PhD in Acoustic Oceanography at the "Université libre de Bruxelles" (ULB). ~~Un~~fortunately, things didn't work out over there and he had the great privilege to restart his PhD research at the Royal Netherlands Institute for Sea Research – NIOZ, which originates this thesis, to be defended at the Utrecht University. From December/2014 to December/2015, parallel with his PhD research, Leandro was appointed as data manager of the National Ocean and Coastal Research Programme (in Dutch: ZKO). This document represents one step towards into the future and the next will follow.